Development of a Biplanar Fluoroscopy System for Characterizing in vivo Foot and Ankle Biomechanics

Eric Thorhauer

A dissertation

submitted in partial fulfillment of the

requirements for the degree of

Doctor of Philosophy

University of Washington

2024

Reading Committee:

William R. Ledoux, Chair

Mohammad Malakooti

Duane Storti

Program Authorized to Offer Degree:

Department of Mechanical Engineering

University of Washington

Abstract

Development of a Biplanar Fluoroscopy System for Characterizing in vivo Foot and Ankle Biomechanics

Eric Thorhauer

Chair of the Supervisory Committee:

William R. Ledoux

Department of Mechanical Engineering

Precise quantification of lower extremity skeletal kinematics during functional tasks is paramount to impactful foot biomechanics research. A custom biplane system for dynamic imaging of the entire foot and ankle complex during gait is presented as a hardware solution to this challenge, as well as the necessary software for preprocessing the data and performing marker-based and model-based tracking from the stereo fluoroscopy images. Additionally, this dissertation explores the accuracy of foot bone models generated from computed tomography scans, comparing the performance of cone beam and fan beam scanners. The findings support the adoption of low-dose cone beam weight-bearing computed tomography for 3D modeling of foot and ankle bones and for generating the digitally reconstructed radiographs needed for model-based tracking of gait trials. The morphology and motion of the first ray is also quantified using

weightbearing computed tomography scans to provide data towards a standardized first metatarsophalangeal joint coordinate system. Finally, this dissertation explores the feasibility of indirectly assessing the intricate biomechanical behavior of the plantar soft tissues of the foot as a natural shock absorber and load-bearing interface by tracking the calcaneus. The spatial and temporal resolutions afforded by biplane fluoroscopy coupled with the methods outlined in this work will contribute to the advancement of the field of lower extremity biomechanics, as these kinematic data underpin various clinical investigations of in vivo function.

Table of Contents

Chapter 1

Biplane fluoroscopy for assessing foot and ankle biomechanics

Eric Thorhauer[1,2] and William Ledoux, PhD[1,2,3]

[1]RR&D Center for Limb Loss and Mobility (CLiMB), Veterans Affairs Puget Sound Health Care System, Seattle, WA 98108

Departments of [2]Mechanical Engineering and [3]Orthopaedics & Sports Medicine, University of Washington, Seattle, WA 98195

Keywords: X-ray Stereophotogrammetry; Biplane Fluoroscopy; Model-based tracking; Marker-based tracking; Foot bone kinematics

Abstract

In the time since Wilhelm Roentgen first accidently made X-ray images of his wife Anna's hand, radiographic technologies have gradually evolved to allow for dynamic imaging of the foot and ankle. In this chapter, we discuss how biplane fluoroscopy systems have been developed and modified specifically with the aim of overcoming the obstacles of quantifying full dynamic foot and ankle biomechanics that are associated with motion capture or computed tomography technologies. Biplane systems can precisely resolve the motions of small foot bones, and they are commonly synchronized with force plates, electromyography systems, and motion capture as part of a multifaceted biomechanical assessment strategy. As noted below, biplane systems have improved from pairs of simple stock intact C-arm fluoroscopy units, to the modification of these stock systems, to fully custom fluoroscopy suites. The initial obstacles of developing and validating hardware and software as well as the challenges involved in administering in vivo foot and ankle studies present exciting challenges and avenues of research that draw on contributors from a variety of technical backgrounds. This chapter provides a general overview of both the biplane hardware and software, and their application to a variety of clinical issues related to ambulation and in revealing the intricate functions of the foot and ankle. The future uses of biplane systems include assessments of joint arthrokinematics, ligament deformations, and soft tissue strains to address both fundamental and complex questions related to foot function, which will serve to elucidate foot and ankle biomechanics and undoubtedly generate valuable insights for clinicians and researchers alike for decades to come.

Introduction

Biplane systems afford the ability to see inside the foot, revealing the motions of all the bones instead of grouping them into kinematic segments like traditional retroreflective motion capture requires. Furthermore, biplane fluoroscopy derives bone motion directly from the imaging instead of inferring it from skin-mounted markers that potentially introduce errors [1, 2]. Compared to other medical imaging modalities like computed tomography (CT), magnetic resonance imaging (MRI) or ultrasound, biplane fluoroscopy has an adequate combination of capture volume size, temporal resolution, and spatial resolution for quantifying subtle differences in 3D bone motion with minimal aliasing. Flexibility in the geometry of biplane fluoroscopy capture volumes permit testing of dynamic, functional tasks by removing obstacles to test subjects like gantry beds and scanning bores. The full power of biplane systems is leveraged when synchronized with other acquisition systems (electromyography, force plates, motion capture, etc.) to round out a more complete biomechanical analysis that can frame the biplane-derived data in the context of the subject's whole-body kinematics and kinetics (e.g., compensation or off-loading strategies or trunk posture). Together, these tools paint a more complete picture of the biomechanical roles of the foot in our daily activities.

The ionizing radiation that is received from two fluoroscopy sources and a CT scan during biplane testing present risk to both subjects and lab personnel. By adhering to ALARA (as low as reasonably achievable) principles [3], biplane systems can ethically and effectively be used for longitudinal in vivo human biomechanical research studies. With proper planning, it is possible to minimize exposure to subjects and staff while simultaneously fulfilling the research needs of producing usable image data that balance and respect the risks involved in radiography. These risks are best addressed in the study design and protocols, but also in the design of the

laboratory layout itself including but not limited to: X-ray shielding and aiming strategies, pre-planning system geometry in virtual biplane software, attempts at dose estimation for subjects, the deliberate and careful selection of X-ray imaging parameters, and the development of software solutions that move towards a reduction in total dose. Two hardware technologies that drastically reduce total dose are pulsed X-ray generators instead of continuous biplane sources, and the newest high-efficiency detector CT systems. A strategy of total dose reduction makes the best use of an IRB-approved dose allowance, and any reduction from that limit facilitates the collection of more trials of the subjects' motion. More trials can better quantify the variation in motion for a given joint or body or assess a different task or a variable of interest (e.g., orthotic elevation or brace stiffness). While the doses subjects receive from biplane imaging equipment are well below the currently recognized thresholds for developing cancers based off of conservative risk estimates [4, 5], dose reduction is still motivated from an ethical standpoint since these exposures are for the purposes of research and not medical diagnostics. Continued advancements in hardware and software will jointly reduce long-term risks to subjects while addressing the challenges of tracking bones in noisy fluoroscopy images and segmenting bones from low-dose CT scans that are inherently noisier than traditional clinical scans.

While the design, execution, and processing of biplane fluoroscopy foot and ankle studies present many technical challenges, the benefits of these efforts are deeply rewarding. Acting as a bridge between the research and clinical realms, biplane laboratories draw on the skills of engineers from a variety of backgrounds to address these obstacles. To effectively answer clinical research questions, the engineers need to foster cooperation and mutual respect with multiple types of clinicians that can aid study design focused around their subjects and ALARA principles. These technologies will continue to evolve, so this chapter cannot possibly cover all

the intricacies of biplanar fluoroscopy. However, we hope it serves as a starting point to motivate collaboration between engineers and clinicians alike to broaden and deepen the impact of this technology on the field of foot and ankle biomechanics research.

Background and history of biplane fluoroscopy

Overview of how X-ray imaging works:

Exploitation of the attenuating properties of X-rays for the purposes of medical imaging was pioneered shortly after Wilhelm Roentgen's initial discovery in 1895. Depending on the composition of the tissue and the energetics of the incident beam, X-rays leaving the source undergo a variety of transport and interaction phenomena with the subject [6]. X-rays may be completely absorbed, attenuated and transmitted on to the detector, or blocked or scattered into a new trajectory. Absorbed rays contribute to subject radiation dose, and subsequently risks associated with ionization radiation. Scattered rays can contribute to image noise. The degree of attenuation for X-rays passing through the subject onto the detector is influenced by the mass density properties of the tissues and the incident beam energetics. The increased attenuation through bony tissues relative to the surrounding soft tissues is what is exploited in radiography to form the familiar X-ray projections. Similar principles are at work in CT imaging, which uses many X-ray back projections from varying angles to reconstruct a full three-dimensional (3D) volume of voxels (i.e., the volumetric equivalent to a pixel) each assigned a Hounsfield Unit related to the tissue's X-ray attenuation properties relative to water. X-ray source parameters like tube voltage and current, and firing rate are adapted to the study of interest with the concurrent goals of maximizing the usable information in the biplane images while adhering to ALARA

principles. These settings may be carefully selected prior to living subjects imaging via experimental testing on cadaveric surrogates simulating the activity of interest and adapted on a per subject basis.

Overview biplane system history and evolution

Biplane X-ray systems were developed in the 1930s [7], driven by the needs of surgeons performing advanced procedures, who greatly benefitted from the real-time imaging afforded by fluoroscopy and the extra spatial information obtained from a second orthogonal X-ray view. In the 1970s, Selvik and colleagues pioneered RSA or "Roentgen stereophotogrammetric analysis" for quantifying subtle migrations of implants in orthopedic patients [8-10]. The technology was next adapted to address orthopaedic questions related to skeletal motion [11-13]. While the methods and techniques associated with biplane X-ray systems for surgical use are a great starting point for developing a powerful tool for biomechanics research, there are limitations and considerations that require extensive modification of original equipment manufacturer (OEM), medical-purpose biplanar and single-plane imaging systems, namely their configurability into arbitrary capture volumes and their sampling rate. As researchers pursue questions related to the dynamic behavior of the foot during tasks like gait or stair navigation, these initial imaging systems will continue gradual evolutions in both hardware and software to address early limitations in bone tracking. Although not directly applicable to the foot and ankle, it should be noted the single and biplane fluoroscopy systems have demonstrated biases and precisions during bone-based tracking on the order of sub mm and degree [12, 14-16].

Intact C-arm systems for foot bone tracking

Early efforts to implement fluoroscopy systems for quantifying foot motion utilized intact C-arm fluoroscopy units that are commonly used intraoperatively and in clinical settings [17, 18]. Manufactured by long-established medical imaging technology companies, these systems mount the X-ray source and image detector on a fixed C-shaped gantry, and include accompanying software and hardware for acquiring and viewing the images. Their fixed source-to-detector distance and the presence of the C-shaped gantry structure impose physical constraints on the types of subjects, anatomy, and functional activities that may be assessed in such a system.

Disarticulated C-arm systems for foot bone tracking

To overcome these constraints, researchers disarticulated the X-ray sources and detectors, mounting them on custom gantries or supports, and opening new opportunities for the kinds of studies possible [19-21]. For example, prior to disarticulation of biplane systems, only quasi-static approximations of gait were possible. Subjects can now walk unimpeded through disarticulated systems.

Custom dedicated biplane hardware for foot bone tracking

The next evolution of biplane systems was to replace the X-ray sources and detectors of the standard fluoroscopy suites; these devices were often developed to study other parts of the body and subsequently used to quantify foot motion [22-24]. By eliminating the physical C-arm, and increasing the source-to-detector distance, more powerful sources are required to produce

images with usable quality. However, the flexibility of these designs allowed for improvements in the hardware, including: larger detectors with sufficiently fast response times, more configurable X-ray sources and system geometry, pulsed fluoroscopy and varying sampling rates, and the use of high-speed cameras at increasing resolutions.

Other techniques for tracking foot bone kinematics

Although it is growing in popularity, biplane fluoroscopy is still somewhat of a niche technology. As of the latest data available (mid-2020), there were less than 50 biplane laboratories worldwide [25], and only about a dozen groups that have studied the foot and ankle (see below). Prior to the implementation of biplane fluoroscopy, foot bone motion has been tracked using near infra-red cameras and retro-reflective markers [26, 27], but these techniques require grouping multiple bones together into simpler rigid bodies. Moreover, skin motion artifact is a major concern at the foot and ankle. Finally, attaching markers to skin requires that subjects walk either barefoot or in severely compromised shoes, which precludes the study of the effects of footwear or orthoses. Despite the growing number of studies using retro-reflective foot models, this technique is ill-suited to study specific foot joints.

Other technologies have been employed to quantify foot bone motion. Marker-based X-ray stereophotogrammetry has been used to evaluate the orientations of the bones of the foot in multiple static positions via implanted tantalum balls and a specialized apparatus [28-31]. Time-sequence magnetic resonance imaging (MRI) has also been used to explore foot bone orientation [32-35]. Both of these techniques are limited by the static nature of the data collections. Retro-reflective markers mounted on bone pins have also been used to quantify foot bone motion during walking and slow running [36-39], however, the invasiveness of this methodology limits

its utility to the research lab and precludes clinical studies. Moreover, none of these techniques work with footwear. In summary, current technologies to track foot bone motion, including: surface markers, marker-based X-ray stereophotogrammetry, time-sequence MRI, or bone pins, are ill-suited to measure barefoot and shod foot bone kinematics.

Biplane fluoroscopy can track 3D joint positions accurately and avoid the inherent errors of marker placement and skin motion artifact present in retro-reflective motion analysis using skin-mounted markers. Single plane (i.e., 2D) fluoroscopy has been used to study heel pad deformation [40], hindfoot kinematics [41], and the effects of various immobilization techniques on ankle motion [42]. 2D fluoroscopy techniques work well in-plane, but are not as accurate out-of-plane. And while the simplicity, flexibility, and utility of using a single fluoroscope is obvious and attractive, the complex anatomy of the foot—with many small, overlapping bones—and the importance of 3D motion, requires a biplane system.

Hereafter, we will review the biplane systems that have been employed to quantify foot bone motion; systems used to study other parts of the body will not be discussed.

Challenges specific to foot and ankle tracking with biplane fluoroscopy

In order to quantify foot bone motion in an assortment of tasks, a biplane system must be configurable into capture volumes that do not impede or alter natural subject motion and, preferably, avoid or minimalize the beams directly hitting the more radiation sensitive anatomical regions. Allowing for six degree-of-freedom positioning of both the X-ray sources

and detectors, however, requires a larger testing space for the equipment and protocols for enforcing proper beam-detector alignment. Subject-specific planning in aiming the biplane system can improve the usability of the fluoroscopy images and reduce subject radiation dose.

Characterizing the motion of each bone in the foot during a full gait cycle in a single trial is only possible when the X-ray image detector is large enough to capture human adult anatomy while also allowing for the small deviations in foot placement from the center of the biplane system capture volume, and fast enough to image moving subjects without blur. Early C-arm based fluoroscopy systems have maximum detector sizes (31 cm) that necessitate the capture of multiple trials specifically targeting the forefoot or hindfoot in isolation, and maximum frame rates (~15-30Hz) that limit assessments to slow or quasi-static activities. Additionally, the X-ray sources must be precisely and consistently controlled to start and stop firing at the appropriate instants to minimize subject dose while still ensuring the motion of interest was captured. This triggering can be initiated by force plate-based gait events (e.g., heel strike or foot placement), optoelectrical switches aimed across the subjects' path of progress, or manually by the system operator.

In many studies of the ankle and hindfoot, oblique sagittal views of the foot are adequate. This greatly simplifies the laboratory setup; all the components can be placed in the same plane as the floor. If the study design warrants imaging the forefoot or the foot in its entirety, the necessary hardware is more involved. A custom walkway traversing a biplane pit (Figure 1.1) has been designed at Veterans Affairs Hospital Puget Sound Center for Limb Loss and Mobility (CLiMB) that is configurable into multiple walkway setups for assessing linear gait, turning tasks, stair negotiation, and more. A panel in the target volume portion of the walkway is made from carbon fiber that does not appear on the fluoroscopic images. The corners of the panels are

mounted with load cells to capture the ground reaction forces. Custom supports hold the X-ray detectors under the walkway as close to the foot as possible and an overhead structure supports the sources without impeding subject motion.

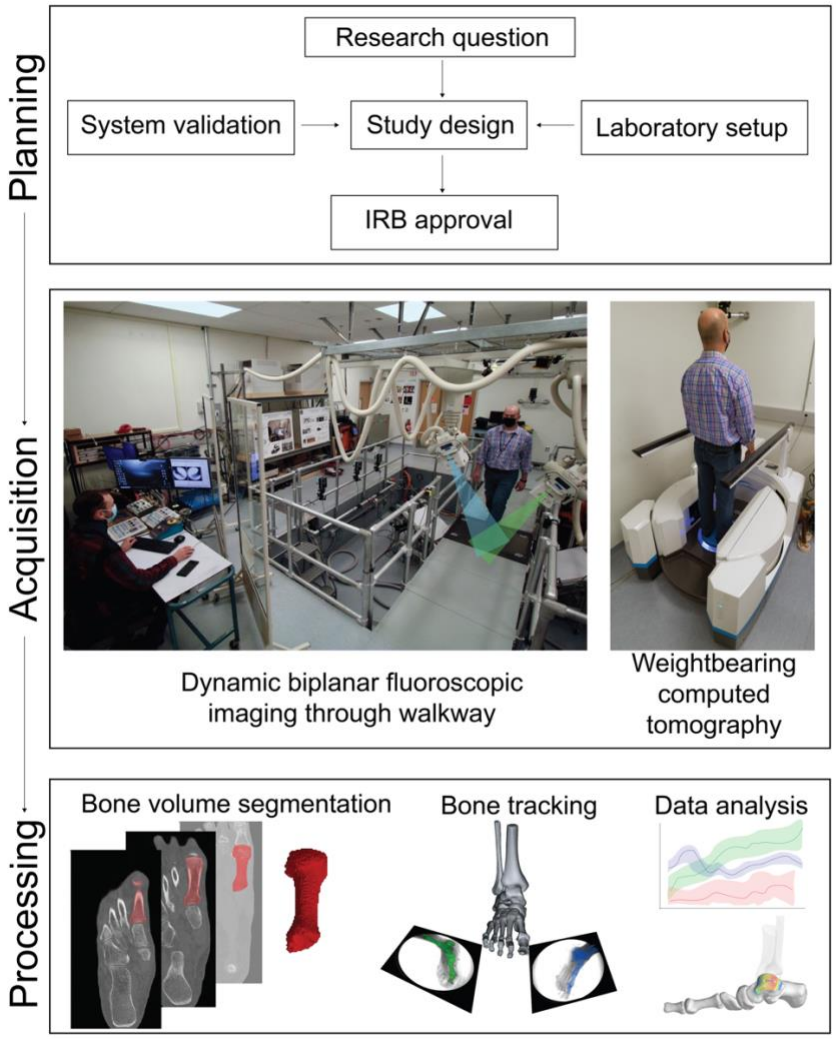

Figure 1.1: An overview of the biplane process from study inception and design during the planning phase, through the acquisition phase utilizing the biplanar fluoroscopy and computed tomography imaging systems, and finally the processing phase of generating useful biomechanical data from the image data. Careful decision-making during study planning and

quality assurance measures during the acquisition phase save considerable time and effort at the complex stages of data processing.

Overview of biplane hardware

The imaging chain of a dedicated custom biplane system consists of an X-ray source and an image intensifier paired with a high-speed digital camera (Figure 1.2). X-ray image intensifier technology was introduced at the end of the 1940s, and despite some technical considerations overviewed below, works adequately for this application. Modern flat panel detectors (FPD) have a high quantum detector efficiency that reduce the dose required to form a useable image without spatial distortions [43-45]. While this technology will continue to evolve, presently, FPD's that are large enough area to image the entire foot are only offered with sampling rates that are inadequate for capturing gait. Consequentially, this section will only detail systems based on the proven coupling of X-ray image intensifiers and high-speed video cameras that permit blur-free imaging of dynamic whole foot function.

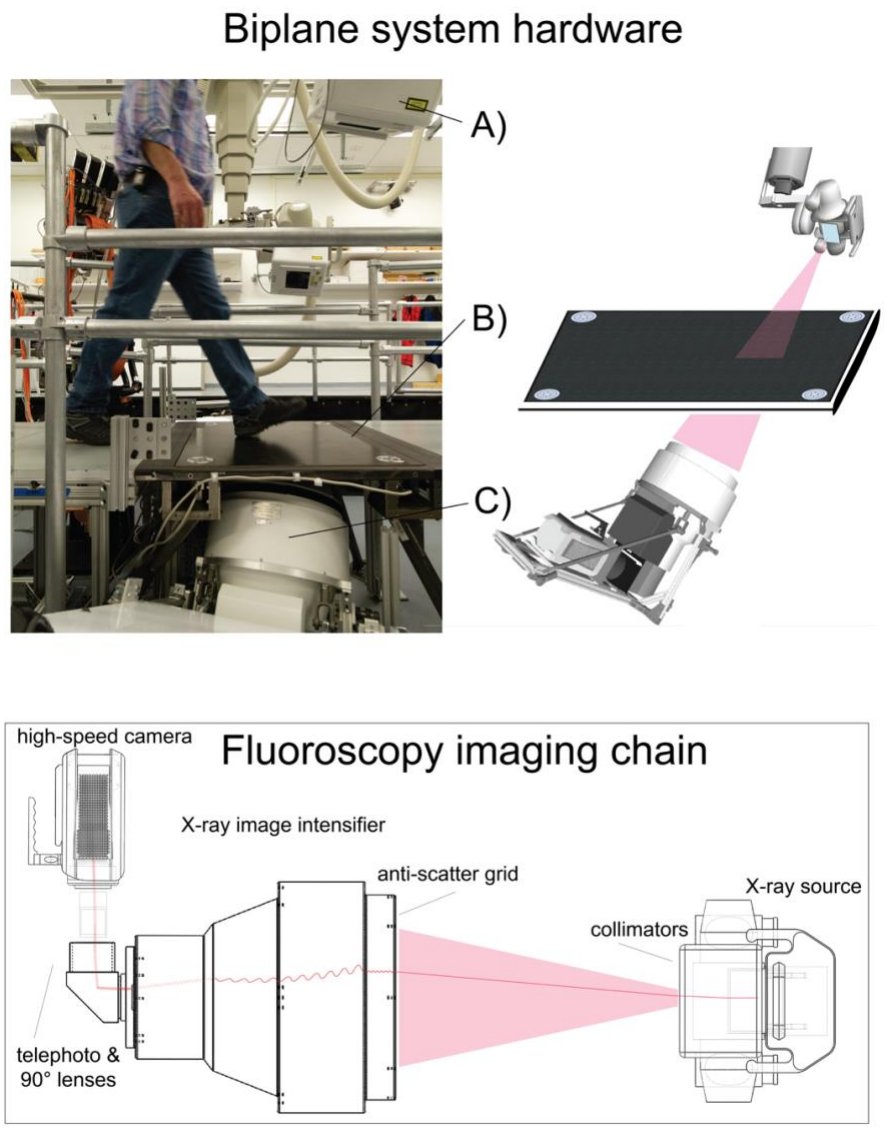

Figure 1.2: An overview of the Center for Limb Loss and MoBility (CLiMB) biplane system hardware, namely: (A) gantry-mounted pulsed X-ray sources, (B) walkway with an X-ray-transparent force plate, and (C) image intensifier and high-speed camera chain. Collimators and anti-scatter grids are utilized to reduce the exposed subject area and cross-scatter, and to improve image quality. The X-ray image intensifier converts the X-ray signal into a visible light signal that is directed to the sensor of a high-speed camera with an array of lenses.

X-ray sources on custom biplane systems can be fully independently controlled in terms of aiming and beam parameters like current (mA), tube potential (kV), continuous vs pulsed beam firing, pulse width/exposure time, collimation, and internal filtering. The latest X-ray generators create precisely synchronized pulses from both biplane sources while the high-speed cameras are triggered at the optimal interval to capture the fluoroscopy images leaving the image intensifiers without appreciable motion blur or detector lag. Collimators allow for shaping of the primary beams to reduce scatter noise incident on the other detector and avoid exposure to anatomical regions of subjects that are not under investigation. Internal filters impede low-energy portions of the polychromatic beam spectrum not strong enough to penetrate the subject and reach the detectors to form an image. This filtering of the beam, also known as “hardening”, also increases contrast between tissues by effectively increasing the mean beam potential by omission of these weaker components. Exiting the sources and passing the filtration and collimators, X-rays proceed towards the image intensifier assembly losing intensity following the inverse square law. At the image intensifier face they are filtered again by anti-scatter grids that act to block incoming scattered rays from oblique angles that contribute to image noise. These grids are optimized for fixed source-to-detector distances. The passing portions of the signal are next absorbed by the image intensifier input screen and converted first into light photons then electrons following a Poisson noise process. In the evacuated tube of the image intensifier body, internal magnetic fields guide the signal of electrons towards the anode of the output phosphor screen where they are converted into visible green light emitted out of back of the image intensifier. By condensing the input signal of the image intensifier face (e.g., 30-40 cm diameter) into a smaller output signal (e.g., 7.5 cm diameter), a minification gain is achieved that amplifies the overall image brightness by several orders of magnitude. This output signal is re-directed via

a 90° lens (to reduce the physical depth requirements of the biplane pit beneath the walkway) with a high-speed cine grayscale video camera with a telephoto lens (>2MP, >100Hz, exposure time <1.5ms). The electron trajectory within the evacuated image intensifier body is highly susceptible to interference from the presence of external electromagnetic fields (i.e., Earth's field and lab equipment) and metal in structures supporting the biplane system and walkway. Additionally, the cine camera lens also introduces optical distortions as a function of its lens geometry, selected aperture and focusing. This corruption of the fluoroscope images, manifest as spatial "S-curve" and pincushion distortion patterns, must be rectified in software in order to accurately reconstruct 3D position in a process known as "distortion correction" [46-48]. A distortion correction map is generated by imaging a known grid object placed directly against the image intensifier input screen. Mathematical models are used to warp and interpolate the distorted raw biplane fluoroscope signals into usable spatially rectified images [49-56]. Additionally, the intensity of the fluoroscope image is not uniform in illumination due to the roll-off characteristics and fewer incident X-rays at the image intensifier periphery. To correct the pixel intensities, which are especially important to model-based bone tracking algorithms, a flatfield correction is required in software to compensate for the dimming image edges [57]. To reconstruct the geometry of the biplane system in software, a camera calibration process is required each time the system configuration is altered or re-aimed [58].

To perform the model-based tracking software procedure (outlined in the following section), volumetric subject-specific bone models are needed from CT scans. Currently, highly efficient low dose weightbearing computed tomography scanners are available for laboratory and clinical application to the foot and ankle [59, 60]. These bilateral foot scans are acquired in under two minutes and at a fraction of the radiation dose (typically < 4 mrem) of clinical scanners

(typically 20 mrem). The dose received from clinical CT scanning typically represents the largest single contribution to the total received dose of biplane test subjects. By reducing the CT dose, more of an IRB-approved per-subject radiation dose budget may be used in biplane trials characterizing motion variation, other tasks, or a longitudinal assessment. By utilizing weightbearing scans, the foot can be assumed to have taken on its usual shape in response to load, and the relative positions of bones in this configuration may be used as a reference configuration to define initial static joint spacings, ligament lengths, and weightbearing kinematics.

Overview of biplane software

Specialized software is required to take the raw biplanar fluoroscopic image sequences, process them into a usable form, reconstruct the laboratory camera geometries, and to finally track objects in 2D space to infer their 3D poses [61] (Figure 1.3). The first steps in the software pipeline address the intensity inhomogeneities and spatial distortions imparted on the fluoroscope data by the image intensifier and video lens. The intrinsic and extrinsic camera parameters that describe the biplane imaging chains are derived from a multi-frame calibration procedure that utilizes bundle adjustment to optimize for minimal reprojection errors [62]. Having performed this preprocessing, the virtual biplane software can then be used to track objects in 3D lab space. *Marker-based tracking* software detects the 2D centroids of X-ray attenuating fiducial marker spheres (beads) on the image pairs. Essentially a modern digitized form of the pioneering radiostereometric analyses, marker-based methods offer the highest degree of kinematic accuracy and have been used to quantify the motion of bones, implants, and soft tissues, however the invasive procedure of rigidly embedding markers into subjects has restricted in vivo use to special cases [28-31]. *Model-based tracking* software optimally aligns

simulated radiographic projections of a volumetric bone model derived from a statistical model or via subject-specific imaging like CT or MRI. After an initial pose guess is provided in the virtually reconstructed biplane system, the volumetric bone models are perturbed in six degrees of freedom iteratively in an optimization routine, and simulated X-ray images, called digitally reconstructed radiographs (DRRs), are projected onto the rectified fluoroscopic image pairs (Figure 1.4). The cost function of this optimization is driven by image similarity metrics typically based on image intensity values or edges that correspond to anatomical osseous features. Extensive user intervention is required during the model-based tracking process, as solutions may fall into local optima or be confounded by the presence of implants, lab hardware, sensors, shoes, and image noise and scatter in the fluoroscope sequences. While model-based tracking is more computationally expensive and slightly less accurate kinematically compared to marker-based tracking, it avoids invasive procedures of marker injection or bone pin fixation on test subjects. These restrictions are greatly reduced in cadaveric testing, and marker-based tracking has been used to validate the precision and accuracy of model-based tracking algorithms [20].

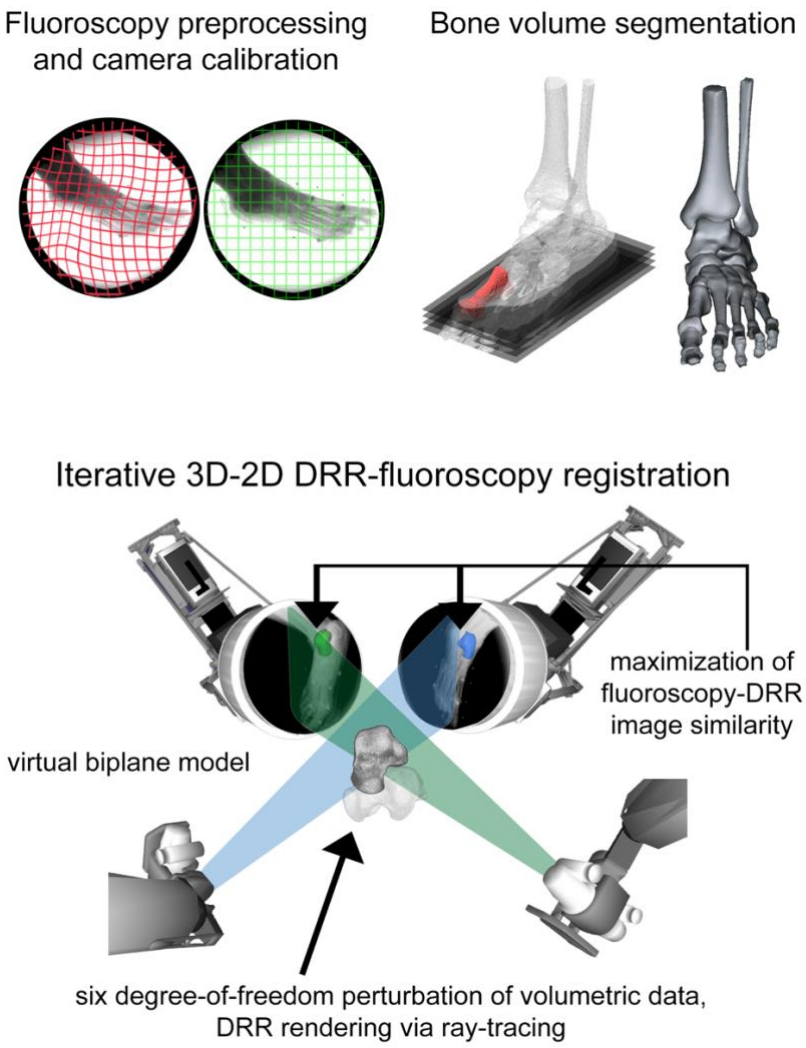

Figure 1.3: The first step of model-based bone tracking involves rectifying the errors imparted on the fluoroscopy images by the image intensifier system and segmenting the bones to be tracked from computed tomography volumes. The biplane system is virtually recreated from a camera calibration procedure and the volumetric bone data manipulated in the reconstructed capture volume while ray-tracing algorithms generate simulated X-ray images called digitally reconstructed radiographs (DRR). The pose of the bone is reconstructed when the simulated X-ray projections maximally match the stereo fluoroscopy data.

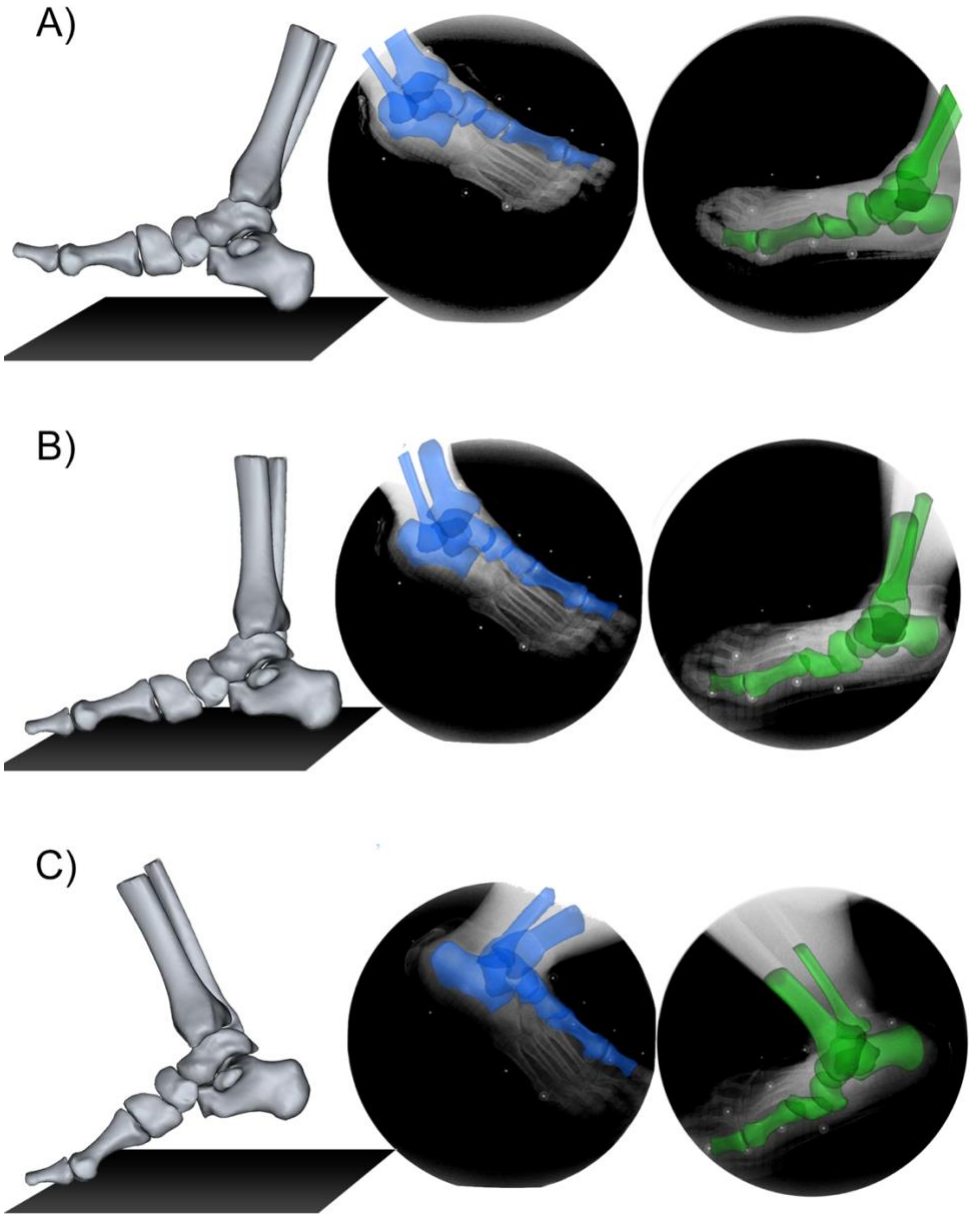

Figure 1.4: Model-based tracking can resolve the three-dimensional positions and orientations of the foot and ankle bones during human gait, including the phases of (A) initial contact, (B) midstance, and (C) terminal stance. The hindfoot and first ray motions are shown reconstructed (left) following the iterative model-based tracking alignment with the stereo fluoroscopy images (right).

Computed tomography scans offer the best contrast between bony and non-bony tissues for the purposes of segmentation. Segmentations of the foot and ankle bones from CT scans are most accurately performed manually or semi-manually, exploiting the knowledgebase of experienced technicians familiar with the bones of interest. However, manual segmentations are time consuming and can form processing bottlenecks in studies with large cohorts or many bones to track. Researchers have made efforts to automate the segmentation process with statistical shape models and machine learning methods for initializing new segmentations based on previously segmented training data [63]. These automated segmentations at the very least provide good initial segmentations that can be manually refined by technicians. Acceptable levels of CT bone segmentation errors have not been rigorously established for model-based tracking, particularly in the context of DRR similarity to the underlying fluoroscope images, anatomical coordinate systems based on the CT bone models, or arthrokinematic measures like joint spacing.

Clinical biplane foot and ankle studies

Biplane fluoroscopy has been employed to explore all ki clinical questions. As the kinds of analyses and variables from biplane systems grow, research thrusts can expand into clinical cohorts that have been unserved or seen limited research due to technological limitations. As a means of organizing previous work, studies will be grouped by the hardware employed.

Biplane systems consisting of two C-arms

The research group at Massachusetts General Hospital (MGH) was one of the first teams to use biplane fluoroscopy to quantify foot bone motion (Figure 11.5A). Their initial study reported normal ankle joint kinematics for five subjects in three static positions (heel strike, midstance, and foot flat) [17]. Fluoroscopy data were collected on two OEC 9800 ESP General Electric (GE) C-arms and volumetric bone scans were collected on a 1.5T GE MRI system. Bone position was manually manipulated in custom software until the projected cortical outlines matched the underlying fluoroscope images. The same methodology was extended to estimate ankle cartilage contact area [64] and cartilage strain [65]. Once the bones of interest from the MRI data were aligned, the overlap of the segmented cartilage models defined the articular contact area; average contact area was reported for nine subjects [64]. The depth of the cartilage overlap was used to calculate compressive strain, which was determined for six subjects [65]. This system was then extended to estimate the lengths of the anterior talofibular and calcaneofibular ligaments as the shortest distances between the centroids of the digitized attachment areas [66]. Finally, the same system was used to demonstrate aberrant ankle joint kinematics in six subjects with unilateral post-traumatic ankle arthritis [67].

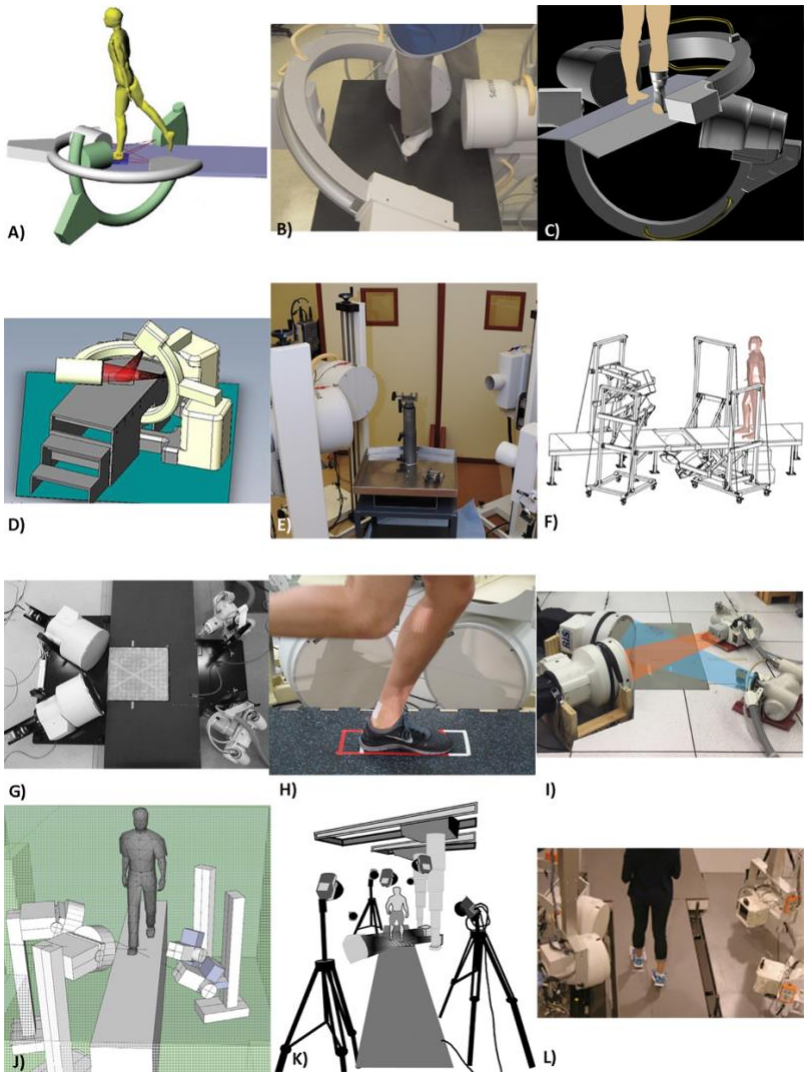

Figure 1.5: (A) Schematic of two OEC 9800 ESP General Electric C-arms at Massachusetts General Hospital [17]; (B) Two Philips Pulsera C-arms at Duke University [68]; (C) Schematic of two Philips BV Pulsera C-arms at Fudan University in Shanghai [69]; (D) Schematic of two Siemens SIREMOBIL Compact-L mobile C-arms at Western University in London, Ontario [70]; (E) Two modified Philips BV Pulsera C-arms at the Steadman Philippon Research Institute [71]; (F) Schematic of two modified Philips BV Pulsera C-arms at the VA Puget Sound; (G) Two modified GE OEC 9000 fluoroscopy systems at Marquette University [72]; (H) Two EMD Technologies pulsed X-ray generators (not shown) and two Shimadzu image intensifiers at

Henry Ford Health Systems [22]; (I) Two Varian X-ray emitters and two Dunlee image intensifiers at the University of Utah [73]; (J) Schematic of a Gemss Medical biplane system at Chung-Ang University in Seoul, Republic of Korea [24]; (K) Schematic of two EMD X-ray generators and two Shimadzu image intensifiers at Brown University [74]; (L) Two EMD high-frequency cardiac cineradiographic generators and two 40 cm Thales image intensifiers at the University of Pittsburgh [75].

A second group at Duke University used a system similar to the MGH set up consisting of two C-arms (Philips Pulsera) and an MRI (Siemens Trio 3T) to study foot bone kinematics (Figure 11.5B). They found increased translation and rotation in anterior talofibular ligament (ATFL)-deficient ankles compared to contralateral normal ankles as subjects stepped onto a level surface [18]. A similar methodology was employed for seven patients with unilateral chronic lateral ankle instability (CAI) [68]. Cartilage strain was calculated based upon the overlap of talar and tibial cartilage. CAI ankles were found to have increased strain compared to the contralateral control limb. Finally, seven patients underwent surgical repair for lateral ankle instability [69]. Post-surgical ankles exhibited significantly less motion while stepping onto a force plate; there was no difference the post-surgical ankles and the contralateral normal ankles.

A third research team, based at Fudan University in Shanghai, used dual fluoroscopes to study ankle motion, but they employed computed tomography (CT) scans (GE Lightspeed) rather than MRI scans for the volumetric bone models [70]. Eleven subjects with CAI were enrolled and imaged with two BV Pulsera (Philips) C-arms (Figure 11.5C) at 30Hz while walking along a flat floor and a 15-degree inversion platform with and without an ankle brace.

The silhouettes of the 3D bone models were semi-automatically matched to the fluoroscopy data at seven key poses during stance. Subtalar joint motion was more inverted when walking barefoot on inversion platform; this motion decreased when the brace was worn. The same group used this technology to study ankle kinematics during five key poses of stair descent for ten controls, ten subjects with functional ankle instability (FAI), and ten lateral ankle sprain copers [71]. In general, the FAI subjects had excessive tibiotalar inversion and subtalar joint hypermobility, while the copers had a stable subtalar joint with tibiotalar inversion only at foot strike.

Finally, a group from Western University in London, Ontario also employed a similar system consisting of two 23 cm fluoroscopes (SIREMOBIL Compact-L mobile C-arms, Siemens, Figure 11.5D). Model-based bone tracking was conducted by generating 3D bone models from an a priori CT scan. The bone models were matched to the edges on the X-ray data by manual manipulation using custom-developed software. This system was used to quantify foot shape (i.e., arch height defined by the calcaneus, navicular, and first metatarsal) across foot type both statically and dynamically for cavus, normal, and planus feet [72]. Next, the team applied the same technique to explore the effect of hard and soft custom foot orthoses using the same foot types and output parameters [73]. The arch shape was significantly different for the custom orthotics conditions, but not the OEM device, as compared to the barefoot and shod conditions.

Biplane systems consisting of two modified C-arms

The systems from MGH, Duke, Shanghai, and London, ON were all essentially OEM C-arms with stock imaging software that were positioned so that a subject could load their foot while be imaged. As such, there are some inherent hardware limitations (e.g., the physical imposition of the "C" support) that precluded uninhibited gait and software limitations (e.g., the sampling rate) that prevented blur-free imaging. To address these specific issues, several groups based the Steadman Philippon Research Institute, VA Puget Sound, and Marquette University developed systems that removed the image intensifiers and X-ray sources from the C-arms and mounted them on custom support stands. Further, the stock cameras were replaced by high-speed video cameras. Steadman Philippon tracked the motion of the calcaneus and tibia for six subjects walking barefoot and shod [19], demonstrating that subjects have different hindfoot motion while wearing shoes. They used BV Pulsera (Philips) C-arms with 30-cm image intensifiers that had been modified by removing the "C", mounting on custom stands (Figure 11.5E), and adding high-speed digital cameras (Phantom V5.1, Vision Research). Model-based RSA software was use to align 3D bone models with bony contours from the fluoroscopes.

A second group with a similar hardware to Steadman Philippon was the VA Puget Sound; they also employed modified BV Pulsera C-arms with Phantom V5.1 high speed cameras and custom support stands (Figure 11.5F). Their initial work consisted of both a marker-based and a bone-based validation for foot bone tracking [20, 61]. Model-based bone tracking software was written in-house and used digital reconstructed radiographs (DRRs) to match 3D bone positions with the 2D fluoroscopy data.

A third research team from Marquette University has conducted several biplane studies with two modified GE OEC 9000 fluoroscopy systems with high-speed video cameras attached (Figure 11.5G). By tracking two points per bone on the calcaneus and talus in the fluoroscopy data, and synchronizing a Vicon retroreflective motion analysis system, motion of the tibiotalar and subtalar joint was determined for 13 subjects [21]. This group also reported the design, calibration, evaluation, and limitations of a single plane version of their system [74], and explored the effect of cross-scatter contamination in biplane fluoroscopy [75]. Next, the system was employed to quantify the effect of short and tall controlled ankle movement (CAM) boots on the talocrural and subtalar joints [76]. It was found that both CAM boots limited motion at both joints. The group validated the bias and precision errors of their model-based tracking algorithm by tracking a cadaver foot embedded with fiducial beads through the system [77]. Finally, the system was used to compare barefoot to shod kinematics in 13 healthy subjects [78], demonstrating that biplane systems could quantify bone motion while subjects wore shoes.

Biplane systems consisting of independent X-ray sources and image intensifiers

A research team based at the Henry Ford Health Systems used a biplane system consisting of 100 kW pulsed X-ray generators (EMD Technologies CPX 3100CV) and two 30 cm image intensifiers (Shimadzu Medical Systems, model AI5765HVP, Figure 11.5H) and custom DRR-based model tracking software [15] to study foot bone motion. The first study compared barefoot running to both an ultra flexible training shoe and motion control shoe, finding subtle difference in the tibiotalar and subtalar joints between the various conditions for 12 normal subjects during over ground running [22]. Next, the navicular drop height for the same

three shoes was studied for 12 subjects during over ground running; there was no change in navicular drop magnitude but with a slower navicular drop rate for the motion control shoes [79].

The University of Utah group has conducted several foot and ankle biplane studies, with the initial hard setup consisting of two Varian X-ray emitters (Housing B-100/Tube A-142) and two 30 cm Dunlee image intensifiers (T12964-P/S), each mounted to a dedicated base around a treadmill. After an initial marker-based validation [23] of their bone tracking software [15], they used their biplane system to explore the potential for using retro-reflective skin-markers for tracking tibiotalar and subtalar joint motion [80]. This system also elucidated the complex 6 degree-of-freedom relationship between the tibiotalar and subtalar joints on ten normal subjects [81], demonstrating that the tibiotalar joint was responsible for sagittal plane motion, while the subtalar joint facilitated coronal and transverse plane motion, with some sagittal plane motion as well. Expanding their work to study four patients with CAI, they preliminarily demonstrated the aberrant kinematics of this pathologic population [82].

Reconfiguring their system around a force plate instead of a treadmill (Figure 11.5I), the Utah group next described a methodology for quantifying tibiotalar kinematics after a total ankle replacement (TAR) by leverage computer-aided design (CAD) models [83]. The reconfigured hardware system was then employed to retrospectively study ten subjects with an ankle arthrodesis [84]. By comparing to the unaffected contralateral limb, it was shown that subtalar joint plantarflexion is the primary compensatory mechanism after ankle arthrodesis. Finally, the biplane system was used to evaluate a multi-segment foot model [85], demonstrating that skin-marker motion is similar to biplane motion for the ankle and midfoot.

Researchers based primarily at Chung-Ang University in Seoul, Republic of Korea, used a biplane system (KMC-1400ST, Gemss Medical, Figure 11.5J) and edge-based 3D/2D

registration to track the tibia, talus, and calcaneus for ten healthy subjects [24]. They reported normal motion of the tibiotalar and subtalar joints. This system was next employed to study the relative movement of the articular surfaces of the tibiotalar and subtalar joints for 18 normal subjects [86]. Both joints demonstrated significant translational and rotational motion in early stance phase, but only the subtalar joint had significant rotational movement in late stance. The midtarsal joint locking mechanism was then explored on the same 18 subjects [87]. The data demonstrated that the midtarsal joint had continuous motion towards the extreme poses in terminal stance, failing to indicate any reduced motion or locking. Finally, this group used their biplane system to compare the hindfoot kinematics of five flat foot subjects to the 18 normal subjects previously studied [88]. The flat foot subjects had larger peak motions and ranges of motion at several joints, demonstrating abnormal kinematics during mid-stance and terminal stance.

A collaborative research effort involving investigators from Australia, Canada, and the United States has conducted biplane foot studies with hardware consisting of two X-ray generators (EMD Technologies CPX 3100CV) and two image intensifiers (Shimadzu Medical Systems, model AI5765HVP, Figure 11.5K), optically coupled to synchronized high-speed video cameras (Phantom IV, Vision Research). DRRs derived from CT scans were projected on the X-ray images and manually manipulated for each bone and participant using an open sources software package [89]. Their first study compared biplane videography to optical motion capture [90], and demonstrated that comparable solutions could be obtained in the sagittal plane, but out-of-plane motion should be carefully considered. Next, the team explored the intra- and inter-rater reliabilities of the system [91], and found root-mean-square errors from 2 to 3 mm and 2 to 3 degrees. Finally, the team used the biplane system to validate a constrained multi-segment foot

model based on OpenSim [92]. The model was contrasted to a conventional multi-segment foot model and found to be more accurate.

Building on their long track record in biplane fluoroscopy, the research team at the University of Pittsburgh has applied their expertise to the foot and ankle. Using a system that consists of two 150-kV constant potential high-frequency cardiac cineradiographic generators (EMD CPX-3100CV, EMD Technologies) and two high-speed digital cameras (4 megapixel phantom v10; Visions Research, Wayne NJ) coupled to 40 cm Thales image intensifiers (Figure 11.5L). Two subjects has metal beads implanted in their tibia, fibula, talus, and calcaneus, and then bead-based validation of the bone-based tracking, achieved by automatically manipulating DRRs to maximize image correlation, was conducted [93]. Errors were less than 1 mm in translation and less than 2 degrees of rotation. Next, this group evaluated 4 techniques for generating hindfoot bone coordinate systems [94]. Rotations as defined by these systems were compared to the functional axes (i.e., helical axes of rotation) determined from biplane radiography. Finally, this team explored kinematic differences at the tibiotalar and subtalar joints due to sex and dominant vs. non-dominant limb in 20 healthy adults [95].

Additionally, several other research teams have conducted biplane foot and ankle studies. A group from Keio University has used a custom biplane system with X-ray sources and flat panel detectors to study cadaveric feet in static loading conditions [96-98]. A Taiwanese research team has developed a refined two-step bone tracking technique they validated on a single cadaver foot [99]. Another group has used two BV Pulsera C-arms to quantify the material properties of the heel pad [100]. There are also at least two published literature reviews on foot and ankle biplane studies [99, 101].

Future applications and directions

The typical goal of a biplane study is to generate six degree-of-freedom kinematic descriptions of joint motion (Figure 11.6A). These are reported using anatomically based coordinate systems embedded in the bones of interest [59, 94]. For many researchers, the precise kinematic data possible with biplane systems are enough on their own to provide insights into subtle differences or changes over time in joints in response to clinical interventions or degradations. However, joint kinematics are only a subset of the possible variables that may be generated based on biplane data. Having accurately tracked the positions of two bones that comprise a joint, arthrokinematic measures of articular interactions (Figure 11.6B) such as centroid of contact, relative shear velocity, and dynamic measurement of joint space and congruity are feasible [23]. By coupling subject-specific definitions of ligamentous insertions and origins based on MRI, CT scans or statistical atlases with rudimentary models of the ligament geometry, estimates of dynamic ligament deformation patterns (Figure 11.6C) offer another avenue of investigation in the realm of soft tissues afforded by first tracking the skeletal motion [102]. Biplane systems have also been applied to tracking the deformation of the heel pad and plantar tissues in vivo [102]. Moreover, as both biplane hardware and software mature, researchers and clinicians will be able to address fundamental and foundational questions on foot function.

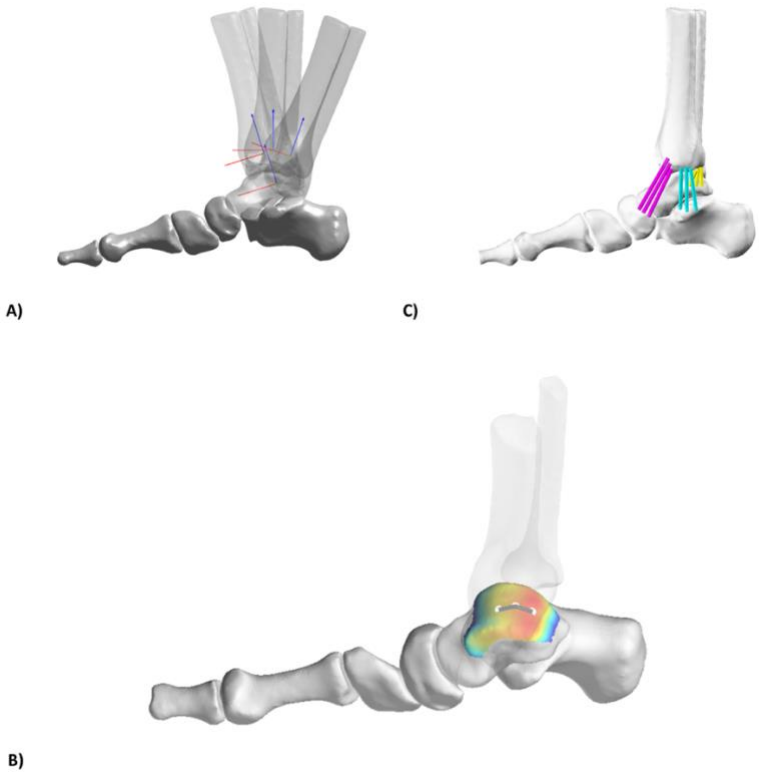

Figure 1.6: Some of the variables obtainable from biplane fluoroscopy. (A) Six degree-of freedom kinematic descriptions of joint motion; (B) Arthrokinematic measures of articular interactions such as centroid of contact or dynamic measurement of joint space; (C) Estimates of dynamic ligament deformation patterns.

References

1. Schallig, W., G.J. Streekstra, C.M. Hulshof, R.P. Kleipool, J.G.G. Dobbe, M. Maas, J. Harlaar, M.M. van der Krogt, and J.C. van den Noort, The influence of soft tissue artifacts on multi-segment foot kinematics. J Biomech, 2021. 120: p. 110359.
2. Shultz, R., A.E. Kedgley, and T.R. Jenkyn, Quantifying skin motion artifact error of the hindfoot and forefoot marker clusters with the optical tracking of a multi-segment foot model using single-plane fluoroscopy. Gait Posture, 2011. 34(1): p. 44-8.
3. National Council on Radiation, P. and B.M.D. Measurements, Implementation of the principle of as low as reasonably achievable (ALARA) for medical and dental personnel. 1990: United States. p. 143.
4. Doss, M., Are We Approaching the End of the Linear No-Threshold Era? J Nucl Med, 2018. 59(12): p. 1786-1793.
5. Oakley, P.A. and D.E. Harrison, Death of the ALARA Radiation Protection Principle as Used in the Medical Sector. Dose Response, 2020. 18(2): p. 1559325820921641.
6. Christensen, E.E.C.T.S.D.J.E.M.R.C.C.E.E., Christensen's physics of diagnostic radiology. 1990, Philadelphia, Pa.; London: Lea & Febiger.
7. Krohmer, J.S., Radiography and fluoroscopy, 1920 to the present. RadioGraphics, 1989. 9(6): p. 1129-1153.
8. Karrholm, J., L.I. Hansson, and G. Selvik, Mobility of the lateral malleolus. A roentgen stereophotogrammetric analysis. Acta Orthop Scand, 1985. 56(6): p. 479-83.
9. Selvik, G., Roentgen stereophotogrammetric analysis. Acta Radiol, 1990. 31(2): p. 113-26.
10. Sturesson, B., G. Selvik, and A. Uden, Movements of the sacroiliac joints. A roentgen stereophotogrammetric analysis. Spine (Phila Pa 1976), 1989. 14(2): p. 162-5.
11. You, B.M., P. Siy, W. Anderst, and S. Tashman, In vivo measurement of 3-D skeletal kinematics from sequences of biplane radiographs: application to knee kinematics. IEEE Trans Med Imaging, 2001. 20(6): p. 514-25.
12. Tashman, S. and W. Anderst, In-vivo measurement of dynamic joint motion using high speed biplane radiography and CT: application to canine ACL deficiency. J Biomech Eng, 2003. 125(2): p. 238-45.
13. Tashman, S., W. Anderst, P. Kolowich, S. Havstad, and S. Arnoczky, Kinematics of the ACL-deficient canine knee during gait: serial changes over two years. J Orthop Res, 2004. 22(5): p. 931-41.
14. Jones, S.C., S.E. Kim, S.A. Banks, B.P. Conrad, A.Z. Abbasi, G. Tremolada, D.D. Lewis, and A. Pozzi, Accuracy of noninvasive, single-plane fluoroscopic analysis for measurement of three-dimensional femorotibial joint poses in dogs treated by tibial plateau leveling osteotomy. Am J Vet Res, 2014. 75(5): p. 486-93.
15. Bey, M.J., R. Zauel, S.K. Brock, and S. Tashman, Validation of a new model-based tracking technique for measuring three-dimensional, in vivo glenohumeral joint kinematics. J Biomech Eng, 2006. 128(4): p. 604-9.
16. Kapron, A.L., S.K. Aoki, C.L. Peters, S.A. Maas, M.J. Bey, R. Zauel, and A.E. Anderson, Accuracy and feasibility of dual fluoroscopy and model-based tracking to quantify in vivo hip kinematics during clinical exams. J Appl Biomech, 2014. 30(3): p. 461-70.
17. de Asla, R.J., L. Wan, H.E. Rubash, and G. Li, Six DOF in vivo kinematics of the ankle joint complex: Application of a combined dual-orthogonal fluoroscopic and magnetic resonance imaging technique. J Orthop Res, 2006. 24(5): p. 1019-27.
18. Caputo, A.M., J.Y. Lee, C.E. Spritzer, M.E. Easley, J.K. DeOrio, J.A. Nunley, 2nd, and L.E. DeFrate, In vivo kinematics of the tibiotalar joint after lateral ankle instability. Am J Sports Med, 2009. 37(11): p. 2241-8.

19. Campbell, K.J., K.J. Wilson, R.F. LaPrade, and T.O. Clanton, Normative rearfoot motion during barefoot and shod walking using biplane fluoroscopy. Knee Surg Sports Traumatol Arthrosc, 2016. 24(4): p. 1402-8.
20. Iaquinto, J.M., R. Tsai, D.R. Haynor, M.J. Fassbind, B.J. Sangeorzan, and W.R. Ledoux, Marker-based validation of a biplane fluoroscopy system for quantifying foot kinematics. Med Eng Phys, 2014. 36(3): p. 391-6.
21. McHenry, B.D., E.L. Exten, J. Long, B. Law, R.M. Marks, and G. Harris, Sagittal subtalar and talocrural joint assessment with weight-bearing fluoroscopy during barefoot ambulation. Foot Ankle Int, 2015. 36(4): p. 430-5.
22. Peltz, C.D., J.A. Haladik, S.E. Hoffman, M. McDonald, N.L. Ramo, G. Divine, M. Nurse, and M.J. Bey, Effects of footwear on three-dimensional tibiotalar and subtalar joint motion during running. J Biomech, 2014. 47(11): p. 2647-53.
23. Wang, B., K.E. Roach, A.L. Kapron, N.M. Fiorentino, C.L. Saltzman, M. Singer, and A.E. Anderson, Accuracy and feasibility of high-speed dual fluoroscopy and model-based tracking to measure in vivo ankle arthrokinematics. Gait Posture, 2015. 41(4): p. 888-93.
24. Koo, S., K.M. Lee, and Y.J. Cha, Plantar-flexion of the ankle joint complex in terminal stance is initiated by subtalar plantar-flexion: A bi-planar fluoroscopy study. Gait Posture, 2015. 42(4): p. 424-9.
25. Brainerd, E.L. Biplane X-ray Video Systems for Biomechanics Research Worldwide. 2020; Available from: https://docs.google.com/spreadsheets/d/1EMvk8u_RpaP-udz7rVyMhM0Sh4iunvxxxhyXCGIe6aY/htmlview#gid=0.
26. MacWilliams, B.A., M. Cowley, and D.E. Nicholson, Foot kinematics and kinetics during adolescent gait. Gait Posture, 2003. 17(3): p. 214-24.
27. Leardini, A., M.G. Benedetti, L. Berti, D. Bettinelli, R. Nativo, and S. Giannini, Rear-foot, mid-foot and fore-foot motion during the stance phase of gait. Gait & posture, 2007. 25(3): p. 453-62.
28. Lundberg, A., I. Goldie, B. Kalin, and G. Selvik, Kinematics of the ankle/foot complex: Plantarflexion and dorsiflexion. Foot and Ankle, 1989. 9(4): p. 194-200.
29. Lundberg, A., O.K. Svensson, C. Bylund, I. Goldie, and G. Selvik, Kinematics of the ankle/foot-Part 2: Pronation and supination. Foot and Ankle, 1989. 9(5): p. 248-253.
30. Lundberg, A., O.K. Svensson, C. Bylund, and G. Selvik, Kinematics of the ankle/foot complex-Part 3: Influence of leg rotation. Foot and Ankle, 1989. 9(6): p. 304-309.
31. van Langelaan, E.J., A kinematic analysis of the tarsal joints, an X-ray photogrammetric study. Acta Orthopaedica Scandinavica Supplement, 1983. 204: p. 1-269.
32. Udupa, J.K., B.E. Hirsch, H.J. Hillstrom, G.R. Bauer, and J.B. Kneeland, Analysis of in vivo 3-D internal kinematics of the joints of the foot. IEEE Trans Biomed Eng, 1998. 45(11): p. 1387-96.
33. Stindel, E., J.K. Udupa, B.E. Hirsch, and D. Odhner, A characterization of the geometric architecture of the peritalar joint complex via MRI: an aid to the classification of foot type. IEEE Trans Med Imaging, 1999. 18(9): p. 753-63.
34. Siegler, S., J.K. Udupa, S.I. Ringleb, C.W. Imhauser, B.E. Hirsch, D. Odhner, P.K. Saha, E. Okereke, and N. Roach, Mechanics of the ankle and subtalar joints revealed through a 3D quasi-static stress MRI technique. J Biomech, 2005. 38(3): p. 567-78.
35. Fassbind, M.J., E.S. Rohr, Y. Hu, D.R. Haynor, S. Siegler, B.J. Sangeorzan, and W.R. Ledoux, Evaluating foot kinematics using magnetic resonance imaging: from maximum plantar flexion, inversion, and internal rotation to maximum dorsiflexion, eversion, and external rotation. J Biomech Eng, 2011. 133(10): p. 104502.
36. Arndt, A., P. Wolf, A. Liu, C. Nester, A. Stacoff, R. Jones, P. Lundgren, and A. Lundberg, Intrinsic foot kinematics measured in vivo during the stance phase of slow running. J Biomech, 2007. 40(12): p. 2672-8.
37. Nester, C., R.K. Jones, A. Liu, D. Howard, A. Lundberg, A. Arndt, P. Lundgren, A. Stacoff, and P. Wolf, Foot kinematics during walking measured using bone and surface mounted markers. J Biomech, 2007. 40(15): p. 3412-23.

38. Lundgren, P., C. Nester, A. Liu, A. Arndt, R. Jones, A. Stacoff, P. Wolf, and A. Lundberg, Invasive in vivo measurement of rear-, mid- and forefoot motion during walking. Gait Posture, 2008. 28(1): p. 93-100.
39. Maiwald, C., A. Arndt, C. Nester, R. Jones, A. Lundberg, and P. Wolf, The effect of intracortical bone pin application on kinetics and tibiocalcaneal kinematics of walking gait. Gait Posture, 2017. 52: p. 129-134.
40. De Clercq, D., P. Aerts, and M. Kunnen, The mechanical characteristics of the human heel pad during foot strike in running: An in vivo cineradiographic study. Journal of Biomechanics, 1994. 27(10): p. 1213-22.
41. Yamaguchi, S., T. Sasho, H. Kato, Y. Kuroyanagi, and S.A. Banks, Ankle and subtalar kinematics during dorsiflexion-plantarflexion activities. Foot Ankle Int, 2009. 30(4): p. 361-6.
42. Nahm, N., M.J. Bey, S. Liu, and S.T. Guthrie, Ankle Motion and Offloading in Short Leg Cast and Low and High Fracture Boots. Foot Ankle Int, 2019. 40(12): p. 1416-1423.
43. Nickoloff, E.L., AAPM/RSNA physics tutorial for residents: physics of flat-panel fluoroscopy systems: Survey of modern fluoroscopy imaging: flat-panel detectors versus image intensifiers and more. Radiographics, 2011. 31(2): p. 591-602.
44. Seibert, J.A., Flat-panel detectors: how much better are they? Pediatr Radiol, 2006. 36 Suppl 2(Suppl 2): p. 173-81.
45. Shi, L., M. Lu, N.R. Bennett, E. Shapiro, J. Zhang, R. Colbeth, J. Star-Lack, and A.S. Wang, Characterization and potential applications of a dual-layer flat-panel detector. Med Phys, 2020. 47(8): p. 3332-3343.
46. Boone, J.M., B.A. Arnold, and J.A. Seibert, Characterization of the point spread function and modulation transfer function of scattered radiation using a digital imaging system. Med Phys, 1986. 13(2): p. 254-6.
47. Boone, J.M., J.A. Seibert, W.A. Barrett, and E.A. Blood, Analysis and correction of imperfections in the image intensifier-TV-digitizer imaging chain. Med Phys, 1991. 18(2): p. 236-42.
48. Bushberg, J.T., J.A. Seibert, E.M. Leidholdt, J.M. Boone, and E.J. Goldschmidt, The Essential Physics of Medical Imaging. Medical Physics, 2003. 30: p. 1936-1936.
49. Cerveri, P., C. Forlani, N.A. Borghese, and G. Ferrigno, Distortion correction for x-ray image intensifiers: local unwarping polynomials and RBF neural networks. Med Phys, 2002. 29(8): p. 1759-71.
50. Cerveri, P., C. Forlani, a. Pedotti, and G. Ferrigno, Hierarchical radial basis function networks and local polynomial un-warping for X-ray image intensifier distortion correction: a comparison with global techniques. Medical & biological engineering & computing, 2003. 41: p. 151-63.
51. Chakraborty, D.P., Image intensifier distortion correction. Medical Physics, 1987. 14: p. 249-252.
52. Fahrig, R., M. Moreau, and D.W. Holdsworth, Three-dimensional computed tomographic reconstruction using a C-arm mounted XRII: correction of image intensifier distortion. Med Phys, 1997. 24(7): p. 1097-106.
53. Gronenschild, E., The accuracy and reproducibility of a global method to correct for geometric image distortion in the x-ray imaging chain. Medical physics, 1997. 24: p. 1875-1888.
54. Gutiérrez, L.F., C. Ozturk, E.R. McVeigh, and R.J. Lederman, A practical global distortion correction method for an image intensifier based x-ray fluoroscopy system. Medical Physics, 2008. 35: p. 997-1007.
55. Holdsworth, D.W., S.I. Pollmann, H.N. Nikolov, and R. Fahrig, Correction of XRII geometric distortion using a liquid-filled grid and image subtraction. Med Phys, 2005. 32(1): p. 55-64.
56. Kedgley, A.E., A.M.V. Fox, and T.R. Jenkyn, Image intensifier distortion correction for fluoroscopic RSA: The need for independent accuracy assessment. Journal of Applied Clinical Medical Physics, 2012. 13: p. 197-204.
57. Pietka, E. and H.K. Huang, Correction of aberration in image-intensifier systems. Comput Med Imaging Graph, 1992. 16(4): p. 253-8.

58. Mery, D., Computer Vision for X-Ray Testing: Imaging, Systems, Image Databases, and Algorithms. 2015: Springer International Publishing.
59. Lenz, A.L., M.A. Strobel, A.M. Anderson, A.V. Fial, B.A. MacWilliams, J.J. Krzak, and K.M. Kruger, Assignment of local coordinate systems and methods to calculate tibiotalar and subtalar kinematics: A systematic review. J Biomech, 2021. 120: p. 110344.
60. Lôbo, C.F.T., E.A. Pires, M. Bordalo-Rodrigues, C. de Cesar Netto, and A.L. Godoy-Santos, Imaging of progressive collapsing foot deformity with emphasis on the role of weightbearing cone beam CT. Skeletal Radiol, 2021.
61. Iaquinto, J.M., M.W. Kindig, D.R. Haynor, Q. Vu, N. Pepin, R. Tsai, B.J. Sangeorzan, and W.R. Ledoux, Model-based tracking of the bones of the foot: A biplane fluoroscopy validation study. Comput Biol Med, 2018. 92: p. 118-127.
62. Lichti, D.D., G.B. Sharma, G. Kuntze, B. Mund, J.E. Beveridge, and J.L. Ronsky, Rigorous geometric self-calibrating bundle adjustment for a dual fluoroscopic imaging system. IEEE Transactions on Medical Imaging, 2015. 34: p. 589-598.
63. Brehler, M., A. Islam, L. Vogelsang, D. Yang, W. Sehnert, D. Shakoor, S. Demehri, J.H. Siewerdsen, and W. Zbijewski, Coupled Active Shape Models for Automated Segmentation and Landmark Localization in High-Resolution CT of the Foot and Ankle. Proc SPIE Int Soc Opt Eng, 2019. 10953.
64. Wan, L., R.J. de Asla, H.E. Rubash, and G. Li, Determination of in-vivo articular cartilage contact areas of human talocrural joint under weightbearing conditions. Osteoarthritis Cartilage, 2006. 14(12): p. 1294-301.
65. Wan, L., R.J. de Asla, H.E. Rubash, and G. Li, In vivo cartilage contact deformation of human ankle joints under full body weight. J Orthop Res, 2008. 26(8): p. 1081-9.
66. de Asla, R.J., M. Kozanek, L. Wan, H.E. Rubash, and G. Li, Function of anterior talofibular and calcaneofibular ligaments during in-vivo motion of the ankle joint complex. J Orthop Surg Res, 2009. 4: p. 7.
67. Kozanek, M., H.E. Rubash, G. Li, and R.J. de Asla, Effect of post-traumatic tibiotalar osteoarthritis on kinematics of the ankle joint complex. Foot Ankle Int, 2009. 30(8): p. 734-40.
68. Bischof, J.E., C.E. Spritzer, A.M. Caputo, M.E. Easley, J.K. DeOrio, J.A. Nunley, and L.E. DeFrate, In vivo cartilage contact strains in patients with lateral ankle instability. Journal of Biomechanics, 2010. 43(13): p. 2561-2566.
69. Wainright, W.B., C.E. Spritzer, J.Y. Lee, M.E. Easley, J.K. DeOrio, J.A. Nunley, and L.E. DeFrate, The effect of modified Brostrom-Gould repair for lateral ankle instability on in vivo tibiotalar kinematics. Am J Sports Med, 2012. 40(9): p. 2099-104.
70. Cao, S., C. Wang, G. Zhang, X. Ma, X. Wang, J. Huang, C. Zhang, and K. Wang, Effects of an ankle brace on the in vivo kinematics of patients with chronic ankle instability during walking on an inversion platform. Gait Posture, 2019. 72: p. 228-233.
71. Cao, S., C. Wang, X. Ma, X. Wang, J. Huang, C. Zhang, L. Chen, X. Geng, and K. Wang, In Vivo Kinematics of Functional Ankle Instability Patients and Lateral Ankle Sprain Copers During Stair Descent. J Orthop Res, 2019. 37(8): p. 1860-1867.
72. Balsdon, M.E., K.M. Bushey, C.E. Dombroski, M.E. LeBel, and T.R. Jenkyn, Medial Longitudinal Arch Angle Presents Significant Differences Between Foot Types: A Biplane Fluoroscopy Study. J Biomech Eng, 2016. 138(10).
73. Balsdon, M., C. Dombroski, K. Bushey, and T.R. Jenkyn, Hard, soft and off-the-shelf foot orthoses and their effect on the angle of the medial longitudinal arch: A biplane fluoroscopy study. Prosthet Orthot Int, 2019. 43(3): p. 331-338.
74. McHenry, B.D., E. Exten, J.T. Long, and G.F. Harris, Sagittal Fluoroscopy for the Assessment of Hindfoot Kinematics. J Biomech Eng, 2016. 138(3): p. 4032445.
75. Cross, J.A., B. McHenry, and T.G. Schmidt, Quantifying cross-scatter contamination in biplane fluoroscopy motion analysis systems. J Med Imaging (Bellingham), 2015. 2(4): p. 043503.

76. McHenry, B.D., E.L. Exten, J.A. Cross, K.M. Kruger, B. Law, J.M. Fritz, and G. Harris, Sagittal Subtalar and Talocrural Joint Assessment During Ambulation With Controlled Ankle Movement (CAM) Boots. Foot Ankle Int, 2017. 38(11): p. 1260-1266.
77. Cross, J.A., B.D. McHenry, R. Molthen, E. Exten, T.G. Schmidt, and G.F. Harris, Biplane fluoroscopy for hindfoot motion analysis during gait: A model-based evaluation. Med Eng Phys, 2017.
78. McHenry, B.D., K.M. Kruger, E.L. Exten, S. Tarima, and G.F. Harris, Sagittal subtalar and talocrural joint assessment between barefoot and shod walking: A fluoroscopic study. Gait Posture, 2019. 72: p. 57-61.
79. Hoffman, S.E., C.D. Peltz, J.A. Haladik, G. Divine, M.A. Nurse, and M.J. Bey, Dynamic in-vivo assessment of navicular drop while running in barefoot, minimalist, and motion control footwear conditions. Gait Posture, 2015. 41(3): p. 825-9.
80. Nichols, J.A., K.E. Roach, N.M. Fiorentino, and A.E. Anderson, Predicting tibiotalar and subtalar joint angles from skin-marker data with dual-fluoroscopy as a reference standard. Gait Posture, 2016. 49: p. 136-143.
81. Roach, K.E., B. Wang, A.L. Kapron, N.M. Fiorentino, C.L. Saltzman, K. Bo Foreman, and A.E. Anderson, In Vivo Kinematics of the Tibiotalar and Subtalar Joints in Asymptomatic Subjects: A High-Speed Dual Fluoroscopy Study. J Biomech Eng, 2016. 138(9).
82. Roach, K.E., K.B. Foreman, A. Barg, C.L. Saltzman, and A.E. Anderson, Application of High-Speed Dual Fluoroscopy to Study In Vivo Tibiotalar and Subtalar Kinematics in Patients With Chronic Ankle Instability and Asymptomatic Control Subjects During Dynamic Activities. Foot Ankle Int, 2017. 38(11): p. 1236-1248.
83. Blair, D.J., A. Barg, K.B. Foreman, A.E. Anderson, and A.L. Lenz, Methodology for Measurement of in vivo Tibiotalar Kinematics After Total Ankle Replacement Using Dual Fluoroscopy. Front Bioeng Biotechnol, 2020. 8: p. 375.
84. Lenz, A.L., J.A. Nichols, K.E. Roach, K.B. Foreman, A. Barg, C.L. Saltzman, and A.E. Anderson, Compensatory Motion of the Subtalar Joint Following Tibiotalar Arthrodesis: An in Vivo Dual-Fluoroscopy Imaging Study. J Bone Joint Surg Am, 2020. 102(7): p. 600-608.
85. Roach, K.E., K.B. Foreman, B.A. MacWilliams, K. Karpos, J. Nichols, and A.E. Anderson, The modified Shriners Hospitals for Children Greenville (mSHCG) multi-segment foot model provides clinically acceptable measurements of ankle and midfoot angles: A dual fluoroscopy study. Gait Posture, 2021. 85: p. 258-265.
86. Phan, C.B., D.P. Nguyen, K.M. Lee, and S. Koo, Relative movement on the articular surfaces of the tibiotalar and subtalar joints during walking. Bone Joint Res, 2018. 7(8): p. 501-507.
87. Phan, C.B., G. Shin, K.M. Lee, and S. Koo, Skeletal kinematics of the midtarsal joint during walking: Midtarsal joint locking revisited. J Biomech, 2019. 95: p. 109287.
88. Phan, C.B., K.M. Lee, S.S. Kwon, and S. Koo, Kinematic instability in the joints of flatfoot subjects during walking: A biplanar fluoroscopic study. J Biomech, 2021. 127: p. 110681.
89. Brainerd, E.L., D.B. Baier, S.M. Gatesy, T.L. Hedrick, K.A. Metzger, S.L. Gilbert, and J.J. Crisco, X-ray reconstruction of moving morphology (XROMM): precision, accuracy and applications in comparative biomechanics research. J Exp Zool A Ecol Genet Physiol, 2010. 313(5): p. 262-79.
90. Kessler, S.E., M.J. Rainbow, G.A. Lichtwark, A.G. Cresswell, S.E. D'Andrea, N. Konow, and L.A. Kelly, A Direct Comparison of Biplanar Videoradiography and Optical Motion Capture for Foot and Ankle Kinematics. Front Bioeng Biotechnol, 2019. 7: p. 199.
91. Maharaj, J.N., S. Kessler, M.J. Rainbow, S.E. D'Andrea, N. Konow, L.A. Kelly, and G.A. Lichtwark, The Reliability of Foot and Ankle Bone and Joint Kinematics Measured With Biplanar Videoradiography and Manual Scientific Rotoscoping. Front Bioeng Biotechnol, 2020. 8: p. 106.
92. Maharaj, J.N., M.J. Rainbow, A.G. Cresswell, S. Kessler, N. Konow, D. Gehring, and G.A. Lichtwark, Modelling the complexity of the foot and ankle during human locomotion: the

development and validation of a multi-segment foot model using biplanar videoradiography. Comput Methods Biomech Biomed Engin, 2021: p. 1-12.
93. Pitcairn, S., J. Kromka, M. Hogan, and W. Anderst, Validation and application of dynamic biplane radiography to study in vivo ankle joint kinematics during high-demand activities. J Biomech, 2020. 103: p. 109696.
94. Brown, J.A., T. Gale, and W. Anderst, An automated method for defining anatomic coordinate systems in the hindfoot. J Biomech, 2020. 109: p. 109951.
95. Yang, S., S.P. Canton, M.V. Hogan, and W. Anderst, Healthy ankle and hindfoot kinematics during gait: Sex differences, asymmetry and coupled motion revealed through dynamic biplane radiography. J Biomech, 2021. 116: p. 110220.
96. Ito, K., K. Hosoda, M. Shimizu, S. Ikemoto, S. Kume, T. Nagura, N. Imanishi, S. Aiso, M. Jinzaki, and N. Ogihara, Direct assessment of 3D foot bone kinematics using biplanar X-ray fluoroscopy and an automatic model registration method. J Foot Ankle Res, 2015. 8: p. 21.
97. Ito, K., K. Hosoda, M. Shimizu, S. Ikemoto, T. Nagura, H. Seki, M. Kitashiro, N. Imanishi, S. Aiso, M. Jinzaki, and N. Ogihara, Three-dimensional innate mobility of the human foot bones under axial loading using biplane X-ray fluoroscopy. R Soc Open Sci, 2017. 4(10): p. 171086.
98. Negishi, T., S. Nozaki, K. Ito, H. Seki, K. Hosoda, T. Nagura, N. Imanishi, M. Jinzaki, and N. Ogihara, Three-Dimensional Innate Mobility of the Human Foot on Coronally-Wedged Surfaces Using a Biplane X-Ray Fluoroscopy. Front Bioeng Biotechnol, 2022. 10: p. 800572.
99. Lin, C.C., J.D. Li, T.W. Lu, M.Y. Kuo, C.C. Kuo, and H.C. Hsu, A model-based tracking method for measuring 3D dynamic joint motion using an alternating biplane x-ray imaging system. Med Phys, 2018.
100. Teng, Z.L., X.G. Yang, X. Geng, Y.J. Gu, R. Huang, W.M. Chen, C. Wang, L. Chen, C. Zhang, M. Helili, J.Z. Huang, X. Wang, and X. Ma, Effect of loading history on material properties of human heel pad: an in-vivo pilot investigation during gait. BMC Musculoskelet Disord, 2022. 23(1): p. 254.
101. Canton, S., W. Anderst, and M.V. Hogan, In Vivo Ankle Kinematics Revealed Through Biplane Radiography: Current Concepts, Recent Literature, and Future Directions. Curr Rev Musculoskelet Med, 2020. 13(1): p. 77-85.
102. Kroupa, N., B. Pierrat, W.S. Han, S. Grange, F. Bergandi, and J. Molimard, Bone Position and Ligament Deformations of the Foot From CT Images to Quantify the Influence of Footwear in ex vivo Feet. Front Bioeng Biotechnol, 2020. 8: p. 560.

Chapter 2

Validation of marker-based tracking with a biplanar fluoroscopy system optimized for the foot and ankle

Eric D. Thorhauer[a,b], Corey Wukelic[a], Will Lin[a], Nick Entress[a], Aerie Grantham[a], William R. Ledoux, PhD[a,b,c]

[a]Center for Limb Loss and MoBility (CLiMB), Department of Veterans Affairs Puget Sound Health Care System, Seattle, Washington, USA

[b]Department of Mechanical Engineering, University of Washington, Seattle, Washington, USA

[c]Department of Orthopaedics & Sports Medicine, University of Washington, Seattle, Washington, USA

Abstract

Biplanar fluoroscopy is a powerful technique for providing clinicians and biomechanists with in vivo functional kinematic data of the human skeleton. Marker-based tracking with biplane systems has applications in both the in vivo and in vitro realms, as well as serving as the established and accepted means of validating model-based tracking algorithms. We have developed a custom biplane system for dynamic imaging of the entire foot and ankle complex during gait as well as a custom software suite to perform the required preprocessing and marker-based and model-based tasks. We demonstrate our ability to model the biplane imaging chain and then accurately and precisely reconstruct the positions of markers in the foot during static and dynamic motion trials. Finally, we demonstrate the effects of marker localization errors in reconstructing the poses of the calcaneus, navicular, and first metatarsal bones to contextualize the extent to which marker-based tracking may be considered ground-truth compared to model-based tracking results.

Introduction

Biomechanical applications of biplanar fluoroscopy systems have matured in recent years to facilitate quantification of in vivo foot and ankle biomechanics [61, 91, 93, 97, 98, 103, 104]. Marker-based tracking is an extension of the Roentgen stereophotogrammetric analysis (RSA) method, which triangulates radiopaque marker positions from stereo image sequences to infer three-dimensional (3D) kinematics [9]. Marker-based tracking approaches have been utilized to quantify in vivo dynamic bone motion [105, 106], soft tissue deformations [107, 108], and to validate model-based tracking software utilizing digitally reconstructed radiographs (DRRs) [103, 109]. Applying these techniques to the foot and ankle will provide clinicians and biomechanists with the means to better understand human gait and the development, prevention, and treatment of numerous foot pathologies.

Biplane marker tracking is performed in custom software, with prerequisites including various image preprocessing and calibration procedures like rectifying spatial and intensity errors in fluoroscopic images and the derivation of camera parameters needed to virtually reconstruct the biplane geometry and imaging chain. Error sources are prevalent throughout the various stages of preprocessing, calibration, and marker position reconstruction. The goal of the tracking software is accurately and precisely reconstructing marker positions, and the degree to which this can be achieved is directly correlated to imaging parameters, system geometry, error correction algorithms, camera modeling, and noise in marker localization. This manuscript outlines our approach to addressing these software needs and provides validation data quantifying tracking accuracy. Additionally, we perform an error propagation analysis of the marker reconstruction process for a foot specimen to establish a performance baseline for future comparisons to model-based tracking validations.

Methods

To perform the various stages of image preprocessing, camera calibration, and marker-based tracking, we developed a custom software suite in MATLAB (The Mathworks, Natick, MA, USA) and in C# utilizing existing open-source software libraries [110, 111]. A custom calibration object was fabricated to facilitate automatic detection and labeling of its X-ray attenuating fiducial markers during dynamic calibration acquisitions sampling throughout the biplane capture volume. Experimental validation of marker position reconstruction via the marker-based tracking process was performed with an acrylic marker lattice phantom and a human foot specimen instrumented with markers. All data were acquired on a custom biplanar fluoroscopy system (Imaging Systems and Services, Painesville, Ohio, USA) with 40 cm image intensifiers (Thales, France) coupled with high-speed video cameras (Phantom v5.2, Vision Research, Wayne, New Jersey, USA) that was configured via overhead cranes (Core Labs HALO) for imaging with an approximately 60-degree inter-beam angle through a walkway with a carbon fiber panel (Figure 1) in order to image in vivo foot and ankle motion. Videos are recorded to 1600 x 1600 pixel 12-bit grayscale frames at 120 Hz with 1 ms exposure times and a typical pixel size of about 0.267 mm in the normal image intensifier magnification mode. The biplane system sources (EMD 80 kW Epsilon generators and Varian 1000 kHU 0.3 m focal spot tubes with Ralco collimators) are configured to fire 1 ms X-ray pulses (100mA, typically between 60-66 kV) that are synchronized to the high-speed cameras at 120 Hz.

Preprocessing image corrections

Raw recorded fluoroscopic images are corrupted with spatial and intensity biases. Image intensity biases manifest as vignetting from the telephoto lens and the image intensifier output

roll-off. As part of the standard biplane data collection protocol, a series of flatfield images are acquired to rectify detector intensity biases [47]. For each X-ray source's unique kilovoltage (kV) used during motion trial acquisitions, flatfield acquisitions of at least 100 image frames are acquired for each image intensifier. To reduce Poisson noise in the raw image data, the mean intensity image of the sequences is obtained via pixel-wise averaging. Residual high-frequency noise is further mitigated by convolving the temporal mean image with a spatially moving local maximum or averaging filter. The smoothed mean flatfield intensity images form the flatfield correction maps representing the detector response's low spatial frequency roll-off characteristics at each source beam kilovoltage level, telephoto lens aperture, and camera exposure time combination. Applying the flatfield correction involves dividing a given raw fluoroscope image frame by the correction map and normalizing the intensity data to a common positive integer range in a 16-bit grayscale representation.

Spatial distortions in the biplanar fluoroscopic video sequences occur due to distortions imparted by the elements of the telephoto lenses mounted to the high-speed camera, the geometry of the input phosphor, and electromagnetic interferences due to external fields within the evacuated X-ray image intensifier bodies. The resulting pincushion and S-shaped distortion patterns may be quantified by imaging a regular grid of detectable points on the image intensifier input face [47, 52]. A 5 mm thick, 400 mm diameter plate was machined (tolerance $\pm$ 0.127 mm, ISO 2768) with a uniformly spaced grid of 5 mm diameter holes and a unique pattern of 10 mm holes (Figure 2A). With the plate mounted flat to the face of each image intensifier, a sequence of fluoroscopy images is acquired and averaged temporally like the flatfield correction maps. An intensity thresholding algorithm extracts the bright holes from the grid images and localizes their centers by fitting circles to the detected regions. Grid point candidates are filtered via minimum

circularity and area criteria to eliminate spurious detections typically resulting in more than 1000 valid sample points. The eight larger 5 mm diameter holes are automatically detected and labeled based on their unique cross pattern. The cross is used to infer the row and column orientations (grid rotation), and the pairwise inter-hole distances in pixels are compared to their nominal distances in millimeters to calculate the pixels per millimeter scaling factor. Detected grid point centroids are centered and scaled such that their mean is subtracted and their RMS distances equal $\sqrt{2}$ as described by Hartley and Zisserman [112]. This scaling operation reduces the condition numbers of the Vandermonde matrices used when solving for polynomial coefficients. These scaled and centered data are used in a two-dimensional (2D) global n^{th} order bipolynomial distortion correction model that uses the same n-degree polynomial in both the x- and y-directions n^{th} degree bipolynomials [47, 49, 51-53, 56, 113]. Distortion corrections are applied to raw fluoroscopy images as pixel-wise row- and column-direction deformations and resampled at the original image resolution via linear intensity interpolation. The distortion correction residual errors were defined as the mean, standard deviation, and root-mean-square of differences in 2D pixel coordinates between the nominal (ideal) grid points and the corrected grid point locations after applying the correction maps [47, 52]. To generate these flatfield and distortion correction maps, we developed custom software called Preprocessor Image Spatial Correction and Exposure Standardization (PISCES) and experimentally validated it as follows.

Distortion correction repeatability analysis

To assess the ability and repeatability of the PISCES distortion correction algorithm across various polynomial degrees, fluoroscopy sequences of the distortion correction grid in various random rotations on the face of the image intensifiers were acquired [52, 53, 56].

Flatfield corrections were applied to the raw grid images, followed by an operator-specified gamma correction. Distortion correction maps were generated for 3rd through 15th-degree models, and each fit's residual errors were recorded.

Camera model and calibration objects

A pair of pinhole camera models are utilized to provide the mappings between the world coordinate frame (lab) and the two 2D image frames. Each camera matrix is a composition of the intrinsic (e.g., focal length, principal point) and extrinsic (e.g., orientation and position) camera parameters. These parameters are derived by imaging a calibration object of known and stable geometry for a given configuration of the biplanar imaging system. Our custom software Camera Reconstruction Utility for X-ray (CRUX) automatically detects and identifies calibration object markers in the fluoroscopy video sequences and establishes their correspondences between the stereo views. Next, using the localized centroids of the markers in pixel coordinates and a priori knowledge of the marker distributions from computed tomography (CT) scanning, an initial guess of the calibration parameters is obtained via the direct linear transformation (DLT) method [114]. These preliminary camera models are refined iteratively using the bundle adjustment method, which seeks to iteratively minimize the reprojection errors in data from additional stereo images of the calibration object in varying poses from the dynamic sequence while enforcing the rigidity constraints between the two cameras of the biplane system [62, 115].

To facilitate CRUX's automatic detection and labeling of the markers, we fabricated a custom camera calibration object using a spiral of stainless-steel spheres distributed in a known pattern [116] of alternating 3 mm and 5 mm diameters (Figure 2B) cast in resin (Master Dyna-Cast Fast-Cast Urethane, Freeman Manufacturing & Supply, Avon, OH, USA) encased in a protective polycarbonate cylindrical shell. The nominal locations of the markers were determined

by imaging the object in a high-resolution CT scanner (North Star Imaging NSI X5000, isotropic voxel size 0.145 mm). An intensity-based iterative 3D Gaussian fitting algorithm was developed in MATLAB to localize the centers of the markers in the CT scan data. To efficiently and safely allow operators to acquire fluoroscopy images of it across multiple poses, the calibration object was mounted to a motorized drive system, which rolls the spiral through the extent of the capture volume as the X-ray data are recorded, yielding thousands of calibration data points in the form of identifiable marker projections. To define a consistent lab coordinate system between subjects and define the plane of the walkway, a custom T-wand object is also imaged at the conclusion of a calibration session (Figure 2C). The lab origin is defined as the intersection of the T-shape, and the offset between the object markers and floor plane is known a priori.

Camera parameter determination sensitivity analysis

Five dynamic calibration trials of the spiral calibration object were acquired, covering the entire extent of the capture volume without altering the biplane system geometry between trials. Camera calibration matrices were determined for each trial, and the variation between the derived camera parameters was compared.

Marker tracking

Before reconstructing the 3D laboratory positions of markers via triangulation, they must first be localized on the two 2D fluoroscopic images. We developed the Utility for Roentgen Stereophotogrammetric Analysis (URSA) software to allow operators to manually provide identification of markers and initial guesses of their centers via a graphical interface (Figure 3). The localization algorithm works as follows: 1) The user identifies the marker of interest on either biplane image view and manually selects the pixel nearest the center of the marker. 2) The

URSA software draws an epipolar line (based on the camera matrices) overlay on the opposite view, along which the marker must reside, and the user selects a point along this line as the initial guess of the marker centroid in the second view. 3) Based on a priori knowledge of the pixels-per-millimeter scaling determined from the distortion correction grid and the physical diameter of the marker being tracked, a search neighborhood based on the equivalent diameter in pixels in each biplane view is used to iteratively refine the marker centroids from operator initial guesses. The software allows for Gaussian and sigmoidal [117] marker signature models for the iterative fitting. 4) Finally, the 3D position of the marker in laboratory space is reconstructed using a triangulation algorithm from the two 2D marker positions.

Marker tracking validation

Two test phantoms were made to quantify the performance of the marker tracking software during both static and dynamic trials. An acrylic plate (300 x 300 x 6.35 mm) was machined, and a regular grid pattern of 2- and 3-mm (20 mm spacing ± 0.1 mm) diameter stainless-steel markers were rigidly embedded (Figure 4A). The minimally attenuating acrylic provides a best-case test scenario for localizing and reconstructing marker positions. For a more realistic simulation of in vivo tracking performance, a human foot specimen (59-year-old male donor) was instrumented with triads of 3 mm stainless-steel markers in hindfoot (calcaneus and talus), midfoot (navicular), and forefoot (first metatarsal and proximal phalanx) bones (Figure 4B).

Both dynamic and static data were acquired. The lattice object swung through the capture volume on a pendulum fabricated on the biplane system walkway at a typical foot gait swing phase speed (1.7 m/s at the bottom of the swing arc). Biplane sequences of the lattice were also

acquired in a static position at the center of the capture volume. To simulate the gait swing phase with the foot specimen, the tibial shaft was rigidly mounted to the end effector of a robotic arm (KR16, KUKA, Augsburg, Germany). At the same time, nominal ankle dorsiflexor tendon loads were applied to maintain a neutral foot angle as the specimen was translated anteriorly through the capture volume at the swing phase speed. Temporal averaging of static trials was used to generate noise-reduced images for each view, which, when tracked, provide the best possible estimate of marker reconstruction in static trials. To assess the stability of the marker localization algorithm, the average variance and range in 3D positions across at least 200 frames of a static trial were quantified relative to the positions calculated from the temporal mean images in both the foot and lattice phantom.

Three operators tracked the markers of both objects across three separate tracking sessions separated by a week to quantify both between-operators agreement and within-operators repeatability of the tracking software. Static, dynamic, and temporally averaged static trials were all tracked.

Marker localization error propagation into bone pose estimation

To estimate the downstream errors in estimating foot bone poses using noisy marker data, a Monte Carlo simulation of 100,000 iterations was performed in MATLAB. The positions of the marker triads for each region/bone (hindfoot = calcaneus, midfoot = navicular, forefoot = first metatarsal) were corrupted with noise based on the results of the dynamic foot specimen tracking bias and precision analyses. The noisy marker positions were rigidly fit to the nominal marker positions in the least squares sense using MATLAB, and the resulting transformation matrices

were decomposed into displacements (mm) and Euler angle rotations (˚) representing the error in pose attributed to the simulated marker localization noise.

Statistical analyses

Statistical analyses were performed in RStudio (version 2023.06.0+421) using the base and PMCMRplus [118] packages and multivariate intra-class correlation (ICC) code from Gwet [119]. Non-parametric tests were utilized on residual error data that violated assumptions of normality or homogeneity of variance. Friedman's test was performed on the distortion grid data, followed by a post-hoc Nemenyi test to detect polynomial models with significantly lower residual errors. The absolute agreement of 3D x-, y- and z- tracked marker coordinates within and between operators was assessed using a multivariate intraclass correlation coefficient measure [119]. Differences between the mean static and dynamic inter-marker distance errors were assessed using paired t-tests.

Results

Distortion correction residual errors

Across all grid points for ten unique distortion correction trials, the mean residual error ranged between 1.25 mm for the 3rd-degree polynomial model and 0.126 mm for a 15th-degree model (Table 1). Polynomial models above the 10th degree generated similar residual errors. However, anecdotally, 14th and 15th-degree models sometimes led to overfitting and

interpolation errors, making the resulting corrected images unusable. All polynomial models above 8th degree produced residual errors with standard deviations better than 5 microns (Table 1).

Camera model reprojection errors and parameter repeatability

Reprojection errors were similar for each of the two camera systems. The mean and standard deviations of reprojection errors for both camera systems were on the order of 50 microns (Table 2). Root-mean-square reprojection errors were on the order of 200 microns. Across nine unique calibration trials, while the biplane system geometry was fixed, the camera spatial positions were reconstructed within 10 mm of each other, and camera orientations were reconstructed within a degree of each other (Table 3). Within each camera, the intrinsic parameters of focal length and principal point exhibited higher coefficients of variation than the respective extrinsic parameters of position and orientation (Table 3). The third z-component angles describing each camera system's orientation were perfectly repeatable across the calibrations within numerical machine precision. The focal length parameter of the camera model varied up to 45 mm between subsequent calibrations of the static, unaltered biplane camera system. Multivariate ICC scores were very good for extrinsic parameters position (ICC = 0.876) and orientation (ICC = 0.863) as well as intrinsic focal length (ICC = 0.869) but were fair for intrinsic principal point (ICC = 0.466).

Marker localization accuracy and repeatability

Marker localization errors were comparable between static and dynamic conditions ($p = 0.768$ for lattice and $p = 0.473$ for foot). Bias and precision in the lattice trials were smaller than the foot trials. The average standard deviations and ranges in reconstructed 3D marker positions, used to characterize localization stability, were 0.011 (0.068) mm during the lattice trials and 0.014 (0.080) mm during foot trials. The average marker bias and precision errors for all raters on all days for the lattice object were 0.022 ± 0.061 mm for static trials and 0.018 ± 0.030 mm for dynamic trials. The average marker localization bias and precision errors for all raters on all days across the foot specimen trials were 0.058 ± 0.184 mm for static trials and 0.048 ± 0.185 for dynamic trials. In the foot specimen, magnitudes of inter-marker distance errors decreased from the higher attenuating hindfoot towards the higher contrast forefoot (Table 4).

Marker localization error propagation into bone pose estimation

Meaningful rotational and translational pose estimation errors were observed in the Monte Carlo marker localization error propagation simulation. However, none of the six-degree-of-freedom parameter error variances significantly differed from zero. The errors for translation (Figure 5) and rotation (Figure 6) pose reconstruction were highest in the hindfoot regions and decreased towards the forefoot. In the hindfoot, maximum pose errors were on the order of 1 mm and 10 degrees for translation and rotation, respectively. In the forefoot, maximum pose translation errors were submillimeter, while maximum rotational errors were on the order of 1 to 2 degrees.

Discussion

The objective of these experiments was to validate our custom software solutions for the image preprocessing, camera calibration, and marker localization tasks that are required for biplanar fluoroscopy marker-based tracking. We quantified the magnitudes of error present at these key processing stages and simulated how marker localization errors would propagate into errors in reconstructing foot bone poses. These results demonstrated that our marker localization software is accurate and highly repeatable within and between operators in both an idealized test case (lattice object) and realistic simulations (foot).

Distortion correction

The global polynomial distortion correction model implemented successfully handles both the pincushion and S-shaped spatial distortions present in the raw fluoroscopy images. In contrast to local warping models, global polynomial models for image distortion correction of sufficiently high degree are sensitive to higher frequency spatial distortions while being robust to errors in grid control point localization [52, 53, 56]. Additionally, polynomial mapping provides a compact undistorting mechanism via closed-form matrix multiplications that are ideal for rapidly processing fluoroscopy images in memory rather than precomputing and saving the rectified images to storage. While increasing the polynomial model degree, we observed the residual errors decreasing until overfitting occurred above 13th-degree models (Table 1). Kedgley et al. explored multiple combinations of mixed-degree global polynomials up to 3rd degree along each direction for undistorting fluoroscopy images using a grid that generated 381 sample points. In their study, using a 3rd-degree polynomial for both the rows and columns resulted in the largest root-mean-square grid errors, on the order of 0.5 mm [56]. In contrast, our

equivalent 3rd-degree model RMS error was 1.143 mm. It has been reported that increasing polynomial degree may lead to overfitting and larger RMS errors as more of the noise is modeled [50, 56]. However, Guan et al. report using a 9th-degree model Field [32], and we were able to fit it up to a 13th-degree model reliably. This is likely due to the large number of over 1000 grid points and use of the preprocessing scaling and centering operation for reducing numerical instabilities when solving for the bipolynomial coefficients. The lowest RMS error achieved using a 15th-degree model (0.126 mm) compares well with the grid manufacturer's machining tolerance (± 0.127 mm). Future improvements to distortion correction performance may be possible with revisions to the grid design and higher machining tolerances.

Camera calibration

We demonstrated adequate repeatability in determining camera parameters across multiple calibrations of an unaltered biplanar imaging system. Our software successfully detected and assigned correspondences between observations of markers in the custom spiral calibration object, which facilitates imaging during dynamic movement throughout the capture volume of the biplane system. By motorizing these dynamic calibration trials, system operators may work behind X-ray shielding to minimize radiation exposure risk.

Standard deviations in the extrinsic camera position and intrinsic focal length parameters on the order of a few centimeters were observed (Table 3). These variances could be reduced in the future by constraining the focal length parameters during bundle adjustment to values close to the physically recorded source-to-detector distances. The small extrinsic rotational parameter variances suggest that the relative geometry between the two camera systems is well-reconstructed, while the absolute position and orientation parameters with respect to the defined laboratory origin are more variable. Despite some of the extrinsic and intrinsic camera

parameters exhibiting variance across the calibrations, the camera reprojection errors for both systems were excellent (Table 2).

Marker position reconstruction

The performance of the marker position reconstruction software is directly affected by the propagated errors in the distortion correction and camera modeling preprocessing steps. Marker tracking was assessed experimentally in both an idealized test case of the lattice object, which provides ideal marker contrast, and a more realistic test case of a human foot specimen, which was assessed by anatomical foot region. Additionally, we compared the performance of both static and dynamic marker tracking at speeds simulating swing phase of normal walking and found no significant decrease in our ability to track dynamic foot markers compared to static trials. Our inter-marker distance error results compare with Lichti et al. (0.2 ± 1.1 mm), Tashman et al., (-0.02 ± 0.10 mm), Brainerd et al. (in bone precision 0.084 mm, in wand phantom precision 0.046 mm), Mery et al. (0.15 ± 0.79 mm), and Kedgley et al. (0.15 ± 0.07 mm) [12, 56, 62, 89, 120]. As expected, tracking the more radiodense hindfoot resulted in higher errors than the forefoot, which has fewer bony occlusions (Table 4).

Marker-based bone pose error

The simulated bone pose errors establish lower limits on the precision of using marker-based tracking results as ground-truth references for model-based tracking experiments (Figures 5 and 6). While translation errors remained submillimeter, rotational errors approached 1 degree. These errors are a result of the residual errors in the camera modeling and image preprocessing and the localization errors of the markers in both the stereo fluoroscopy images and the CT volumes. The spread and configuration of the markers within a given bone can influence the

lower limit on tracking accuracy [121], and smaller bones like the navicular may inherently have higher noise floors for marker-based tracking.

Limitations

This study is not without multiple limitations, including not exhaustively testing alternative methods of distortion correction (e.g., radial basis functions, local weighted means, or mixed polynomials), only testing a single biplane system configuration that is specific to imaging the foot and ankle during gait, and modeling pose reconstruction errors in only a subset of possible bones. Some beam hardening artifact was present in the regions of the markers in the CT data, which likely *introduced* errors in estimating the nominal marker configurations of both the calibration object and the foot specimen. Nevertheless, these configurations represent the constraints and parameters of research trials collected in our laboratory while studying foot and ankle motion.

Conclusion

Accurately modeling and characterizing the biplanar fluoroscopy imaging chain and how its errors propagate into marker-based tracking results is essential to understanding the limitations of using marker-based tracking as a ground-truth reference for bone tracking. Despite the limitations and errors in distortion correction and camera modeling, our implementation of marker-based tracking software produces reliable and accurate data across multiple operators and sessions. Based on these experimental results, we are confident in using this pipeline of preprocessing and marker tracking algorithms for both validation of our model-based tracking software and various applications of in vivo tracking of radiopaque markers.

Acknowledgment

The authors would like to thank the following for technical assistance in bringing this project to fruition: Alex Berardo-Cates, Lynda Brady, Kalle Chastain, Isaac Hall, Matt Kindig, Dennis Knippel, Morgan Leslie, Michael Sours, Tess Velo, and Arri Willis.

This work was partially funded by Department of Veterans Affairs grant numbers RX002357 and RX002970.

Figures & Tables

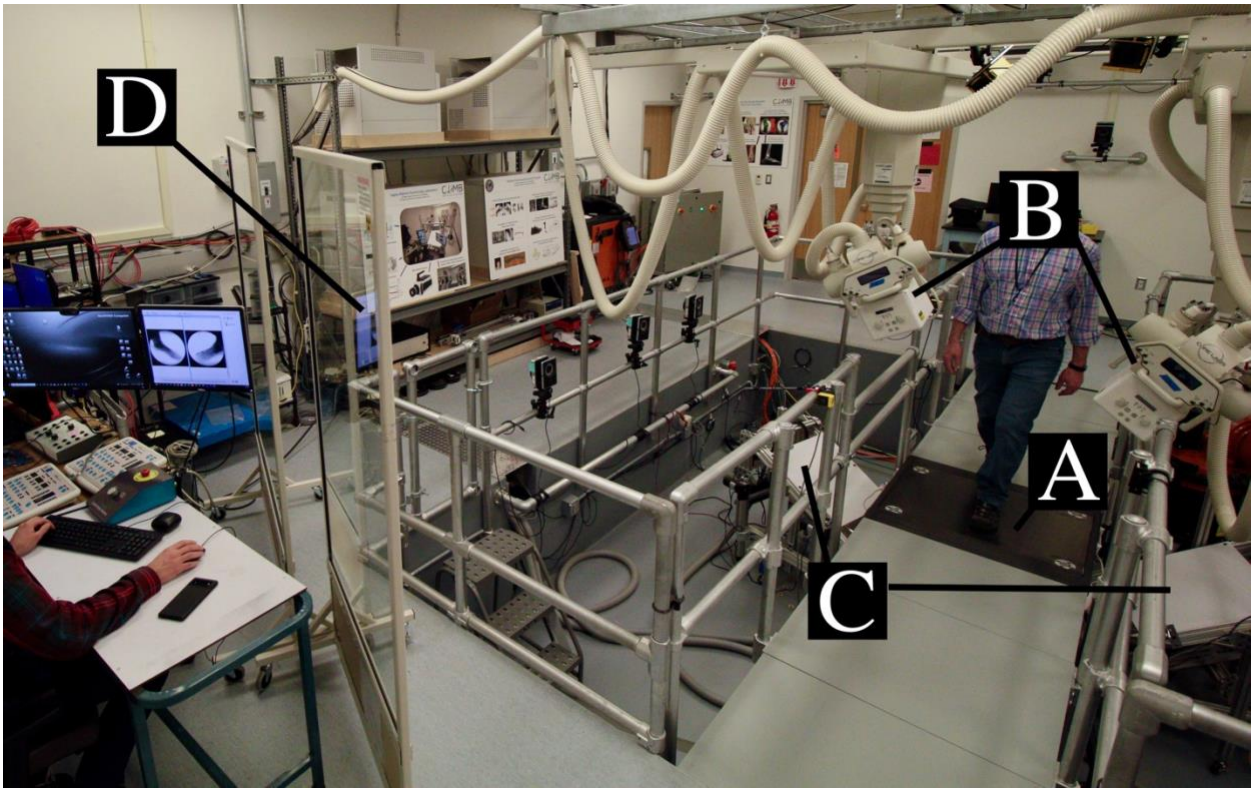

Figure 1: Biplanar fluoroscopy system configured to obliquely image the foot and ankle through a custom walkway with a minimally X-ray attenuating carbon fiber force plate panel (A). The system consists of synchronously pulsed X-ray sources (B) aimed at image intensifiers coupled with high-speed cameras (C). Operators control the system safely from behind X-ray shielding (D).

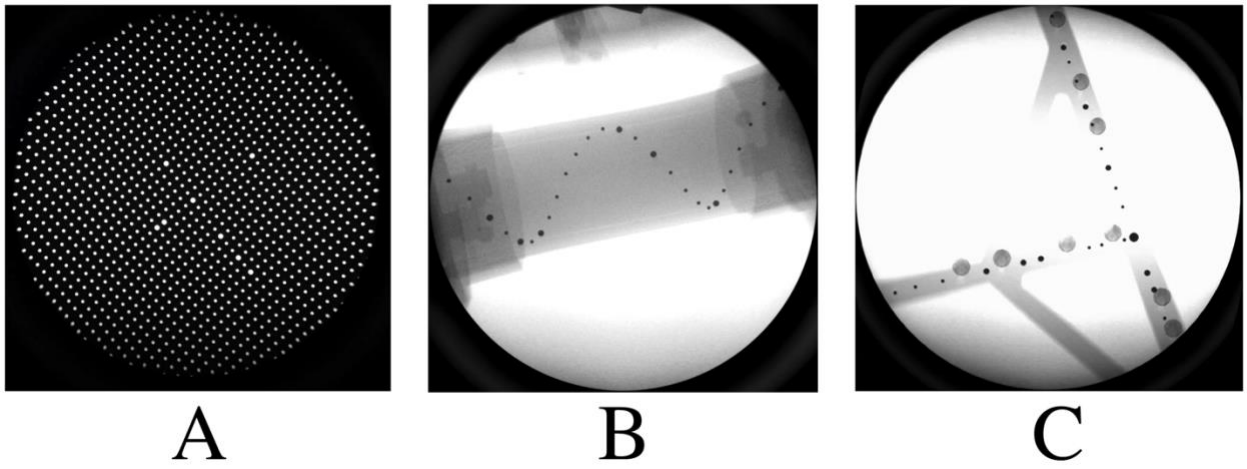

Figure 2: Custom calibration objects fabricated for the biplanar fluoroscopy system. A distortion correction grid (A) with a regular grid of 3 mm holes for reference points and a unique pattern of 5 mm holes used to detect grid orientation and scale factors. The spiral calibration object (B) imaged during a dynamic pose sequence that is used to determine the biplanar camera parameters. A planar “T” marker object (C) that mounts repeatability to the custom walkway panel and is used to set the lab origin and coordinate system.

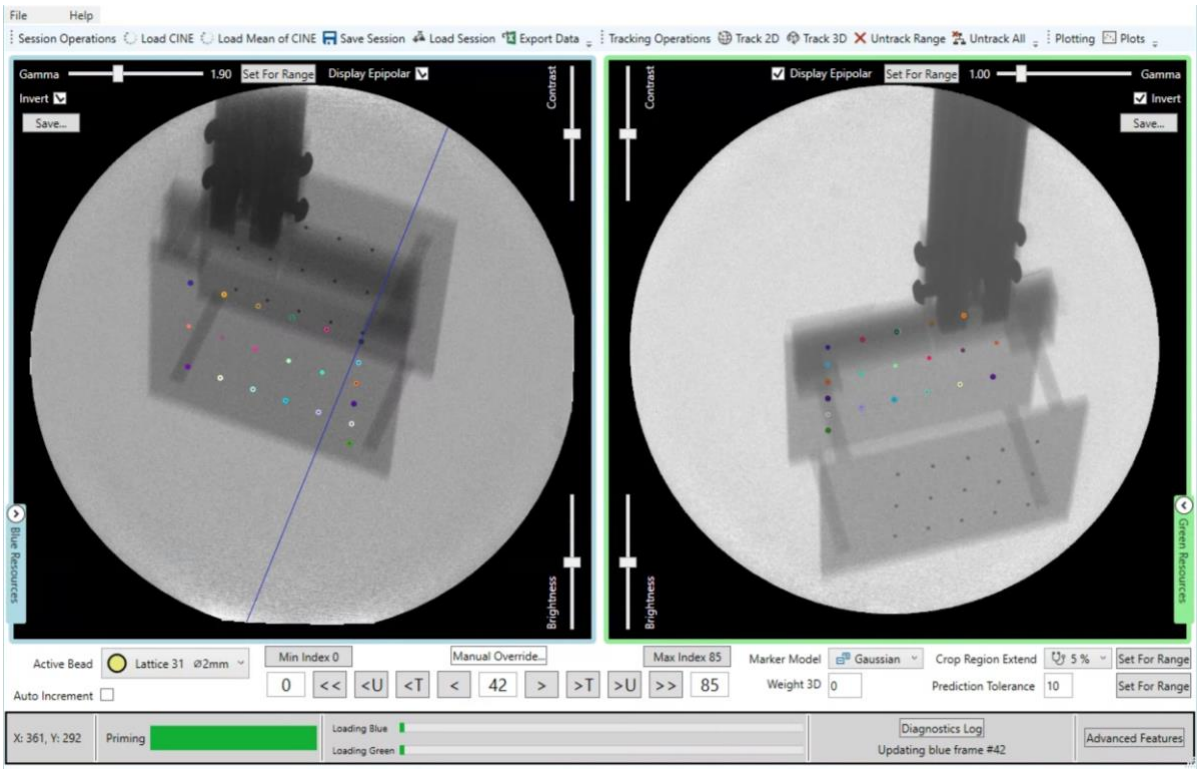

Figure 3: A screenshot of the Utility for Roentgen Stereophotogrammetric Analysis (URSA) software developed for marker-based tracking. The corrected stereo fluoroscope views are rendered, and markers are manually identified in each view and subsequently localized and triangulated by the software.

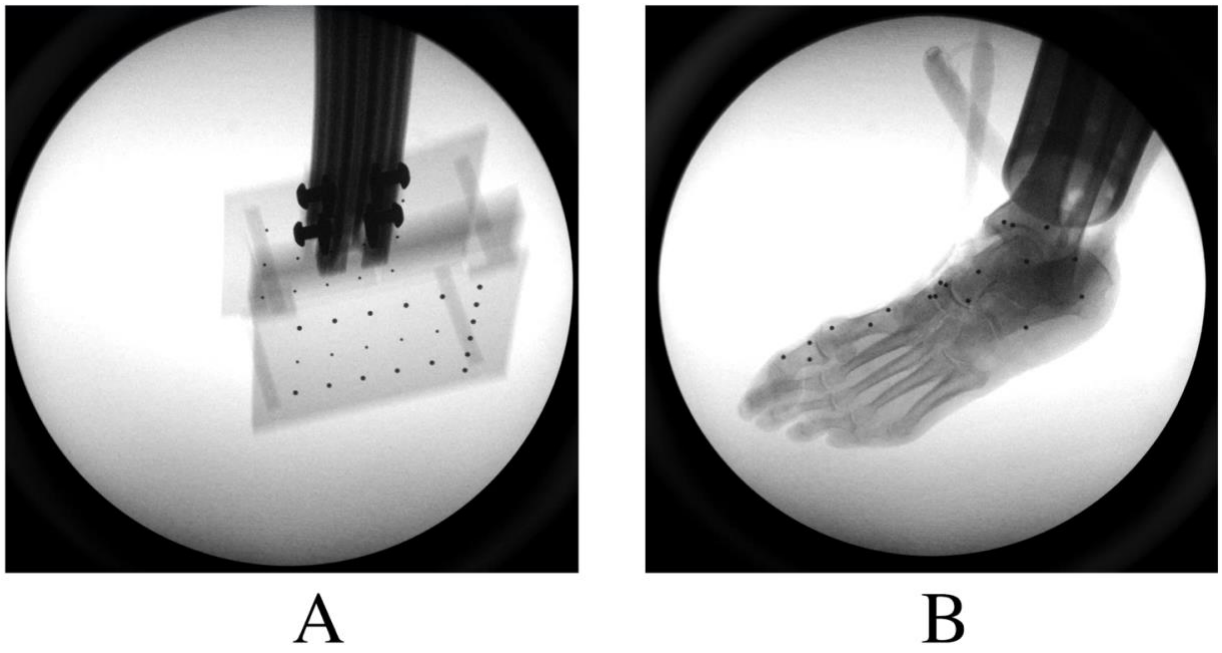

Figure 4: The lattice test object (A) and human foot specimen (B) instrumented with stainless steel beads and used to quantify the accuracy and inter-operator repeatability of the marker-based tracking software in both static and dynamic tests.

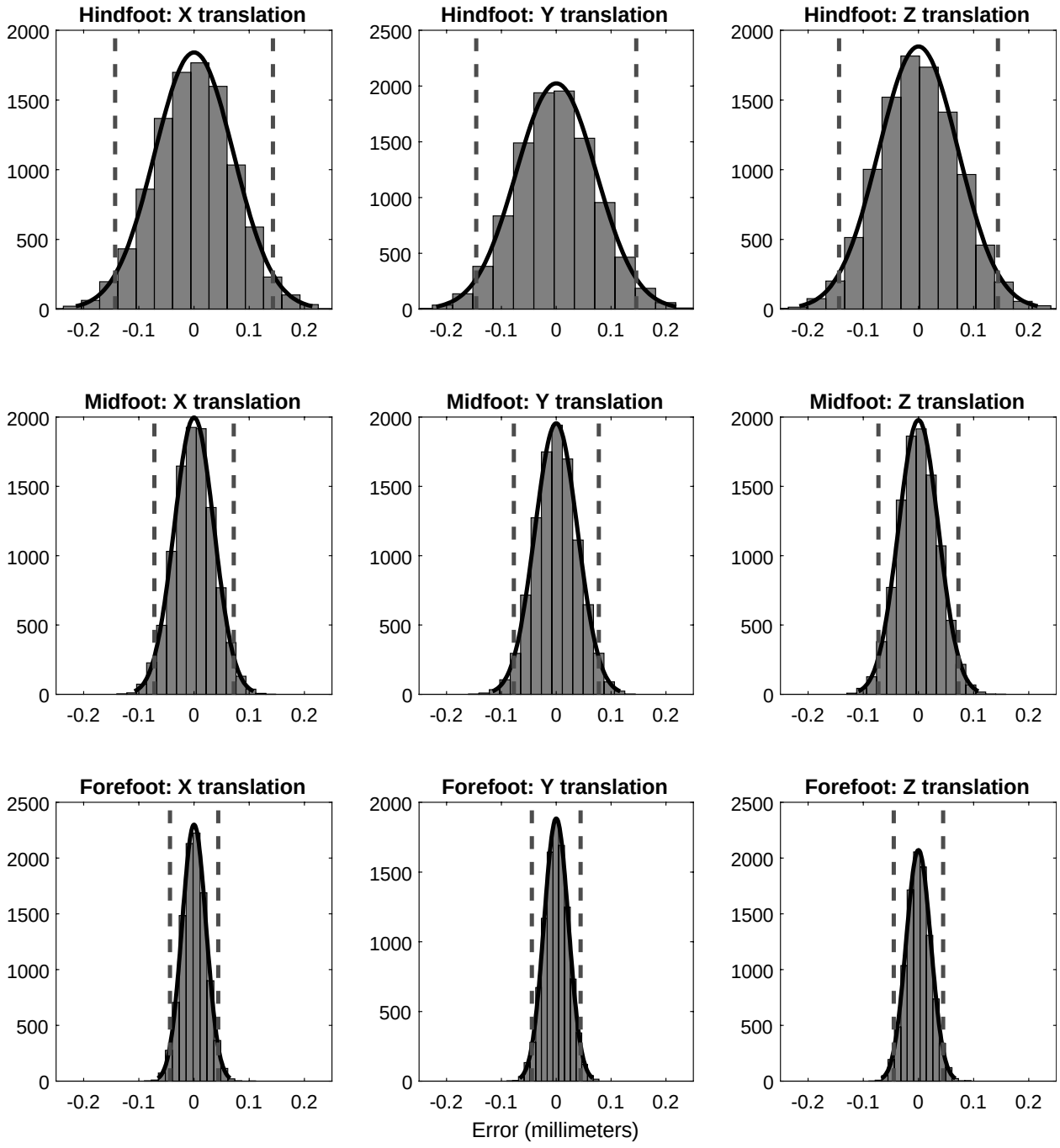

Figure 5: Distributions of hindfoot (top), midfoot (middle), forefoot (bottom) translation errors in millimeters resulting from the Monte Carlo simulation of marker localization errors propagating into bone pose estimation errors. Errors decreased from the hindfoot to the forefoot due to increased localization precision in the forefoot regions of better marker contrast.

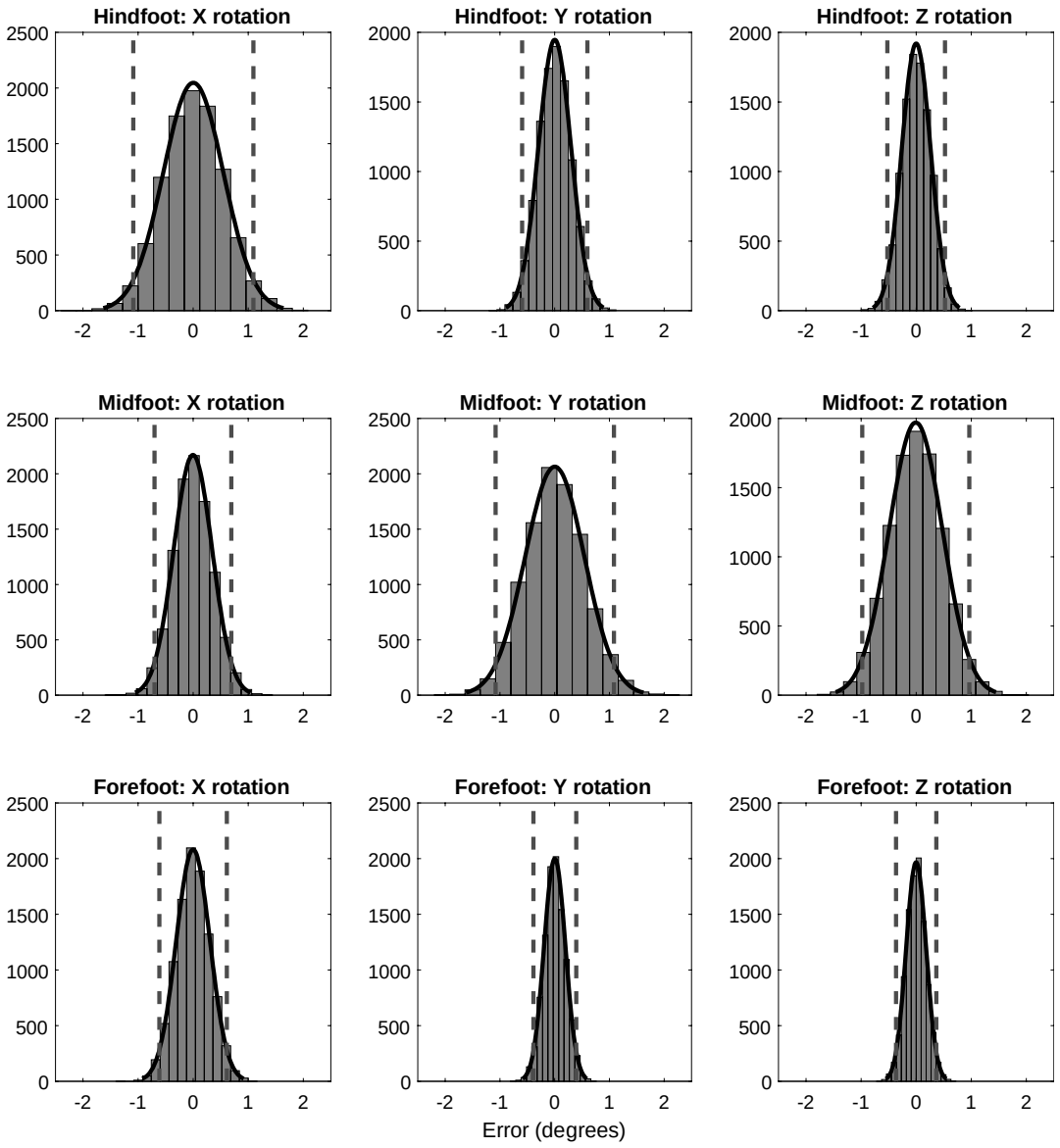

Figure 6: Histograms of hindfoot (top), midfoot (middle), forefoot (bottom) rotation errors in degrees resulting from the Monte Carlo simulations of marker localization error propagation into bone pose estimation errors. Errors decreased from the hindfoot and midfoot to the forefoot because of the better localization precision in regions with better marker contrast.

Table 1: Distortion correction residual errors for each degree polynomial correction model applied to 10 individual grid images.

Polynomial degree	**Residual error (mm)**		
	mean	standard deviation	root-mean-square
3	1.254	0.229	1.143
4	0.708	0.064	0.748
5	0.417	0.026	0.391
6	0.394	0.024	0.376
7	0.261	0.013	0.248
8	0.252	0.012	0.241
9	0.181	0.004	0.176
10	0.178	0.004	0.172
11	0.140	0.003	0.138
12	0.137	0.002	0.136
13	0.132	0.002	0.131
14	0.131	0.002	0.130
15	0.126	0.002	0.126

Table 2: The mean, standard deviation, and root-mean-square errors of the camera reprojection errors across nine calibration sessions.

	Camera model reprojection errors (mm)		
	mean	**standard deviation**	**root-mean-square**
Camera system 1	0.051	0.038	0.243
Camera system 2	0.040	0.030	0.192

Table 3: The mean, standard deviation, and range of extrinsic and intrinsic camera parameters for both biplane camera systems across 9 repeated calibration trials without altering the system geometry or imaging parameters between trials.

	Camera system 1									**Camera system 2**								
Camera parameter	**Position (mm)**			**Orientation (degrees)**			**Focal length (mm)**	**Principal point (pixels)**		**Position (mm)**			**Orientation (degrees)**			**Focal length (mm)**	**Principal point (pixels)**	
	X	Y	Z	X	Y	Z	source-detector	horizontal	vertical	X	Y	Z	X	Y	Z	Source-detector	horizontal	vertical
mean	223.6	-677.2	1026.1	-145.5	-9.0	-19.5	1487.2	836.5	815.9	246.6	643.7	1371.4	151.4	-8.0	-166.5	1808.8	709.0	793.4
standard deviation	2.9	7.8	9.8	0.5	0.4	0.0	17.9	41.2	39.1	0.5	3.9	4.5	0.3	0.0	0.0	7.1	7.9	30.0
range	7.2	19.7	24.9	1.8	1.2	0.0	45.2	133.9	124.2	1.6	11.9	13.2	0.5	0.0	0.0	20.6	27.6	80.3
coefficient of variation	1.3%	-1.2%	1.0%	-0.4%	-4.4%	0.0%	1.2%	4.9%	4.8%	0.2%	0.6%	0.3%	0.2%	-0.2%	0.0%	0.4%	1.1%	3.8%

Table 4: The mean, standard deviation, and root-mean-square errors of the inter-marker distances in the hindfoot, midfoot, and forefoot regions during static and dynamic tracking.

		Inter-marker distance error (mm)		
Trial type		**Hindfoot**	**Midfoot**	**Forefoot**
static	mean	-0.24	0.08	-0.02
	root-mean-square	0.25	0.19	0.05
	standard deviation	0.09	0.11	0.05
dynamic	mean	-0.23	0.10	-0.02
	root-mean-square	0.24	0.20	0.05
	standard deviation	0.09	0.11	0.06

References

[1] J. M. Iaquinto *et al.*, "Model-based tracking of the bones of the foot: A biplane fluoroscopy validation study," *Comput Biol Med,* vol. 92, pp. 118-127, Jan 1 2018, doi: 10.1016/j.compbiomed.2017.11.006.

[2] J. A. Cross, B. D. McHenry, R. Molthen, E. Exten, T. G. Schmidt, and G. F. Harris, "Biplane fluoroscopy for hindfoot motion analysis during gait: A model-based evaluation," *Med Eng Phys,* vol. 43, pp. 118-123, May 2017, doi: 10.1016/j.medengphy.2017.02.009.

[3] J. N. Maharaj *et al.*, "The Reliability of Foot and Ankle Bone and Joint Kinematics Measured With Biplanar Videoradiography and Manual Scientific Rotoscoping," (in eng), *Front Bioeng Biotechnol,* vol. 8, p. 106, 2020, doi: 10.3389/fbioe.2020.00106.

[4] T. Miyamoto *et al.*, "4D-foot analysis on effect of arch support on ankle, subtalar, and talonavicular joint kinematics," (in eng), *J Orthop Sci,* Jan 27 2023, doi: 10.1016/j.jos.2022.10.009.

[5] T. Negishi *et al.*, "Three-Dimensional Innate Mobility of the Human Foot on Coronally-Wedged Surfaces Using a Biplane X-Ray Fluoroscopy," (in eng), *Front Bioeng Biotechnol,* vol. 10, p. 800572, 2022, doi: 10.3389/fbioe.2022.800572.

[6] S. Pitcairn, J. Kromka, M. Hogan, and W. Anderst, "Validation and application of dynamic biplane radiography to study in vivo ankle joint kinematics during high-demand

activities," (in eng), *J Biomech,* vol. 103, p. 109696, Apr 16 2020, doi: 10.1016/j.jbiomech.2020.109696.

[7] K. Ito *et al.*, "Three-dimensional innate mobility of the human foot bones under axial loading using biplane X-ray fluoroscopy," (in eng), *R Soc Open Sci,* vol. 4, no. 10, p. 171086, Oct 2017, doi: 10.1098/rsos.171086.

[8] G. Selvik, "Roentgen stereophotogrammetric analysis," *Acta Radiol,* vol. 31, no. 2, pp. 113-26, Mar 1990. [Online]. Available: https://www.ncbi.nlm.nih.gov/pubmed/2196921.

[9] T. Ahl, N. Dalen, A. Lundberg, and G. Selvik, "Mobility of the ankle mortise. A roentgen stereophotogrammetric analysis," *Acta Orthop Scand,* vol. 58, no. 4, pp. 401-2, Aug 1987. [Online]. Available: https://www.ncbi.nlm.nih.gov/pubmed/3673536.

[10] A. Lundberg, "Kinematics of the ankle and foot. In vivo roentgen stereophotogrammetry," *Acta Orthop Scand Suppl,* vol. 233, pp. 1-24, 1989. [Online]. Available: https://www.ncbi.nlm.nih.gov/pubmed/2686345.

[11] J. W. Arner *et al.*, "The Effects of Anterior Cruciate Ligament Deficiency on the Meniscus and Articular Cartilage: A Novel Dynamic In Vitro Pilot Study," *Orthop J Sports Med,* vol. 4, no. 4, p. 2325967116639895, Apr 2016, doi: 10.1177/2325967116639895.

[12] J. N. Irvine *et al.*, "Is There a Difference in Graft Motion for Bone-Tendon-Bone and Hamstring Autograft ACL Reconstruction at 6 Weeks and 1 Year?," *Am J Sports Med,* vol. 44, no. 10, pp. 2599-2607, Oct 2016, doi: 10.1177/0363546516651436.

[13] M. J. Bey, S. K. Kline, S. Tashman, and R. Zauel, "Accuracy of biplane x-ray imaging combined with model-based tracking for measuring in-vivo patellofemoral joint motion," *Journal of orthopaedic surgery and research,* vol. 3, p. 38, Sep 4 2008, doi: 10.1186/1749-799X-3-38.

[14] *OpenCV: Open Source Computer Vision Library*. (2022). [Online]. Available: https://opencv.org/

[15] *Eigen*. (2021). [Online]. Available: https://eigen.tuxfamily.org/

[16] J. M. Boone, J. A. Seibert, W. A. Barrett, and E. A. Blood, "Analysis and correction of imperfections in the image intensifier-TV-digitizer imaging chain," *Med Phys,* vol. 18, no. 2, pp. 236-42, Mar-Apr 1991, doi: 10.1118/1.596718.

[17] R. Fahrig, M. Moreau, and D. W. Holdsworth, "Three-dimensional computed tomographic reconstruction using a C-arm mounted XRII: correction of image intensifier distortion," *Med Phys,* vol. 24, no. 7, pp. 1097-106, Jul 1997, doi: 10.1118/1.598013.

[18] R. a. Z. Hartley, Andrew, *Multiple View Geometry in Computer Vision*, Second ed. Cambridge University Press, 2003, p. 652.

[19] P. Cerveri, C. Forlani, N. A. Borghese, and G. Ferrigno, "Distortion correction for x-ray image intensifiers: local unwarping polynomials and RBF neural networks," *Med Phys,* vol. 29, no. 8, pp. 1759-71, Aug 2002, doi: 10.1118/1.1488602.

[20] D. P. Chakraborty, "Image intensifier distortion correction," *Medical Physics,* vol. 14, pp. 249-252, 1987, doi: 10.1118/1.596078.

[21] E. Gronenschild, "The accuracy and reproducibility of a global method to correct for geometric image distortion in the x-ray imaging chain.," *Medical physics,* vol. 24, pp. 1875-1888, 1997, doi: 10.1118/1.598101.

[22] A. E. Kedgley, A. M. V. Fox, and T. R. Jenkyn, "Image intensifier distortion correction for fluoroscopic RSA: The need for independent accuracy assessment," *Journal of Applied Clinical Medical Physics,* vol. 13, pp. 197-204, 2012, doi: 10.1120/jacmp.v13i1.3441.

[23] R. R. Liu, S. Rudin, and D. R. Bednarek, "Super-global distortion correction for a rotational C-arm x-ray image intensifier," *Med Phys,* vol. 26, no. 9, pp. 1802-10, Sep 1999, doi: 10.1118/1.598684.

[24] N. M. Alem, J. W. Melvin, and G. L. Holstein, "Biomechanics applications of direct linear transformation in close-range photogrammetry," in *Proceedings of the Sixth New England Bioengineering Conference*, D. Jaron Ed.: Pergamon, 1978, pp. 202-206.

[25] Y. Furukawa and J. Ponce, "Accurate camera calibration from multi-view stereo and bundle adjustment," *International Journal of Computer Vision,* vol. 84, pp. 257-268, 2009, doi: 10.1007/s11263-009-0232-2.

[26] D. D. Lichti, G. B. Sharma, G. Kuntze, B. Mund, J. E. Beveridge, and J. L. Ronsky, "Rigorous geometric self-calibrating bundle adjustment for a dual fluoroscopic imaging system," *IEEE Transactions on Medical Imaging,* vol. 34, pp. 589-598, 2015, doi: 10.1109/TMI.2014.2362993.

[27] A. Rougee, C. Picard, C. Ponchut, and Y. Trousset, "Geometrical calibration of X-ray imaging chains for three-dimensional reconstruction," *Comput Med Imaging Graph,* vol. 17, no. 4-5, pp. 295-300, Jul-Oct 1993. [Online]. Available: https://www.ncbi.nlm.nih.gov/pubmed/8306301.

[28] N. Borlin, T. Thien, and J. Karrholm, "The precision of radiostereometric measurements. Manual vs. digital measurements," *J Biomech,* vol. 35, no. 1, pp. 69-79, Jan 2002. [Online]. Available: https://www.ncbi.nlm.nih.gov/pubmed/11747885.

[29] *PMCMRplus: Calculate Pairwise Multiple Comparisons of Mean Rank Sums Extended*. (2023). [Online]. Available: http://CRAN.R-project.org/package=PMCMRplus

[30] K. L. Gwet, "Handbook of Inter-Rater Reliability," in *The Definitive Guide to Measuring the Extent of Agreement Among Raters - Volume 2: Analysis of Quantitative Ratings*, 5th ed. United States of America: AgreeStat Analytics, 2021, sec. Chapter 9: Intraclass Correlation and Multivariate Analysis.

[31] P. Cerveri, C. Forlani, a. Pedotti, and G. Ferrigno, "Hierarchical radial basis function networks and local polynomial un-warping for X-ray image intensifier distortion correction: a comparison with global techniques.," *Medical & biological engineering & computing,* vol. 41, pp. 151-63, 2003.

[32] D. Mery, "Explicit geometric model of a radioscopic imaging system," *NDT & E International,* vol. 36, no. 8, pp. 587-599, 2003/12/01/ 2003, doi: https://doi.org/10.1016/S0963-8695(03)00084-7.

[33] E. L. Brainerd *et al.*, "X-ray reconstruction of moving morphology (XROMM): precision, accuracy and applications in comparative biomechanics research," *J Exp Zool A Ecol Genet Physiol,* vol. 313, no. 5, pp. 262-79, Jun 1 2010, doi: 10.1002/jez.589.

[34] S. Tashman and W. Anderst, "In-vivo measurement of dynamic joint motion using high speed biplane radiography and CT: application to canine ACL deficiency," (in eng), *J Biomech Eng,* vol. 125, no. 2, pp. 238-45, Apr 2003, doi: 10.1115/1.1559896.

[35] I. Söderkvist and P. A. Wedin, "Determining the movements of the skeleton using well-configured markers," (in eng), *J Biomech,* vol. 26, no. 12, pp. 1473-7, Dec 1993, doi: 10.1016/0021-9290(93)90098-y.

Chapter 3

Validation of foot bone segmentation from fan beam and cone beam computed tomography scans

Eric D. Thorhauer[a,b], Corey Wukelic[a], Nicholas Entress[a,b], Jane B. Shofer[a], William R. Ledoux, PhD[a,b,c]

[a]Center for Limb Loss and MoBility (CLiMB), Department of Veterans Affairs Puget Sound Health Care System, Seattle, Washington, USA

[b]Department of Mechanical Engineering, University of Washington, Seattle, Washington, USA

[c]Department of Orthopaedics & Sports Medicine, University of Washington, Seattle, Washington, USA

Keywords: computed tomography, foot and ankle, bone segmentation, validation

Abstract

Accurate segmentation of foot and ankle bones from computed tomography scans is an essential precursor to morphological comparison studies and model-based biplanar fluoroscopic tracking. Errors in modeling the bones may propagate into coordinate system definitions or affect arthrokinematic calculations. Cone beam computed tomography scanners with sensitive detectors offer a lower dose alternative to fan beam scanners, although with signal-to-noise ratio and tissue contrast tradeoffs. The primary aims of this study were to validate the accuracy of foot bone models generated using established semi-automatic segmentation techniques relative to ground truth laser scans of the dissected bone specimens and to compare the errors in models segmented from a fan beam scanner to those from a cone beam scanner. We found excellent between and within-operator intra-class correlation scores for segmentations (all > 0.90). Voxel-based metrics revealed small but significant differences between scanner types when comparing the Dice score and precision of segmentations, with cone beam having higher scores for nearly every metric type. Surface-based error data also revealed cone beam scans to be more accurate to the actual bone morphology despite having noisier images. The small isotropic voxels of the cone beam scanner produced bone models with errors averaging 0.43 ± 0.11 mm compared to the fan beam average 0.74 ± 0.15 mm error across all bones. The findings suggest that voxel resolution is more critical than detector type for modeling foot bones and that these segmentation techniques may overcome the limitations in cone beam scanners. These outcomes support the growing movement towards more widespread adoption of low-dose cone beam weight-bearing computed

tomography imaging for 3D modeling of foot and ankle bones both clinically and for research purposes.

Introduction

Segmentation of subject-specific bone models from computed tomography (CT) is an essential step in studies utilizing model-based biplanar fluoroscopy tracking [61, 93, 97, 98, 103, 104], CT bone tracking [122-124], and statistical shape analyses [125-127]. The accuracy of the segmented bones also directly influences and places a lower limit on the resolution of arthrokinematic measures estimated as dynamic inter-bone distance fields [23, 128]. Low-dose cone beam CT scanners with efficient detectors now provide a viable alternative to the fan beam scanners for lower limb imaging [60, 129, 130]. These scanners expose subjects to a fraction of the radiation dose of fan beam scanners with the tradeoff of degradation in image quality, exhibited by higher noise in the voxel Hounsfield units and weaker cortical bone contrast at joint margins. During longitudinal biplane fluoroscopy research studies, using a traditional fan beam scanner for the CT scans required to model bones and generate digitally reconstructed radiographs contributes most of the total radiation dose experienced by subjects compared to the total dose received by pulsed biplane X-ray trials. Shifting towards low-dose scanners can allow researchers to allocate more of the subjects' received radiation budget towards additional fluoroscopy trials or reduce the subjects' dose without altering the study design.

Bone segmentations from CT data may be performed using various techniques, ranging from manual to semi-automatic and fully automatic [131, 132]. While advances in machine learning have led to algorithms for segmenting organs and bones from CT, these segmentation results are less precise and often need human operator refinement. Fully manual CT

segmentation methods have proven to be among the most accurate, but they require the most user time, effort, and expertise. Semi-automatic tools like smart thresholding, LiveWire or Intelligent Scissors boundary detection, and active contours algorithms reduce the segmentation burden on the human operator and yield highly accurate and precise results required for discerning the subtle differences expected in most biomechanical studies. Previously, bone segmentation validation has been performed using laser scans of denuded bone specimens as the reference ground truth dataset [133-135]. An external reference is essential for understanding the true geometric errors in bone modeling in the context of the most critical regions of anatomical interest.

The primary aims of this study were to 1) validate the accuracy of foot and ankle bone segmentations from CT by using laser scanning as the ground truth and to 2) quantify the accuracy and repeatability of segmenting bones from a low-dose cone beam CT compared to a traditional fan beam scanner, and to 3) assess the between and within segmentation operator agreement and repeatability.

Methods

Specimen preparation

Three fresh-frozen human foot specimens (48 ± 12.8 years old, two males, one female, 28.5 ± 7.0 BMI) were obtained, including the distal tibia shaft. Specimens were screened for radiographic evidence of osteoarthritis and foot deformities via fluoroscopy. Custom-made registration clusters were rigidly embedded in each specimen's tibia, calcaneus, talus, navicular, first metatarsal, and proximal phalanx bones (Figure 1A). Each cluster consisted of three solid 10 mm diameter acrylic spherical fiducials rigidly connected with 3 mm diameter carbon fiber

shafts. Clusters were cemented into pre-drilled undersized bone holes through minimally invasive incisions to preserve as much of the native specimen tissue as possible.

Computed tomography scanning

Before and following fiducial cluster installation CT scans were acquired for each specimen in both a fan beam (Siemens Biograph 16, voxel size: 0.67 x 0.67 x 0.75 mm, 130kVp, 134mA, 0.95 mm focal spot) and a low-dose cone beam scanner (CurveBeam LineUp, voxel size: 0.3 x 0.3 x 0.3 mm, 120kVp, 5mA, 0.5 mm focal spot) with the specimens held fixed in a neutral foot posture during acquisition (Figure 1B). Voxel volumes were reconstructed using the B70s bone convolution kernel for the Siemens and the BEPS2 kernel for the CurveBeam.

Laser scanning

A six-axis coordinate measurement machine probe and coupled laser scan head (Kreon ACES-7, Kreon Solano Blue laser) were calibrated before scanning each specimen. The calibrated bias and precision of the system were 0.005 ± 0.016 mm for the contacting probe and 0.003 ± 0.041 mm for the laser scanner. Each specimen was carefully dissected to excise each bone of interest, which was subsequently denuded of soft tissues and cartilage by manual scalpel removal and soaking in a 2% bleach solution for up to two hours. Each excised specimen was rigidly clamped in place. Then, laser scans of the bone surfaces and the fiducial markers were acquired (Figure 1C) via the Kreon arm into Geomagic Wrap 2022 software (3DS, North Carolina, USA).

The raw laser point clouds from each scan pass were denoised and co-registered in Geomagic and then converted into unified polygonal mesh surface models of each bone and fiducial sphere (Figure 1D). Any mesh holes or isolated triangular elements were removed using

the Geomagic repair tools, and the meshes were filtered using the quick smoothing operation and resampled for more uniform mesh element sizes and distributions.

Computed tomography scan segmentation

The CT scan data were segmented in Mimics software (v22, Materialise, Leuven, Belgium) to produce separate segmentation masks for each bone of interest and the corresponding fiducial clusters (Figure 1B). Each segmentation was performed on anonymized copies of the original scans by three blinded operators on three separate days, a week apart. Each operator started with an initial threshold segmentation of all the bone regions, followed by semi-automatic LiveWire segmentation, region-growing, and Boolean operations to separate the initial full foot mask into the unique bone regions, and final refinement of each bone segmentation masks using intermediate 3D surface renderings of the bones for guidance. The final segmentations were exported as a series of 2D mask images, and the corresponding bone and sphere surfaces were exported as stereolithography files (STL).

Aligning laser scan and CT data

The fiducial cluster data were used to iteratively co-register each bone's laser scan surface to the respective CT dataset. Iterative registration was performed in MATLAB via least-squares optimization of the Euclidean distance error between the laser scan surfaces and the CT bone model surfaces. Across all bones and scans, the average root-mean-square sphere registration error was 0.11 ± 0.17 mm. The resulting transformations were used to map both the CT bone surface data to the laser scan surface data, and to transform the laser scan surfaces into the CT voxel domain.

Voxel domain segmentation error analysis

After being registered appropriately to the CT data, laser scan surface models were voxelized in Mimics to convert the surface models into filled binary 3D volumes, which could be assessed as 2D segmentation masks in the native CT slice plane (Figure 1E). The volume similarity, Dice coefficient, recall, and precision segmentation agreement metrics were quantified for each bone between the operators' CT segmentations and the ground-truth laser scan data [136, 137].

Surface domain segmentation error analysis

Point-wise Euclidean distance errors between laser scan and CT-derived bone surface models were computed over each bone surface. Surface errors were calculated at each surface model vertex as the distance to the nearest neighbor in the CT surface model. The mean, standard deviation, and maximum surface errors were computed for each bone. Within each CT scanner type and for each bone type, the three specimens' morphologies were combined to generate mean bone surfaces (ShapeWorks Studio, University of Utah) on which to represent the average segmentation errors in an anatomically meaningful sense.

Statistical analyses

Linear mixed-effects regression was used to assess the association between agreement (the dependent variable) and scanner type, bone type, and rater (segmentation operator) (independent covariate fixed effects). Random effects were modeled for differences in intercepts across specimens, specimen by bone, specimen by scanner, specimen by rater interactions, and

within specimen/scanner/bone/rater across segmentation sessions. Since the dependent variables were proportions, they were modeled as logits ($\log \frac{p}{1-p}$) to produce more accurate errors. Using conditional F-tests, hypothesis testing was carried out to assess the overall association between agreement and scanner, bone, and rater. Means (SEs) and mean differences (95% confidence intervals) were estimated by back-transforming model estimates into proportions using Taylor approximations. Analyses were carried out using R 4.2.3 [138] and packages tidyverse [139], lme4 [140], lmerTest [141] and emmeans [142]. Intraclass correlation coefficients were calculated in MATLAB to assess the agreement in voxel volume segmentations between operators and repeatability within operators for each bone type. All analyses ignored the fibular regions due to motion relative to the tibia and a lack of a dedicated fibular fiducial cluster.

Results

Segmentation accuracy

Voxel-based segmentation metrics indicate a high degree of overlap between the operator segmentations and ground truth data was achieved for every foot bone investigated with minimal variance between sessions and scanner types (Table 1). A significant difference in precision across bone types was observed ($p = 0.034$), evident in the high differences between the calcaneus and the proximal phalanx (Table 1). Similarly, Dice scores were higher in the hindfoot bones apart from the tibia. However, their association across bone types was not significant ($p = 0.073$). Comparing segmentation results between CT scanner types, the cone beam had significantly higher precision ($p = 0.014$) and Dice scores ($p = 0.024$) than fan beam (Table 2). Recall and volume similarity were not different between scanners.

The root-mean-squared surface errors differed between scanner types and bones in the case of the fan beam segmentations (Table 3). Cone beam segmentation errors averaged 0.43 ± 0.11 mm across all bones and were lower than the respective fan beam average error 0.74 ± 0.15 mm. The surface-based segmentation errors were worst in the fan beam subtalar joint regions of the talus and calcaneus and in most of the navicular (Figure 2). Those corresponding regions in the cone beam data exhibited significantly less error (Figure 3). Most of the errors were over-segmentations of the bones, whereby the CT-based models were slightly larger than the laser scan surfaces. In the cone beam data, under-segmentation tended to occur in regions of very high local curvature, such as the distal malleolus of the tibia, or in the bony processes of the talus and calcaneus (Figure 3).

Segmentation agreement and repeatability

Intraclass correlation coefficients for between-operators agreement were excellent for all segmentations (Table 4), and no significant differences between bones were observed. There were no significant differences between fan beam and cone beam segmentation between-operators ICC scores. Within-operator repeatability scores were excellent across for all bones in both fan beam and cone beam scans (Table 5), and there were no significant differences observed between scanner types.

Discussion

This study successfully characterized the segmentation errors of generating foot and ankle bones from fan beam and cone beam CT scanners. We found high repeatability within and

agreement between segmentation operators for all bones. The ground truth laser scan data provided an objective external metric for assessing the physical accuracy of the bone models, and the laser scanner calibration errors were an order of magnitude lower than the segmentation errors, while the average laser-to-CT registration error was nearly a quarter of the lowest segmentation surface error and less than half the CT voxel sizes. Mapping the specimen errors to a common mean bone highlights the relative magnitudes in errors when segmenting the various articular surfaces, facets, bone shafts, and other osseous features used for fitting anatomical coordinate systems and classifying bone morphological types.

Compared to previous CT segmentation validations using a laser scan ground truth, our segmentation results in the foot are comparable to the results of other studies of the hand and knee. In the case of hand phalanx bones, DeVries et al. reported an average Euclidean error of 0.20 ± 0.15 mm between smoothed models manually segmented from CT and laser scan surfaces [135]. These hand segmentation results are more accurate than our foot proximal phalanx results, but the precisions are similar. In both cases, the surrounding tissues present less of a hindrance to obtaining good scans and segmenting the bones of interest. Pietrobelli et al. report mean errors of 0.35 and 0.70 mm and maximum errors between 1.23 and 4.16 mm in distal fibula segmentations using thresholding techniques. In full tibia segmentations from CT using Mimics software, Stephen et al. report root-mean-square errors averaging 0.82 ± 0.20 mm. Both studies compare well with our tibia segmentation errors.

Some bone regions exhibited higher segmentation errors than others. Regions of higher X-ray attenuation, like the hindfoot, suffer from lower contrast and a higher degree of noise in the reconstructed Hounsfield units. The subtalar joint, for example, was the highest region of error in the fan beam CT data and the highest overall. The subtalar joint consists of narrowly

spaced facets typically oriented oblique to the scanner planes and that are more sensitive to the larger voxel sizes of the fan beam scanner. Another source of the higher fan beam errors could be the voxelization algorithm in the Mimics software that converted the laser scan surfaces into voxel volumes at a grid resolution equal to the fan beam voxel sizes. The fan beam voxels could be more sensitive to partial volume effects because they are anisotropic and larger than the cone beam scanner. This potentially explains why noticeable differences between scanner types were observed in the surface metrics but not in voxel metrics.

The results suggest a minimum voxel resolution is required to quantify foot bone morphology reliably without substantial aliasing. However, segmentation of noisier and lower contrast cone beam scans, when assisted by the semi-automated segmentation tools utilized in this study, can overcome the inherent limitations and produce usable bone models. Cone beam scanners offer a few advantages over fan beam systems: the ability to image the foot in a natural weight-bearing position at a fraction of the radiation dose. The results of this study provide confidence in the further utilization of cone beam systems for foot and ankle bone modeling.

The many limitations of this study included only testing two scanners without varying the voxel sizes beyond the minimum possible sizes or the type of reconstruction kernel, not recording the time or quantifying the effort of segmentation required for each bone and scanner type, only testing three specimens, and not including the fibula as a separate analysis. Errors from segmenting and registering the fiducial clusters and voxelizing the surface models into binary volumes certainly introduced noise into the ground truth data. Despite these limitations, we believe these data may be useful for benchmarking future foot bone segmentation algorithms, image preprocessing treatments, and reconstructions from scanners with more sensitive detectors.

This study illustrated the importance of using an external ground truth for comparing segmentation accuracy. The voxel-based metrics alone cannot highlight the specific anatomical regions of lower segmentation accuracy or a physically meaningful lower bound on the model errors. Understanding these errors will aid the design of studies investigating dynamic joint arthrokinematics and joint spacing assessments using biplane fluoroscopy and bone tracking across multiple CT volumes. Additionally, these data will motivate future work to improve the segmentation pipeline, including automation and quality control algorithms to maintain the high throughput and accuracy required for large clinically motivated studies.

Figures and Tables

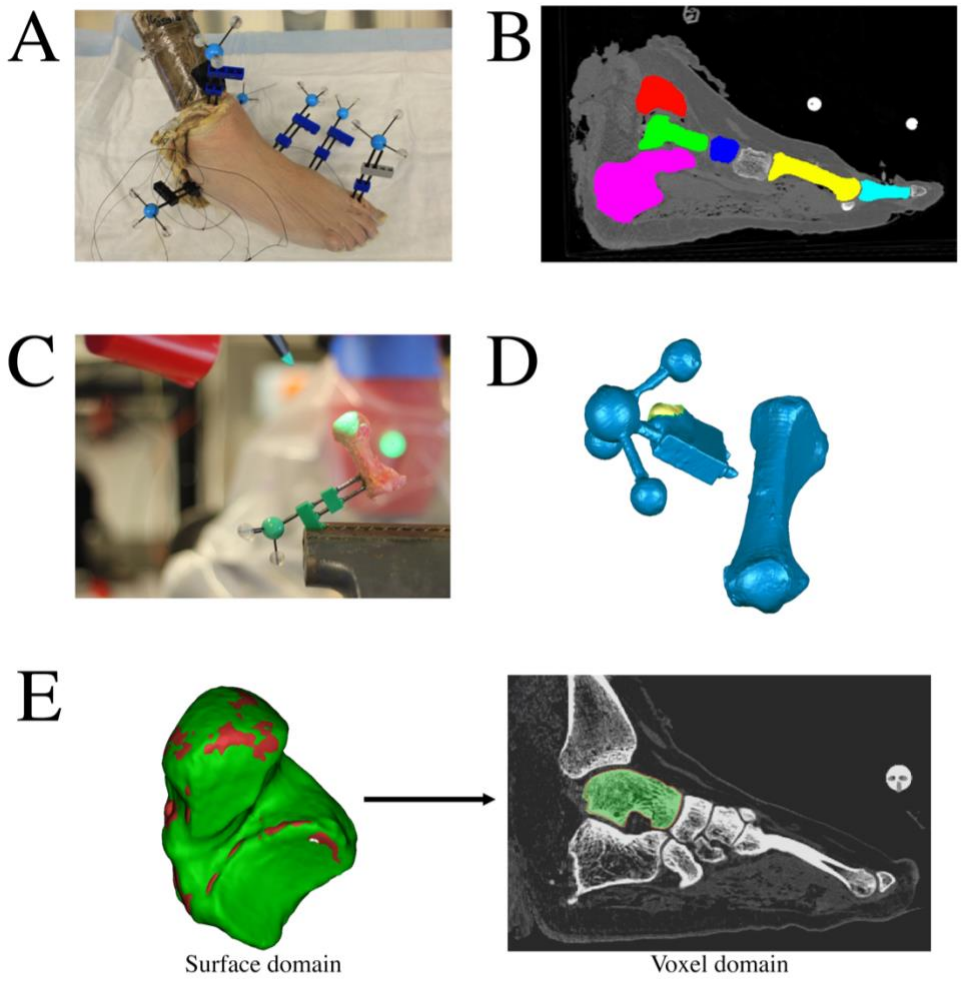

Figure 1: Fiducial marker clusters were (A) rigidly installed into the tibia, talus, calcaneus, navicular, first metatarsal, and proximal phalanx of three human foot specimens. (B) Computed tomography scans were acquired on both fan beam and cone beam scanners, and bones were segmented by three operators over three sessions. (C) Specimens were dissected to excise the bones of interest, denuded of soft tissues, and clamped into place for laser scanning. (D) Laser scan data were processed into surface meshes for each bone. The co-registered laser data were compared to bone models segmented from CT as surface models and voxelized binary volumes (E).

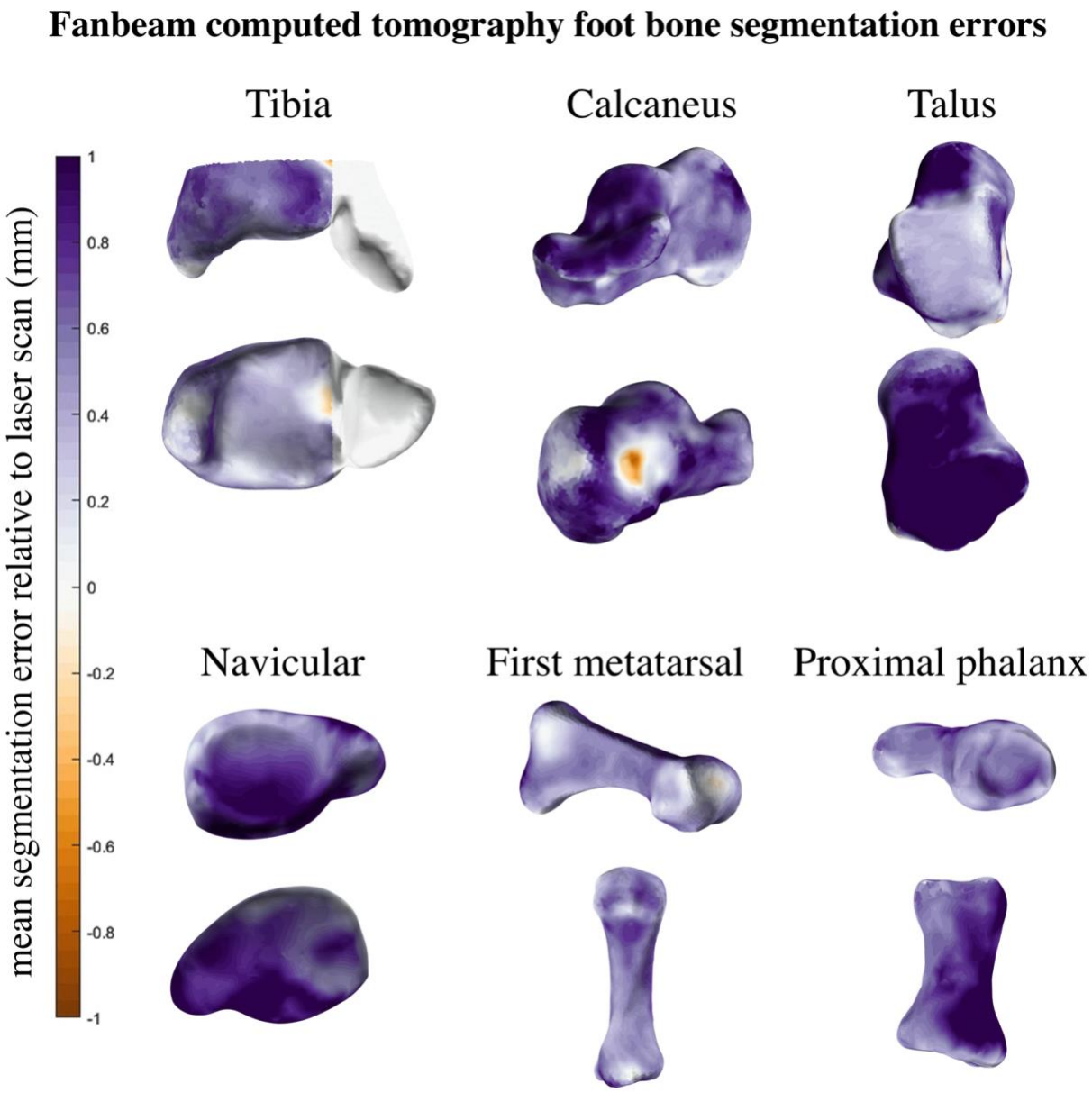

Figure 2: The average errors for segmenting each bone from fan beam computed tomography scans. Positive values (purple) indicate over-segmentation and negative values (orange) indicate under-segmentation relative to the ground truth laser scan data. The fibula regions were excluded from the analysis. The subtalar regions of both the talus and calcaneus had the worst errors. Most of the navicular and portions of the proximal phalanx were over-segmented.

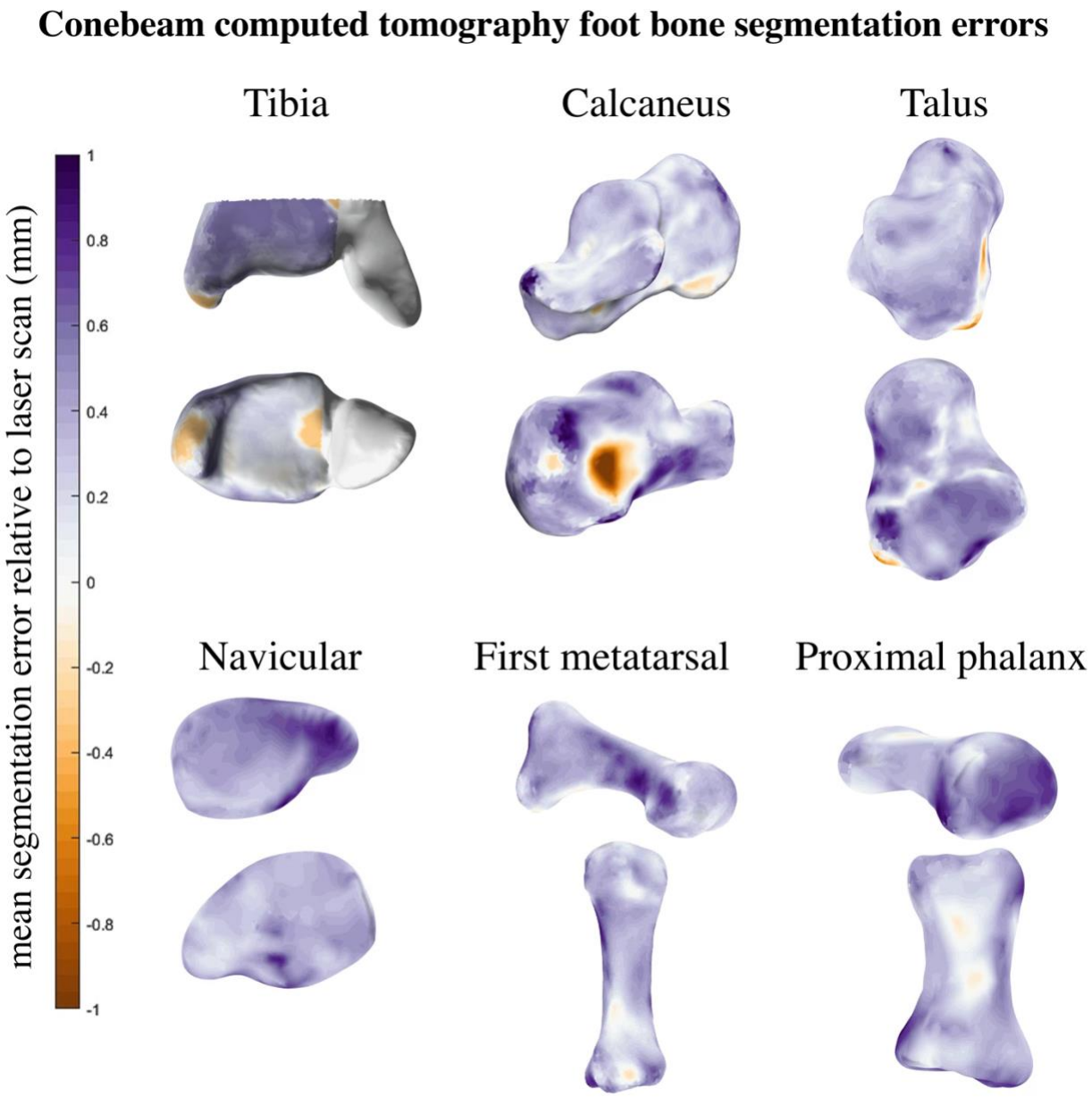

Figure 3: The average errors for segmenting each bone from cone beam computed tomography scans. Positive values (purple) indicate over-segmentation and negative values (orange) indicate under-segmentation relative to the ground truth laser scan data. The fibula regions were excluded from the analysis. Sharp bony prominences were the locations of the largest errors in all bones.

Table 1: Voxel-based segmentation quality metric means and standard deviations by bone type, averaged across all operators, sessions, and scanner types. Summary of mean (± SE) agreement and mean difference (95% CI) by bone from linear mixed effects regression of outcomes (modeled as logits) on scanner, rater, and bone. Within each metric, the pair of bones with the maximum difference based on their means are highlighted in bold and the difference between their means and the p-values for the associated t-test are listed. P-values are listed for the omnibus F-test for the association between metric score and bone. (†) The mean for talus is slightly less than that for calcaneus, but the 95% CI for the difference between tibia and talus was wider: (-0.048, 0.093).

	Tibia	Calcaneus	Talus	Navicular	First metatarsal	Proximal phalanx	Max difference between bones (95% CI)	t-test p-value	F-test p-value
volume similarity	0.969 ± 0.011	**0.988 ± 0.005**	0.978 ± 0.004	0.967 ± 0.004	0.976 ± 0.009	**0.957 ± 0.016**	0.031 (-0.045, 0.094)	0.27	0.23
Dice score	0.936 ± 0.018	**0.965 ± 0.005**	0.958 ± 0.003	0.947 ± 0.004	0.946 ± 0.006	**0.921 ± 0.007**	0.044 (-0.016, 0.071)	0.020*	0.073
recall	**0.953 ± 0.022**	**0.978 ± 0.014**	0.978 ± 0.004	0.976 ± 0.006	0.972 ± 0.007	0.967 ± 0.007	†0.025 (-0.024, 0.070)	0.17	0.10
precision	0.930 ± 0.026	**0.959 ± 0.005**	0.939 ± 0.004	0.925 ± 0.004	0.926 ± 0.013	**0.885 ± 0.018**	0.074 (-0.02, 0.163)	0.078	0.034*

Table 2: Voxel-based segmentation quality metric means of agreement (± standard errors) by CT scanner type and their mean difference (95% CI) from linear mixed effects regression of outcomes (modeled as logits) on scanner type, rater and bone. P-values are listed for the t-tests between scanner types and for the omnibus F-test for the association between segmentation metric and bone. Significant differences (*) between scanners and the association between metric score and bone were found for precision and Dice score.

	Fan beam	Cone beam	Between-scanners difference (95% CI)	t-test p-value	F-test p-value
volume similarity	0.967 ± 0.005	0.981 ± 0.004	-0.014 (-0.031, 0.009)	0.17	0.20
Dice score	0.940 ± 0.007	0.954 ± 0.005	-0.013 (-0.022, -0.004)	0.024*	<0.0001*
recall	0.972 ± 0.007	0.971 ± 0.006	0.001 (-0.019, 0.021)	0.87	0.88
precision	0.915 ± 0.007	0.943 ± 0.005	-0.029 (-0.044, -0.012)	0.014*	0.018*

Table 3: Summary of the surface-based root-mean-square segmentation errors for each bone, within the fan beam and cone beam scanner types.

	Fan beam		Cone beam
tibia	0.91 ± 0.15		0.46 ± 0.10
talus	0.85 ± 0.15		0.42 ± 0.07
calcaneus	0.68 ± 0.12		0.43 ± 0.10
navicular	0.72 ± 0.14		0.45 ± 0.13
first metatarsal	0.66 ± 0.13		0.43 ± 0.15
proximal phalanx	0.64 ± 0.21		0.41 ± 0.11

Table 4: The means and standard deviations of the intraclass correlation coefficients for between-raters agreement listed for each bone and CT scanner type.

	Tibia	Calcaneus	Talus	Navicular	First metatarsal	Proximal phalanx
fan beam	0.970 ± 0.007	0.996 ± 0.002	0.993 ± 0.003	0.992 ± 0.005	0.994 ± 0.001	0.991 ± 0.003
cone beam	0.980 ± 0.003	0.992 ± 0.003	0.992 ± 0.001	0.987 ±0.006	0.987 ± 0.002	0.984 ± 0.001

Table 5: Intraclass correlation coefficients for within-operators, between-sessions segmentation repeatability assessments in each CT scanner type for each bone.

		Tibia	Calcaneus	Talus	Navicular	First metatarsal	Proximal phalanx
fan beam	Operator 1	0.998	0.996	0.993	0.992	0.995	0.990
	Operator 2	0.995	0.995	0.993	0.994	0.999	0.999
	Operator 3	0.996	0.998	0.998	0.998	0.999	0.999
cone beam	Operator 1	0.985	0.993	0.993	0.989	0.988	0.982
	Operator 2	0.998	0.998	0.998	0.999	0.999	0.999
	Operator 3	0.996	0.995	0.996	0.999	0.998	0.999

References

[1] J. M. Iaquinto *et al.*, "Model-based tracking of the bones of the foot: A biplane fluoroscopy validation study," *Comput Biol Med,* vol. 92, pp. 118-127, Jan 1 2018, doi: 10.1016/j.compbiomed.2017.11.006.

[2] S. Pitcairn, J. Kromka, M. Hogan, and W. Anderst, "Validation and application of dynamic biplane radiography to study in vivo ankle joint kinematics during high-demand activities," (in eng), *J Biomech,* vol. 103, p. 109696, Apr 16 2020, doi: 10.1016/j.jbiomech.2020.109696.

[3] T. Miyamoto *et al.*, "4D-foot analysis on effect of arch support on ankle, subtalar, and talonavicular joint kinematics," (in eng), *J Orthop Sci,* Jan 27 2023, doi: 10.1016/j.jos.2022.10.009.

[4] T. Negishi *et al.*, "Three-Dimensional Innate Mobility of the Human Foot on Coronally-Wedged Surfaces Using a Biplane X-Ray Fluoroscopy," (in eng), *Front Bioeng Biotechnol,* vol. 10, p. 800572, 2022, doi: 10.3389/fbioe.2022.800572.

[5] J. A. Cross, B. D. McHenry, R. Molthen, E. Exten, T. G. Schmidt, and G. F. Harris, "Biplane fluoroscopy for hindfoot motion analysis during gait: A model-based evaluation," *Med Eng Phys,* vol. 43, pp. 118-123, May 2017, doi: 10.1016/j.medengphy.2017.02.009.

[6] K. Ito *et al.*, "Three-dimensional innate mobility of the human foot bones under axial loading using biplane X-ray fluoroscopy," (in eng), *R Soc Open Sci,* vol. 4, no. 10, p. 171086, Oct 2017, doi: 10.1098/rsos.171086.

[7] E. Thorhauer, M. French, T. Kimura, and W. R. Ledoux, "A Cadaveric Comparison of the Kinematic and Anatomical Axes and Arthrokinematics of the Metatarsosesamoidal and First Metatarsophalangeal Joints," (in eng), *J Biomech Eng,* vol. 145, no. 4, Apr 1 2023, doi: 10.1115/1.4056060.

[8] J. J. Crisco, E. Halilaj, D. C. Moore, T. Patel, A.-P. C. Weiss, and A. L. Ladd, "In Vivo kinematics of the trapeziometacarpal joint during thumb extension-flexion and abduction-adduction," (in eng), *The Journal of hand surgery,* vol. 40, no. 2, pp. 289-296, 2015, doi: 10.1016/j.jhsa.2014.10.062.

[9] W. Schallig *et al.*, "Precision of determining bone pose and marker position in the foot and lower leg from computed tomography scans: How low can we go in radiation dose?," (in eng), *Med Eng Phys,* vol. 69, pp. 147-152, Jul 2019, doi: 10.1016/j.medengphy.2019.05.004.

[10] S. Telfer, M. W. Kindig, B. J. Sangeorzan, and W. R. Ledoux, "Metatarsal shape and foot type: A geometric morphometric analysis," *Journal of Biomechanical Engineering,* vol. 139, no. 3, 2017, doi: 10.1115/1.4035077.

[11] M. R. Requist, T. Rolvien, A. Barg, and A. L. Lenz, "Morphologic analysis of the 1st and 2nd tarsometatarsal joint articular surfaces," (in eng), *Scientific reports,* vol. 13, no. 1, p. 6473, Apr 20 2023, doi: 10.1038/s41598-023-32500-z.

[12] T. M. Grant *et al.*, "Development and validation of statistical shape models of the primary functional bone segments of the foot," *PeerJ,* vol. 2020, no. 2, pp. 1-19, 2020, doi: 10.7717/peerj.8397.

[13] L. Zheng, R. Carey, E. Thorhauer, S. Tashman, C. Harner, and X. Zhang, "In vivo tibiofemoral skeletal kinematics and cartilage contact arthrokinematics during decline

walking after isolated meniscectomy," *Med Eng Phys,* vol. 51, pp. 41-48, Jan 2018, doi: 10.1016/j.medengphy.2017.10.014.
[14] B. Wang *et al.*, "Accuracy and feasibility of high-speed dual fluoroscopy and model-based tracking to measure in vivo ankle arthrokinematics," *Gait Posture,* vol. 41, no. 4, pp. 888-93, May 2015, doi: 10.1016/j.gaitpost.2015.03.008.
[15] M. French, E. D. Thorhauer, T. Kimura, B. J. Sangeorzan, and W. R. Ledoux, "Displacement of the Metatarsal Sesamoids in Relation to First Metatarsophalangeal Joint Extension," (in eng), *Foot Ankle Orthop,* vol. 7, no. 3, p. 24730114221126457, Jul 2022, doi: 10.1177/24730114221126457.
[16] C. F. T. Lôbo, E. A. Pires, M. Bordalo-Rodrigues, C. de Cesar Netto, and A. L. Godoy-Santos, "Imaging of progressive collapsing foot deformity with emphasis on the role of weightbearing cone beam CT," (in eng), *Skeletal Radiol,* Oct 25 2021, doi: 10.1007/s00256-021-03942-1.
[17] F. Lintz, P. Beaudet, G. Richardi, and J. Brilhault, "Weight-bearing CT in foot and ankle pathology," (in eng), *Orthop Traumatol Surg Res,* vol. 107, no. 1s, p. 102772, Feb 2021, doi: 10.1016/j.otsr.2020.102772.
[18] Y. Hu, W. R. Ledoux, M. Fassbind, E. S. Rohr, B. J. Sangeorzan, and D. Haynor, "Multi-rigid image segmentation and registration for the analysis of joint motion from three-dimensional magnetic resonance imaging," *J Biomech Eng,* vol. 133, no. 10, p. 101005, Oct 2011, doi: 10.1115/1.4005175.
[19] C. Li, C. Xu, C. Gui, and M. D. Fox, "Distance regularized level set evolution and its application to image segmentation," *IEEE Trans Image Process,* vol. 19, pp. 3243-3254, 2010, doi: 10.1109/TIP.2010.2069690.
[20] A. Pietrobelli *et al.*, "Comparability of skeletal fibulae surfaces generated by different source scanning (dual-energy CT scan vs. high resolution laser scanning) and 3D geometric morphometric validation," (in eng), *J Anat,* vol. 241, no. 3, pp. 667-682, Sep 2022, doi: 10.1111/joa.13714.
[21] J. M. Stephen, J. D. Calder, A. Williams, and H. El Daou, "Comparative accuracy of lower limb bone geometry determined using MRI, CT, and direct bone 3D models," *Journal of Orthopaedic Research,* vol. 39, no. 9, pp. 1870-1876, 2021, doi: https://doi.org/10.1002/jor.24923.
[22] N. A. DeVries, E. E. Gassman, N. A. Kallemeyn, K. H. Shivanna, V. A. Magnotta, and N. M. Grosland, "Validation of phalanx bone three-dimensional surface segmentation from computed tomography images using laser scanning," (in eng), *Skeletal Radiol,* vol. 37, no. 1, pp. 35-42, Jan 2008, doi: 10.1007/s00256-007-0386-3.
[23] A. A. Taha and A. Hanbury, "Metrics for evaluating 3D medical image segmentation: analysis, selection, and tool," (in eng), *BMC Med Imaging,* vol. 15, p. 29, Aug 12 2015, doi: 10.1186/s12880-015-0068-x.
[24] K. H. Zou *et al.*, "Statistical validation of image segmentation quality based on a spatial overlap index," (in eng), *Acad Radiol,* vol. 11, no. 2, pp. 178-89, Feb 2004, doi: 10.1016/s1076-6332(03)00671-8.
[25] *R: A language and environment for statistical computing.* (2023). R Foundation for Statistical Computing, Vienna, Austria.
[26] *Welcome to the tidyverse.* (2019).
[27] D. Bates, Maechler, M., Bolker, B., Walker, S., "Fitting Linear Mixed-Effects Models Using lme4," *Journal of Statistical Software* vol. 67 no. 1, pp. 1-48, 2015.

[28] A. Kuznetsova, Brockhoff, P., Christensen R., "lmerTest Package: Tests in Linear Mixed Effects Models," *Journal of Statistical Software,* vol. 82, no. 13, pp. 1-26, 2017, doi: 10.18637/jss.v082.i13.

[29] *Estimated Marginal Means, aka Least-Squares Means*. (2022). [Online]. Available: https://CRAN.R-project.org/package=emmeans

Chapter 4

A data-driven, anatomical definition for first metatarsophalangeal joint coordinate systems

Eric D. Thorhauer[a,b], William R. Ledoux, PhD[a,b,c]

[a]Center for Limb Loss and MoBility (CLiMB), Department of Veterans Affairs Puget Sound Health Care System, Seattle, Washington, USA

[b]Department of Mechanical Engineering, University of Washington, Seattle, Washington, USA

[c]Department of Orthopaedics & Sports Medicine, University of Washington, Seattle, Washington, USA

Keywords: joint coordinate system, MTPJ1, bone morphology, statistical shape analysis

Abstract

Accurate representation of joint motion in clinically relevant terms of translations and Euler rotations requires the establishment of coordinate systems within the bones of interest. Standardizing these coordinate systems facilitates data comparison across different research groups, reduces variances in kinematics due to mathematical artifacts, and enhances the interpretability of biomechanical findings. The study addresses the need for an MTPJ1 joint coordinate systems sensitive to natural variations in metatarsal bone shape, particularly those affecting the distal articular surface. These variations are identified through statistical shape analysis, highlighting regions of significant anatomical variance that could affect the performance of automatic joint coordinate system algorithms based on fitting geometric primitives.

Introduction

Biplane fluoroscopy and computed tomography technologies afford unprecedented precision in quantifying forefoot kinematics. To express subtle differences in joint motion in clinically meaningful terms of translations and Euler rotations, coordinate systems must be embedded into the bones of interest. By standardizing the definition of these coordinate systems, direct data comparisons between labs and cohorts are possible and as well as a reduction in variances of kinematics due to mathematical artifacts. An effective coordinate system definition must also be repeatable between and within subjects from various clinical cohorts of interest while also considering the primary morphological features that guide and constrain joint motions. Natural variation in the shape of the metatarsals has been observed across primates in computed tomography scans [1]. In humans, the distal head portions of the metatarsal that guide first metatarsal phalangeal joint (MTPJ1) motion may exhibit torsion such that they are everted about 11-13 degrees (range: -2 to 25) in the frontal plane [1]. Such localized articular surface shape variations are in addition to gross bone morphological variations that have been revealed through statistical shape modeling [2].

As maturing technology like biplane fluoroscopy facilitates precise quantification of in vivo MTPJ1 motion, there is a growing need for metatarsal joint coordinate systems that are sensitive to these natural variations. This study aimed to 1) identify anatomical regions of shape variation in the first metatarsal and proximal phalanx bones that may affect fitting MTPJ1 joint coordinate systems and to 2) automate this mathematical definition algorithmically such that it can be repeatability utilized within and between research groups.

Methods

A statistical shape analysis of the bones from living subjects was performed to highlight the key anatomical regions of variation across individuals, with special attention turned to the articular features responsible for guiding MTPJ1 motion.

Metatarsal and proximal phalanx bone statistical shape analysis

Following approval of the Institutional Review Board, subjects (N = 73, 33 females, 40 males, age: 49.6 ± 9.6 years) were screened by an orthopedic foot and ankle surgeon and classified as neutrally aligned (21), planus (38), or cavus (14). Subjects underwent partial weight-bearing computed tomography (CT) scans of the foot and ankle (voxel size 0.9 x 0.9 x 0.5 mm). CT segmentations were performed using MultiRigid software to produce subject-specific first metatarsal and proximal phalanx models [3]. The resulting segmented bone volumes were imported into ShapeWorks Studio software (v6.4.2, University of Utah) to generate a statistical model of shape variance for the first metatarsal and the proximal phalanx [4, 5]. In the shape model, 1500 correspondence points were iteratively placed on the bone surface using geodesic distance metrics to drive a coherent point drift optimization. The mean bone shapes were reconstructed along with ± 2 standard deviations in shape along the first five primary modes of variation. The models were inspected to identify anatomical regions and variations associated with each mode of variation. A bone surface model was generated representing each mode/standard deviation level, and coordinate systems were embedded using two methods: 1) principal component analysis of the bone surface (PCA) and 2) fitting cylinders in a least-squares sense (CYL) to the bone shaft and distal articular surface to define the bone axes [6]. The angular

deviations between these resultant coordinate systems across the mode/variance levels were compared in the three anatomical planes.

Joint coordinate system definitions

For the first MPTJ1 definition type, both bones' inertial axes were calculated by computing the principal components of the cortical surfaces, and an MTPJ1 coordinate system based on these axes was defined and placed at the centers of mass of each of the respective bones. This coordinate system, labeled henceforth as PCA, is depicted in Figure 2A.

A second MTJP1 definition algorithm upweighting the role of and accounting for variation in the cartilage surfaces was developed based on fitting cylindrical primitives to the bones and their articular regions (CYL). The algorithm uses the bone surface data to infer and label the anatomical ends of the bones, extract the bone shaft midsubstance, isolate the articular regions of the distal metatarsal head and proximal phalanx, and determine the coordinate system axes by performing a series of geometric primitive fits to the isolated bone regions. The algorithm starts by orienting the bone lengthwise using its principal axes and scaling it to have a normalized unity length (Figure 3A). Marching along the first principal axis in 0.1% increments of the normalized length, the cross-sectional size is computed at each slice location in the sagittal plane to generate a width profile of the bone. The profile's derivative is taken to detect the inflection points corresponding to rapid changes in cross-sectional size that occur at the condylar ends of the bone. The cross-sectional size profile is also used to determine the proximal from the distal end and isolate the shaft regions (Figure 3B). Specifically, the two highest peaks in cross-sectional size are detected. For both bones, the point of the smallest cross-section between the two peaks exists along the middle of the bone shaft. In metatarsals, the largest peak corresponds

to the proximal end of the bone, and the second peak corresponds to the distal end near the sesamoids. To define the bone shaft regions in both bones, downhill searches from the proximal peak and distal peak are performed to find the inflection points between the relatively constant cross-section midsubstance region and the rapidly varying ends. The articular regions of the MTPJ1 in both bones are detected via a region-growing algorithm that starts on the mesh surface at a seed point in the articulation. This seed point is automatically determined as the intersection between the bone surface and the vector of the first principal axis of the bone passing through the bone's center of mass (oriented distally for the metatarsal and proximally for the proximal phalanx). The region-growing marches along neighboring mesh elements, comparing the local surface normal orientation to a pre-specified reference vector (first principal direction) and adding the element to the growing set if the deviation between vectors is within a specified tolerance (60°). The final contiguous region-growing result defines the patch of MTPJ1 articulation to be considered in the geometric primitive fitting processing.

In the metatarsal, parametric models of a cylinder are iteratively fit in a least-squares sense to the bone shaft region and distal head. The long axis of the cylinder fit to the distal metatarsal surface is used as a second reference vector in another pass of the region-growing, seeking to remove bone regions on the left and right faces of the distal metatarsal that are not a part of the articulation. A final distal cylinder fitting is performed to the remaining surface points, and its height spans the medial-lateral width of the bone. The point on the cylinder's long axis, halfway between the medial and lateral ends, defines the origin of the metatarsal MTPJ1 coordinate system. The anatomical axes are defined as follows: 1) the long axis of the cylinder fit to the bone shaft defines the proximal-distal axis, 2) the cross-product of the proximal-distal axis

and the long axis of the distal cylinder defines the superior-inferior axis, and 3) the cross-product of the superior-inferior axis and the proximal-distal axis defines the medial-lateral axis.

In the proximal phalanx, the cylinder fitting procedure is performed on the isolated bone shaft regions. The region-growing operation extracts the proximal articular region that interfaces with the metatarsal. The center of mass of this bowl-shaped region defines the origin of the proximal phalanx MTPJ1 coordinate system. The principal component axes of the bowl-shaped articular region are also calculated. The first and second principal axes are aligned with the height and width of the articulation, while the third axis is aligned normal to the articulation. The anatomical axes are defined as follows: 1) the long axis of the cylinder fit to the bone shaft defines the proximal-distal axis, 2) the second principal axis of the articular patch defines the superior-inferior axis, and 3) the first principal axis of the articular patch defines the medial-lateral axis.

Region-growing algorithm validation

Three cadaveric specimens from the bone segmentation validation study of Chapter 3 were used to test the ability of the automated algorithm to correctly identify the articular cartilage regions based on the subchondral bone surface model. Prior to denuding the specimens of cartilage, the articular peripheries of the distal first metatarsal and proximal end of the proximal phalanx were manually marked with ink and contact probed using the coordinate measurement machine (Kreon ACES-7, Kreon Solano Blue laser). The data were processed in Geomagic Wrap 2022 software (3DS, North Carolina, USA) to generate surface patches that were overlaid onto the original segmented bone surfaces as a ground-truth reference for the true cartilage boundaries.

Results

The shape analysis revealed variations in the underlying anatomy of both the first metatarsal and proximal phalanx. The resulting statistical shape model described 56.2% of the total variance in the first three modes and about 90% in the first five modes (Figure 1). The first three modes revealed variation in both the gross metatarsal shape and the extent of the distal head's cam shape (Figures 2 and 3). Mode 2 variations were associated with changes in the metatarsal aspect ratio (long and thin vs short and broader). Modes 2 and 3 exhibited varying degrees of prominence in the region of the distal head crista (Figure 4). Torsion of the distal head in the frontal plane was also observed in the second and third modes (Figure 4). The proximal phalanx variations did not exhibit as much shearing of the aspect ratios in the sagittal and transverse planes as in the metatarsal (Figures 5 and 6). Rather, the primary mode of phalanx variation was overall length and width in the transverse plane.

The automated coordinate system algorithm successfully isolated the regions of interest on the bone surfaces of both the first metatarsal (Figure 7) and proximal phalanx (Figure 8) and performed robust fitting of the cylindrical primitives with no user interventions. Processing time using the MATLAB-based code was on the order of 1 minute per bone model. The algorithm successfully handled the chirality of both left and right foot bones and variations in the bones' initial poses with respect to the CT scanner coordinate system. The articular surface region-growing code automatically detected most of the true cartilage interfaces (Figure 9), however peripheral regions were under- and overestimated compared to ground-truth laser scan boundaries. (Figure 10).

Coordinate systems defined using the CYL method adapted better than PCA to the morphological differences within each mode of the statistical model. The standard deviations of

the inclination angles in the frontal, sagittal, and transverse planes were smaller for PCA (0.5°, 0.1°, 0.2°, respectively) than CYL (2.7°, 2.6°, 1.2°, respectively) (Table 1). This suggests that the PCA coordinate systems were less sensitive to the observed variations in metatarsal head shape.

Discussion

This study investigated the natural variations in first metatarsal shape that are most likely to affect the articular surface of the MTPJ1 and highlighted the anatomical regions of greatest variance with respect to their effects on automatically embedded joint coordinate systems. These regions include the articular surfaces of the distal head directly responsible for guiding and determining the MTPJ1 kinematics and the bone shafts which are used to define the anterior-posterior axes.

The results of the shape analysis agree with the limited published data on first metatarsal shape variation. We observed a spectrum of distal head torsional patterns similar to those reported by Kitashiro et al [1]. Using a landmark-based shape modeling approach, Telfer et al. observed variations in first metatarsal frontal and sagittal plane cross-sectional area for the first mode [2]. These biplanar area deviations are indicative of aspect ratio variations we observed in the present study. In the second mode of variation, Telfer observed changes in the sagittal plane angle of the distal and proximal heads, which is an analog for the torsion described by Kitashiro [1]. While the cohort investigate by Telfer et al. was very similar to that investigated in the present study, the inclusion of the sesamoid bones in the model and the decreased resolution of the landmark-based shape modeling approach, as opposed to the more complex modeling permitted by ShapeWorks Studio, may account for differences in the anatomical variations associated with a given mode.

Automated algorithms for embedding coordinate systems into bones must be robust to anatomical variations without being overly sensitive to noise and errors in the segmented models. Before these automated scripts for embedding MTPJ1 coordinate frames are released to the greater biomechanics community for use, additional work on the sensitivity of the cylinder fitting to surface model deviations is required to understand if and mesh pre-processing steps, such as smoothing or resampling for mesh uniformity, are required to generate consistent definitions. Additionally, simulations of the presence of a cartilage boundary in the articular cylinder fittings will elucidate if soft tissue specific medical imaging such as magnetic resonance imaging adds any benefit to the protocol, or if the uniformity of the cartilage is such that the subchondral bone surface suffices for the purposes of defining the joint axis. Lastly, these coordinate systems will be exercised in living subjects and their resultant kinematics during functional tasks compared.

Acknowledgment

Supported in part by VA Rehabilitation Research and Development Grants A2180R, A3030R, RX 002008, and RX002970.

Figures and Tables

Table 1: Angular deviations between the three anatomical axis coordinate directions, defined using the PCA and CYL methods.

	Medial-lateral axis		**Anterior-posterior axis**		**Superior-inferior axis**	
	PCA	**CYL**	**PCA**	**CYL**	**PCA**	**CYL**
mean	3.7°	4.4°	3.2°	4.5°	3.9°	5.6°
stdev	2.1°	2.5°	1.3°	2.0°	2.4°	2.5°
range	7.1°	9.3°	4.1°	9.7°	8.1°	9.7°

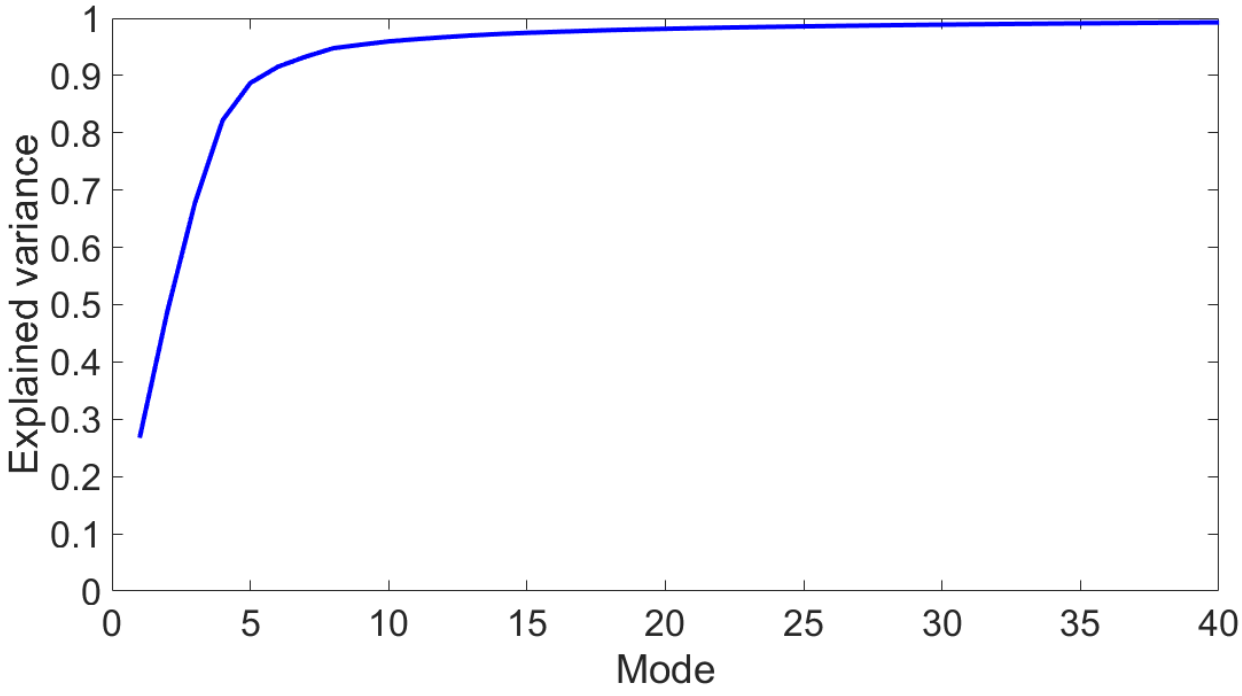

Figure 1: The amount of total shape variance explained as a function of the number of modes in the statistical model. The first five modes encapsulated roughly 90% of the total morphological variance.

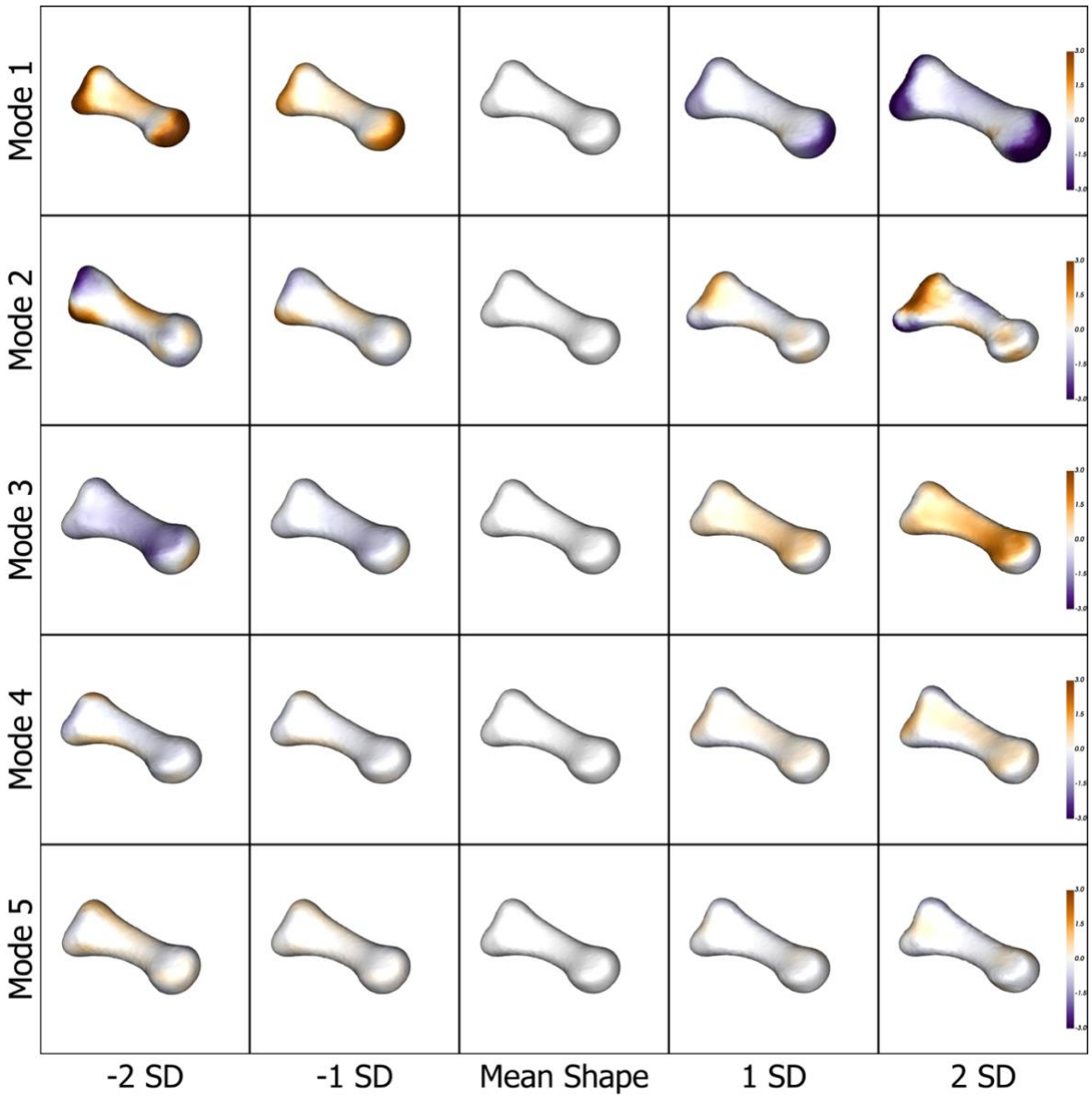

Figure 2: The first five modes of variation in first metatarsal bone shape. Two standard deviations from the mean shape are depicted for each mode. The colormaps indicate the distance from the mean shape (mm). As viewed from the sagittal plane, the first mode is associated with overall length, the second mode relates to the aspect ratio, and the third mode is related to the medial-lateral width.

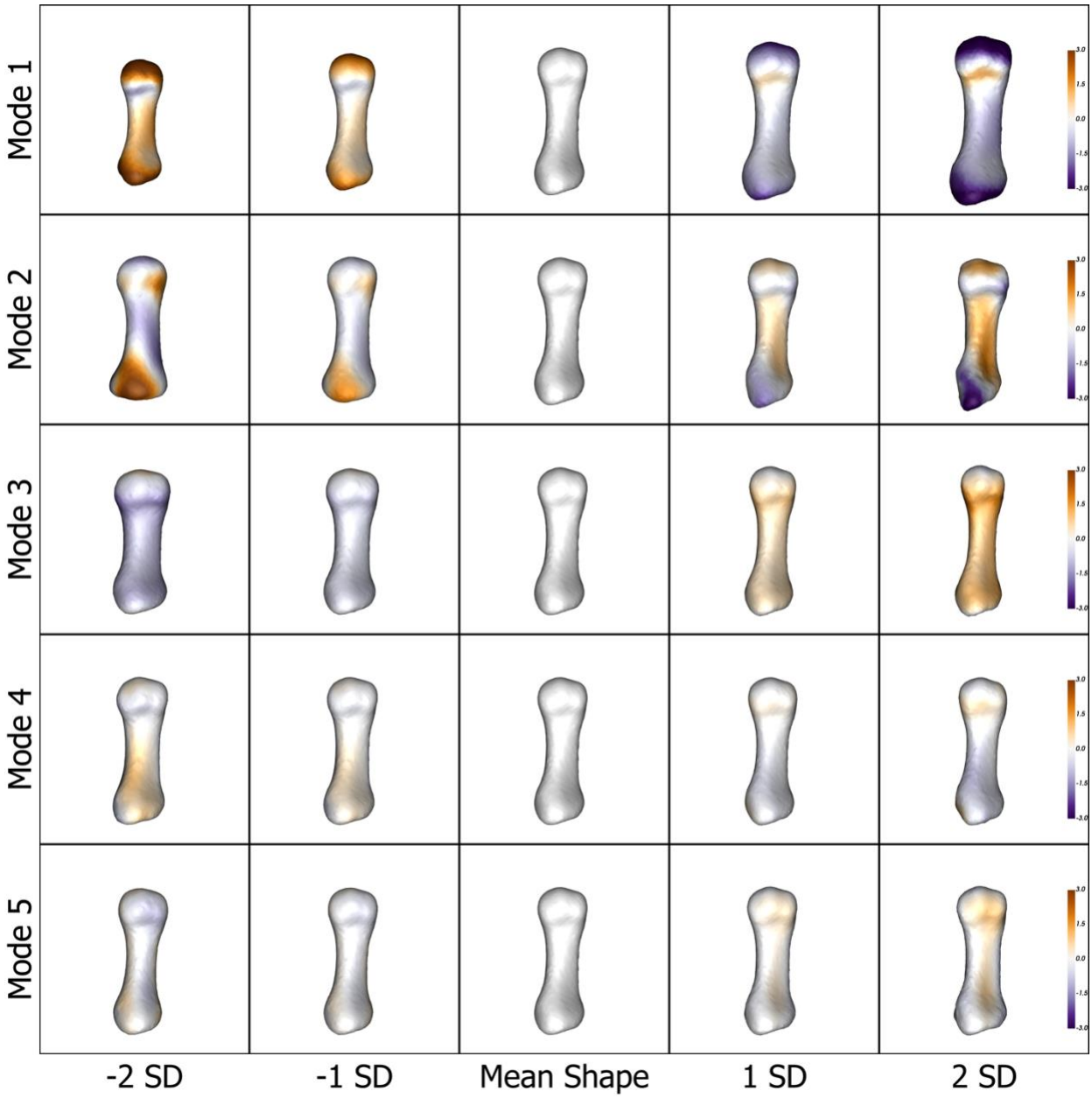

Figure 3: The first five modes of variation in first metatarsal bone shape. Two standard deviations from the mean shape are depicted for each mode. The colormaps indicate the distance from the mean shape (mm). As viewed from the plantar aspect, the first mode is associated with overall length, the second mode relates to the aspect ratio, and the third mode is related to the thickness of the bone shaft.

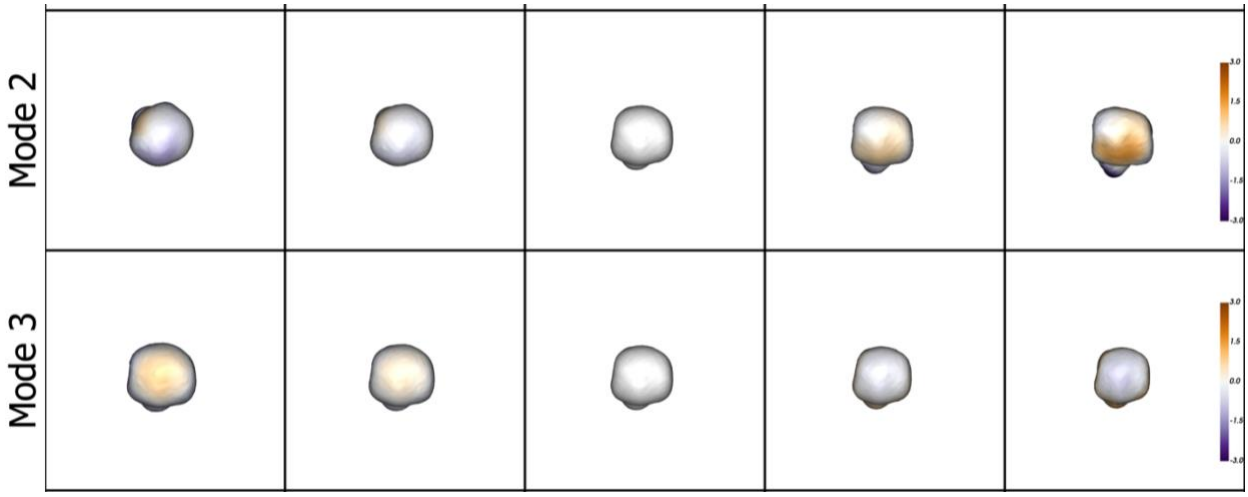

Figure 4: The second and third modes of variation in first metatarsal distal head bone shape. Two standard deviations from the mean shape are depicted for each mode, viewed from distal/anterior aspect.

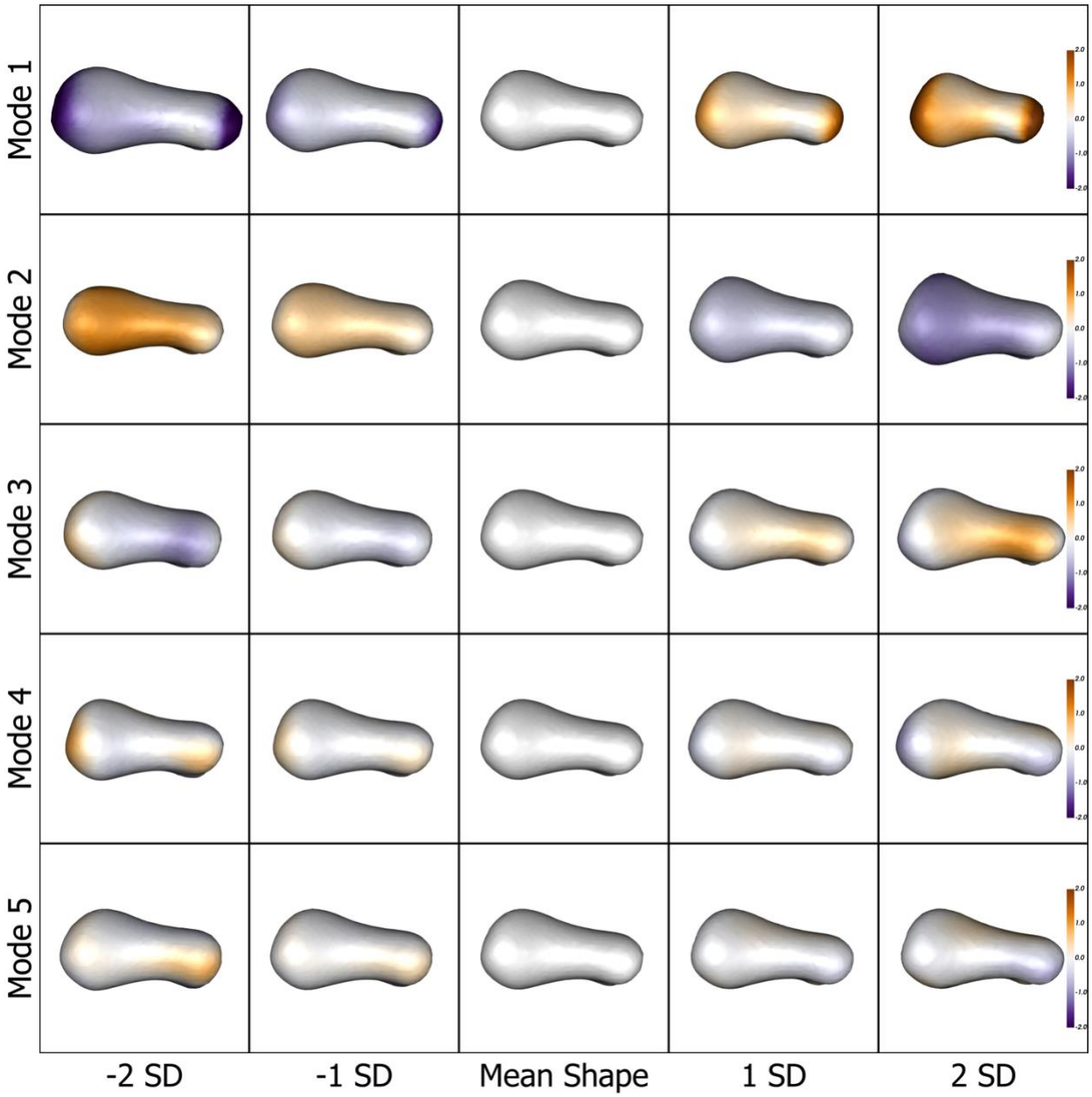

Figure 5: The first five modes of variation in proximal phalanx bone shape. Two standard deviations from the mean shape are depicted for each mode. The colormaps indicate the distance from the mean shape (mm). As viewed from the sagittal view, the first mode is associated with overall length, the second mode relates to the aspect ratio, and the third mode is related to the medial-lateral width.

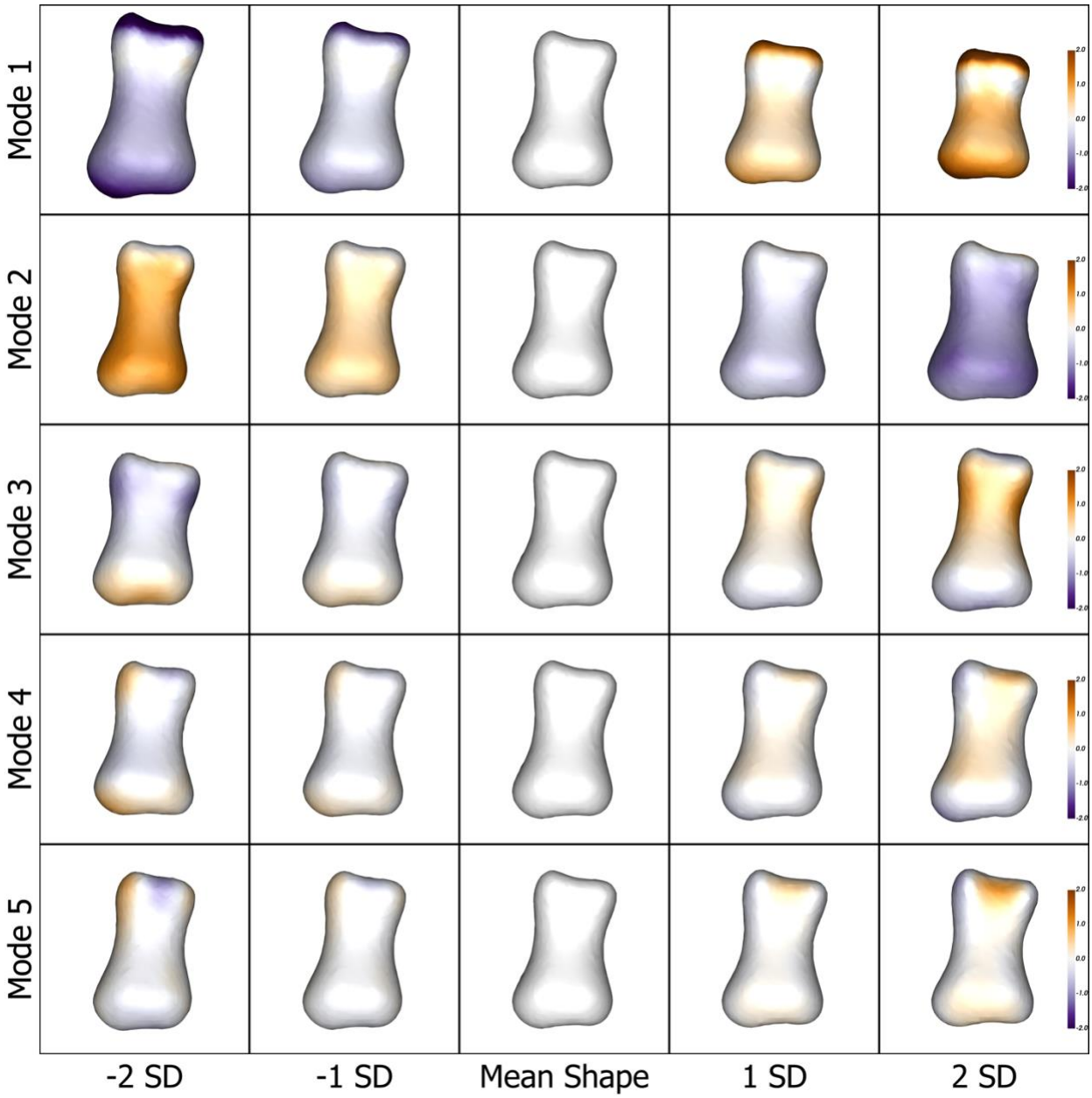

Figure 6: The first five modes of variation in proximal phalanx bone shape. Two standard deviations from the mean shape are depicted for each mode. The colormaps indicate the distance from the mean shape (mm). As viewed from the plantar aspect, the first mode is associated with overall length, the second mode relates to the aspect ratio, and the third mode is related to the thickness of the bone shaft.

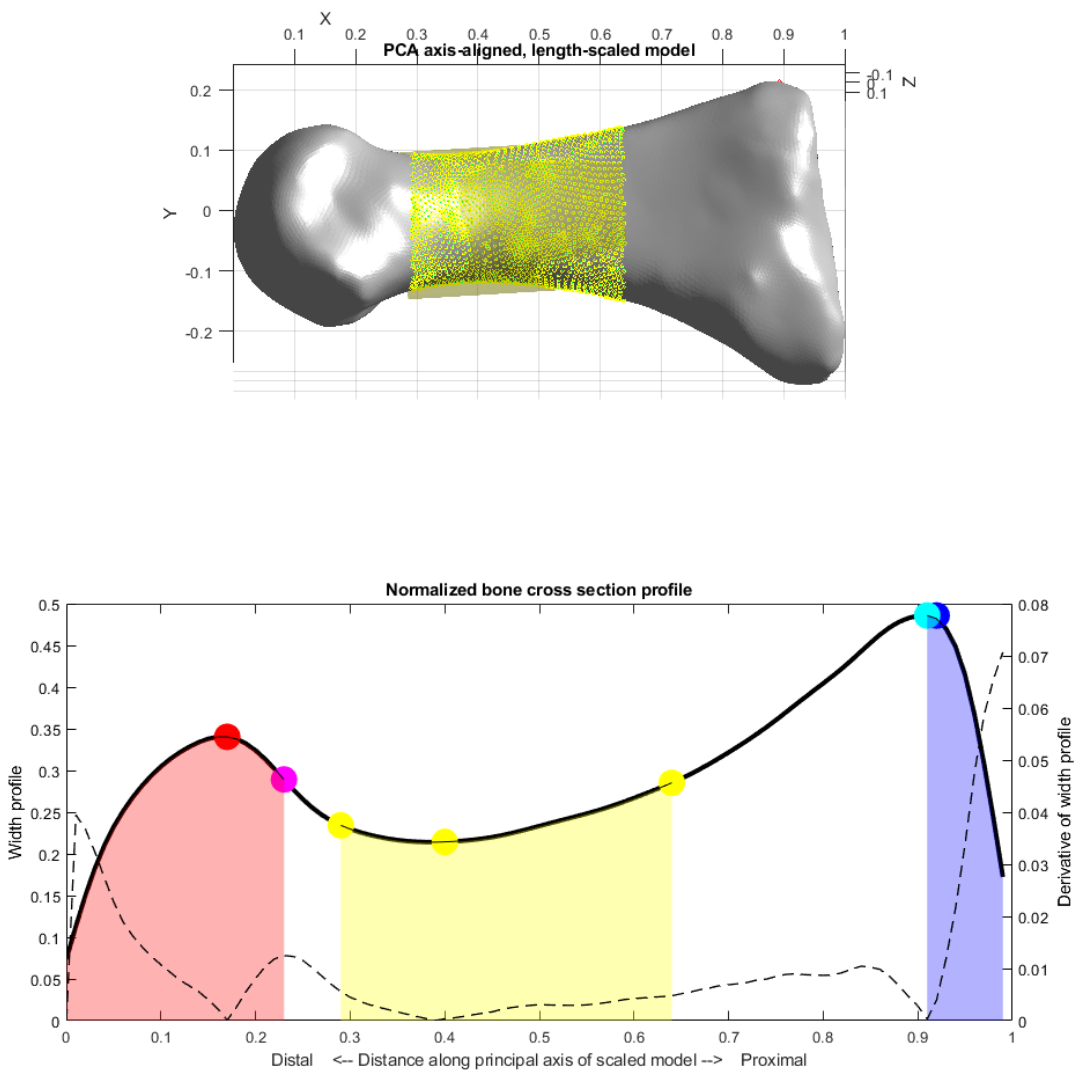

Figure 7: The first metatarsal bone aligned to its inertial axes and scaled to a unit length (top) and the profile of the cross-sectional size along the first principal axis (bone long axis), which is used to automatically partition the metatarsal into the distal (red), shaft midsubstance (yellow) and proximal end (blue) regions prior to fitting cylindrical primitives to the red and yellow regions.

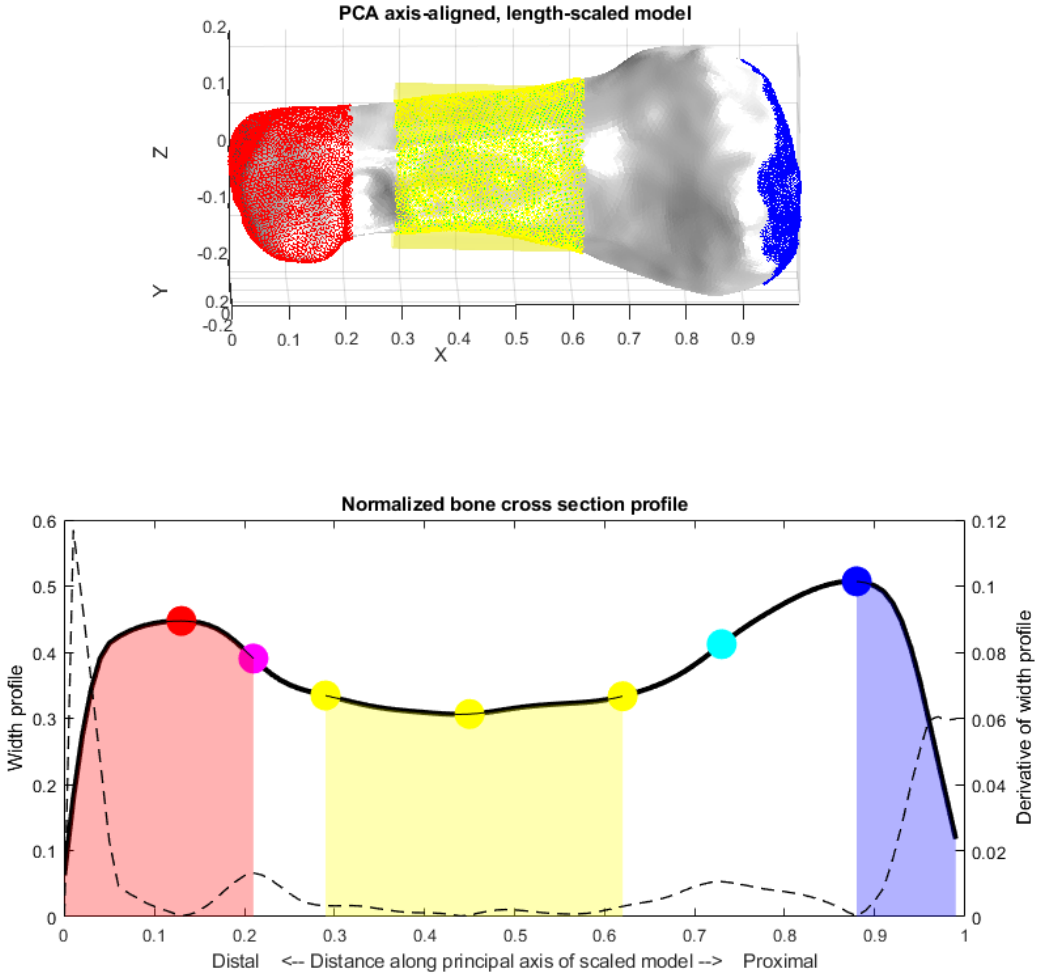

Figure 8: The proximal phalanx bone aligned to its inertial axes and scaled to a unit length (top) and the profile of the cross-sectional size along the first principal axis (bone long axis), which is used to automatically partition the metatarsal into the distal (red), shaft midsubstance (yellow) and proximal end (blue) regions prior to fitting cylindrical primitives to yellow shaft region and determining the principal components of the isolated proximal facet (blue).

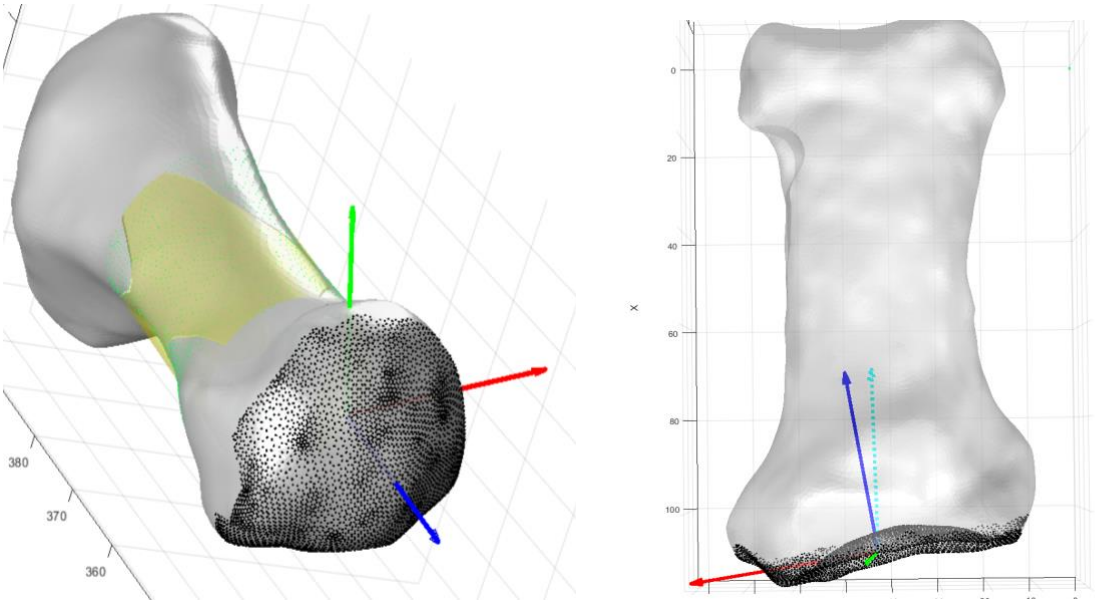

Figure 9: Results of the automatic fitting algorithm for embedding the metatarsal coordinate system into the distal articular surface (left) and the proximal end of the proximal phalanx (right). Black dots highlight the automatically detected articular cartilage region used in the coordinate system fitting routine.

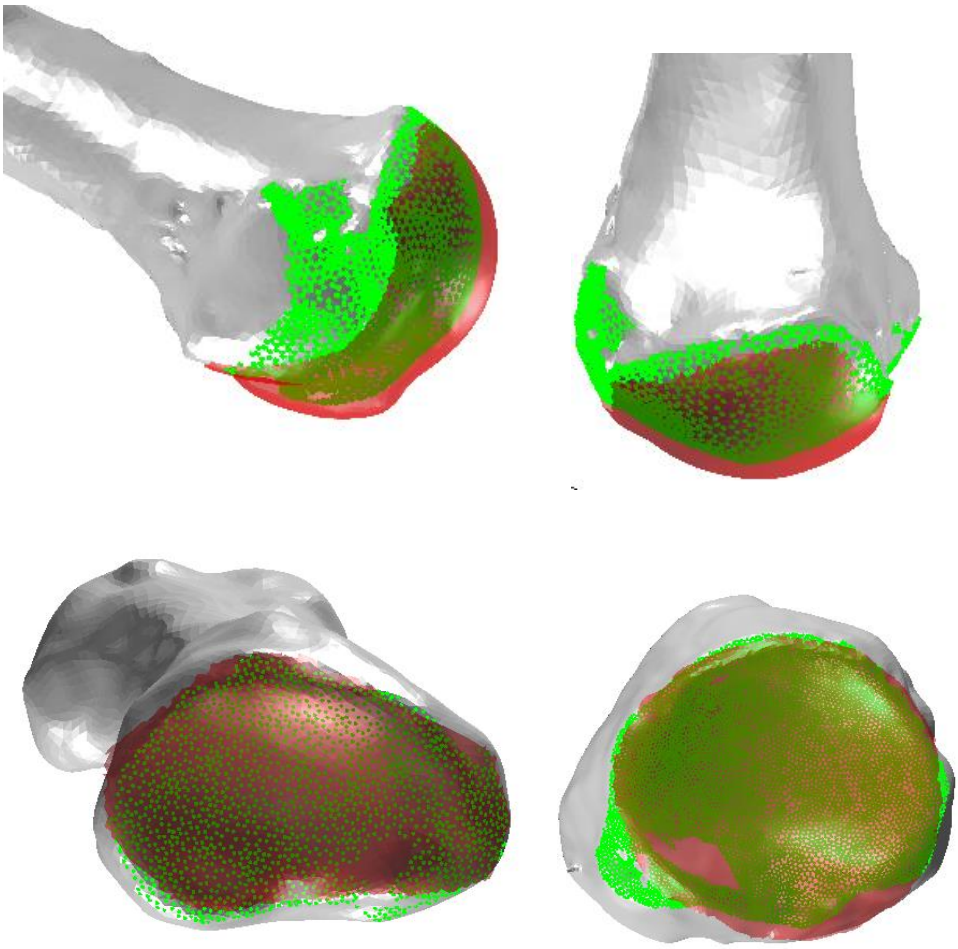

Figure 10: Results of the automatic region-growing algorithms for detecting the articular cartilage boundary priory to fitting the appropriate geometric primitive approximating that facet for the first metatarsal (top) and proximal phalanx (bottom). Red regions were detected via the algorithm while the green points indicate the true cartilage regions, as determined from laser scanning and dissection.

References

[1] M. Kitashiro, N. Ogihara, T. Kokubo, M. Matsumoto, M. Nakamura, and T. Nagura, "Age- and sex-associated morphological variations of metatarsal torsional patterns in humans," *Clinical Anatomy,* vol. 30, no. 8, pp. 1058-1063, 2017, doi: 10.1002/ca.22944.

[2] S. Telfer, M. W. Kindig, B. J. Sangeorzan, and W. R. Ledoux, "Metatarsal shape and foot type: A geometric morphometric analysis," *Journal of Biomechanical Engineering,* vol. 139, no. 3, 2017, doi: 10.1115/1.4035077.

[3] Y. Hu, W. R. Ledoux, M. Fassbind, E. S. Rohr, B. J. Sangeorzan, and D. Haynor, "Multi-rigid image segmentation and registration for the analysis of joint motion from three-dimensional magnetic resonance imaging," *J Biomech Eng,* vol. 133, no. 10, p. 101005, Oct 2011, doi: 10.1115/1.4005175.

[4] J. Cates, S. Elhabian, and R. Whitaker, "Chapter 10 - ShapeWorks: Particle-Based Shape Correspondence and Visualization Software," in *Statistical Shape and Deformation Analysis*, G. Zheng, S. Li, and G. Székely Eds.: Academic Press, 2017, pp. 257-298.

[5] S. Elhabian, P. Agrawal, J. Cates, M. Datar, and R. Whitaker, "ShapeWorksStudio v2.2 Particle-based Shape Correspondence and Visualization Software," 2012. [Online]. Available: https://github.com/SCIInstitute/ShapeworksStudio/releases

[6] E. Thorhauer, M. French, T. Kimura, and W. R. Ledoux, "A Cadaveric Comparison of the Kinematic and Anatomical Axes and Arthrokinematics of the Metatarsosesamoidal and First Metatarsophalangeal Joints," (in eng), *J Biomech Eng,* vol. 145, no. 4, Apr 1 2023, doi: 10.1115/1.4056060.

Chapter 5

A cadaveric comparison of the kinematic and anatomical axes and arthrokinematics of the metatarsosesamoidal and first metatarsophalangeal joints

Eric D. Thorhauer[a,b], Mackenzie French, MD[a], Tadashi Kimura, MD[a,d], William R. Ledoux, PhD[a,b,c]

[a]Center for Limb Loss and MoBility (CLiMB), Department of Veterans Affairs Puget Sound Health Care System, Seattle, Washington, USA

[b]Department of Mechanical Engineering, University of Washington, Seattle, Washington, USA
[c]Department of Orthopaedics & Sports Medicine, University of Washington, Seattle, Washington, USA
[d]Department of Orthopaedic Surgery, The Jikei University School of Medicine, Tokyo, Japan

Keywords: joint coordinate system, MTPJ1, foot, sesamoid; metatarsal; kinematics; helical axes; weightbearing computed tomography

Abstract

Presently, developments in weightbearing computed tomography and biplanar fluoroscopy technologies offer exciting avenues for investigating normative and pathologic foot function with increasing precision. Still, data quantifying sesamoid bone and proximal phalange motion are currently sparse. To express joint kinematics and compare various clinical cohorts, future studies of first ray motion will necessitate robust coordinate frames that respect the variations in underlying anatomy while also aligning closely with the functional, physiological axes of motion. These activity-dependent functional axes may be represented by a mean helical axis of the joint motion. Our cadaveric study quantified joint kinematics from weightbearing computed tomography scans during simulated toe lift and heel rise tasks. We compared the spatial orientations of the mean finite helical axes of the metatarsosesamoidal and metatarsophalangeal joints to the primary joint axis of two relevant methods for defining metatarsal coordinate frames: inertial axes and fitting of geometric primitives. The resultant kinematics exhibited less crosstalk when using a metatarsal coordinate system based on fitting cylindrical primitives to the bony anatomy compared to using principal component axes. Respective metatarsophalangeal and metatarsosesamoidal arthrokinematic contact paths and instantaneous centers of rotation were similar between activities and agree well with currently published data. This study outlines a methodology for quantitatively assessing the efficacy and utility of various anatomical joint coordinate system definitions. Improvements in our ability to characterize the shape and motion of foot bones in the context of functional tasks will elucidate their biomechanical roles and aid clinicians in refining treatment strategies.

Introduction

Essential to our daily ambulation and general foot function, the first metatarsal and proximal phalanges, along with the medial and lateral sesamoids, are responsible for transmitting a significant percentage of bodyweight during gait [146]. The sesamoids embedded in the flexor hallucis brevis tendon glide on the distal plantar metatarsal head in the metatarsosesamoidal joints (MTSJ). They simultaneously act to increase the moment arms of the flexor hallucis longus and brevis tendons of the first metatarsophalangeal joint (MTPJ1) and protect the metatarsal cartilage from compressive and shear stresses [147]. Dysfunction and degradation in these joints are of interest to clinicians studying and treating maladies such as hallux valgus, hallux rigidus, and clawed hallux [146, 148-151]. By quantifying the motion of these small bones in both healthy and pathological joints, clinical treatment strategies and our understanding of bone function in the foot will evolve.

Precise data describing the motion of the sesamoids and first proximal phalanges are sparse, due to limitations in traditional, non-invasive techniques for assessing foot and ankle biomechanics. Their small sizes and locations encased in supporting tissue structures, make the sesamoids particularly challenging targets for conventional imaging methods; they require static, partial-weightbearing, tangential radiographic views [146, 152] and they cannot be tracked using optical motion capture. As a result, MTPJ1 and MTSJ studies have been limited to cadaveric dissections that required disruption of the native anatomy [153-155] or low-load in vivo magnetic resonance studies of the plantar plate [156-158] to quantify bone motion. Various motion capture models have been developed to improve forefoot motion quantification [159-161], but have inherent limitations in the degrees of freedom that can be tracked accurately for each bone. Recently, weightbearing computed tomography (WBCT) technology has advanced

with cone-beam sources and high-efficiency detectors, offering low-dose, high-resolution volumetric scans of clinical patients' extremities [130, 162]. Such systems allow for assessing the full three-dimensional shapes of the foot bones and their six-degree-of-freedom kinematics via in vivo or controlled cadaveric experiments.

Given the current lack of precise forefoot kinematic data, there are no standardized methods for establishing coordinate systems and reporting kinematics for the MTSJ and MTPJ1 as in other joints, such as the knee and ankle [163-165]. Coordinate systems may utilize anatomical landmarks, the fitting of geometric primitives, or calculating the inertial axes (principal components) of the bone [59, 143, 166, 167]. To mitigate crosstalk and between-subjects variances in the resultant kinematics that confound or dilute differences between cohorts, the natural variation in bone shapes and the role of articulations should be considered when defining anatomical coordinate systems. Such articular surface-based coordinate systems have been utilized in the upper extremity, knee, and hindfoot [23, 168-171]. Additionally, motion-based finite helical axes, which have characterized knee and wrist joints [172, 173], invite a comparison to these coordinate systems based on osseous morphology. Quantitative comparisons in resultant kinematics between coordinate systems and their sensitivity to crosstalk have been performed in the knee joint [174-176]. A quantitative method is needed for assessing and justifying the definitions of anatomically based joint coordinate systems, especially as technology for foot joint tracking improves and facilitates more precise analyses. The primary aims of this study were to quantify the arthrokinematics (estimations of joint contact foci), instantaneous centers of rotation, and joint kinematics of the MTPJ1 and MTSJ, and to compare the orientation and distribution of the joint mean finite helical axes (MFHA) to the medial-lateral axes of first metatarsal coordinate systems based on two methods: principal components analysis

(PCA) and fitting cylindrical primitives (CYL) to the bony anatomy. For MTPJ1 and MTSJ, their primary motions are flexion-extension about the distal metatarsal head, so the MFHA representing these motions should closely align with the coordinate system medial-lateral axes. PCA equally weights the entire metatarsal in the coordinate system definition, including proximal portions away from the distal joints of interest. A localized fitting method like CYL can adapt to variations in torsion of the distal metatarsal head relative to the shaft [143, 177-179]. We hypothesize, firstly, (H1) that vector directions of the MFHA of MTPJ1 and MTSJ will exhibit stronger spatial correlations with medial-lateral metatarsal axis definitions that are based on the CYL method compared to PCA, and, secondly, (H2) that coordinate systems defined using the CYL method will produce MTPJ1 rotation data with less kinematic crosstalk and less inter-subject variability compared to data derived from PCA-based coordinate systems.

Methods

Twelve fresh-frozen tibia-foot specimens were obtained from accredited tissue banks (Innoved Institute, LLC, Elk Grove Village, IL, and Lonetree Medical Donation, Centennial, CO) and screened for abnormal bony alignment or deformity via donor history, manual palpation, and radiographic imaging. Normal range of motion and lack of osteoarthritis was confirmed by an orthopaedic surgeon using palpation, radiographs, and WBCT (pedCAT, CurveBeam, Hatfield, PA; isotropic voxel size of 0.3 mm). Two specimens having bipartite sesamoids were omitted. For the remaining ten specimens (age: 46.3 ± 17.2 years, body mass index: 25.8 ± 4.7, sex: 6 male, 4 female), all subsequent scans were performed with the pedCAT. Specimen-specific segmentations in Mimics software (v21, Materialise, Leuven, Belgium) by a

single operator produced a volumetric template of each specimen's first metatarsal, proximal phalange, medial sesamoid, and lateral sesamoid for tracking in subsequent scans.

Joint coordinate system determination

To express kinematic and arthrokinematic data between specimens in a common frame of reference, standardized specimen-specific anatomical coordinate systems were defined for each bone. In the metatarsals, two methods of embedded coordinate systems were compared: one from the principal components of the entire bone surface [59, 166] (PCA) and the other by fitting cylindrical primitives to the metatarsal surfaces [143, 167] (CYL). For our CYL protocol (Figure 3), one cylinder was fit to the diaphysis of the metatarsal, and a second was fit to the distal metatarsal articular surfaces. The axis of the second cylinder defined the anatomical medial-lateral axis in CYL, and a series of vector cross products between the cylinder axes produced the orthogonal coordinate system CYL, which is essentially aligned with the metatarsal head and shaft. CYL fitting was performed by a single operator in Geomagic software (Geomagic Studio, Geomagic, USA). All proximal phalange coordinate systems were defined using principal components of the phalanges. Given the varying, oblate shape of the two sesamoids, both of their coordinate system orientation definitions were simply copied from the proximal phalange and moved to their respective volumetric centroids.

Biomechanical testing

Six foot and ankle tendons responsible for great toe and ankle articulation and stabilization (Achilles, extensor digitorum longus, extensor hallucis longus, peroneus longus, peroneus brevis, and tibialis posterior) were dissected by an orthopaedic surgeon and sutured

with surgical monofilament using Krackow stitches to interface via loops with braided aluminum tendon pull cables. Tibia and fibula shafts were exposed 60 mm proximal to the ankle mortise, denuded of tissues, and cast in resin cylinders. A custom loading rig allowing for four tibial segment kinematic degrees of freedom (ab/adduction and medial-lateral translation were fixed) was assembled around the WBCT scanner in a manner that did not interfere with scan quality. Given the lack of in vivo muscle force data for these activities, tendon excursions and loadings were extrapolated from previous cadaveric experiments mimicking foot function [180-182]. Static axial half-bodyweight donor-specific loads were applied through the tibial shafts with free weights. A computer-controlled actuator with a load cell mounted in series with the Achilles tendon induced the target ankle plantarflexion and consequent physiologic distal foot motion. All other tendons were nominally and statically loaded with 15 N.

Two motions were simulated: 1) an isolated toe lift (extension of the great toe) and 2) heel rise of the entire foot via Achilles tendon actuated ankle plantarflexion while the forefoot remains on the ground. For the toe lift, a custom foot plate made of acrylic and adjustable to specimen size was machined and instrumented with a potentiometer to control and record the precise amount of toe extension (Figure 1). Toe extension targets ranged from 0° (neutral foot) to the maximum of the specimen (approximately 50° or 60°) in 10° increments. For each toe lift pose target, the extensor hallucis longus tendon was pulled to induce the motion, and the instrumented toe plate was used to set the exact rotation amount and lock the specimen into a supported position at the desired extension angle with the tendon clamped in tension. For the heel rise testing, specimens were positioned directly on the floor of the WBCT as living subjects would stand. By varying the Achilles load and allowing natural articulation of the joints and translation of the tibial shaft in the testing apparatus, seven scan positions equally spaced

between a neutral foot flat pose and the maximum stable heel rise pose were achieved. Specimens were held for 30 seconds at each pose prior to scanning to allow tissues to reach a viscoelastic steady state. If tissue creep or clamp slippages were detected during the post-scan review, scans were re-collected.

Reconstructing bone poses from WBCT scans

Volumetric rigid registration was performed between the specimen-specific template volumes and the experimental scans for each of the four bones to determine their positions and orientations across all poses. Registrations were performed in custom MATLAB (Mathworks; Natick, MA) software that optimally aligns the specimen- and bone-specific template volumes to the raw WBCT volumes using a cost function based on the mutual information between volumes [183, 184]. This optimization metric proved to be robust to the noise present in our low-dose WBCT data. A validation of this registration process is presented in the Appendix.

Kinematics determination

Joint kinematics were derived using the transformations describing each template volume to the global CT frame and the local bone coordinate systems. Motions were expressed relative to the metatarsal CYL and PCA coordinate system, separately. The resulting matrix was decomposed into Euler angles in the following order: sagittal plane flexion-extension rotation, transverse plane ab/adduction rotation, frontal plane inversion-eversion rotation.

Arthrokinematics determination

Surface models of each bone were generated in Mimics and filtered with Laplacian smoothing to reduce segmentation noise. For the MTPJ1, medial MTSJ, and lateral MTSJ the weighted centroids of articular joint contact were estimated using the opposing subchondral bone surface distances at each reconstructed pose [185]. Centroid locations were combined over sequential poses to define contact paths of the proximal phalange and sesamoids on the metatarsal articular surface.

Functional screw axis determination

The finite helical axes (FHA) of motion were determined for the MTPJ1, medial MTSJ, and lateral MTSJ using the method described by Spoor and Veldpaus [186] and Woltring [187]. Using all permutations of pose pairings within each simulated activity, the mean FHA (MFHA) was determined using the symmetrical axis of rotation analysis (SARA) approach described by Ehrig with a $w = \sin(\frac{\theta}{2})$ weighting term to minimize errors from small rotations [188, 189]. This produced robust estimations of the mean functional axes of each joint for both simulated activities. The median locations of the instantaneous centers of rotation (ICR) in the sagittal plane were also calculated using the R package Gmedian (v 1.2.5) [190] for MTPJ1 and each MTSJ [191, 192].

Comparison of axis orientations

Left foot specimen data were mirrored to appear as right, and all metatarsals were co-registered together iteratively in MATLAB. From these data, a mean metatarsal model was generated in the University of Utah's ShapeWorks Studio software [144, 145]. In MATLAB, the affine transformations of each specimen's metatarsal to the volume representing the mean bone

shape were determined and used to scale, mirror, and map the MFHA, and arthrokinematic data of each specimen onto the common metatarsal model for illustration and statistical comparison. The mean morphological flexion-extension axis was calculated across all PCA and CYL definitions. Angles of inclination of this flexion-extension axis relative to the MFHA were calculated in both the transverse plane (α) and frontal plane (β).

Statistical analyses

With all data mapped into a common reference frame centered in the mean metatarsal head, directional statistics [193] were utilized to quantify the spatial orientations of the morphological (PCA and CYL) and functional axes (MFHA) from each joint/activity (Figure 2). Correlations were calculated between the MFHA vector spatial orientations and the first metatarsal medial-lateral axes for both PCA and CYL definitions (H1). To assess differences in the resultant kinematics between the PCA and CYL methods (H2), a repeated measures ANOVA was performed across all poses with the axis definition type (PCA or CYL) as the within-subjects factor. Kinematic crosstalk was quantified by correlating the metatarsophalangeal flexion-extension data with the two remaining orthogonal rotational components. Analyses were performed in R statistical software using the base and Directional (v4.8) packages [194, 195]. This investigation tested the following hypotheses: (H1) MFHA of MTPJ1 and MTSJ will exhibit stronger spatial correlations to medial-lateral metatarsal axis definitions based on CYL compared to PCA, and (H2) that CYL-based coordinate systems will produce MTPJ1 kinematic data with less crosstalk and less inter-subject variability compared PCA.

Results

Repeatability summary

The biomechanical testing rig produced physiological foot poses for each specimen and activity. The Achilles tendon failed in the clamp for one specimen during the heel rise simulation, but enough tissue remained for re-clamping and continued testing without noticeable effect. Repeatability of the CYL axis definitions was assessed via single-rater intra-class correlation for consistency of measurement (ICC = 0.985). Details of the bone tracking validation, and bias and precision data for each bone are presented in the Appendix.

Arthrokinematics

Qualitatively, contact paths for each bone were consistent within specimens (low variability, data not shown) and grossly similar across activities (Figure 4). MTPJ1 contact paths deviated slightly laterally in the heel rise activity, compared to the nearly vertical pattern observed in toe lift (Figure 4). The lateral sesamoid path moved more medially in heel rise compared to toe lift. Qualitatively, the longest paths of contact were observed in the MTPJ1 compared to the sesamoids (Figure 5). Heel rise activities induced longer contact paths than simple toe extension. In all conditions, the shortest contact paths were observed in the lateral sesamoid compartment.

Instantaneous centers of rotation

Median ICRs for all bones were in the metatarsal head (Figure 6). Sesamoid ICRs were located proximal and dorsal to the phalange ICRs, which were essentially centered in the distal metatarsal head. Qualitatively, proximal phalange ICRs were clustered in tighter distributions compared to both sesamoids for both activities. Compared to toe lift, the heel rise-activity sesamoid ICRs were shifted distally and dorsally (Figure 6).

Morphological axes and mean finite helical axes

The orientations of the morphological axes and mean finite helical axes for each joint (metatarsophalangeal, lateral metatarsal-sesamoid, and medial metatarsal-sesamoid) were approximately normal to the sagittal plane (Figure 7 and Table 1). For the PCA and CYL axes, there was no significant difference in the transverse plane orientation (mean difference 1.7°; $p = 0.173$), while the frontal plane orientation difference approached significance (mean difference 7.1°; $p = 0.051$). The medial sesamoid MFHA orientation was significantly different from the PCA and CYL in seven of eight comparisons across both planes and activities (Table 1). Qualitatively, in heel rise activities, the MFHA orientations were less variable in the anterior-posterior direction and spread more along the vertical (head-ground) direction (Figure 7). The orientations of the MFHA were strongly correlated with both the PCA and CYL flexion-extension axes for both toe off and heel rise (Table 2).

Kinematics

Joint kinematics resulting from each of the two metatarsal coordinate system definitions (PCA and CYL) were similar in appearance for the primary flexion-extension motion across both activities, with a significant near-constant offset between the curves ($p = 0.006$, partial eta squared = 0.201) (Figure 8A and 8B). Larger variability was observed between PCA and CYL kinematics in the motions about the two remaining orthogonal axes (Figure 8C, 8D, 8E, and 8F). For the ab/adduction axis, the two definitions were not different ($p = 0.155$, partial eta squared = 0.1), likely because the PCA method exhibited a large variance at each pose (Figure 8C and 8D). For inversion-eversion ($p = 0.041$, partial eta squared = 0.117), the PCA group exhibited a larger variance and a bias of about 5° of inversion.

Correlation between flexion-extension and inversion-eversion rotations was moderate for CYL ($R^2 = 0.30$) and strong for PCA ($R^2 = 0.51$). Correlation between flexion-extension and

ab/adduction was weak for both CYL (R^2 = -0.18) and PCA (R^2 = -0.10). Crosstalk between inversion-eversion and ab/adduction was moderate for CYL (R^2 = -0.37) and strong for PCA (R^2 = -0.54).

Discussion

This study quantified the kinematics and arthrokinematics of the MTPJ1 and MTSJs during two relevant simulated foot motions and compared the orientations of the mean functional helical axes of motion (MFHA) to the primary flexion-extension axes in two methods (PCA and CYL) for embedding anatomical metatarsal coordinate systems. While these data are based on controlled cadaveric experiments, the resultant sesamoidal and phalangeal arthrokinematics for both simulated activities are qualitatively physiological (Figures 4 and 5), and agree with the limited published data, as discussed below.

Our ex vivo kinematic data (Figure 4) compare well with previous reports of proximal phalange motion and sesamoid motion in cadavers [153-155]. As also reported by Ahn et al., we observed the dorsal migration of the MTPJ1 contact region [155]. Shereff et al. reported that both sesamoids displaced 10 to 12 mm over an arc of motion of 111°, whereas we found 4 to 6 mm of sesamoid motion over 50 to 60° of arc (Figure 5) [153]. Jamal et al. quantified ex vivo sesamoid motion through 70° of rotation; they reported comparable lateral sesamoid sagittal excursions (7.5 mm), but found more medial sesamoid excursion (14.7 mm) [154]. These discrepancies may be due to limitations in biofidelity of the applied loads to cadavers or in the methodology for quantifying and reporting the motion in the previous studies.

Analysis of various joints' ICRs during functional tasks has proven useful in quantifying unstable articulations and for designing optimal joint replacement hardware and installation

procedures [172, 196]. We found the median ICR locations of all bones agreed well with Shereff's report that they reside well within the confines of the metatarsal head in normal feet (Figures 6 and 7) [153]. In hallux valgus and rigidus patients, Shereff reported that ICRs of the proximal phalange and sesamoids are located in more variable positions than those typically found in the "normal" cases, indicating how MTPJ1 pathology can disrupt joint kinematics. In a theoretical model, Durrant argued the ICRs of both the MTPJ1 and MTSJs should reside within the metatarsal head, and their distributions would be influenced by the cam shape of the distal head; specifically the flatter distal plantar surface [197]. The distributions (Figure 7) of our proximal phalange ICR data fell roughly along the metatarsal long axes, while the sesamoid ICRs were distributed towards the dorsum. This may be indicative of the sesamoids having greater translation and sliding motion rather than pure rotation about the cam-shaped distal plantar surface compared to the proximal phalange's motion relative to the metatarsal. Further quantification of ICR locations and MFHA orientations may be clinically useful in diagnosing forefoot issues and in designing joint replacement strategies that respect the native relationships between these functional axes.

This study also compared the downstream effects of embedding two types of coordinate systems in the metatarsal. Our first hypothesis (H1), that spatial correlations to MFHA would be stronger for CYL than PCA was not supported (Table 2). Our second hypothesis (H2), that resultant kinematics from PCA would be more variable (Figure 8) and have greater crosstalk compared to CYL, as indicated by stronger correlations between primary and secondary kinematic rotations with PCA, is currently supported by our data. While the PCA method uses the entire bone surface geometry and may account for gross morphological differences [125], natural variation in twisting of the metatarsal head relative to the diaphysis exists that may bias

definitions of the medial-lateral axis at the MTPJ1. Kitashiro described a natural 11 to 13 degree mean bias towards eversion in first metatarsal torsion (range: -2 to 25°) [143]. Drapeau compared this torsion across primates and found a mean bias of 7.6 ± 5.5° towards eversion for homo sapiens [178]. Both reports agree well with our observed PCA axis biases in the frontal plane (6.3 ± 9.4° of eversion). Additionally, Mortier suggested that metatarsal torsional patterns and the orientation of the crista, which is responsible for guiding sesamoid motion, have direct connections to hallux valgus progression [179]. Furthermore, Brenner reported 7.99 ± 3.71° of crista tilt relative to the metatarsal long axis, which may account for the larger transverse plane variances in sesamoid MFHA orientations in our study [177]. These studies suggest that more data characterizing the relationships between form and function in the MTPJ1 and MTSJs are required.

While great care was taken to simulate physiological motions in minimally dissected specimens, there are many limitations with our methodologies. Repeated trials were not collected for each specimen, the same tendon load scaling was applied to all specimens regardless of the sex or size of the donor, and the intrinsic muscles of the foot were not loaded in order to preserve specimen integrity against excessive dissection. Differences in kinematics observed between coordinate system types may be exacerbated or nullified in different tasks or with a larger pool of subjects, or by exploring alternative methods for defining the coordinate systems. We utilized an affine registration procedure to align all specimen data to a common mean metatarsal model, and while the vector orientation differences are not appreciably different when recalculated using rigid alignments (Appendix Table A.2), the mean model to which each specimen was registered is a function of the study sample size and is assumed to represent a population mean. Given the presence of rotations in the other two planes, it might be an oversimplification to model the

MTPJ1 joint as a hinge normal to the sagittal plane. While the robust SARA approach was utilized to characterize MFHA, measurement noise and small rotations contribute to errors and the resultant axes are specific to the prescribed tasks and ranges of motion simulated [188, 189]. Therefore, the efficacy of these methods must be tested during in vivo functional tasks like gait and stair navigation and in cohorts with atypical and highly varying bony morphologies.

In conclusion, our study outlines a protocol for quantitatively assessing the efficacy and utility of anatomically derived joint coordinate systems by comparing the geometric parameters of the articulations (axes of best-fit) to dynamic kinematic data (helical axes of motion). Our findings demonstrated the benefit of utilizing joint coordinate systems based on fitting geometric primitives to the underlying anatomic metatarsal bone geometry and articulations over the simpler method using the principal components of the entire bone. While embedding coordinate systems based on PCA is computationally straightforward to implement, the downstream effects of this decision on joint kinematic crosstalk errors must be considered. The relationships between the geometric and kinematic axes need to be further investigated in living-subjects performing multiple activities, and with various clinical diagnoses of MTPJ1 and sesamoid-related issues. Despite the challenges associated with imaging these small bones, their function and motion are essential to normal toe biomechanics, and more quantitative data on their motion during relevant tasks may inform and advance foot treatment and understanding.

Acknowledgement

This study was funded in part by Department of Veterans Affairs grants RX002357 and RX002970, and the University of Washington Medical School Scholarship of Discovery Program.

Nomenclature

α = transverse plane inclination angle

β = frontal plane inclination angle

CYL = cylinder fitting-based coordinate system

ICR = instantaneous center of rotation

MFHA = mean finite helical axis

MTPJ1 = first metatarsal phalangeal joint

MTSJ = metatarsosesamoidal joint

PCA = principal component analysis-based coordinate system

WBCT = weightbearing computed tomography

Tables and Figures

Table 1: Inclination angles (mean and standard deviations in degrees) of the morphological and mean finite helical axes (MFHAs) in the transverse and frontal planes. Transverse plane (positive = more anterior) and frontal plane (positive = more superior) are both relative to the sagittal plane normal vector (orientated medially). Significant differences in inclination of the MFHAs relative to the medial-lateral axes as defined in the PCA or CYL methods are indicated with (^{a}) and (^{b}), respectively ($p < 0.05$).

		Transverse plane angle		*Frontal plane angle*	
		mean	± SD	mean	± SD
Coordinate system	*PCA*	-0.9	1.7	-3.2	9.4
medial-lateral axis	*CYL*	0.8	3.0	3.9	3.9
	phalanx	-2.2	5.1	2.0	9.0
	lateral sesamoid	-3.5	6.5	2.8	10.2
MFHA: toe lift	*medial sesamoid*	7.0 [a,b]	8.3	12.5 [a,b]	7.3
	phalanx	2.0	4.3	2.6	13.6
	lateral sesamoid	-0.6	7.6	6.2	9.6
MFHA: heel rise	*medial sesamoid*	9.0 [a,b]	6.0	15.1[a]	19.3

Table 2: Correlations (R^2) of the spatial orientations of the mean finite helical axes (MFHA) for each bone by activity and the metatarsal coordinate system flexion-extension axis for the principal component analysis (PCA) and cylindrical (CYL) definition methods.

Activity	**Bone**	**PCA-based definition**		**CYL-based definition**	
		R^2	*P-value*	*R^2*	*P-value*
MFHA: toe lift	*phalanx*	0.854	< 0.001	0.930	< 0.001
	lateral sesamoid	0.933	< 0.001	0.914	< 0.001
	medial sesamoid	0.912	< 0.001	0.899	< 0.001
MFHA: heel rise	*phalanx*	0.793	< 0.001	0.866	< 0.001
	lateral sesamoid	0.853	< 0.001	0.907	< 0.001
	medial sesamoid	0.675	< 0.001	0.739	< 0.001

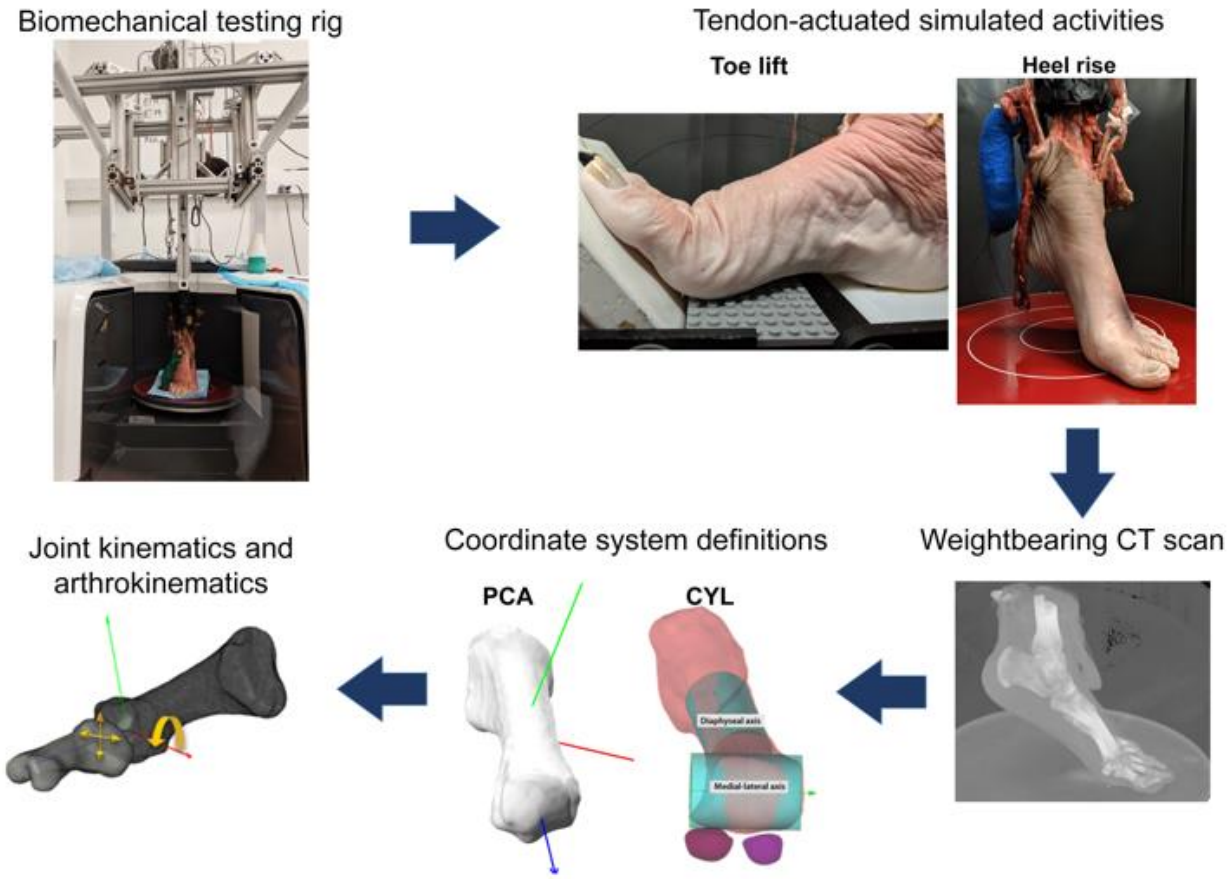

Figure 1: Experimental overview: a biomechanical testing rig was fashioned around a cone-beam weightbearing computed tomography (WBCT) scanner. Appropriate tendon loads were applied to induce simulated heel rise and toe lift activities, and at each pose a WBCT scan was collected. Two versions of bone coordinate systems were defined, one based on principal component analysis (PCA) and the other based on fitting cylindrical (CYL) primitives and the resultant kinematics calculated and expressed in each.

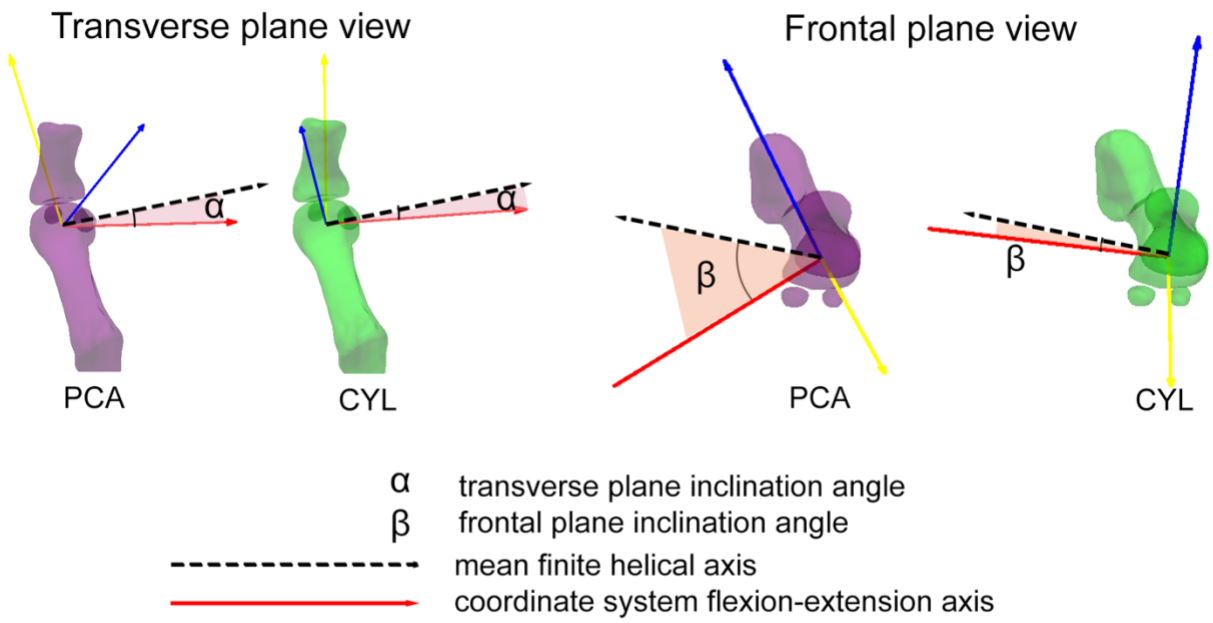

Figure 2: The inclination angles of the mean finite helical axes (MFHA) relative to the primary flexion-extension axis defined using the principal component analysis (PCA)-based and cylindrical (CYL)-based bone coordinate system methods, expressed in the frontal and transverse planes of the foot.

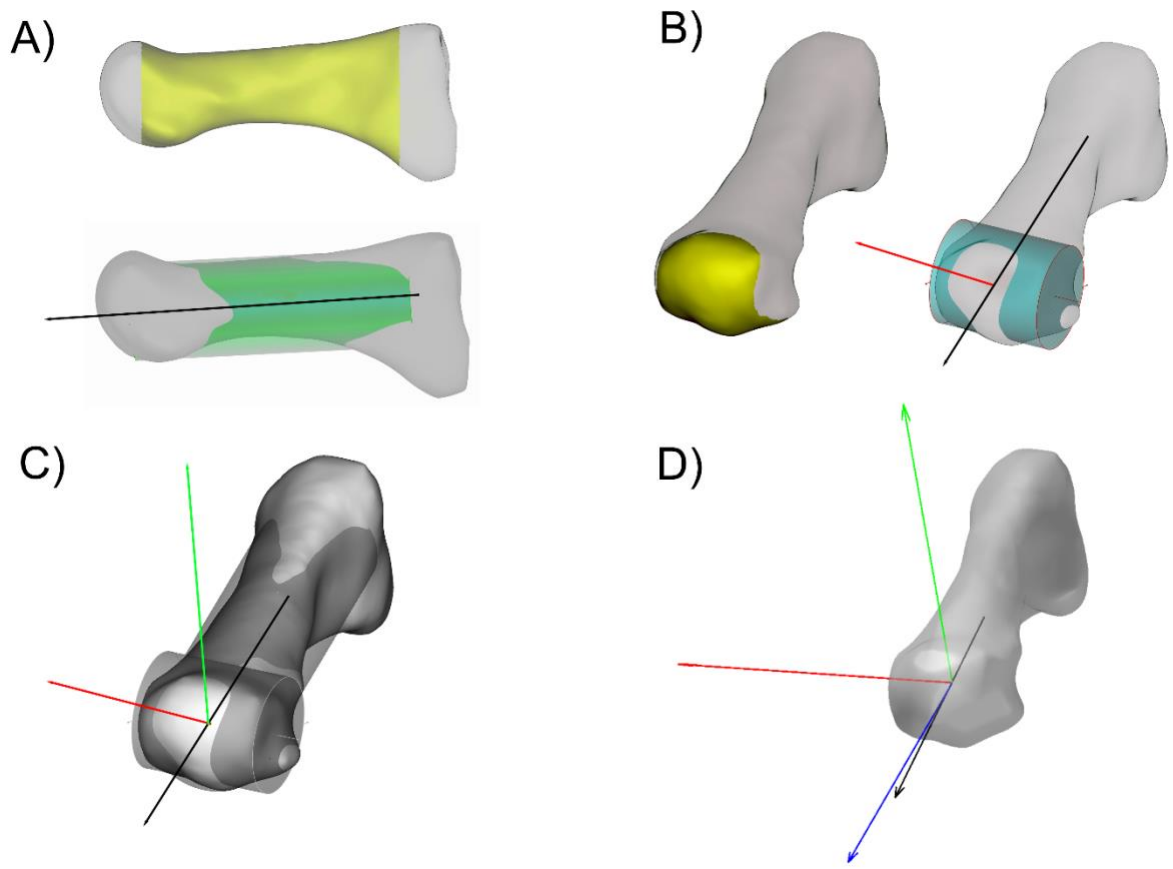

Figure 3: Protocol for establishing coordinate system based on fitting cylindrical primitives (CYL). (A) The central 80% of the bone along the first axis of inertia is selected, and a cylinder is fit to define a dummy axis. (B) The distal articular surface is selected, and a second cylinder fit; its axis defines the flexion-extension axis. (C) A cross product between the medial-lateral axis and the dummy axis defines the ab/adduction axis. (D) A final cross product between the ab/adduction axis and the flexion-extension axis defines the inversion-eversion axis and an orthogonal coordinate system.

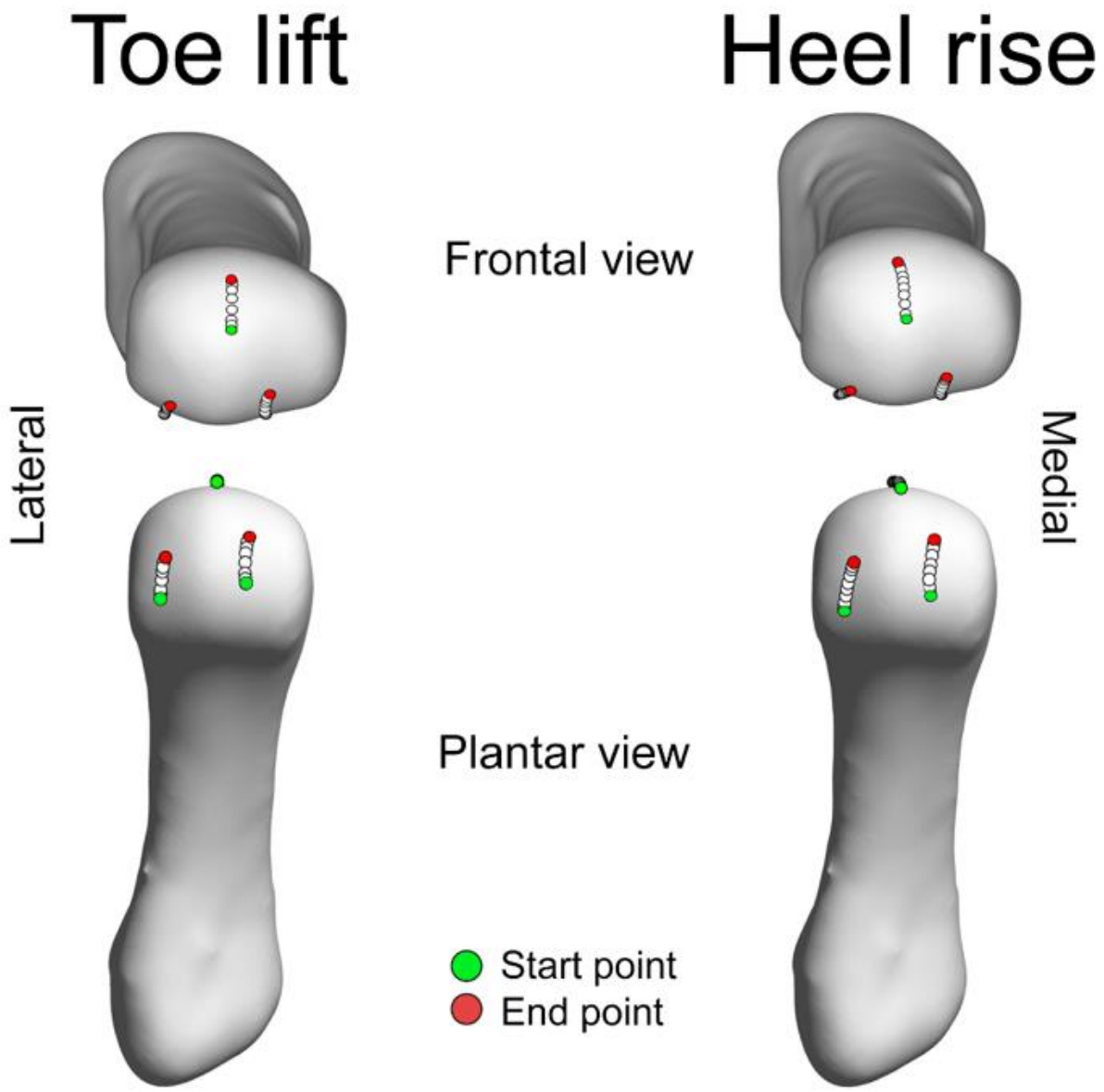

Figure 4: Mean arthrokinematic contact paths for the toe lift (left) and heel rise (right) activities for each compartment mapped onto the mean right metatarsal model. Natural increased abduction of the phalanx relative to the metatarsal during heel rise led to slightly different contact paths for the first metatarsophalangeal and lateral metatarsosesamoidal joints compared to the toe lift.

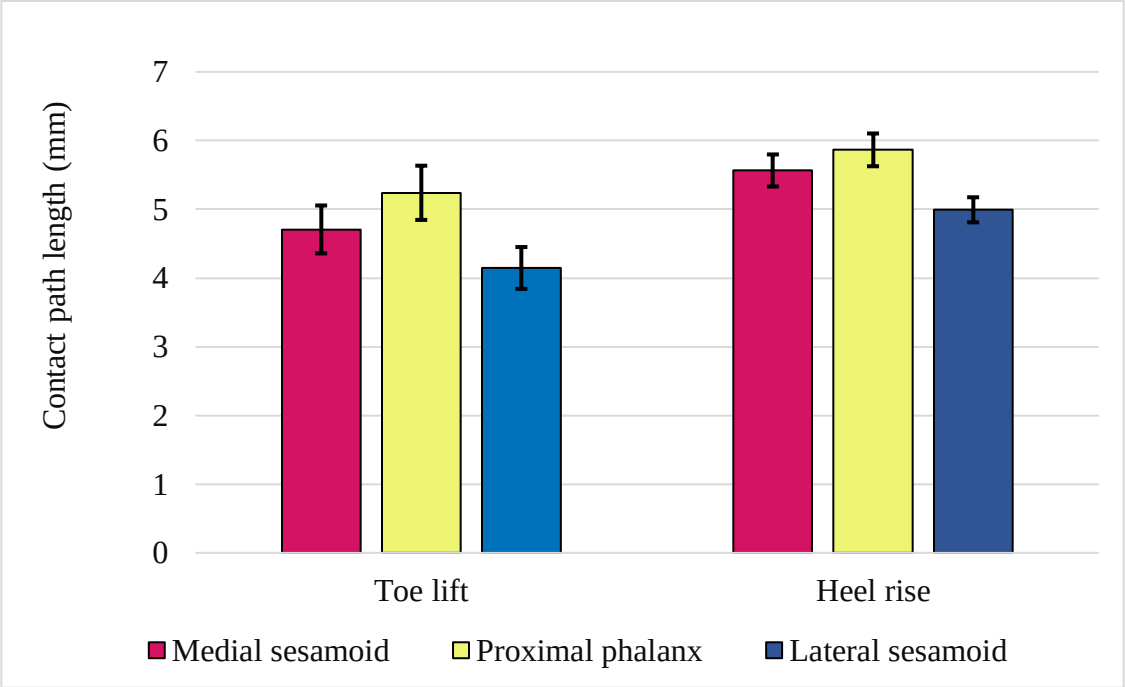

Figure 5: Mean joint compartment contact path lengths for the toe lift (left) and heel rise (right) activities. Ratios of contact path lengths between compartments were similar between the two activities, and paths were slightly longer in each compartment during heel rise.

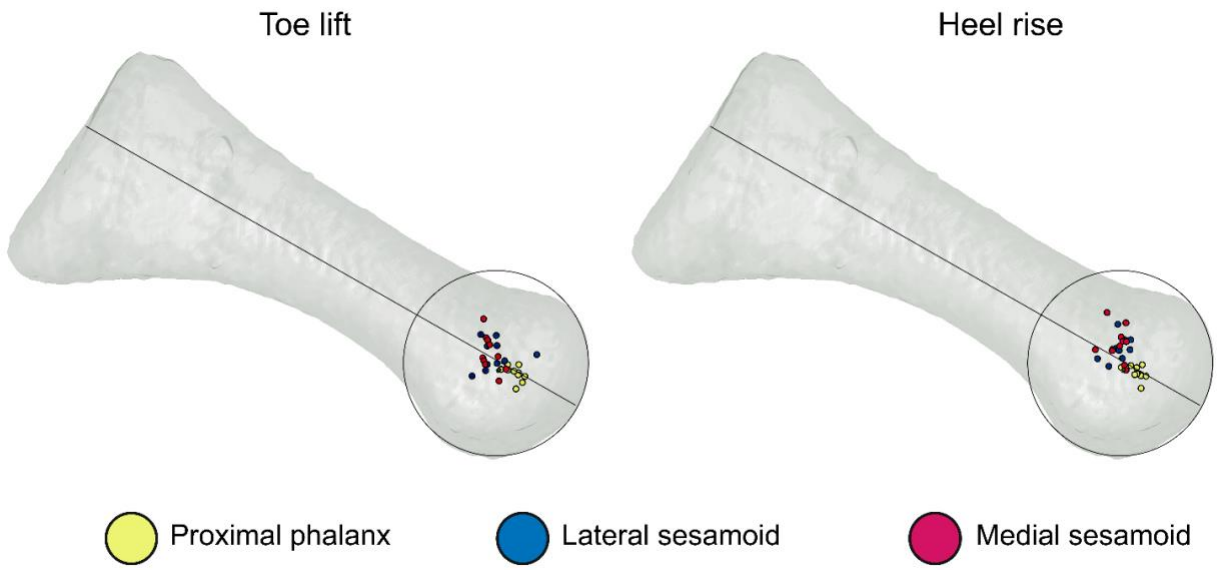

Figure 6: The median instantaneous centers of rotation of the first metatarsophalangeal (MTPJ1) and both metatarsosesamoidal (MTSJ) joints for a toe lift (left) and heel rise (right) activity, viewed from the lateral aspect of the mean metatarsal. Each marker represents the median ICR of a specimen.

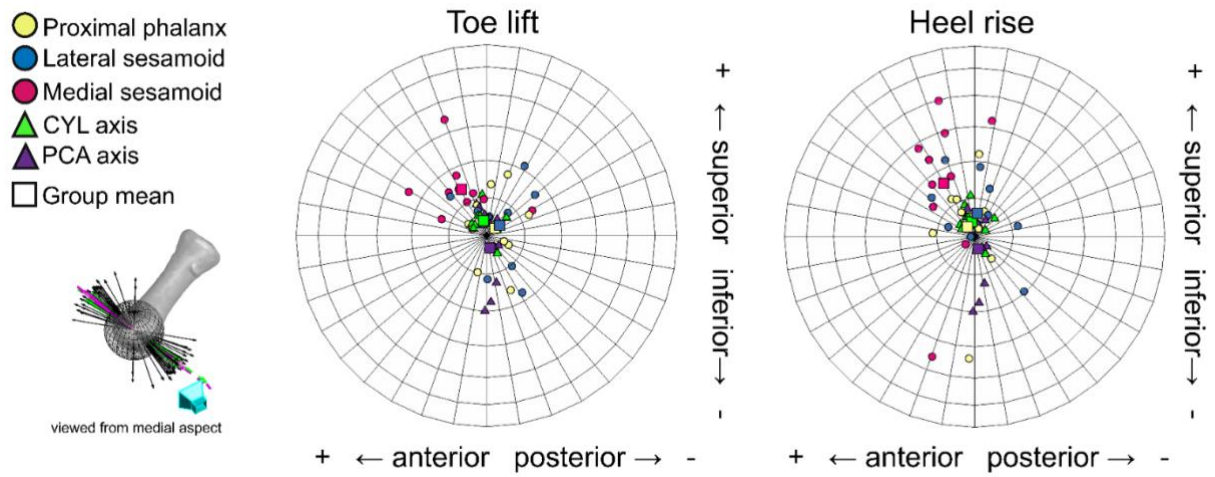

Figure 7: The orientations of the morphological (i.e., principal component analysis (PCA) and cylindrical (CYL-based) axes and the kinematic mean finite helical axes (MFHAs) mapped to a common unit sphere embedded in the distal metatarsal head and viewed from the medial aspect of the mean right metatarsal (i.e., in the sagittal plane). Each group mean is indicated by a square and the origin is the mean morphological axes calculated across all PCA and CYL definitions. Transverse plane orientation (positive = more anterior) and frontal plane orientation (positive = more superior) are both relative to the sagittal plane normal vector (orientated out of the page).

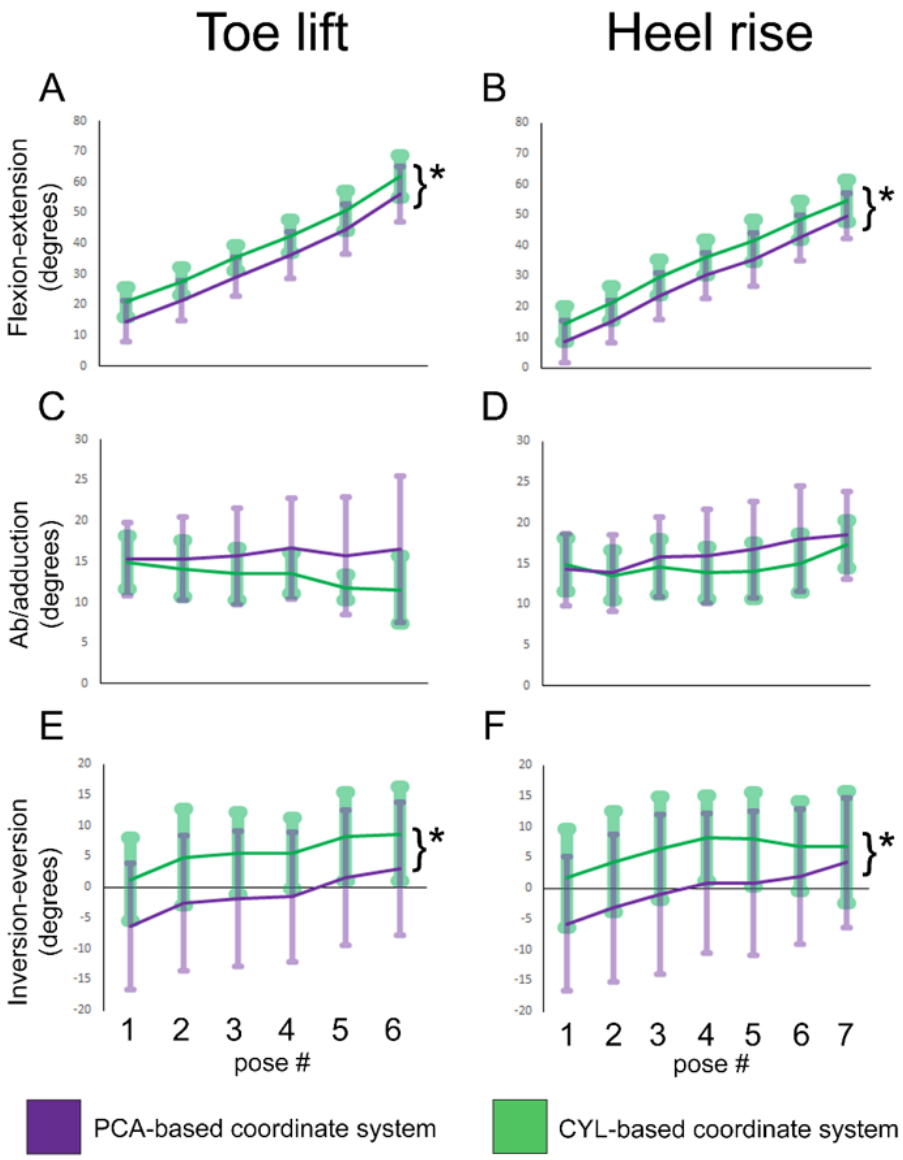

Figure 8: Mean first metatarsophalangeal kinematic curves derived using the PCA-based coordinate system (purple) and the CYL-based coordinate system (green) for toe lift (left) and heel rise (right) activities). Error bars are between-subjects standard deviations. For both toe lift and heel rise, pose 1 was neutral and pose 6 or 7, respectively, was maximum metatarsophalangeal extension, with intermediate poses incremented between neutral and the maximum. Significant differences ($p < 0.05$) between PCA and CYL observed via repeated measures analysis of variance indicated by (*).

Appendix

Effects of affine registration

We utilized an affine registration of each specimen's metatarsal model to the mean bone shape of all specimens. Affine registration allows for non-uniform scaling and shear in addition to rotations and translations. This morphs the specimen model, particularly the geometric relationships between the distal head of the metatarsal and its body towards the mean shape. It may also have the potential to artificially distort the differences between the various vector orientations examined in this study. We decomposed the affine transformation matrices used for each specimen into the rigid (translations and rotations) and non-rigid (shear and scale) matrices in MATLAB (qr.m function) and recomposed the transformations with only the rigid components. The vector orientations for the MFHA, and the CYL and PCA axes were remapped to the mean metatarsal model using these rigid transformations, and the angular deviations between each are reported in Table A.1.

Bone tracking validation

The accuracy and precision of reconstructing the first metatarsal, proximal phalanx, and medial and lateral sesamoid bones with our volumetric registration algorithm were assessed via a cadaveric validation study. Upon conclusion of the study, a specimen that best represented the median size and motion across all tested specimens was selected for further imaging in the weightbearing computed tomography (WBCT) scanner. A custom set of fiducial registration clusters were fabricated consisting of carbon fiber shafts and Delrin spheres. Carbon fiber material was chosen for its lightweight and minimally attenuating properties; essential to

avoiding artifacts during scanning or bending moments on the small sesamoid bones. The Delrin spheres (5 and 8 mm diameter) were mounted in triad configurations, and the base of each carbon shaft rigidly embedded into each pre-drilled bone (Figure A.1). Plantar fat and skin were dissected to allow uninhibited movement of the carbon shafts when the bones were actuated via tendon pulling. WBCT scanning was performed with the great toe flexed and extended through its range of motion in five equally spaced positions. For each scan, the poses of the four bones of interest were reconstructed three separate times using our custom software utilizing volumetric tracking with a mutual information cost function[184]. The resultant poses were compared to the "gold standard" positions determined by segmenting the fiducial sphere clusters in Mimics software (Materialise, Belgium) and determining the appropriate transformations. The translational and rotational bias and precision errors for each joint are listed in Table A.2. Our bone registration algorithm could accurately track the translations of all the bones, and accurately determined the rotations of the metatarsal and phalanx. The rotational orientations of the sesamoids bones had larger errors, which was expected given their smaller bone volumes and oblate shapes. The limitations for this validation include the sample size (N = 1) and the inability to directly validate the heel rise activity, as our design for the sesamoid marker clusters could be constrained by the ground.

Appendix Tables and Figures

Table A.1: The data from Table 1 presented again based on rigid alignments rather than affine alignments to the mean metatarsal model. Inclination angles (mean and standard deviations in degrees) of the morphological and mean finite helical axes (MFHAs) in the transverse and frontal planes. Transverse plane (positive = more anterior) and frontal plane (positive = more superior) are both relative to the sagittal plane normal vector (orientated medially). Significant differences in inclination of the MFHAs relative to the medial-lateral axes as defined in the PCA or CYL methods are indicated with ([a]) and ([b]), respectively ($p < 0.05$). These findings agree well with those generated from the affine registration process (Table 1), indicating minimal distortion of the vector orientations resulting from the affine matching process.

		Transverse plane angle		*Frontal plane angle*	
		mean ±	SD	mean ±	SD
Coordinate system	*PCA*	-1.2	1.6	-2.9	9.9
medial-lateral axis	*CYL*	0.3	2.8	4.1	4.1
	phalanx	-0.6	6.7	-0.2	12.1
	lateral sesamoid	-2.3	9.2	0.5	16.6
MFHA: toe lift	*medial sesamoid*	8.6 [a,b]	11.1	10.9 [a,b]	8.2

	phalanx	2.8	7.0	0.6	13.8
	lateral sesamoid	0.5	10.8	4.2	11.2
MFHA: heel rise	*medial sesamoid*	9.6 [a,b]	5.1	13.0[a]	19.3

Table A.2: Bone registration validation errors in joint kinematics relative to the fiducial-based kinematics. Translational and rotational biases are expressed in both coordinate system definitions.

		PCA coordinate system			**CYL coordinate system**		
Rotation errors (degrees)		flexion	adduction	inversion	flexion	adduction	inversion
metatarsophalangeal	*mean*	1.79	-1.16	-0.38	-1.78	0.50	1.67
	stdev	0.31	4.68	2.71	0.35	4.79	2.56
lateral metatarsosesamoidal	*mean*	2.15	-2.21	6.53	-1.55	4.82	7.74
	stdev	1.61	4.29	5.34	1.65	4.35	5.29
medial metatarsosesamoidal	*mean*	0.83	-3.20	-1.86	-1.95	-4.60	2.90
	stdev	2.97	4.52	8.56	2.84	4.34	8.69
Translation errors (mm)		medial-lateral	inferior-superior	anterior-posterior	medial-lateral	inferior-superior	anterior-posterior
metatarsophalangeal	*mean*	0.30	-0.41	0.64	-0.14	0.25	-0.65
	stdev	0.94	0.19	0.07	0.95	0.15	0.08
lateral metatarsosesamoidal	*mean*	-0.41	-0.44	-0.03	0.27	0.28	0.03
	stdev	0.22	0.23	0.03	0.22	0.24	0.03
medial metatarsosesamoidal	*mean*	-0.20	-0.27	-0.19	-0.23	-0.05	-0.04
	stdev	0.34	0.17	0.06	0.82	0.50	0.13

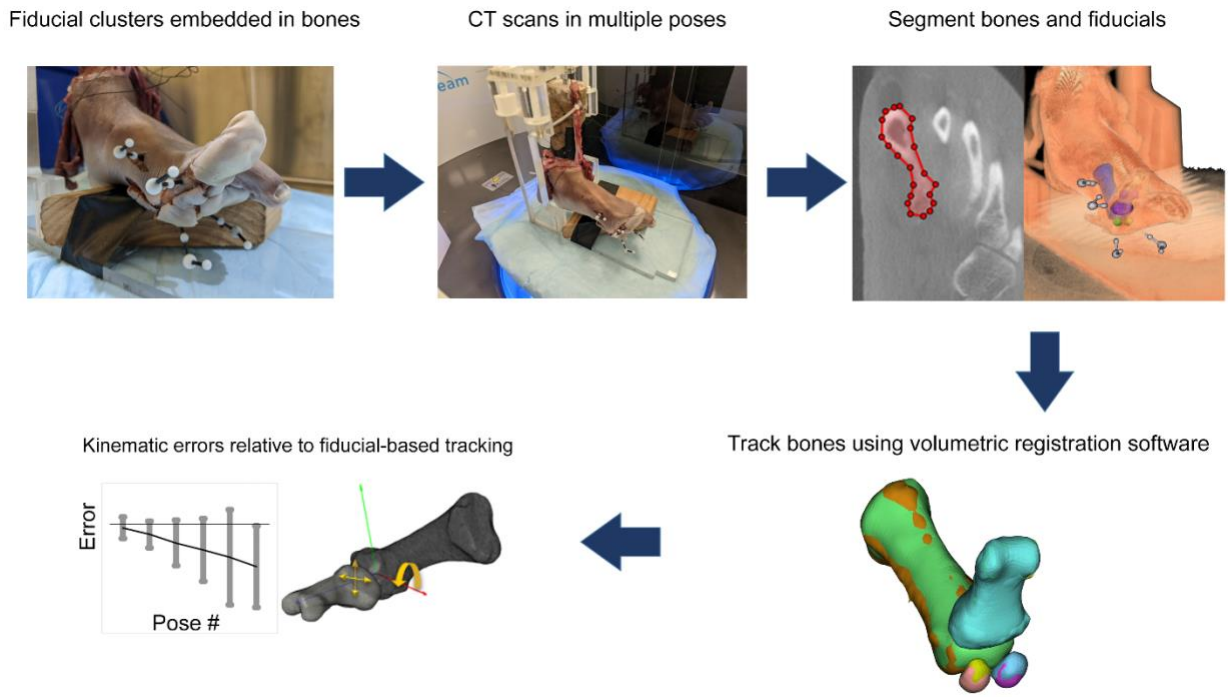

Figure A.1: Custom fiducial marker cluster triads were embedded into each bone. The specimen's tendons were used to actuate into five different poses for weightbearing computed tomography scanning. The volumetric registration process was carried out and the resultant bone poses were compared to those derived from the fiducial spheres.

References

[1] Anwar, R., Anjum, S. N., and Nicholl, J. E., 2005, "Sesamoids of the foot," Current Orthopaedics, 19(1), pp. 40-48.

[2] Richardson, E. G., 1999, "Hallucal sesamoid pain: causes and surgical treatment," The Journal of the American Academy of Orthopaedic Surgeons, 7(4), pp. 270-278.

[3] Boike, A., Schnirring-Judge, M., and McMillin, S., 2011, "Sesamoid disorders of the first metatarsophalangeal joint," Clinics in Podiatric Medicine and Surgery, 28(2), pp. 269-285.

[4] Leventen, E. O., 1991, "Sesamoid disorders and treatment: An update," Clinical Orthopaedics and Related Research(269), pp. 236-240.

[5] Goldberg, I., and Nathan, H., 1987, "Anatomy and pathology of the sesamoid bones - The hand compared to the foot," International Orthopaedics, 11(2), pp. 141-147.

[6] Derner, R., Goss, K., Postowski, H. N., and Parsley, N., 2005, "A plantarflexory-shortening osteotomy for hallux rigidus: A retrospective analysis," Journal of Foot and Ankle Surgery, 44(5), pp. 377-389.

[7] Smith, R. W., Reynolds, J. C., and Stewart, M. J., 1984, "Hallux valgus assessment: report of research committee of American Orthopaedic Foot and Ankle Society," Foot & ankle, 5(2), pp. 92-103.

[8] Shereff, M. J., Bejjani, F. J., and Kummer, F. J., 1986, "Kinematics of the first metatarsophalangeal joint," Journal of Bone and Joint Surgery - Series A, 68(3), pp. 392-398.

[9] Jamal, B., Pillai, A., Fogg, Q., and Kumar, S., 2015, "The metatarsosesamoid joint: An in vitro 3D quantitative assessment," Foot and Ankle Surgery, 21(1), pp. 22-25.

[10] Ahn, T. K., Kitaoka, H. B., Luo, Z. P., and An, K. N., 1997, "Kinematics and contact characteristics of the first metatarsophalangeal joint," Foot and Ankle International, 18(3), pp. 170-174.

[11] Karasick, D., and Schweitzer, M. E., 1998, "Disorders of the hallux sesamoid complex: MR features," Skeletal Radiol, 27(8), pp. 411-418.

[12] Nery, C., Baumfeld, D., Umans, H., and Yamada, A. F., 2017, "MR Imaging of the Plantar Plate: Normal Anatomy, Turf Toe, and Other Injuries," Magnetic resonance imaging clinics of North America, 25(1), pp. 127-144.

[13] Duan, X., Li, L., Wei, D. Q., Liu, M., Yu, X., Xu, Z., Long, Y., and Xiang, Z., 2017, "Role of magnetic resonance imaging versus ultrasound for detection of plantar plate tear," Journal of orthopaedic surgery and research, 12(1), p. 14.

[14] Deschamps, K., Staes, F., Bruyninckx, H., Busschots, E., Jaspers, E., Atre, A., and Desloovere, K., 2012, "Repeatability in the assessment of multi-segment foot kinematics," Gait Posture, 35(2), pp. 255-260.

[15] Leardini, A., Benedetti, M. G., Berti, L., Bettinelli, D., Nativo, R., and Giannini, S., 2007, "Rear-foot, mid-foot and fore-foot motion during the stance phase of gait," Gait Posture, 25(3), pp. 453-462.

[16] Okita, N., Meyers, S. A., Challis, J. H., and Sharkey, N. A., 2013, "Segmental motion of forefoot and hindfoot as a diagnostic tool," J Biomech, 46(15), pp. 2578-2585.

[17] de Cesar Netto, C., Myerson, M. S., Day, J., Ellis, S. J., Hintermann, B., Johnson, J. E., Sangeorzan, B. J., Schon, L. C., Thordarson, D. B., and Deland, J. T., 2020, "Consensus for the Use of Weightbearing CT in the Assessment of Progressive Collapsing Foot Deformity," Foot & ankle international, 41(10), pp. 1277-1282.

[18] Lintz, F., Beaudet, P., Richardi, G., and Brilhault, J., 2021, "Weight-bearing CT in foot and ankle pathology," Orthop Traumatol Surg Res, 107(1s), p. 102772.

[19] MacWilliams, B. A., and Davis, R. B., 2013, "Addressing some misperceptions of the joint coordinate system," Journal of Biomechanical Engineering, 135(5), pp. 9-11.

[20] Dabirrahmani, D., and Hogg, M., 2017, "Modification of the Grood and Suntay Joint Coordinate System equations for knee joint flexion," Med Eng Phys, 39, pp. 113-116.

[21] Grood, E. S., and Suntay, W. J., 1983, "A joint coordinate system for the clinical description of three-dimensional motions: application to the knee," J Biomech Eng, 105(2), pp. 136-144.

[22] Brown, J. A., Gale, T., and Anderst, W., 2020, "An automated method for defining anatomic coordinate systems in the hindfoot," Journal of Biomechanics, 109, pp. 109951-109951.
[23] Lenz, A. L., Strobel, M. A., Anderson, A. M., Fial, A. V., MacWilliams, B. A., Krzak, J. J., and Kruger, K. M., 2021, "Assignment of local coordinate systems and methods to calculate tibiotalar and subtalar kinematics: A systematic review," J Biomech, 120, p. 110344.
[24] Kitashiro, M., Ogihara, N., Kokubo, T., Matsumoto, M., Nakamura, M., and Nagura, T., 2017, "Age- and sex-associated morphological variations of metatarsal torsional patterns in humans," Clinical Anatomy, 30(8), pp. 1058-1063.
[25] Matsuura, Y., and Ogihara, N., 2010, "A Method for Quantifying Articular Surface Morphology of Metacarpals Using Quadric Surface Approximation," International Journal of Primatology(31), pp. 263-274.
[26] Halilaj, E., Rainbow, M. J., Got, C. J., Moore, D. C., and Crisco, J. J., 2013, "A thumb carpometacarpal joint coordinate system based on articular surface geometry," Journal of biomechanics, 46(5), pp. 1031-1034.
[27] Renault, J.-B., Aüllo-Rasser, G., Donnez, M., Parratte, S., and Chabrand, P., 2018, "Articular-surface-based automatic anatomical coordinate systems for the knee bones," Journal of Biomechanics, 80, pp. 171-178.
[28] Miranda, D. L., Rainbow, M. J., Leventhal, E. L., Crisco, J. J., and Fleming, B. C., 2010, "Automatic determination of anatomical coordinate systems for three-dimensional bone models of the isolated human knee," Journal of Biomechanics, 43(8), pp. 1623-1626.
[29] Wang, B., Roach, K. E., Kapron, A. L., Fiorentino, N. M., Saltzman, C. L., Singer, M., and Anderson, A. E., 2015, "Accuracy and feasibility of high-speed dual fluoroscopy and model-based tracking to measure in vivo ankle arthrokinematics," Gait Posture, 41(4), pp. 888-893.
[30] Parr, W. C., Chatterjee, H. J., and Soligo, C., 2012, "Calculating the axes of rotation for the subtalar and talocrural joints using 3D bone reconstructions," J Biomech, 45(6), pp. 1103-1107.
[31] Yin, L., Chen, K., Guo, L., Cheng, L., Wang, F., and Yang, L., 2015, "Identifying the Functional Flexion-extension Axis of the Knee: An In-Vivo Kinematics Study," PloS one, 10(6), p. e0128877.
[32] Best, G. M., Mack, Z. E., Pichora, D. R., Crisco, J. J., Kamal, R. N., and Rainbow, M. J., 2019, "Differences in the Rotation Axes of the Scapholunate Joint During Flexion-Extension and Radial-Ulnar Deviation Motions," The Journal of hand surgery, 44(9), pp. 772-778.
[33] Hull, M. L., 2020, "Coordinate system requirements to determine motions of the tibiofemoral joint free from kinematic crosstalk errors," Journal of biomechanics, 109, pp. 109928-109928.
[34] Nagle, T. F., Erdemir, A., and Colbrunn, R. W., 2021, "A generalized framework for determination of functional musculoskeletal joint coordinate systems," Journal of Biomechanics, 127, p. 110664.
[35] Most, E., Axe, J., Rubash, H., and Li, G., 2004, "Sensitivity of the knee joint kinematics calculation to selection of flexion axes," J Biomech, 37(11), pp. 1743-1748.
[36] Brenner, E., 2003, "The intersesamoidal ridge of the first metatarsal bone: anatomical basics and clinical considerations," Surgical and radiologic anatomy : SRA, 25(2), pp. 127-131.
[37] Drapeau, M. S., and Harmon, E. H., 2013, "Metatarsal torsion in monkeys, apes, humans and australopiths," Journal of human evolution, 64(1), pp. 93-108.
[38] Mortier, J. P., Bernard, J. L., and Maestro, M., 2012, "Axial rotation of the first metatarsal head in a normal population and hallux valgus patients," Orthop Traumatol Surg Res, 98(6), pp. 677-683.
[39] Hintermann, B., Nigg, B. M., and Sommer, C., 1994, "Foot Movement and Tendon Excursion: An In Vitro Study," Foot & Ankle International, 15(7), pp. 386-395.
[40] Aubin, P. M., 2010, "The Robotic Gait Simulator: A Dynamic Cadaveric Foot and Ankle Model for Biomechanics Research," University of Washington.
[41] Jackson, L. T., Aubin, P. M., Cowley, M. S., Sangeorzan, B. J., and Ledoux, W. R., 2011, "A robotic cadaveric flatfoot analysis of stance phase," Journal of Biomechanical Engineering, 133(5), pp. 1-6.

[42] Hu, Y., Ledoux, W. R., Fassbind, M., Rohr, E. S., Sangeorzan, B. J., and Haynor, D., 2011, "Multi-rigid image segmentation and registration for the analysis of joint motion from three-dimensional magnetic resonance imaging," Journal of Biomechanical Engineering, 133(10), pp. 1-8.
[43] Mattes, D., Haynor, D. R., Vesselle, H., Lewellyn, T. K., and Eubank, W., "Nonrigid multimodality image registration," SPIE, pp. 1609-1620.
[44] Beveridge, J. E., Shrive, N. G., and Frank, C. B., 2014, "Repeatability and precision of a weighted centroid method for estimating dynamic in vivo tibiofemoral surface interactions in sheep," Computer Methods in Biomechanics and Biomedical Engineering, 17(16), pp. 1853-1863.
[45] Spoor, C. W., and Veldpaus, F. E., 1980, "Rigid body motion calculated from spatial co-ordinates of markers," J Biomech, 13(4), pp. 391-393.
[46] Woltring, H. J., Huiskes, R., de Lange, A., and Veldpaus, F. E., 1985, "Finite centroid and helical axis estimation from noisy landmark measurements in the study of human joint kinematics," J Biomech, 18(5), pp. 379-389.
[47] Ehrig, R. M., and Heller, M. O., 2019, "On intrinsic equivalences of the finite helical axis, the instantaneous helical axis, and the SARA approach. A mathematical perspective," Journal of Biomechanics, 84, pp. 4-10.
[48] Ehrig, R. M., Taylor, W. R., Duda, G. N., and Heller, M. O., 2007, "A survey of formal methods for determining functional joint axes," Journal of Biomechanics, 40(10), pp. 2150-2157.
[49] Cardot, H., 2020, "Gmedian: Geometric Median, k-Medians Clustering and Robust Median PCA.."
[50] Woltring, H. J., 1990, "Estimation of the trajectory of the instantaneous centre of rotation in planar biokinematics," Journal of Biomechanics, 23(12), pp. 1273-1274.
[51] Woltring, H. J., de Lange, A., Kauer, J. M. G., and Huiskes, R., 1987, "Instantaneous Helical Axis Estimation Via Natural, Cross-Validated Splines," Biomechanics: Basic and Applied Research., G. Bergmann, R. Kolbel, and A. Rolhmann, eds., Springer, Dordrecht.
[52] Elhabian, S., Agrawal, P., Cates, J., Datar, M., and Whitaker, R., 2012, "ShapeWorksStudio v2.2 Particle-based Shape Correspondence and Visualization Software."
[53] Cates, J., Elhabian, S., and Whitaker, R., 2017, "Chapter 10 - ShapeWorks: Particle-Based Shape Correspondence and Visualization Software," Statistical Shape and Deformation Analysis, G. Zheng, S. Li, and G. Székely, eds., Academic Press, pp. 257-298.
[54] Mardia, K. V., and Jupp, P. E., 2000, Directional Statistics, J Wiley.
[55] R Core Team, 2019, "R: A language and environment for statistical computing.," R Foundation for Statistical Computing, Vienna, Austria.
[56] Tsagris, M., Athineou, G., Sajib, A., Amson, E., Waldstein, M., 2021, "Directional: A Collection of R Functions for Directional Data Analysis."
[57] Peña Fernández, M., Hoxha, D., Chan, O., Mordecai, S., Blunn, G. W., Tozzi, G., and Goldberg, A., 2020, "Centre of Rotation of the Human Subtalar Joint Using Weight-Bearing Clinical Computed Tomography," Scientific reports, 10(1), p. 1035.
[58] Durrant, M., Durrant, L., and McElroy, T., 2019, "Establishing a common instantaneous center of rotation for the metatarso-phalangeal and metatarso-sesamoid joints: A theoretical geometric model based on specific morphometrics," Journal of Orthopaedic Surgery and Research, 14(1), pp. 1-10.
[59] Telfer, S., Kindig, M. W., Sangeorzan, B. J., and Ledoux, W. R., 2017, "Metatarsal shape and foot type: A geometric morphometric analysis," Journal of Biomechanical Engineering, 139(3).

Chapter 6

Validation of DRACO model-based foot and ankle bone tracking software

Eric D. Thorhauer[a,b], Nick Entress[a], Aerie Grantham[a], William R. Ledoux, PhD[a,b,c]

[a]Center for Limb Loss and MoBility (CLiMB), Department of Veterans Affairs Puget Sound Health Care System, Seattle, Washington, USA

[b]Department of Mechanical Engineering, University of Washington, Seattle, Washington, USA

[c]Department of Orthopaedic Surgery, University of Washington, Seattle, Washington, USA

Keywords: biplanar fluoroscopy, model-based tracking, computer vision, digitally reconstructed radiographs

Abstract

Model-based bone tracking with biplanar fluoroscopy is a powerful technique to clinicians and biomechanists with in vivo functional kinematic data of the human skeleton. Model-based bone tracking with biplane systems has applications in both the in vivo and in vitro realms, serving as a non-invasive means for accurately quantifying skeletal motion. We have developed a custom biplane system for dynamic imaging of the entire foot and ankle complex during gait as well as a custom software suite to perform the model-based tracking process. We demonstrate our ability to reconstruct the pose of foot bones accurately and precisely in both static and dynamic motion trials approximating physiological activities. Finally, we demonstrate the accuracy of tracking bones using digitally reconstructed radiographs acquired on a low-dose computed tomography scanner.

Introduction

Biplanar fluoroscopy systems allow biomechanists to precisely quantify in vivo skeletal kinematics by directly tracking bones on stereo radiographic sequences. Advances in fluoroscopy and camera hardware have facilitated the extension of this technique into the domain of foot and ankle biomechanics [1-10]. Using a model-based tracking approach avoids the invasiveness of embedding radiopaque markers into each bone of interest. This method utilizes image similarity metrics to optimally align simulated X-ray images called digitally reconstructed radiographs (DRRs) to the acquired stereo image sequences in order to reconstruct the three-dimensional (3D) kinematics [7]. To perform this registration process, the respective research groups developed custom software using these biplane systems [11-13]. However, the current offerings of model-based tracking software are either prohibitively expensive, ill-suited for foot and ankle tracking or not available for public use.

To meet the immediate research needs of our laboratory and address the tracking challenges specific to the foot and ankle, we have pursued the development of a custom model-based tracking software solution [7]. Before this software can be confidently applied to clinically related research, its kinematic accuracy must be validated in order to establish a lower limit on bone pose reconstruction errors. Traditionally, biplane fluoroscopy labs have utilized marker-based tracking kinematics as the ground-truth reference to compare the performance of their model-based tracking algorithms [7, 8, 10, 12]. These validation trials have been performed using surrogate phantom objects (e.g., cylinders, blocks, lattice) embedded with radiopaque markers; however, these objects do not have the same tracking challenges associated with human anatomy like bony occlusions and soft tissue scatter and attenuation that complicate the in vivo tracking process [14-16]. Therefore, the best way to validate the model-based software is by

using cadaver specimens of the anatomy of interest, moved in a manner that approximates the physiological motion to be tracked, and with the biplane system configured as it would be for in vivo trials [12].

The simulated X-rays required for the model-based tracking approach are generated from volumetric computed tomography (CT) scans. Typically, fan beam CT scanners are utilized, as they provide the best bone contrast, signal-to-noise ratio, and accuracy in Hounsfield units that correspond to the local tissue X-ray attenuation of each voxel. Recently, cone beam scanners with highly efficient detectors requiring a fraction of the radiation dose of fan beam scanners have come to market for the weight bearing foot and ankle imaging community. If the issues inherent to cone beam CT image quality can be addressed in a custom model-based tracking solution, and these scan volumes can be reliably used to accurately reconstruct skeletal motion, the total radiation dose experienced by test subjects is drastically reduced. In addition to the ethical responsibility of using As Low As Reasonably Achievable (ALARA) principles with respect to X-ray, by lowering the total dose received, research subjects might be more willing to volunteer for studies involving radiation, their risk of developing cancers is drastically reduced even further, and the acquisition of more biplane X-ray trials quantifying the natural within-subject variation in kinematics or additional trials covering a more diverse array of motion tasks can be explored.

We describe the details of our model-based tracking software solution and the cadaveric simulation of gait using a robotic arm to “walk” specimens through our capture volume to validate the resultant bone kinematics generated by our software in realistic gait scenarios. By developing and validating this model-based technique for the foot and ankle, we provide clinicians and biomechanists with a tool to better understand human gait and the development,

prevention, and treatment of numerous pathologies. Additionally, these validation data will directly guide our future research goals and software development needs by quantifying how subtle of kinematic differences we are able to reliably detect and identifying the remaining challenges in bone tracking, which will permit the administration of large clinical trials.

Methods

We developed DRACO (Digitally-reconstructed-radiograph-based Roentgen Analysis via CUDA Optimization), our custom software based in MATLAB and in C# utilizing existing open-source software libraries [17] to serve our bone tracking needs (Figure 1). This software was experimentally validated using human foot specimens to realistically mimic the in vivo imaging challenges associated with model-based tracking.

Foot specimen preparation

Three human cadaver specimens, including the tibia and foot (males aged 59, 65, and 73 and weighing 63, 89, and 70 kg, respectively), were carefully dissected to expose the tibial shaft and primary extrinsic tendons (Achilles, flexor hallucis longus, flexor digitorum longus, extensor digitorum longus, extensor hallucis longus, tibialis anterior, tibialis posterior, peroneus longus, peroneus brevis). Tibia shafts were potted in resin cylinders about 8 cm proximal to the malleoli to facilitate mounting to the end-effector of a robotic arm (Figure 2). Three 3 mm stainless steel marker beads were rigidly inserted into each of the following bones through minimally invasive skin portals: tibia, talus, calcaneus, navicular, first metatarsal, and proximal phalanx (Figure 2). Before and following the marker bead installations, each specimen was scanned using a weight bearing low-dose CT scanner (LineUp, Curvebeam, voxel size: 0.3 x 0.3 x 0.3 mm,

120kVp, 5mA, 0.5 mm focal spot)) as well as a standard clinical fan beam scanner (Siemens Biograph 16, voxel size: 0.67 x 0.67 x 0.75 mm, 130kVp, 134mA, 0.95 mm focal spot). Each marker center was localized in the CT scans using an iterative intensity-weighted spherical fitting algorithm implemented in MATLAB. For each specimen, both the CT scans with and without the marker beads installed were segmented (Mimics v22, Materialise, Belgium) to generate specimen-specific volumetric models of each bone of interest. Those CT volumes with the markers present were iteratively co-registered to the corresponding scan without beads. The resulting transformations allow us to track the bones using CT volumes uncorrupted by the noise and scatter artifacts due to the presence of the marker beads, which is more realistic to the minimally invasive living subjects studies the laboratory seeks to perform. Additionally, removing the marker beads prevents the tracking algorithm from "cheating" by using their high-contrast radiographic signatures to dominate and drive the tracking process.

Specimens were affixed to the end effector of a KUKA KR-16 robot (KUKA, Germany) capable of 0.1 mm positional precision (Figure 3). This stock KR-16 robot was modified by BioRobotics (Cleveland, OH, USA) to include a bank of electromechanical actuators responsible for applying tension loads to the prepared tendons via clamps connected to stainless steel cables and inline force transducers. The robot base was positioned in the laboratory to not interfere with the standard biplane imaging configuration for in vivo gait while allowing the robot to "walk" foot specimens through the capture volume. The gait reaction forces during simulated walking trials were monitored and recorded with a custom Kistler force plate sampled at 2000 Hz. A custom LabView control suite (simVitro, BioRobotics, Cleveland, OH, USA) specifically designed to control the KR-16 while simulating biomechanical tasks was used to execute the gait trials. Due to limitations in the maximum appliable load of the robotic arm, full gait simulations

were performed at ¼ normal walking speed. In addition to the full gait cycle simulation, separate trials were performed at full speed simulating 1) the swing phase of gait and 2) the end of stance phase through toe-off. Due to biplane capture volume size limitations, the swing phase portion was simulated by translating specimens at full speed through the capture volume.

Biplane fluoroscopy trials

All fluoroscopy data were acquired on a custom biplanar system (Imaging Systems and Services, Painesville, Ohio, USA) with 40 cm image intensifiers (Thales, France) coupled with high-speed video cameras (Phantom v5.2, Vision Research, Wayne, New Jersey, USA) that was configured for imaging with an approximately 60-degree inter-beam angle through a walkway with a carbon fiber panel (Figure 1) to image in vivo foot and ankle motion. Videos are recorded to 1600 x 1600 pixel 12-bit grayscale frames with a typical pixel size of about 0.267 mm in the normal image intensifier magnification mode. The biplane system is configured to fire 1 ms X-ray pulses at 120 Hz that are synchronized to the acquisition triggers of the high-speed cameras.

Model-based tracking algorithm

The model-based tracking algorithm generates simulated X-ray images called digitally reconstructed radiographs (DRRs) for a given bone pose in the virtual laboratory space and compares them to the recorded stereo fluoroscopy images via an image similarity metric. The bone data from the segmented CT scans are scalar volumes, with each voxel element having an assigned Hounsfield unit related to the average X-ray attenuation in that subvolume of the scanning region. The ray-casting algorithm casts virtual X-rays from each biplane source to each pixel location on the virtual detectors and sums the values of the Hounsfield units that are

traversed to provide a simulated X-ray signature for each pixel of the detectors. These resulting images are the DRRs, which are compared to the fluoroscopy images that have been corrected for spatial and intensity distortions using our PISCES pre-processing software. The image similarity metrics (ISM) implemented in DRACO include intensity-based comparisons like normalized correlation coefficient (NCC) and edge-based feature matching in gradient correlation (GC) and gradient orientation (GO) metrics [18]. The DRACO user can specify a weighted combination of ISMs and specify the relative weighting between the two stereo views. The DRACO user interface includes controls for manipulating bone objects in the virtual laboratory by translating and rotating with respect to the bone's center of mass and inertial axes. This provides an intuitive means for operators to set the initial pose guess of a given bone before the optimizer is employed to iteratively refine the solution. DRACO allows the user to specify bounds in terms of maximum rotational and translational displacements from the current pose to prevent the optimization from falling into the many local minima and an iteration limit and tolerances on the allowable amount of change in the ISM score to terminate the optimizer in a timely fashion. Since the solution space of the ISMs as a function of the bone pose is wrought with many false local optima, and the merit function response is noisy, expensive to compute, and has no closed-form solution, a derivative-free optimization method was selected. DRACO allows the user to choose which optimization algorithm to use. The default algorithm is the Nelder-Mead downhill simplex method [19]. Anecdotally, this algorithm performs well when the initial pose guess is close to the true final solution (within about 3 mm and 10° of the correct pose). For some bones in certain instances of the gait cycle, more bony overlap and occlusion are present, creating even more false minima in the ISM merit function response. A surrogate optimization model is utilized to find the globally optimal solution of this computationally

expensive merit function by approximating the merit function as a quadratic. Regardless of the algorithm used, the optimizer seeks the six parameters required to fully specify the bone pose in the biplane system (i.e., $x_{translation}$, $y_{translation}$, $z_{translation}$, $x_{rotation}$, $y_{rotation}$, $z_{rotation}$). The rotations are represented by Euler angles in the interval of ± 180° on the user interface. Within the context of the optimizer, the six degree-of-freedom (DOF) pose parameters are scaled to be close to unity to assist the optimizer's performance.

Because of the many false local optima present, for the tracking problem to be tractable, good initial guesses of the bone poses are needed for a given frame for the software to generate a viable pose solution. DRACO can either extrapolate the previous pose solutions into the neighboring frames of fluoroscopy data to generate initial guesses of the poses, or the user can interpolate between two frames they have tracked and generate solutions they are confident in. This pose interpolation is achieved by transforming the homogeneous transformation matrices representing bone positions and orientations into special orthogonal Lie groups SE(3) [20]. The intermediate poses between two tracked frames may be smoothly estimated in this representation. In practice, the user would track a given bone in multiple, disparate fluoroscopy frames, then interpolate between these frames which would place the bone close enough to the final solutions of the untracked frames that the Nelder-Mead algorithm can refine the poses from these initial guesses. In addition to optimizing a bone represented as the 6 DOF pose with respect to the laboratory coordinate frame, the DRACO interface and optimization merit functions can manipulate and optimize poses in the contexts of the respective stereo views by utilizing the appropriate extrinsic camera parameters to move the bone “up or down” or “in and out” of the image plane, for example. These in-plane movements are much more intuitive for the end user. They can decompose the complexity of establishing guesses for six independent pose parameters

into a subset for a given fluoroscopy view (e.g., a single rotation about the camera focal axis and 3 translations in the context of the image plane).

The DRACO interface also allows the user to specify multiple types of image manipulations, filters, and enhancements for both aiding visual cues used to set the initial pose guess and to assist the optimizer by increasing the similarity between the DRRs and fluoroscopy images or by reducing noise present in the images. The user can set gamma corrections, apply various edge detection and smoothing algorithms and spatial convolutional denoising, and get immediate feedback on how the applied settings affected the ISM score for a given pose.

Model-based tracking validation

Using our custom URSA marker tracking software, ground-truth bone kinematics were determined by tracking the embedded triads of marker beads. The transformations between the assumed rigid triad of markers from each frame of the tracked marker data in the fluoroscopy laboratory coordinate system to the CT coordinate system of a given bone were determined using Horn's method of absolute orientations fitted in a least squares sense and implemented in MATLAB [21]. These transformation matrices were decomposed into the three orthogonal Euler angles and three translational components and compared to the six pose parameters of DRACO to quantify the kinematic errors.

Results

Presently, the first metatarsal and proximal phalanx data, which comprise the first metatarsophalangeal joint (MTPJ1), for one of the specimens that were exercised through all three gait simulations are available using the DRRs generated from cone beam CT.

Static trial tracking stability

Across 50 frames of a static trial (specimen did not move), the standard deviations in first metatarsal pose parameters were 0.11, 0.10, and 0.12 mm for the X, Y, and Z translations, respectively. The first metatarsal orientation standard deviations were 1.04°, 0.30° , and 0.50° for the X, Y, and Z rotational Euler angles, respectively. In the proximal phalanx, translational standard deviations were 0.07, 0.02, and 0.02 mm for the X, Y, and Z translation components. Proximal phalanx orientation standard deviations were 0.61°, 0.21° , and 0.30° for the X, Y, and Z rotational Euler angles, respectively.

Dynamic trial tracking accuracy

Swing phase simulation translation errors in model-based tracking of MTPJ1 were submillimeter for almost every tracked frame, and first metatarsal tracking errors (Figure 5) were larger than proximal phalanx errors (Figure 6), which exhibited error magnitudes below 0.5 mm. Toe off simulation errors in the first metatarsal were largest for the X-axis, which corresponds to rotation about the bone's long axis (Figure 7). An increase in the X-axis rotational errors was observed towards the end of the sequence when the MTPJ1 was in deep flexion (after frame 30 in Figure 7). For proximal phalanx toe off tracking, errors were smaller (submillimeter and sub-degree) compared to the metatarsal (Figure 8), and no large bias occurred at the deep flexion portion of the frame range. The full gait simulation trials exhibited the largest rotational tracking

errors for the metatarsal (Figure 9). Proximal phalanx errors were slightly higher in the gait simulation tracking compared to the toe off trials.

Tracking computational run times

A summary of the per-subroutine execution times for the various functions called during optimization is presented in Table 1. Edge detection and image enhancement times were negligible compared to the ISM computation times. The gradient correlation (GC) image similarity metric took 15 times longer to evaluate the images than the normalized cross-correlation (NCC) metric. The combination of gradient orientation (GO) and gradient correlation (GC) led to the highest computational run time (Table 1).

Discussion

This work aimed to develop the model-based tracking software and subsequently perform experiments with the software for validating in vivo foot bone tracking using digitally reconstructed radiographs from low-dose computed tomography. The software successfully tracked the bones of MTPJ1 during clinically important phases of the gait cycle. Proximal phalanx tracking errors across all activities were lower than those for the first metatarsal. This is likely due to the lack of bony occlusions that occur for the first metatarsal. The neighboring sesamoid bones and second metatarsal cortical bone regions introduce edges that cause basins of attraction for the optimizer when aligning the DRRs about the bone's long axis. The user could manually refine these tracking errors, or future work could introduce constraints for the long-axis rotations of the metatarsal to limit the amount of allowable frame-to-frame variation in the Euler angle. Lastly, post-processing smoothing of the kinematics could be performed using a

Butterworth filter, as is typically performed for biomechanics kinematic data. All data presented here are the raw, unfiltered poses returned by the optimizer after a first optimization pass for each frame.

Our tracking bias and precision errors for the first metatarsal and phalanx are higher than those reported by Iaquinto et al. (better than 0.45 degrees and 0.05 mm) [7]. However, in that validation, the bones were excised from foot specimens and embedded in foam blocks before being tracked in isolation in the capture volume. The absence of neighboring bones to confound tracking greatly simplifies the task and artificially increases the bias and precision errors. By tracking bones in intact specimens and using the robot to mimic physiological motions as best as possible, the resultant validation data more accurately reflects the real-world in vivo errors.

The highest computational burdens outside of generating the DRRs themselves are the image similarity metric calculations performed for each iteration of the optimization routines. Gradient-based ISMs significantly increased the run time compared to the purely intensity-based NCC metric. This is because both the horizontal and vertical edges of the fluoroscopy and DRR images must be computed via convolution operations, and those edge maps are then passed into either the NCC function for GC or another subroutine for the GO calculation. Future work will look at speeding up these gradient-based calculations or parallelizing them, as tracking with only the intensity-based NCC is unreliable. To further reduce the overall optimization times, the optimization for each frame could be parallelized rather than tracked sequentially and serially. However, this formulation complicates the enforcement of frame-to-frame variability constraints and global smoothness of the kinematic trajectories and might require multiple optimization passes for a given frame sequence to achieve the true global pose optima.

Limitations to this validation include the lack of a shod trial which would complicate tracking due to increased attenuation from the shoe materials, and a low sample size (currently N=1 specimens) to test across a spectrum of anatomical variation that would be present in vivo. Only a subset of possible ISM metrics were utilized in the present study, and additional ISMs could be tested either in isolation or as part of the weighted combination of the ISM score for each fluoroscopy view. Only the MTPJ1 bones of the forefoot were tracked. Future work will quantify tracking performance for the midfoot and hindfoot. The hindfoot presents more challenges associated with X-ray scatter, attenuation, and bony overlap, likely leading to larger tracking errors than observed in the forefoot.

In summary, we have developed a model-based tracking solution for the foot and ankle. Preliminary validation results suggest this software can reliably reconstruct the dynamic skeletal kinematics during gait tasks. Further work is necessary to decrease tracking errors, computation costs, and user interaction times. However, once the rest of the foot has been validated, this software should become an invaluable tool for researchers and clinicians seeking to understand the complexities of dynamic foot function.

Acknowledgment

This work was partially funded by Department of Veterans Affairs grant numbers RX002357 and RX002970.

Figures & Tables

Table 1: The run times for the subroutines executed during a single frame optimization in seconds.

Subroutine	**Context**	**Run time (s)**
Edge detection	Used in gradient based ISMs	0.03
Crop image	Limit ISM calculation to DRR region	0.02
Image filtering	User-specified smoothing and gamma corrections	0.003
NCC ISM	Normalized cross-correlation image similarity metric	0.01
GC ISM	Gradient correlation image similarity metric	0.15
GO ISM	Gradient orientation image similarity metric	0.12
Combination NCC and GC ISMs	Calling both the normalized cross-correlation and gradient correlation image similarity metrics	0.15

Combination GC and GO ISMs	Calling both the gradient correlation and gradient orientation image similarity metrics	0.28

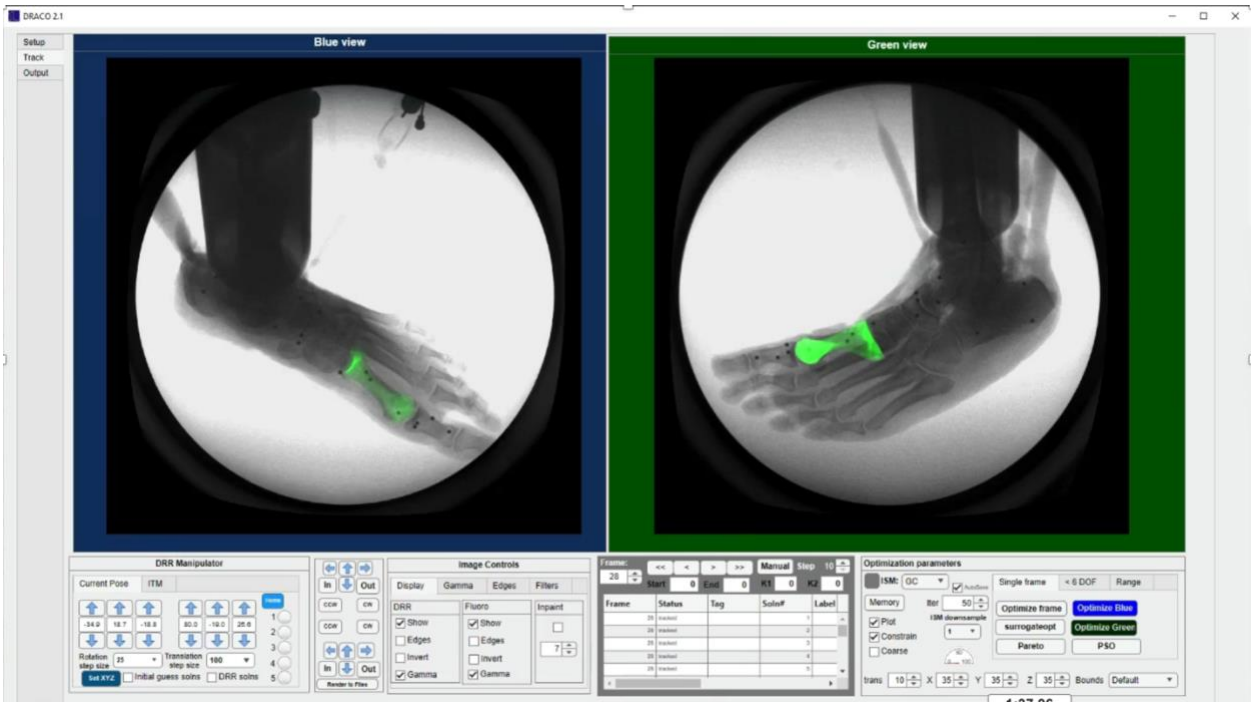

Figure 1: Graphical user interface of the DRACO software. The stereo fluoroscopy views are displayed with the DRR of the currently selected bone overlaid. Translation and rotation manipulators allow the user to set the initial guess pose of the bone prior to optimization. The user also has control of various image processing and edge detection parameters to enhance and aid the alignment via the optimizer.

Figure 2: A KUKA KR-16 robotic arm with a potted tibial shaft affixed to the end-effector and a bank of electromechanical actuators to pull on cables attached to the extrinsic tendons of the specimen. The KR-16 was positioned in the biplane fluoroscopy laboratory such that it can "walk" specimens through the capture volume without interfering or colliding with the imaging equipment, striking the center of the carbon fiber force plate like a living subject would during a gait trial.

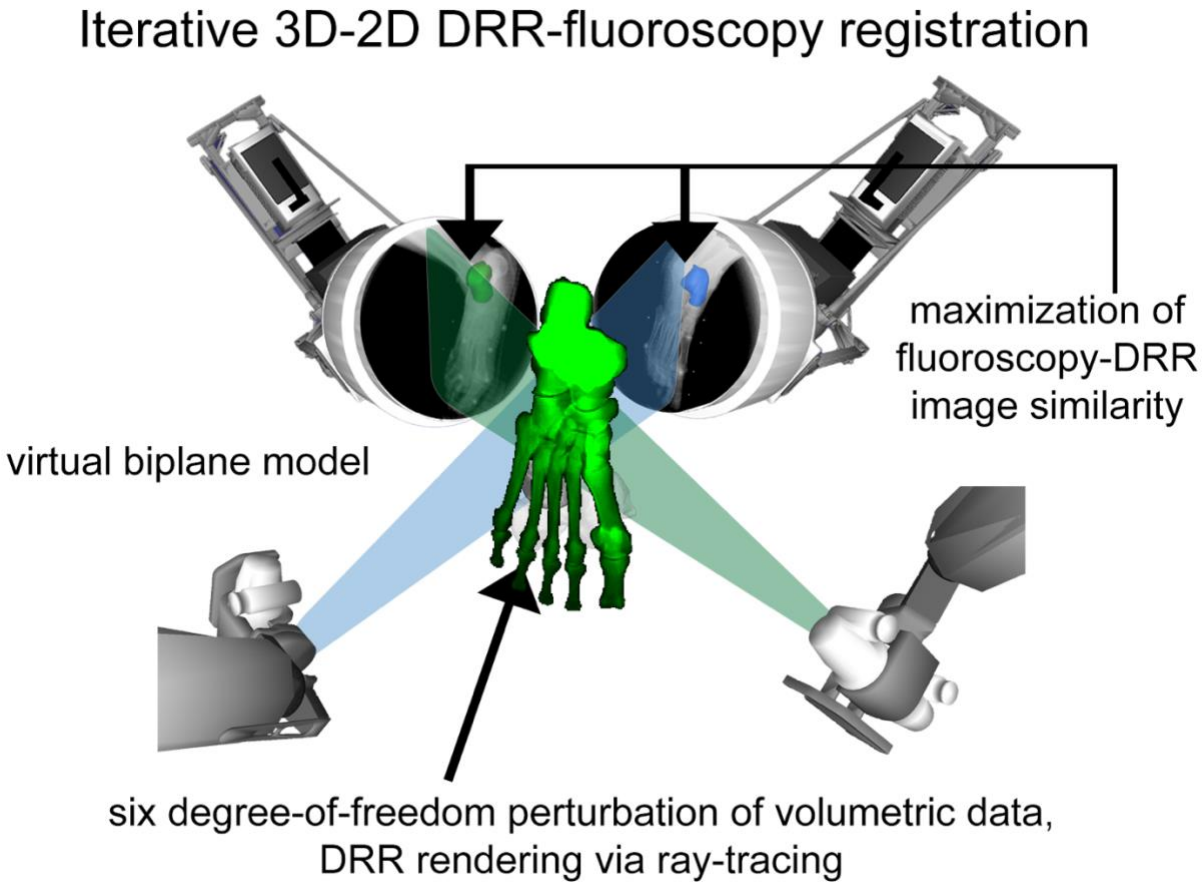

Figure 3: Schematic of the DRACO tracking registration process. The biplane fluoroscopy geometry is virtually recreated via the calibration processes. A segmented CT volume of the bones of interest are posed by the user and virtual X-rays are cast through the volume to generate simulated projections called DRRs on each virtual detector plane. The DRRs are compared to the original fluoroscopy images for each frame. Image similarity metrics are used to quantify the amount of agreement between the simulated and true X-ray projections. When the similarity between the DRR projections and fluoroscopy images for both views are maximized, the 3D pose of the bone in the capture volume approximates the true pose of the subject's bone for that

frame of the video sequence. This process is repeated for all frames and bones of interest until the kinematics of the bones are reconstructed.

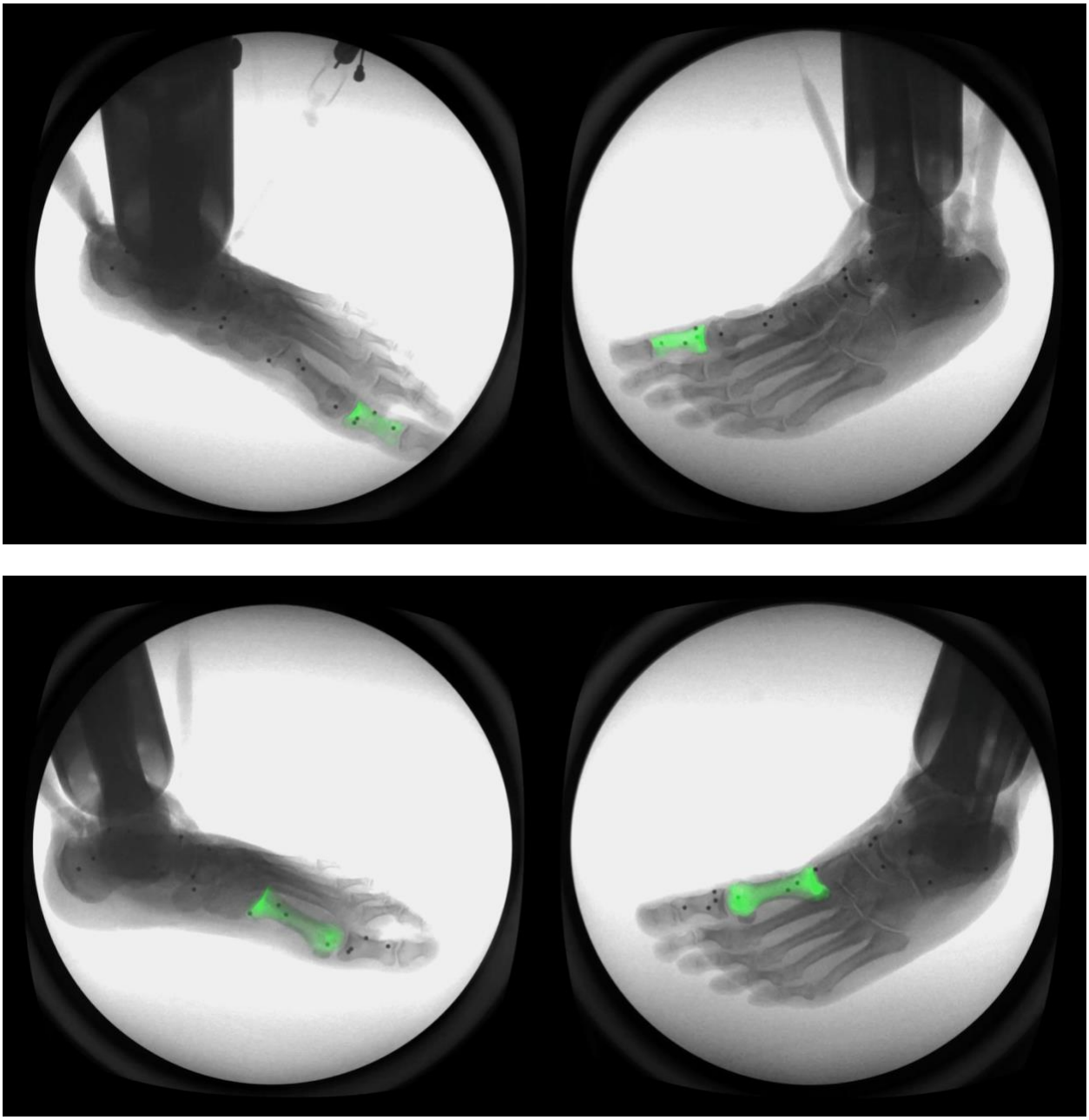

Figure 4: The result of a successful optimization alignment of the DRR projections to the stereo fluoroscopy images for the first metatarsal (top) and proximal phalanx (bottom).

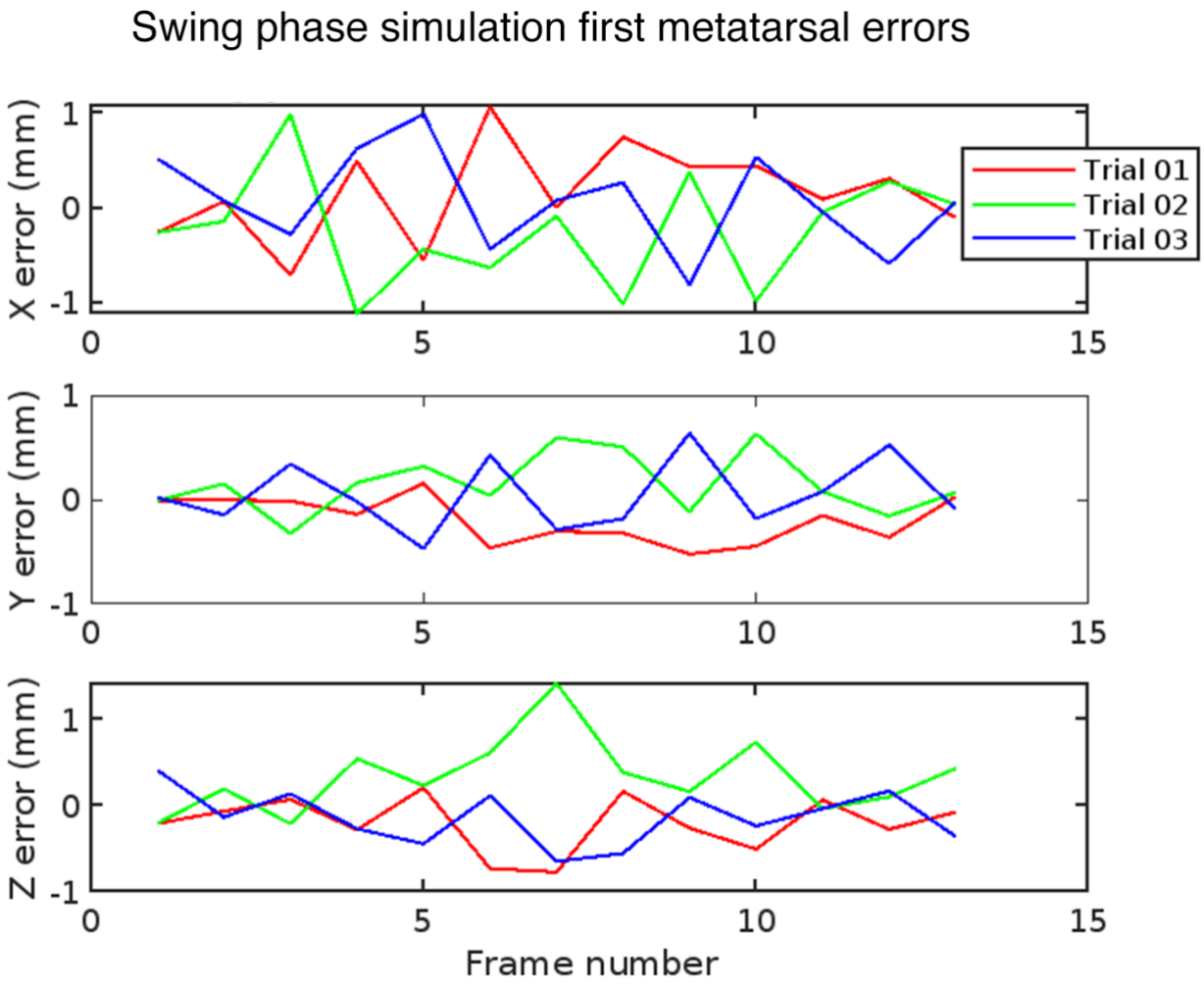

Figure 5: The first metatarsal model-based tracking translation errors for the swing phase simulation trials. Each line (red, blue, green) is a separate tracking session of the same experimental trial.

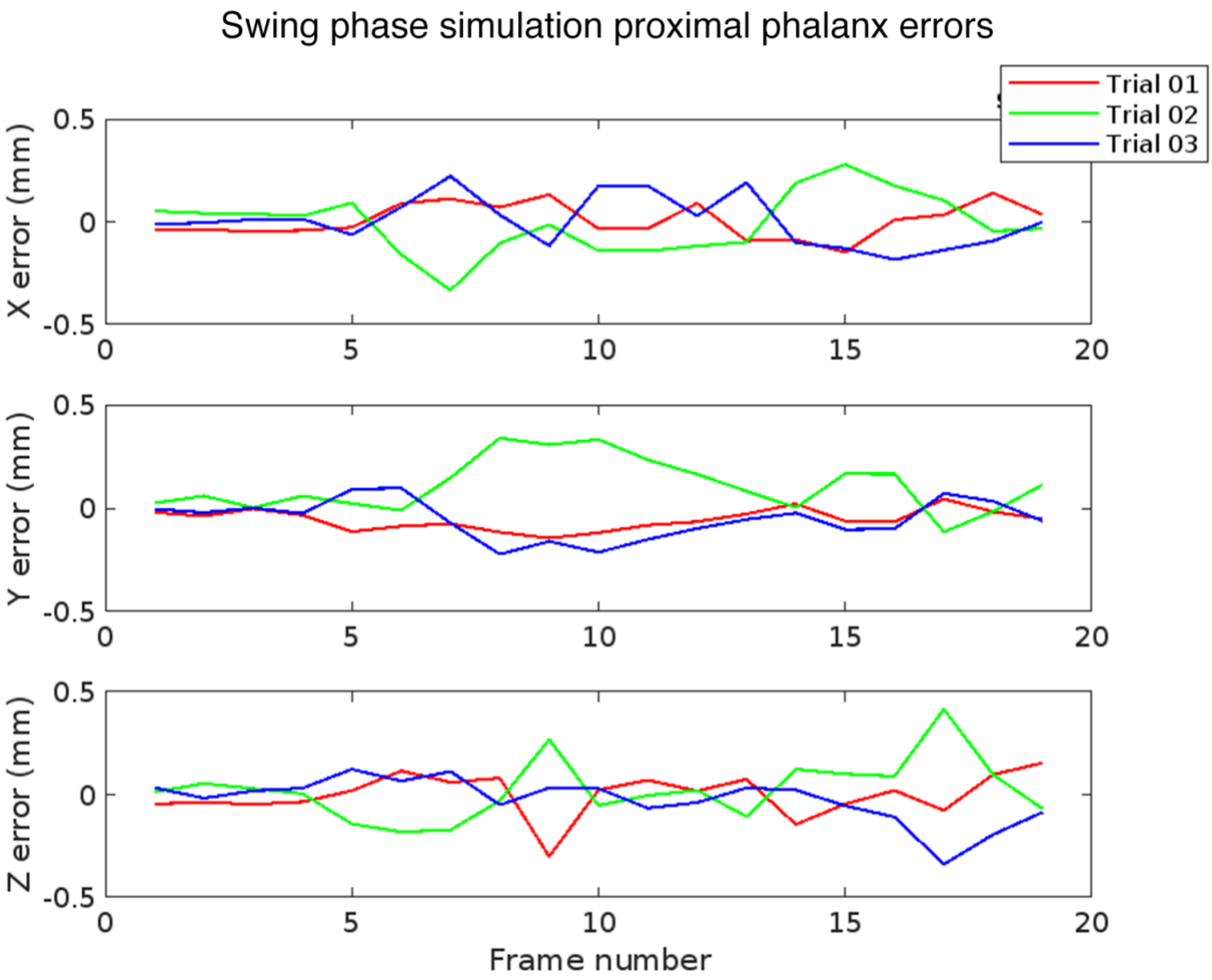

Figure 6: The proximal phalanx model-based tracking translation errors for the swing phase simulation trials. Each line (red, blue, green) is a separate tracking session of the same experimental trial.

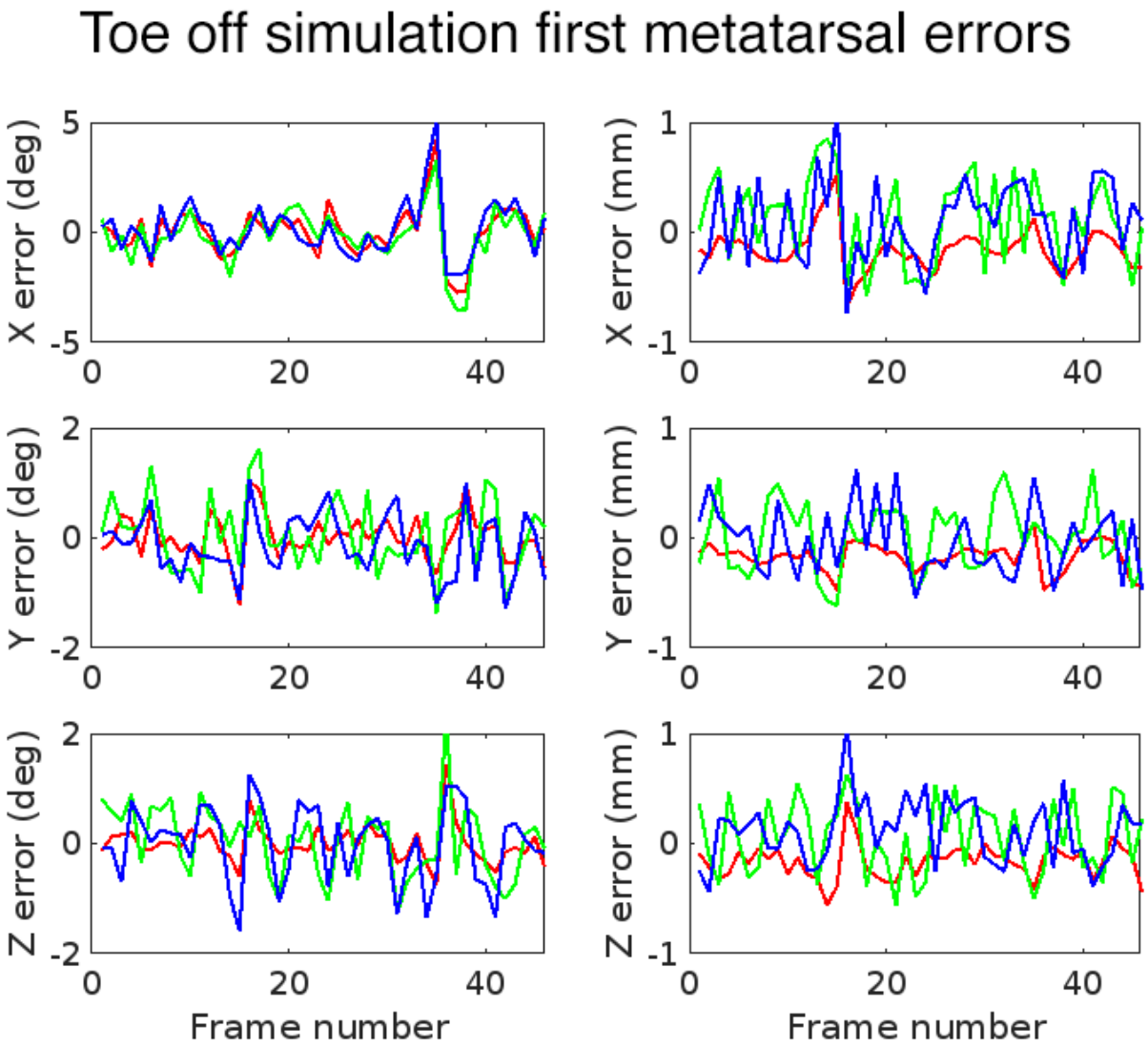

Figure 7: The first metatarsal model-based tracking errors for the toe off simulation trials. Each line (red, blue, green) is a separate tracking session of the same experimental trial. The X-axis rotations correspond to the bone's long axis (proximal-distal). Y-axis rotations are about the medial-lateral axis, and Z-axis rotations are about the superior-inferior axis.

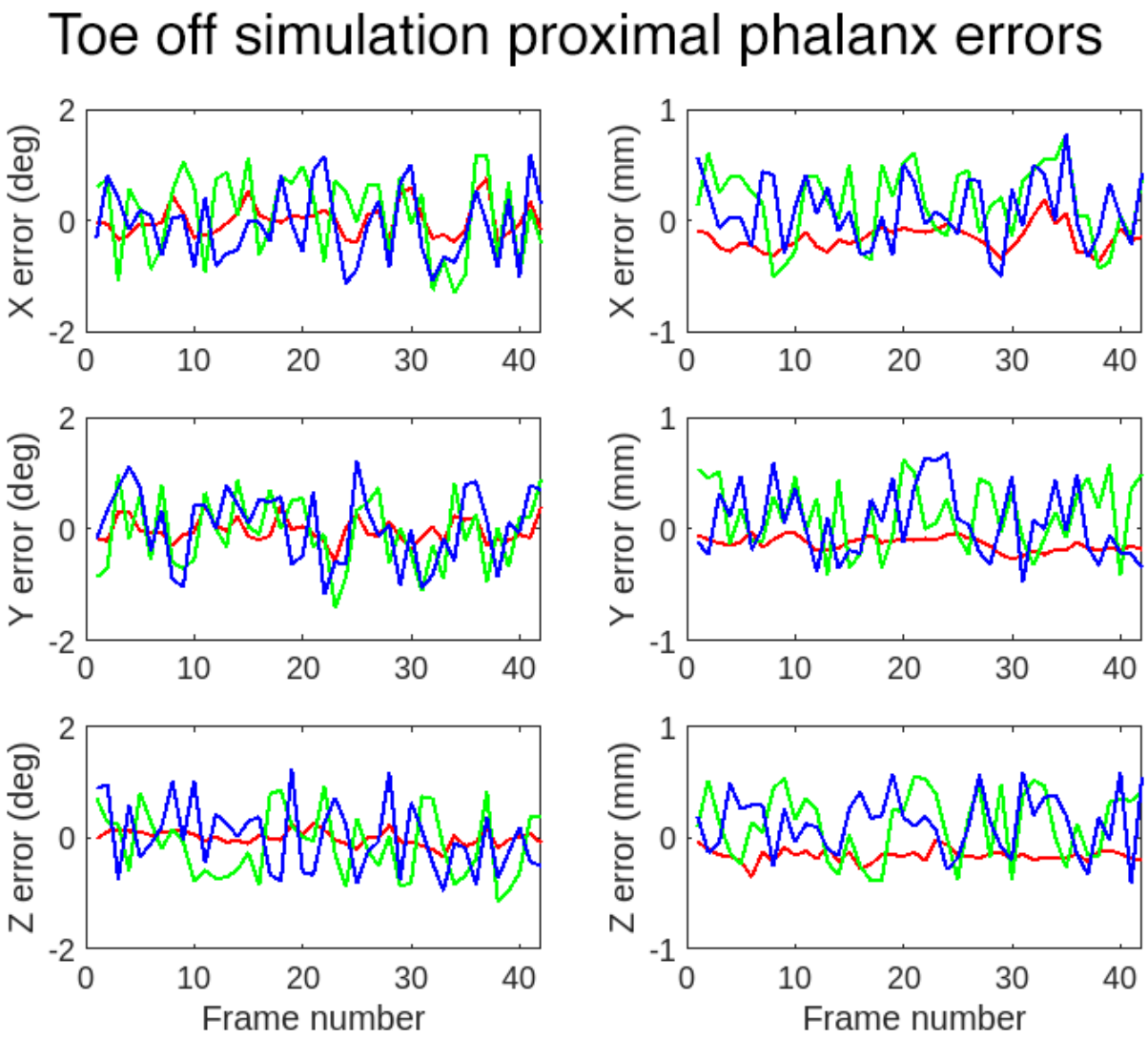

Figure 8: The proximal phalanx model-based tracking errors for the toe off simulation trials. Rotational errors are presented in the left column, translation errors in the right column, and the three components are presented in each row. Each line (red, blue, green) is a separate tracking session of the same experimental trial. The X-axis rotations correspond to the bone's long axis (proximal-distal). Y-axis rotations are about the medial-lateral axis, and Z-axis rotations are about the superior-inferior axis.

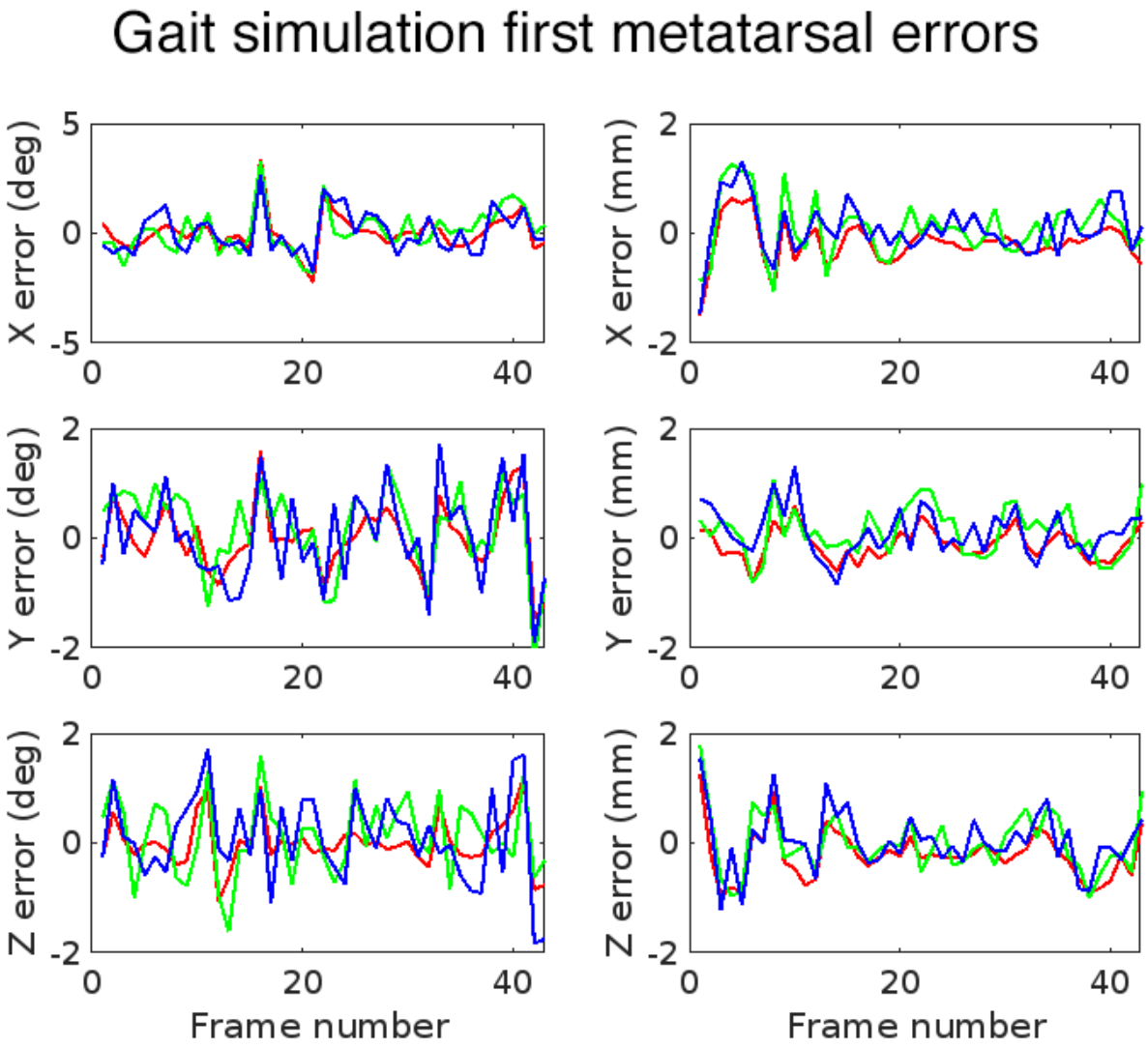

Figure 9: The first metatarsal model-based tracking errors for the full gait simulation trials. Rotational errors are presented in the left column, translation errors in the right column, and the three components are presented in each row. Each line (red, blue, green) is a separate tracking session of the same experimental trial. The X-axis rotations correspond to the bone's long axis (proximal-distal). Y-axis rotations are about the medial-lateral axis, and Z-axis rotations are about the superior-inferior axis.

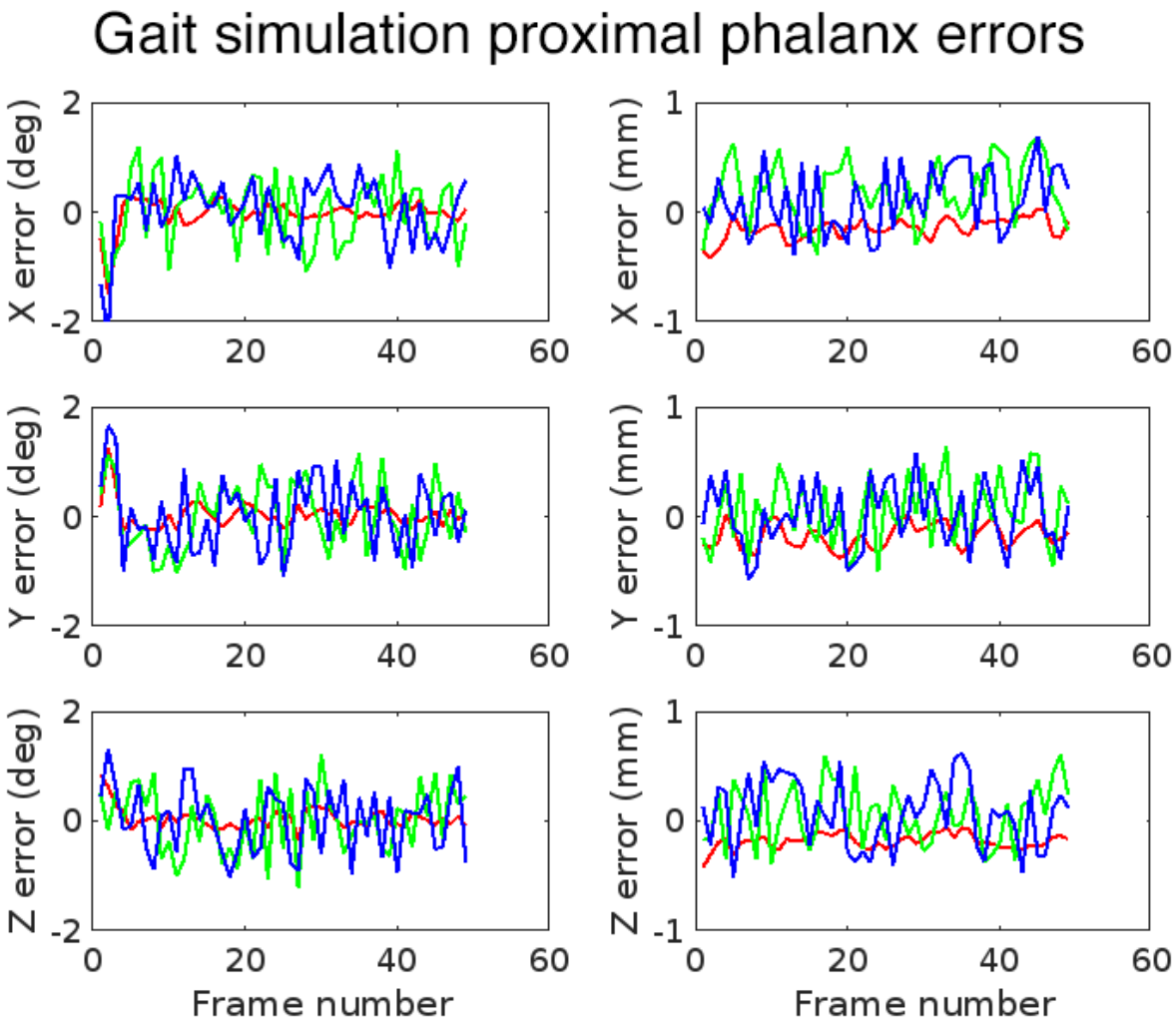

Figure 10: The proximal phalanx model-based tracking errors for the full gait simulation trials. Rotational errors are presented in the left column, translation errors in the right column, and the three components are presented in each row. Each line (red, blue, green) is a separate tracking session of the same experimental trial. The X-axis rotations correspond to the bone's long axis (proximal-distal). Y-axis rotations are about the medial-lateral axis, and Z-axis rotations are about the superior-inferior axis.

References

[1] Balsdon, M. E., Bushey, K. M., Dombroski, C. E., LeBel, M. E., and Jenkyn, T. R., 2016, "Medial Longitudinal Arch Angle Presents Significant Differences Between Foot Types: A Biplane Fluoroscopy Study," J Biomech Eng, 138(10).

[2] Campbell, K. J., Wilson, K. J., LaPrade, R. F., and Clanton, T. O., 2016, "Normative rearfoot motion during barefoot and shod walking using biplane fluoroscopy," Knee Surg Sports Traumatol Arthrosc, 24(4), pp. 1402-1408.

[3] Cross, J. A., McHenry, B., and Schmidt, T. G., 2015, "Quantifying cross-scatter contamination in biplane fluoroscopy motion analysis systems," Jounral of Medical Imaging, 2, p. 043503.

[4] Cross, J. A., McHenry, B. D., Molthen, R., Exten, E., Schmidt, T. G., and Harris, G. F., 2017, "Biplane fluoroscopy for hindfoot motion analysis during gait: A model-based evaluation," Med Eng Phys, 43, pp. 118-123.

[5] Guan, S., Gray, H. A., Keynejad, F., and Pandy, M. G., 2016, "Mobile biplane X-Ray imaging system for measuring 3D dynamic joint motion during overground gait," IEEE Transactions on Medical Imaging, 35, pp. 326-336.

[6] Hoffman, S. E., Peltz, C. D., Haladik, J. A., Divine, G., Nurse, M. A., and Bey, M. J., 2015, "Dynamic in-vivo assessment of navicular drop while running in barefoot, minimalist, and motion control footwear conditions," Gait Posture, 41(3), pp. 825-829.

[7] Iaquinto, J. M., Kindig, M. W., Haynor, D. R., Vu, Q., Pepin, N., Tsai, R., Sangeorzan, B. J., and Ledoux, W. R., 2018, "Model-based tracking of the bones of the foot: A biplane fluoroscopy validation study," Comput Biol Med, 92, pp. 118-127.

[8] Iaquinto, J. M., Tsai, R., Haynor, D. R., Fassbind, M. J., Sangeorzan, B. J., and Ledoux, W. R., 2014, "Marker-based validation of a biplane fluoroscopy system for quantifying foot kinematics," Med Eng Phys, 36(3), pp. 391-396.

[9] Ito, K., Hosoda, K., Shimizu, M., Ikemoto, S., Nagura, T., Seki, H., Kitashiro, M., Imanishi, N., Aiso, S., Jinzaki, M., and Ogihara, N., 2017, "Three-dimensional innate mobility of the human foot bones under axial loading using biplane X-ray fluoroscopy," R Soc Open Sci, 4(10), p. 171086.

[10] Pitcairn, S., Kromka, J., Hogan, M., and Anderst, W., 2020, "Validation and application of dynamic biplane radiography to study in vivo ankle joint kinematics during high-demand activities," J Biomech, 103, p. 109696.

[11] Brainerd, E. L., Baier, D. B., Gatesy, S. M., Hedrick, T. L., Metzger, K. A., Gilbert, S. L., and Crisco, J. J., 2010, "X-ray reconstruction of moving morphology (XROMM): precision, accuracy and applications in comparative biomechanics research," J Exp Zool A Ecol Genet Physiol, 313(5), pp. 262-279.

[12] Tashman, S., and Anderst, W., 2003, "In-vivo measurement of dynamic joint motion using high speed biplane radiography and CT: application to canine ACL deficiency," J Biomech Eng, 125(2), pp. 238-245.

[13] Bey, M. J., Kline, S. K., Tashman, S., and Zauel, R., 2008, "Accuracy of biplane x-ray imaging combined with model-based tracking for measuring in-vivo patellofemoral joint motion," Journal of orthopaedic surgery and research, 3, p. 38.

[14] Lichti, D. D., Sharma, G. B., Kuntze, G., Mund, B., Beveridge, J. E., and Ronsky, J. L., 2015, "Rigorous geometric self-calibrating bundle adjustment for a dual fluoroscopic imaging system," IEEE Transactions on Medical Imaging, 34, pp. 589-598.
[15] Englander, Z. A., Martin, J. T., Ganapathy, P. K., Garrett, W. E., and DeFrate, L. E., 2018, "Automatic registration of MRI-based joint models to high-speed biplanar radiographs for precise quantification of in vivo anterior cruciate ligament deformation during gait," J Biomech, 81, pp. 36-44.
[16] Knorlein, B. J., Baier, D. B., Gatesy, S. M., Laurence-Chasen, J. D., and Brainerd, E. L., 2016, "Validation of XMALab software for marker-based XROMM," J Exp Biol, 219(Pt 23), pp. 3701-3711.
[17] Bradski, G., 2022, "OpenCV: Open Source Computer Vision Library."
[18] Penney, G. P., Weese, J., Little, J. a., Desmedt, P., Hill, D. L., and Hawkes, D. J., 1998, "A comparison of similarity measures for use in 2-D-3-D medical image registration.," IEEE transactions on medical imaging, 17, pp. 586-595.
[19] Powell, M. J. D., 1973, "On search directions for minimization algorithms," Mathematical Programming, 4, pp. 193-201.
[20] Corke, P., 2017, "Robotics, vision and control fundamental algorithms in MATLAB.."
[21] Horn, B. K. P., Hilden, H. M., and Negahdaripour, S., 1988, "Closed-form solution of absolute orientation using orthonormal matrices," J. Opt. Soc. Am. A, 5(7), pp. 1127-1135.

Chapter 7

Feasibility of assessing plantar deformation response using biplane fluoroscopy

Eric Thorhauer[1,2] and William Ledoux, PhD[1,2,3]

[1]RR&D Center for Limb Loss and Mobility (CLiMB), Veterans Affairs Puget Sound Health Care System, Seattle, WA 98108

Departments of [2]Mechanical Engineering and [3]Orthopaedics & Sports Medicine, University of Washington, Seattle, WA 98195

Keywords: Biplane fluoroscopy; heel pad, plantar deformation

Abstract

Characterization of the in vivo deformation of the plantar tissue during gait could aid clinicians in diagnosing pathologies like diabetic foot disease, in the design of offloading orthotics, and for biomechanists performing computational modeling of soft tissues. Biplanar fluoroscopy has matured to accurately track foot and ankle bones during gait. This study assessed the feasibility of estimating plantar tissue deformation using our custom biplane system coupled with a carbon fiber floor panel that permits oblique transverse plane imaging of all the foot bones during gait. A series of experiments were conducted to measure the deflection of the floor panel under physiological loading and assess its suitability in virtually defining the surface boundary conditions. Gravity-driven drop impact tests simulating the initial contact phase of gait were performed with three cadaver specimens. The resting thickness of the plantar tissue was taken from the computed tomography scan acquired for rendering the calcaneus bone models. Panel deformation was below 0.4 mm. Peak plantar deformations averaged 9.55 ± 1.50 mm and agreed well with previous cadaveric testing and in vivo studies. The peak percentage deformation averaged 74.4% of the tissue thickness under the inferior portion of the calcaneal tuberosity. The sampling rates of the biplane system (120 Hz) and plantar pressure measurement systems (25 Hz) were inadequate in characterizing the time-dependent response of the tissues. The tissue deformation results compare well with available in vivo and cadaveric testing data, and the panel deflection results support the continued development of this technique at a higher biplane sampling rate, although a more complex contact model is required to accurately model the true tissue behavior.

Introduction

Understanding the biomechanical behavior of the foot, particularly the plantar tissue's role as a natural shock absorber and load-bearing interface, is crucial in lower extremity biomechanics. This understanding begins with accurately quantifying plantar tissue deformation in vivo during dynamic activities like walking and running. Such quantification is vital for biomechanical insights and has significant clinical implications. It aids in diagnosing foot abnormalities, prescribing corrective measures for atypical foot kinematics, and managing painful regions or diabetic ulcers through effective off-loading strategies. To achieve this, various techniques have been developed, each with its strengths and limitations, including plantar pressure measurement mats, which capture reaction forces across a grid of small sensors of known areas, resolving the reaction pressures but not any kinematics. Ultrasound, which can delineate tissue boundaries and assess material properties, suffers from noise, acoustic impedance issues, and a limited sampling volume [198]. Magnetic resonance imaging (MRI) can generate full three-dimensional (3D) volumes of the anatomy at high resolution under controlled quasi-static loading within its limited capture volume, and scan parameters may be configured to map the signal returned by the tissue to its local structural properties [199, 200]. Biplanar fluoroscopy, traditionally used for skeletal motion reconstruction, is now being adapted to analyze soft tissue behavior [100, 107, 108]. By making simplifications and using the rigid bone geometry as a reference, the kinematics from biplane bone tracking define boundary conditions at the osseous interface, allowing the deformation of the tissue to be inferred. Impact testing of the plantar tissues has been performed in vivo on subjects to discern differences in heel pad stiffnesses [201], however these tests could be painful for some subjects and only serve as

approximations to gait loading conditions. Therefore, ideally, these subject-specific structural properties should be inferred from functional ambulatory tasks.

Specific to the foot and ankle, this fluoroscopy-based method has been applied to the problem of assessing plantar tissue deformation in vivo [100, 202, 203]. De Clercq et al. estimated plantar deformation by measuring the vertical displacement of the inferior aspect of the calcaneus bone during running using a single X-ray view recorded at 150 Hz. Researchers have recently used biplanar fluoroscopy systems to characterize the plantar tissue response to loading history in repeated walking trials [100, 204]. These studies all utilized a sagittal imaging view to try and visualize and measure the gap between the calcaneus and the walking surface. That particular double sagittal-view biplane system configuration is limiting in that it only permits reliable quantification of ankle motion due to overlap between all the other bones distal to the hindfoot. To address the overlap issue, our laboratory has specifically developed a system configurable to view both feet from oblique views, yielding optimal separation of the bones on the images for tracking and reconstructing skeletal motion. A key component of this system is the custom removable carbon fiber walkway panel that allows for X-ray imaging through the floor plane and visualization of all the foot bones. Subjects traverse this panel, which is instrumented with force sensors, during walking trials. The primary aims of this work were to assess the feasibility of inferring plantar deformation using our biplanar fluoroscopy system, quantify the deformation of the carbon panel under load to see how simple a floor boundary condition might be assumed in the contact model, and investigate a rudimentary plantar tissue ground contact estimation using bone tracking from the biplane system combined with 3D models of the heel tissue from computed tomography (CT) and the boundary condition assumption.

Methods

Three human cadaver specimens, including the tibia and foot (males aged 59,65, and 73 and weighing 63, 89, and 70 kg, respectively), were carefully dissected to expose the tibial shaft and primary extrinsic tendons. Tibias were potted in resin cylinders to facilitate mounting in a custom biomechanical testing rig (Figure 1). Three 3 mm stainless steel marker beads were rigidly inserted into the calcanei through medial skin portals. A testing rig was constructed around the capture volume of a biplanar fluoroscopy system configured for imaging dynamic in vivo gait in oblique transverse planes. The rig consisted of an aluminum frame rigidly connected to the ground, built in a manner that would not block or otherwise interfere with the X-ray imaging. A vertically mounted shaft with axially applied weight was free to slide relative to linear bearings towards the floor panel upon triggered release. The rig performed gravity-driven foot drop trials, with nominal loads applied to the dorsiflexor tendons with springs to induce as much ankle dorsiflexion as possible, simulating foot posture just before the initial contact phase of gait while allowing for plantarflexion during the loading response. A static load equal to 40% of the donor bodyweight was applied through the top of the axial shaft to simulate loads during in vivo gait. The rig frame permitted the positioning of the specimens to strike the floor plate at the location living subjects would contact during walking trials. Specimen tissues were preconditioned by performing three drop trials immediately before each recorded (fourth) trial, with typically 30-45 seconds between preconditioning drops. All trials were collected in the same test session (day) after only one tissue freeze-thaw cycle from specimen reception.

The biplane fluoroscopy system fires discrete X-ray pulses at 120Hz while high-resolution videos of the image intensifier outputs are recorded. The biplane calibration procedure involves imaging a T-shaped wand object with fiducial markers laid in the plane of the walkway.

The plane of the walkway is defined virtually using the a priori offset between the wand object's markers and the floor surface. To assess its rigidity under load, an array of 3 mm diameter X-ray markers was taped to the top and bottom faces of the floor panel (Figure 2), and trials were acquired. Panel marker kinematics between subsequent loading trials, determined using custom software (URSA, Utility for Roentgen Stereophotogrammetric Analysis), were used to determine the panel rigidity. In URSA, the temporal mean of each fluoroscopy sequence of the static marker array was calculated pixel-wise to reduce noise due to fluctuations in the detected and transformed X-ray signal. Kinetic responses to the drop trials were recorded by a custom Kistler force plate (2000 Hz) and a pliance® (novel, Munich, Germany) plantar pressure mat (0.54cm^2 sensor areas, 25 Hz). The force plate integrated into the carbon fiber panel could be synchronized with the biplanar fluoroscopy system, but the plantar pressure system clock could not. The biplane system is capable of imaging faster than 120 Hz. However, this is the highest speed for pulsed exposures, which is the de facto acquisition type used for in vivo studies in order to drastically reduce radiation dose.

Computed tomography scans (LineUp, Curvebeam, 0.3 mm isotropic voxel size) were acquired for each specimen. Calcanei and plantar tissue were segmented using Mimics software (Materialise, Belgium) and rendered as triangular element surface mesh models. The markers embedded into the calcanei were localized with respect to the bone volumes using an iterative intensity-weighted sphere fitting routine implemented in MATLAB. Marker-based tracking of the calcaneal markers in the biplanar fluoroscopy trials was performed using URSA. Raw marker trajectories were filtered using a zero-lag 4th-order Butterworth filter with a 20 Hz cutoff frequency. The marker positions localized from the CT scan were registered to the filtered markers trajectories in a least-squares sense and converted into the homogeneous transformation

matrix representation using Horn's method of absolute orientations [205]. These transformations representing calcaneal motion with respect to the lab were applied to the soft tissue model for each frame of fluoroscopy data, rigidly moving the plantar tissue surface with the displacement of the calcaneus.

A simple algorithm to approximate the plantar deformation using the CT bone and tissue models and bone kinematic data was implemented in MATLAB (Figure 3). For each frame of fluoroscopy data, the surface of the plantar tissue model in the current pose set by calcaneal bone tracking was compared to the virtual floor plane, defined from the T-wand calibration object. Points on the plantar surface in the plane or below the plane were considered part of the deformed region (Figure 4). The area of this intersection was considered as the contact area of the plantar tissue to the walking surface. The mean plantar pressure was predicted as the vertical ground reaction force divided by the predicted contact area. The vertical distance of any deformed points to the floor plane was considered the deformation amount, $\mathbf{t}_{\text{deformed}}$. The maximum and average amount of plantar deformation was calculated for each trial. In the region directly under the calcaneal tuberosity (Figure 3, boxed region), the percentage deformation, relative to the resting tissue thickness during CT scanning, was defined as the deformed thickness amount ($\mathbf{t}_{\text{deformed}}$) divided by the total thickness of the deformed region and the soft immediately above the floor plane that anchors into the inferior surface of the calcaneus, $\mathbf{t}_{\text{above plane}}$. Force plate vertical reaction force data were interpolated to the fluoroscopy frame rate, and force vs peak deformation curves were generated.

Results

The X-ray marker tracking of both the calcaneus and panel using URSA was successfully and precisely achieved. For the panel deformation test, the vertical displacement of the markers toward the ground as the loading of the panel increased was observed (Figure 5). Across all markers and loading magnitudes, vertical displacements averaged -0.165 ± 0.08 mm while maximum deflection magnitude was less than 0.4 mm (Figure 5).

During the specimen drop trials, the rig had an issue during one of the tests, leaving 8 trials of valid data. In the remaining trials, all specimens tended to bounce after initial contact due to the elastic properties of the system. As a result, all specimen trials contact phases were limited to the first five fluoroscopy frames characterizing this initial response. Peak deformation curves were repeatable within specimens (Figure 6). The maximum deformations occurred in the first 30 ms, and the final timepoint exhibited unloading relative to the peak in all trials except one (Figure 6). Non-linear force versus deformation relationships were observed for all specimens (Figure 7), however a limited number of samples were available to characterize these responses. The mean and peak deformations averaged 3.84 ± 1.78 mm and 9.55 ± 1.50 mm across all time points in all specimen trials (Table 1). The percentage of heel deformation peaked at nearly 75% at 25 ms after initial contact. By the fifth frame of fluoroscopy data, the rebound of the tissue is evident by the decreased mean deformations and contact areas (Table 1). The predicted mean and peak deformations across all specimens and trials were less variable than the predicted contact areas (Table 1). In comparison to the plantar pressure recording mat, the predicted pressures did not match the measured values well (Figure 8). In half of the trials, the predicted contact areas agreed well with the measured values (Figure 8).

Discussion

The deformation of the panel was sub-millimeter and only slightly greater than the tracking precision of URSA. Some of the marker coordinate shifts across loading conditions, assumed to be true motion, were corrupted with noise in the imaging process with this hardware setup. The temporal mean of the fluoroscopy sequences was taken to reduce the effects of this noise in the localization. However other residual artifacts from the distortion correction process and camera calibration procedure may introduce small errors in the apparent marker location. The panel deformation magnitude under physiological loading was small (mean less than 0.165 and peak less than 0.4 mm). The peak panel deformation was about 10% of the mean and 4% of the peak plantar tissue deformation amounts. This suggests that peak plantar deformations might be a more reliable biomechanical measure from biplane processing, given all the errors inherent in the calibration, segmentation, and tracking steps. Confidently detecting subtle differences in deformation between individual trials within a given subject or between similar clinical cohorts may prove difficult until these noise sources are mitigated.

The peak deformations observed in this study agree well with previous reports of in vivo deformations during standing, gait, and running. Prichasuk reported heel pad compressibility of 53 ± 9% in 400 healthy subjects performing loaded and unloaded standing radiograph trials [206]. De Clercq reported an average maximum deformation of 9.0 ± 0.5 mm in barefoot running of two subjects, which agrees very well with our results. In the first 50 ms of contact of barefoot running, De Clercq reported 60.5 ± 5.5% maximum deformation of the heel pad, which also matches our results for the first 30 ms following drop impact. De Clercq's two subjects' time to maximum deformation were 27.9 ± 3.0 and 25.8 ± 2.8 ms across eight running trials. The vertical reaction forces of these subjects were about 1.3 kN and 2.1 kN, respectively. These data agree with our peak deformation vs time curves (Figure 6) and vertical ground reaction force vs

percentage deformation curves (Figure 7). Our force-deformation curves for barefoot cadavers match the trends reported by De Clercq for shod running, although the higher sampling rate of their study (150 Hz) vs the current study (120 Hz) effectively yielded one or two additional frames in the initial 50 ms of tissue response comparatively. Using biplanar fluoroscopy sampled at 50 Hz during in vivo trials of walking steps to simulate full gait, Yang estimated peak strains of plantar tissue ranging from 41.09 to 71.85% in non-diabetic subjects and 40.64 to 92.92 % in diabetic subjects and Teng reported peak strains ranging from 67 to 73 % in ten healthy individuals. Both Yang and Tang reported in vivo peak strains that agree well with our peak percentage heel deformations (Table 1). We deliberately do not call these values ‘strains’ in this study because the true unloaded configuration is not known, and this is a simplified 1D model of the complex 3D behavior of the multiple types of tissues comprising the heel pad.

The contact area estimates from our model were inaccurate in half of the trials and errors relative to the true area due to the differences between the dorsiflexed positions of the specimens during drop testing and the more plantarflexed positions during the CT scans, which acted as reference configurations for the soft tissue models. Differences in tension in the plantar tissue between these configurations would affect their apparent thicknesses, and the motion of the intrinsic muscles would also deform the exterior boundaries of the foot. Contact area estimates could be improved by shifting towards a finite element model or suitable alternative.

Limitations of this work include the simplified biomechanical cadaveric foot contact model, which was a pure vertical drop without any of the shear motion or tibial shaft rotation that naturally occur in gait. Only three specimens were tested, and all were males heavily skewed towards higher ages. To provide further insight, the panel deformation experiment could have included an additional series of acquisitions performed by removing the applied incremental

static weights in the reverse order to see if the markers returned to the previously displaced positions or if marker localization noise dominated the apparent shifts in marker positions. Continuous fluoroscopy mode, which decouples the synchronized firing of X-rays with the video frame recording allows for higher frame rate imaging of more than 900Hz, would drastically reduce temporal aliasing of the contact model. However, this would be at the cost of noisier fluoroscopy images that impair tracking and substantially larger radiation doses received by test participants. Technical issues such as data dropouts and a slow, unsynchronized acquisition process prevented the plantar pressure mat data from being used to any great effect besides serving as an established and accurate reference for comparing contact area estimates. The low temporal resolution of the plantar pressure data is due to a maximum readout speed of 20,000 sensor elements per second. Increased frame rates could be achieved by binning together adjacent sensor elements at a cost to spatial resolution. However, the plantar tissue mat sampling interval was not the only limiting factor, as the biplane data (pulsed at 120 Hz) were also apparently not sampled at the appropriate rate to resolve the force-displacement relationships of the tissue effectively and confidently. The velocities of the specimens during the drop trials approximated running speeds more than gait, but the pulsed biplane sampling rate may be adequate for walking or require the collection of quasi-static stepping trials [100, 204].

Future efforts will include repeating the drop experiments using the biplanar fluoroscopy system in continuous exposure mode, which will require optimization of the imaging parameters and the development of image processing algorithms to contend with the increased noise levels of that mode while simultaneously attempting to minimize the radiation received by subjects with appropriate X-ray source settings. While this study's peak deformation values agree well with other studies investigating the same limited region under the inferior posterior calcaneal

tuberosity, this region represents only a small fraction of the entire plantar foot surface that is of interest to researchers. To be a more useful tool to clinicians and engineers alike, a complete biomechanical modeling approach that accurately characterizes the full heel pad deformation response is needed [207, 208]. This approach could range from complex finite element models, which require subject-specific meshes from volumetric imaging like CT or morphed from a statistical database of meshes, or discrete element or peridynamic models, which have the potential to investigate the complexities of floor-plantar tissue contact patterns at reduced computational burden. As the process of segmenting bones and tracking them in biplanar fluoroscopy sequences is automated, simple analyses of joint angles will become as routine as generating motion capture-based data in the present day. The efforts of researchers will turn towards extending the information gleaned from the precise skeletal kinematic data generated by biplane systems into developing subject-specific biomechanical models to better understand our bodies' responses to interactions with our world and track longitudinal changes over time and in response to treatments.

Acknowledgement

I would like to thank Nicholas Entress and Aerie Grantham for their assistance in operating the biplane system while collecting the experimental trials, and Corey Wukelic and Takumi Kihara for assisting with specimen dissection and preparation.

Figures and Tables

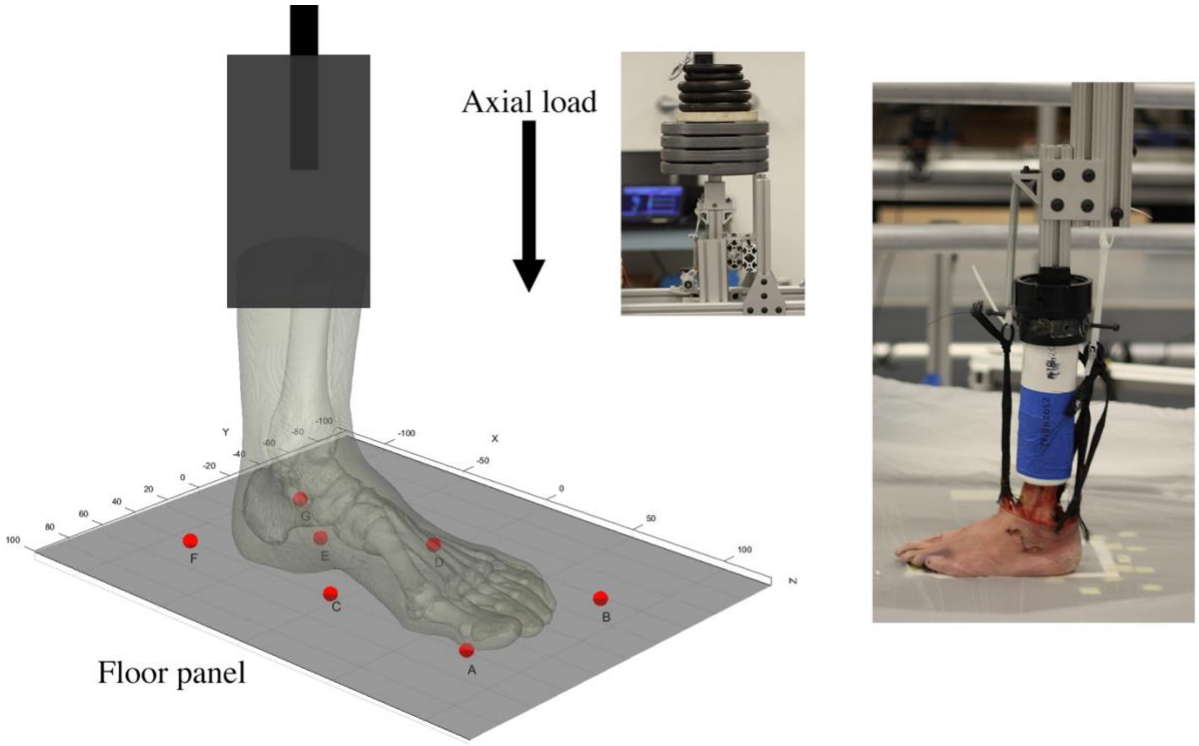

Figure 1: An overview of the testing rig setup for applying axial loads through the tibial shafts of specimens in addition to gravity-driven drop trials. The feet were positioned to load the center of the carbon fiber walkway panel of the biplanar fluoroscopy system. Nominal loads were applied to the primary foot tendons to prevent drop of the toes during trials. An array of X-ray markers was taped to the floor panel to quantify the deformation of the panel under loading. A to G represent a representative distribution of markers.

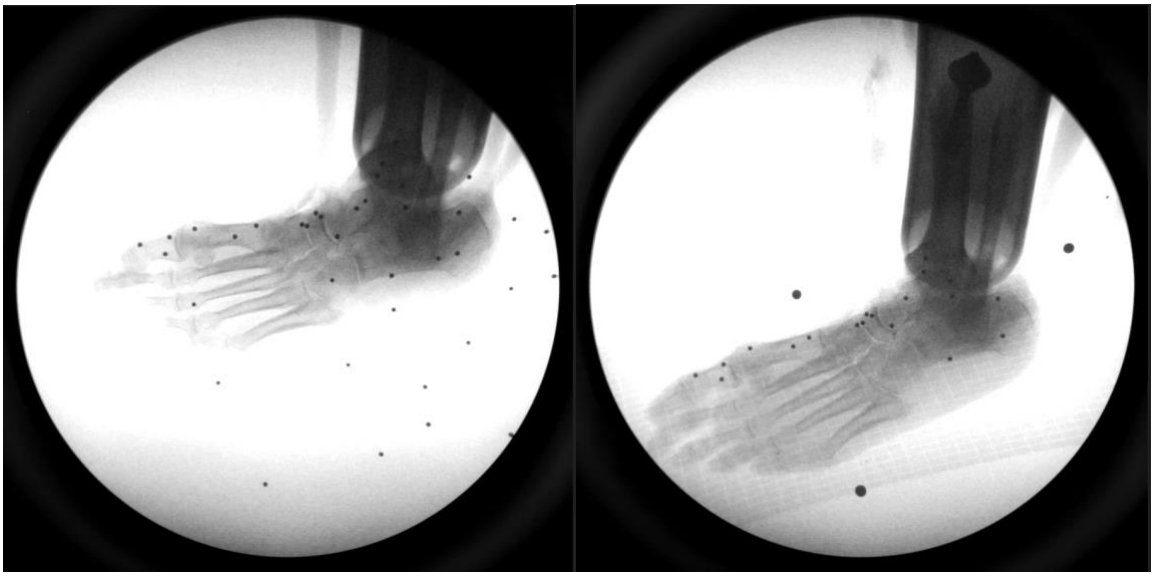

Figure 2: Fluoroscopy view of the marker array used in the panel deformation test (left) and of a foot specimen instrumented with bone markers (right) on top of a pliance plantar pressure measurement mat. The plantar pressure mat is minimally attenuating of the X-rays and does not introduce artifacts that interfere with tracking accuracy. The X-ray markers quantify the local deflection of the panel surface under the loading of the specimen and are used to track the pose of the calcaneus.

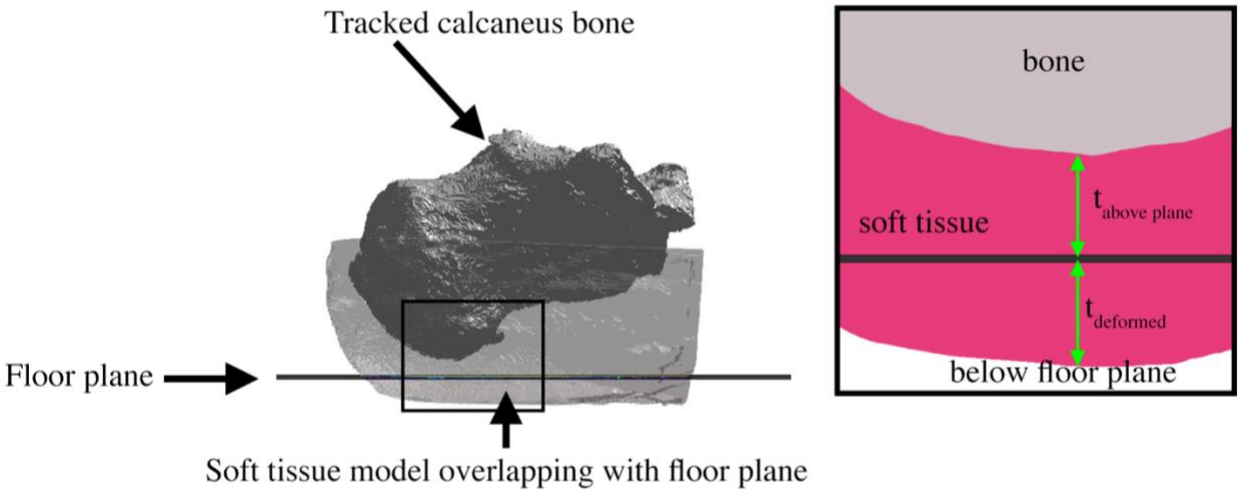

Figure 3: The simple plantar tissue contact and deformation model using tracked biplane bone trajectories and geometries derived from computed tomography combined with the floor plane boundary condition. For each frame of tracked calcaneal data, the same rigid transformation is applied to the heel tissue model, which is checked against the floor plane for intersection. Regions of the heel at or under the floor plane coordinate are defined as part of the deformed domain. The distance from the inferior surfaces of the rigid heel model to the walkway plane defines the thickness of the deformation, $\mathbf{t}_{\text{deformed}}$. The percentage deformation was defined as the ratio of $\mathbf{t}_{\text{deformed}}$ to the total thickness of $\mathbf{t}_{\text{deformed}}$ plus $\mathbf{t}_{\text{above plane,}}$ the thickness above the floor to the bone surface.

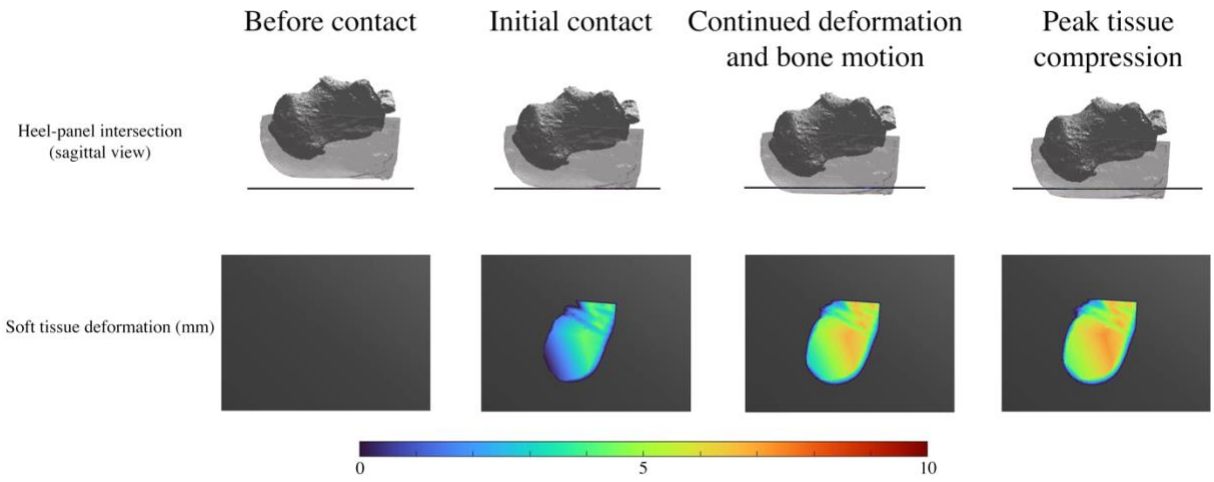

Figure 4: The motion of the calcaneus and heel pad relative to the floor panel, viewed in the sagittal plane (top) and the estimation of soft tissue deformations based on the rigid heel model's intersection with the assumed to be rigid floor plane.

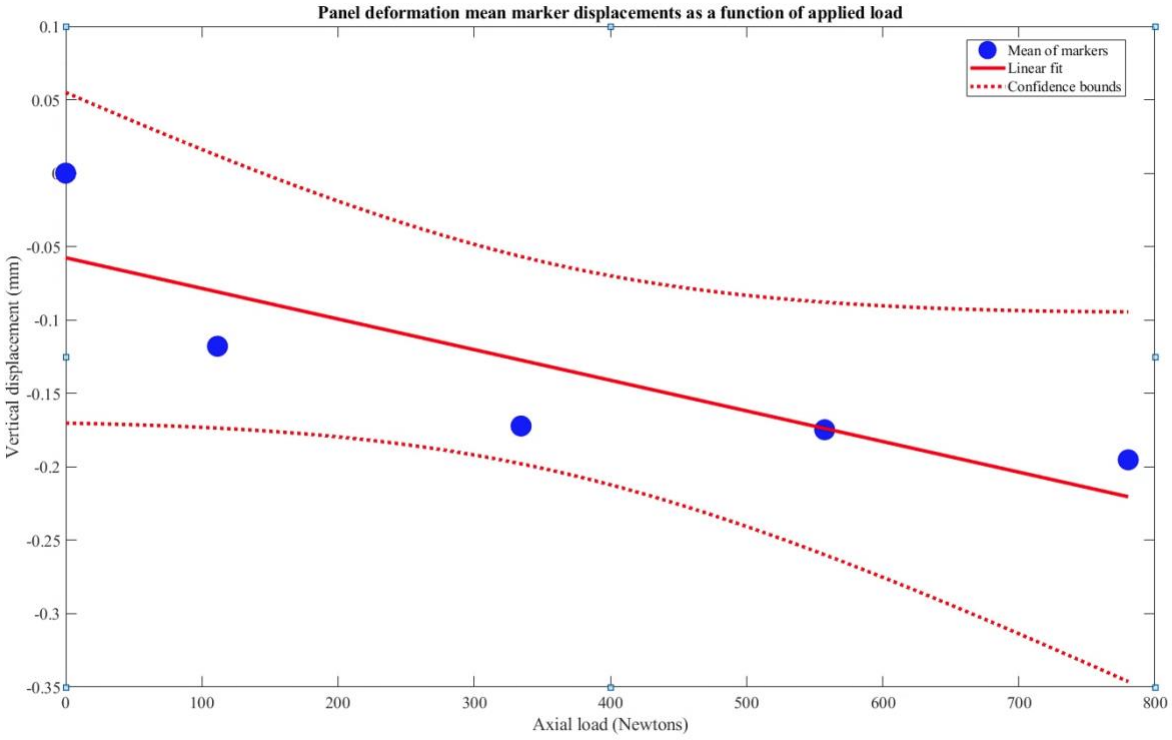

Figure 5: The mean vertical displacement of the panel rigidity test markers as a function of the applied loading. The displacement vs load magnitude trend was linear, and the maximum displacement was less than 0.4 mm.

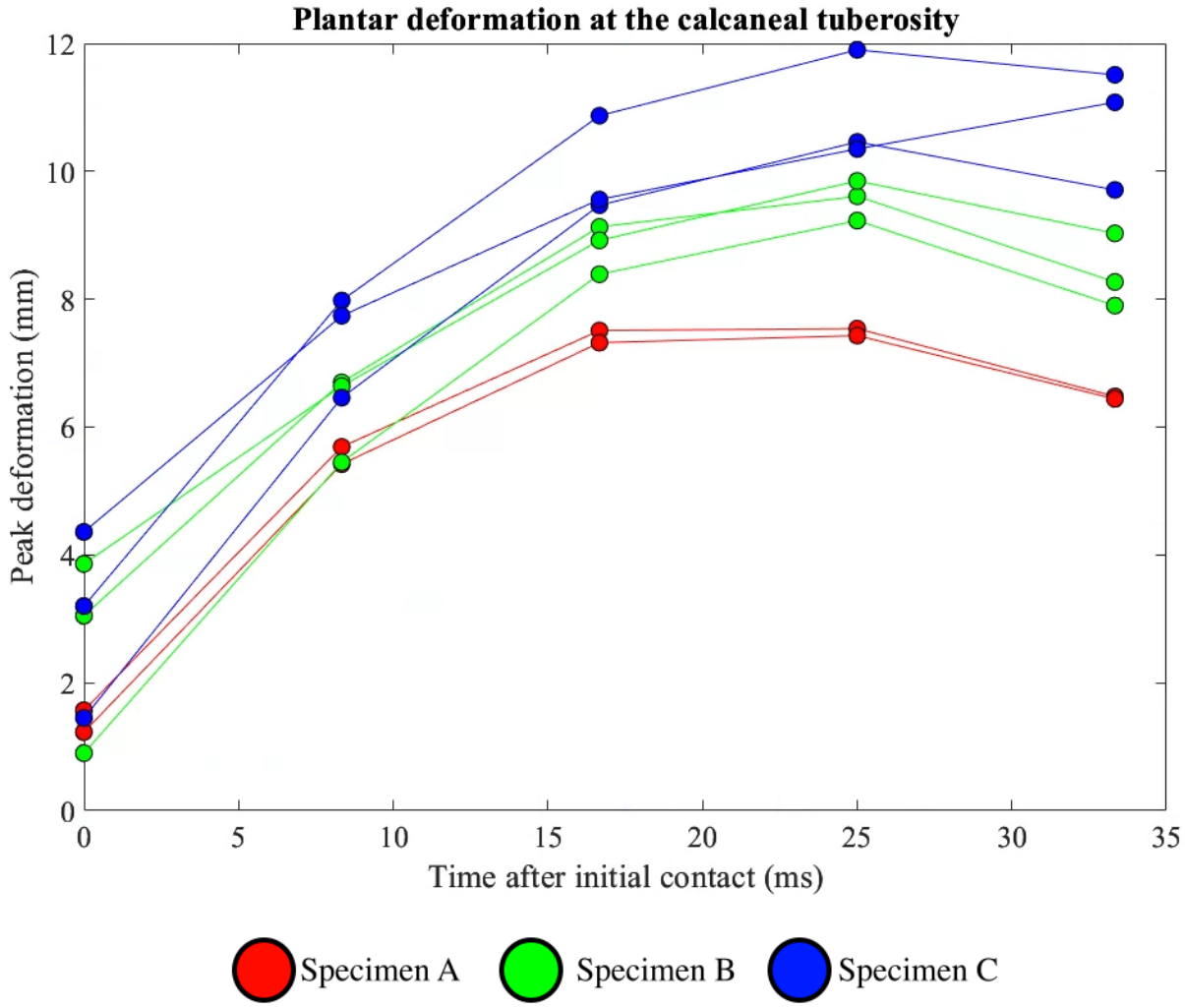

Figure 6: Peak deformation (mm) of the heel pad under the calcaneal tuberosity for the duration of the initial response phase of ground contact during impact drop testing. Deformation curves were consistent within specimens. Peak deformations occurred in under 30 ms.

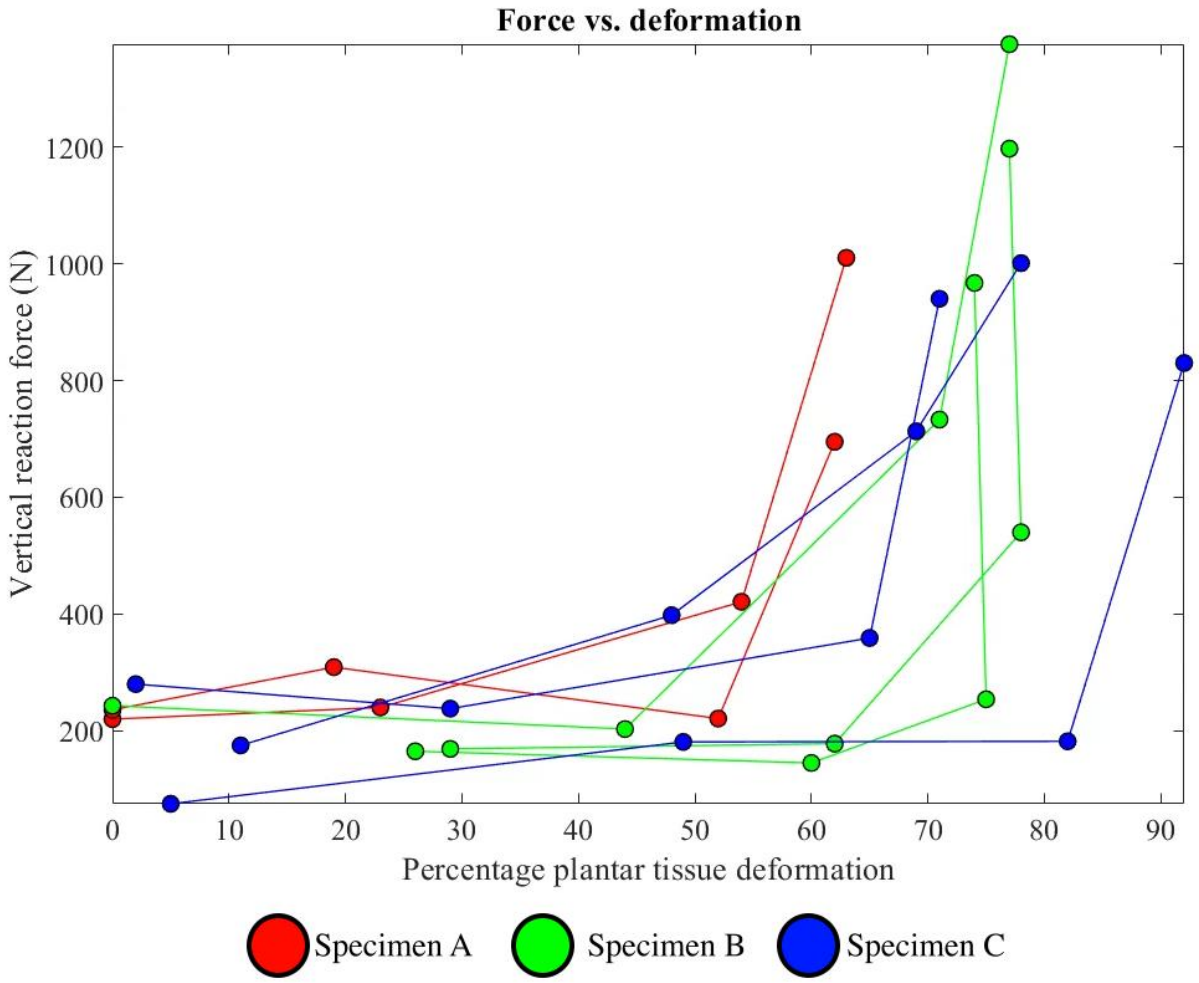

Figure 7: The force-percentage deformation curves of each drop trial. Vertical reaction force was recorded by force plate (2000 Hz) and resampled to match the bone tracking rate of 120 Hz. Five frames of data at 120 Hz captured all of the initial contact response, but as evident in the curves this sampling rate was inadequate for determining the heel pad stiffness.

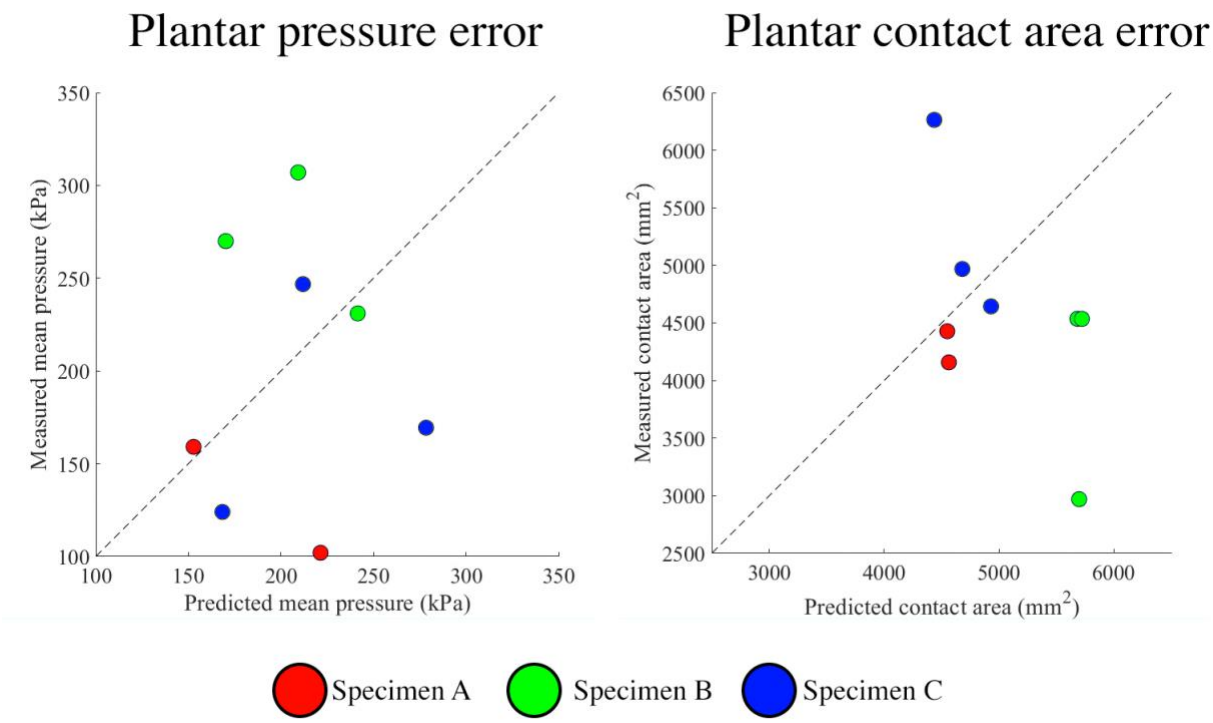

Figure 8: The plantar pressures (left) and contact areas (right) as measured via the plantar pressure recording mat plotted versus the predicted values from biplane tracking.

Table 1: Heel pad contact results for three specimens estimated with the simple model-plane intersection algorithm.

Time after contact (ms)	**Mean deformation (mm)**		**Peak deformation (mm)**		**Contact area (mm^2)**		**Percentage heel deformation (%)**	
	mean	stdev	mean	stdev	mean	stdev	mean	stdev
0.00	0.95	0.72	2.45	1.32	1742	1630	9.1	11.9
8.33	3.40	0.77	6.51	0.98	4005	1163	41.8	16.4
16.66	4.85	0.79	8.90	1.16	4854	684	68.2	10.6
25.00	5.25	0.71	9.55	1.50	5032	571	74.4	9.5
33.33	4.74	0.60	8.80	1.91	4877	612	64.8	12.2

References

[1] W. Schallig *et al.*, "The influence of soft tissue artifacts on multi-segment foot kinematics," (in eng), *J Biomech,* vol. 120, p. 110359, May 7 2021, doi: 10.1016/j.jbiomech.2021.110359.

[2] R. Shultz, A. E. Kedgley, and T. R. Jenkyn, "Quantifying skin motion artifact error of the hindfoot and forefoot marker clusters with the optical tracking of a multi-segment foot model using single-plane fluoroscopy," (in eng), *Gait Posture,* vol. 34, no. 1, pp. 44-8, May 2011, doi: 10.1016/j.gaitpost.2011.03.008.

[3] P. National Council on Radiation and B. M. D. Measurements, "Implementation of the principle of as low as reasonably achievable (ALARA) for medical and dental personnel," United States, 0-929600-15-0, 1990. [Online]. Available: http://inis.iaea.org/search/search.aspx?orig_q=RN:22043412

[4] M. Doss, "Are We Approaching the End of the Linear No-Threshold Era?," (in eng), *J Nucl Med,* vol. 59, no. 12, pp. 1786-1793, Dec 2018, doi: 10.2967/jnumed.118.217182.

[5] P. A. Oakley and D. E. Harrison, "Death of the ALARA Radiation Protection Principle as Used in the Medical Sector," (in eng), *Dose Response,* vol. 18, no. 2, p. 1559325820921641, Apr-Jun 2020, doi: 10.1177/1559325820921641.

[6] E. E. C. T. S. D. J. E. M. R. C. C. E. E. Christensen, *Christensen's physics of diagnostic radiology*. Philadelphia, Pa.; London: Lea & Febiger (in English), 1990.

[7] J. S. Krohmer, "Radiography and fluoroscopy, 1920 to the present," *RadioGraphics,* vol. 9, no. 6, pp. 1129-1153, 1989, doi: 10.1148/radiographics.9.6.2685938.

[8] J. Karrholm, L. I. Hansson, and G. Selvik, "Mobility of the lateral malleolus. A roentgen stereophotogrammetric analysis," *Acta Orthop Scand,* vol. 56, no. 6, pp. 479-83, Dec 1985. [Online]. Available: https://www.ncbi.nlm.nih.gov/pubmed/4090949.

[9] G. Selvik, "Roentgen stereophotogrammetric analysis," *Acta Radiol,* vol. 31, no. 2, pp. 113-26, Mar 1990. [Online]. Available: https://www.ncbi.nlm.nih.gov/pubmed/2196921.

[10] B. Sturesson, G. Selvik, and A. Uden, "Movements of the sacroiliac joints. A roentgen stereophotogrammetric analysis," *Spine (Phila Pa 1976),* vol. 14, no. 2, pp. 162-5, Feb 1989. [Online]. Available: https://www.ncbi.nlm.nih.gov/pubmed/2922636.

[11] B. M. You, P. Siy, W. Anderst, and S. Tashman, "In vivo measurement of 3-D skeletal kinematics from sequences of biplane radiographs: application to knee kinematics," *IEEE Trans Med Imaging,* vol. 20, no. 6, pp. 514-25, Jun 2001. [Online]. Available: http://www.ncbi.nlm.nih.gov/entrez/query.fcgi?cmd=Retrieve&db=PubMed&dopt=Citation&list_uids=11437111

[12] S. Tashman and W. Anderst, "In-vivo measurement of dynamic joint motion using high speed biplane radiography and CT: application to canine ACL deficiency," (in eng), *J Biomech Eng,* vol. 125, no. 2, pp. 238-45, Apr 2003, doi: 10.1115/1.1559896.

[13] S. Tashman, W. Anderst, P. Kolowich, S. Havstad, and S. Arnoczky, "Kinematics of the ACL-deficient canine knee during gait: serial changes over two years," *J Orthop Res,* vol. 22, no. 5, pp. 931-41, Sep 2004, doi: 10.1016/j.orthres.2004.01.008.

[14] S. C. Jones *et al.*, "Accuracy of noninvasive, single-plane fluoroscopic analysis for measurement of three-dimensional femorotibial joint poses in dogs treated by tibial

plateau leveling osteotomy," *Am J Vet Res,* vol. 75, no. 5, pp. 486-93, May 2014, doi: 10.2460/ajvr.75.5.486.

[15] M. J. Bey, R. Zauel, S. K. Brock, and S. Tashman, "Validation of a new model-based tracking technique for measuring three-dimensional, in vivo glenohumeral joint kinematics," (in eng), *J Biomech Eng,* vol. 128, no. 4, pp. 604-9, Aug 2006, doi: 10.1115/1.2206199.

[16] A. L. Kapron *et al.*, "Accuracy and feasibility of dual fluoroscopy and model-based tracking to quantify in vivo hip kinematics during clinical exams," *J Appl Biomech,* vol. 30, no. 3, pp. 461-70, Jun 2014, doi: 10.1123/jab.2013-0112.

[17] R. J. de Asla, L. Wan, H. E. Rubash, and G. Li, "Six DOF in vivo kinematics of the ankle joint complex: Application of a combined dual-orthogonal fluoroscopic and magnetic resonance imaging technique," *J Orthop Res,* vol. 24, no. 5, pp. 1019-27, May 2006. [Online]. Available: http://www.ncbi.nlm.nih.gov/entrez/query.fcgi?cmd=Retrieve&db=PubMed&dopt=Citation&list_uids=16609963

[18] A. M. Caputo *et al.*, "In vivo kinematics of the tibiotalar joint after lateral ankle instability," (in eng), *Am J Sports Med,* vol. 37, no. 11, pp. 2241-8, Nov 2009, doi: 0363546509337578 [pii]
10.1177/0363546509337578.

[19] K. J. Campbell, K. J. Wilson, R. F. LaPrade, and T. O. Clanton, "Normative rearfoot motion during barefoot and shod walking using biplane fluoroscopy," (in eng), *Knee Surg Sports Traumatol Arthrosc,* vol. 24, no. 4, pp. 1402-8, Apr 2016, doi: 10.1007/s00167-014-3084-4.

[20] J. M. Iaquinto, R. Tsai, D. R. Haynor, M. J. Fassbind, B. J. Sangeorzan, and W. R. Ledoux, "Marker-based validation of a biplane fluoroscopy system for quantifying foot kinematics," *Med Eng Phys,* vol. 36, no. 3, pp. 391-6, Mar 2014, doi: 10.1016/j.medengphy.2013.08.013.

[21] B. D. McHenry, E. L. Exten, J. Long, B. Law, R. M. Marks, and G. Harris, "Sagittal subtalar and talocrural joint assessment with weight-bearing fluoroscopy during barefoot ambulation," *Foot Ankle Int,* vol. 36, no. 4, pp. 430-5, Apr 2015, doi: 10.1177/1071100714559540.

[22] C. D. Peltz *et al.*, "Effects of footwear on three-dimensional tibiotalar and subtalar joint motion during running," *J Biomech,* vol. 47, no. 11, pp. 2647-53, Aug 22 2014, doi: 10.1016/j.jbiomech.2014.05.016.

[23] B. Wang *et al.*, "Accuracy and feasibility of high-speed dual fluoroscopy and model-based tracking to measure in vivo ankle arthrokinematics," *Gait Posture,* vol. 41, no. 4, pp. 888-93, May 2015, doi: 10.1016/j.gaitpost.2015.03.008.

[24] S. Koo, K. M. Lee, and Y. J. Cha, "Plantar-flexion of the ankle joint complex in terminal stance is initiated by subtalar plantar-flexion: A bi-planar fluoroscopy study," *Gait Posture,* vol. 42, no. 4, pp. 424-9, Oct 2015, doi: 10.1016/j.gaitpost.2015.07.009.

[25] E. L. Brainerd. "Biplane X-ray Video Systems for Biomechanics Research Worldwide." https://docs.google.com/spreadsheets/d/1EMvk8u_RpaP-udz7rVyMhM0Sh4iunvxxxhyXCGIe6aY/htmlview#gid=0 (accessed.

[26] B. A. MacWilliams, M. Cowley, and D. E. Nicholson, "Foot kinematics and kinetics during adolescent gait," *Gait Posture,* vol. 17, no. 3, pp. 214-24., 2003.

[27] A. Leardini, M. G. Benedetti, L. Berti, D. Bettinelli, R. Nativo, and S. Giannini, "Rear-foot, mid-foot and fore-foot motion during the stance phase of gait," (in eng), *Gait & posture,* vol. 25, no. 3, pp. 453-62, Mar 2007, doi: 10.1016/j.gaitpost.2006.05.017.
[28] A. Lundberg, I. Goldie, B. Kalin, and G. Selvik, "Kinematics of the ankle/foot complex: Plantarflexion and dorsiflexion," *Foot and Ankle,* vol. 9, no. 4, pp. 194-200, 1989.
[29] A. Lundberg, O. K. Svensson, C. Bylund, I. Goldie, and G. Selvik, "Kinematics of the ankle/foot-Part 2: Pronation and supination," *Foot and Ankle,* vol. 9, no. 5, pp. 248-253, 1989.
[30] A. Lundberg, O. K. Svensson, C. Bylund, and G. Selvik, "Kinematics of the ankle/foot complex-Part 3: Influence of leg rotation," *Foot and Ankle,* vol. 9, no. 6, pp. 304-309, 1989.
[31] E. J. van Langelaan, "A kinematic analysis of the tarsal joints, an X-ray photogrammetric study," *Acta Orthopaedica Scandinavica Supplement,* vol. 204, pp. 1-269, 1983.
[32] J. K. Udupa, B. E. Hirsch, H. J. Hillstrom, G. R. Bauer, and J. B. Kneeland, "Analysis of in vivo 3-D internal kinematics of the joints of the foot," *IEEE Trans Biomed Eng,* vol. 45, no. 11, pp. 1387-96, 1998.
[33] E. Stindel, J. K. Udupa, B. E. Hirsch, and D. Odhner, "A characterization of the geometric architecture of the peritalar joint complex via MRI: an aid to the classification of foot type," *IEEE Trans Med Imaging,* vol. 18, no. 9, pp. 753-63., 1999.
[34] S. Siegler *et al.*, "Mechanics of the ankle and subtalar joints revealed through a 3D quasi-static stress MRI technique," *J Biomech,* vol. 38, no. 3, pp. 567-78, Mar 2005. [Online]. Available: http://www.ncbi.nlm.nih.gov/entrez/query.fcgi?cmd=Retrieve&db=PubMed&dopt=Citation&list_uids=15652556
[35] M. J. Fassbind *et al.*, "Evaluating foot kinematics using magnetic resonance imaging: from maximum plantar flexion, inversion, and internal rotation to maximum dorsiflexion, eversion, and external rotation," (in eng), *J Biomech Eng,* vol. 133, no. 10, p. 104502, Oct 2011, doi: 10.1115/1.4005177.
[36] A. Arndt *et al.*, "Intrinsic foot kinematics measured in vivo during the stance phase of slow running," (in eng), *J Biomech,* vol. 40, no. 12, pp. 2672-8, 2007, doi: S0021-9290(07)00006-1 [pii]
10.1016/j.jbiomech.2006.12.009.
[37] C. Nester *et al.*, "Foot kinematics during walking measured using bone and surface mounted markers," (in eng), *J Biomech,* vol. 40, no. 15, pp. 3412-23, 2007, doi: S0021-9290(07)00237-0 [pii]
10.1016/j.jbiomech.2007.05.019.
[38] P. Lundgren *et al.*, "Invasive in vivo measurement of rear-, mid- and forefoot motion during walking," (in eng), *Gait Posture,* vol. 28, no. 1, pp. 93-100, Jul 2008, doi: S0966-6362(07)00264-0 [pii]
10.1016/j.gaitpost.2007.10.009.
[39] C. Maiwald, A. Arndt, C. Nester, R. Jones, A. Lundberg, and P. Wolf, "The effect of intracortical bone pin application on kinetics and tibiocalcaneal kinematics of walking gait," *Gait Posture,* vol. 52, pp. 129-134, Feb 2017, doi: 10.1016/j.gaitpost.2016.10.023.
[40] D. De Clercq, P. Aerts, and M. Kunnen, "The mechanical characteristics of the human heel pad during foot strike in running: An in vivo cineradiographic study," *Journal of Biomechanics,* vol. 27, no. 10, pp. 1213-22, 1994.

[41] S. Yamaguchi, T. Sasho, H. Kato, Y. Kuroyanagi, and S. A. Banks, "Ankle and subtalar kinematics during dorsiflexion-plantarflexion activities," (in eng), *Foot Ankle Int,* vol. 30, no. 4, pp. 361-6, Apr 2009, doi: 50022909 [pii]
10.3113/FAI.2009.0361.
[42] N. Nahm, M. J. Bey, S. Liu, and S. T. Guthrie, "Ankle Motion and Offloading in Short Leg Cast and Low and High Fracture Boots," *Foot Ankle Int,* vol. 40, no. 12, pp. 1416-1423, Dec 2019, doi: 10.1177/1071100719868721.
[43] E. L. Nickoloff, "AAPM/RSNA physics tutorial for residents: physics of flat-panel fluoroscopy systems: Survey of modern fluoroscopy imaging: flat-panel detectors versus image intensifiers and more," (in eng), *Radiographics,* vol. 31, no. 2, pp. 591-602, Mar-Apr 2011, doi: 10.1148/rg.312105185.
[44] J. A. Seibert, "Flat-panel detectors: how much better are they?," (in eng), *Pediatr Radiol,* vol. 36 Suppl 2, no. Suppl 2, pp. 173-81, Sep 2006, doi: 10.1007/s00247-006-0208-0.
[45] L. Shi *et al.*, "Characterization and potential applications of a dual-layer flat-panel detector," (in eng), *Med Phys,* vol. 47, no. 8, pp. 3332-3343, Aug 2020, doi: 10.1002/mp.14211.
[46] J. M. Boone, B. A. Arnold, and J. A. Seibert, "Characterization of the point spread function and modulation transfer function of scattered radiation using a digital imaging system," *Med Phys,* vol. 13, no. 2, pp. 254-6, Mar-Apr 1986, doi: 10.1118/1.595906.
[47] J. M. Boone, J. A. Seibert, W. A. Barrett, and E. A. Blood, "Analysis and correction of imperfections in the image intensifier-TV-digitizer imaging chain," *Med Phys,* vol. 18, no. 2, pp. 236-42, Mar-Apr 1991, doi: 10.1118/1.596718.
[48] J. T. Bushberg, J. A. Seibert, E. M. Leidholdt, J. M. Boone, and E. J. Goldschmidt, "The Essential Physics of Medical Imaging," *Medical Physics,* vol. 30, pp. 1936-1936, 2003, doi: 10.1118/1.1585033.
[49] P. Cerveri, C. Forlani, N. A. Borghese, and G. Ferrigno, "Distortion correction for x-ray image intensifiers: local unwarping polynomials and RBF neural networks," *Med Phys,* vol. 29, no. 8, pp. 1759-71, Aug 2002, doi: 10.1118/1.1488602.
[50] P. Cerveri, C. Forlani, a. Pedotti, and G. Ferrigno, "Hierarchical radial basis function networks and local polynomial un-warping for X-ray image intensifier distortion correction: a comparison with global techniques.," *Medical & biological engineering & computing,* vol. 41, pp. 151-63, 2003.
[51] D. P. Chakraborty, "Image intensifier distortion correction," *Medical Physics,* vol. 14, pp. 249-252, 1987, doi: 10.1118/1.596078.
[52] R. Fahrig, M. Moreau, and D. W. Holdsworth, "Three-dimensional computed tomographic reconstruction using a C-arm mounted XRII: correction of image intensifier distortion," *Med Phys,* vol. 24, no. 7, pp. 1097-106, Jul 1997, doi: 10.1118/1.598013.
[53] E. Gronenschild, "The accuracy and reproducibility of a global method to correct for geometric image distortion in the x-ray imaging chain.," *Medical physics,* vol. 24, pp. 1875-1888, 1997, doi: 10.1118/1.598101.
[54] L. F. Gutiérrez, C. Ozturk, E. R. McVeigh, and R. J. Lederman, "A practical global distortion correction method for an image intensifier based x-ray fluoroscopy system.," *Medical Physics,* vol. 35, pp. 997-1007, 2008, doi: 10.1118/1.2839099.
[55] D. W. Holdsworth, S. I. Pollmann, H. N. Nikolov, and R. Fahrig, "Correction of XRII geometric distortion using a liquid-filled grid and image subtraction," *Med Phys,* vol. 32, no. 1, pp. 55-64, Jan 2005, doi: 10.1118/1.1827751.

[56] A. E. Kedgley, A. M. V. Fox, and T. R. Jenkyn, "Image intensifier distortion correction for fluoroscopic RSA: The need for independent accuracy assessment," *Journal of Applied Clinical Medical Physics,* vol. 13, pp. 197-204, 2012, doi: 10.1120/jacmp.v13i1.3441.
[57] E. Pietka and H. K. Huang, "Correction of aberration in image-intensifier systems," *Comput Med Imaging Graph,* vol. 16, no. 4, pp. 253-8, Jul-Aug 1992. [Online]. Available: https://www.ncbi.nlm.nih.gov/pubmed/1511398.
[58] D. Mery, *Computer Vision for X-Ray Testing: Imaging, Systems, Image Databases, and Algorithms*. Springer International Publishing, 2015.
[59] A. L. Lenz *et al.*, "Assignment of local coordinate systems and methods to calculate tibiotalar and subtalar kinematics: A systematic review," (in eng), *J Biomech,* vol. 120, p. 110344, May 7 2021, doi: 10.1016/j.jbiomech.2021.110344.
[60] C. F. T. Lôbo, E. A. Pires, M. Bordalo-Rodrigues, C. de Cesar Netto, and A. L. Godoy-Santos, "Imaging of progressive collapsing foot deformity with emphasis on the role of weightbearing cone beam CT," (in eng), *Skeletal Radiol,* Oct 25 2021, doi: 10.1007/s00256-021-03942-1.
[61] J. M. Iaquinto *et al.*, "Model-based tracking of the bones of the foot: A biplane fluoroscopy validation study," *Comput Biol Med,* vol. 92, pp. 118-127, Jan 1 2018, doi: 10.1016/j.compbiomed.2017.11.006.
[62] D. D. Lichti, G. B. Sharma, G. Kuntze, B. Mund, J. E. Beveridge, and J. L. Ronsky, "Rigorous geometric self-calibrating bundle adjustment for a dual fluoroscopic imaging system," *IEEE Transactions on Medical Imaging,* vol. 34, pp. 589-598, 2015, doi: 10.1109/TMI.2014.2362993.
[63] M. Brehler *et al.*, "Coupled Active Shape Models for Automated Segmentation and Landmark Localization in High-Resolution CT of the Foot and Ankle," (in eng), *Proc SPIE Int Soc Opt Eng,* vol. 10953, Feb 2019, doi: 10.1117/12.2515022.
[64] L. Wan, R. J. de Asla, H. E. Rubash, and G. Li, "Determination of in-vivo articular cartilage contact areas of human talocrural joint under weightbearing conditions," *Osteoarthritis Cartilage,* vol. 14, no. 12, pp. 1294-301, Dec 2006, doi: 10.1016/j.joca.2006.05.012.
[65] L. Wan, R. J. de Asla, H. E. Rubash, and G. Li, "In vivo cartilage contact deformation of human ankle joints under full body weight," (in eng), *J Orthop Res,* vol. 26, no. 8, pp. 1081-9, Aug 2008, doi: 10.1002/jor.20593.
[66] R. J. de Asla, M. Kozanek, L. Wan, H. E. Rubash, and G. Li, "Function of anterior talofibular and calcaneofibular ligaments during in-vivo motion of the ankle joint complex," *J Orthop Surg Res,* vol. 4, p. 7, 2009, doi: 10.1186/1749-799X-4-7.
[67] M. Kozanek, H. E. Rubash, G. Li, and R. J. de Asla, "Effect of post-traumatic tibiotalar osteoarthritis on kinematics of the ankle joint complex," *Foot Ankle Int,* vol. 30, no. 8, pp. 734-40, Aug 2009, doi: 10.3113/FAI.2009.0734.
[68] J. E. Bischof *et al.*, "In vivo cartilage contact strains in patients with lateral ankle instability," (in English), *Journal of Biomechanics,* vol. 43, no. 13, pp. 2561-2566, Sep 17 2010, doi: 10.1016/j.jbiomech.2010.05.013.
[69] W. B. Wainright *et al.*, "The effect of modified Brostrom-Gould repair for lateral ankle instability on in vivo tibiotalar kinematics," *Am J Sports Med,* vol. 40, no. 9, pp. 2099-104, Sep 2012, doi: 10.1177/0363546512454840.

[70] S. Cao *et al.*, "Effects of an ankle brace on the in vivo kinematics of patients with chronic ankle instability during walking on an inversion platform," *Gait Posture,* vol. 72, pp. 228-233, Jul 2019, doi: 10.1016/j.gaitpost.2019.06.020.
[71] S. Cao *et al.*, "In Vivo Kinematics of Functional Ankle Instability Patients and Lateral Ankle Sprain Copers During Stair Descent," *J Orthop Res,* vol. 37, no. 8, pp. 1860-1867, Aug 2019, doi: 10.1002/jor.24303.
[72] M. E. Balsdon, K. M. Bushey, C. E. Dombroski, M. E. LeBel, and T. R. Jenkyn, "Medial Longitudinal Arch Angle Presents Significant Differences Between Foot Types: A Biplane Fluoroscopy Study," (in eng), *J Biomech Eng,* vol. 138, no. 10, Oct 1 2016, doi: 10.1115/1.4034463.
[73] M. Balsdon, C. Dombroski, K. Bushey, and T. R. Jenkyn, "Hard, soft and off-the-shelf foot orthoses and their effect on the angle of the medial longitudinal arch: A biplane fluoroscopy study," *Prosthet Orthot Int,* vol. 43, no. 3, pp. 331-338, Jun 2019, doi: 10.1177/0309364619825607.
[74] B. D. McHenry, E. Exten, J. T. Long, and G. F. Harris, "Sagittal Fluoroscopy for the Assessment of Hindfoot Kinematics," *J Biomech Eng,* vol. 138, no. 3, p. 4032445, Mar 2016, doi: 10.1115/1.4032445.
[75] J. A. Cross, B. McHenry, and T. G. Schmidt, "Quantifying cross-scatter contamination in biplane fluoroscopy motion analysis systems," *J Med Imaging (Bellingham),* vol. 2, no. 4, p. 043503, Oct 2015, doi: 10.1117/1.JMI.2.4.043503.
[76] B. D. McHenry *et al.*, "Sagittal Subtalar and Talocrural Joint Assessment During Ambulation With Controlled Ankle Movement (CAM) Boots," *Foot Ankle Int,* vol. 38, no. 11, pp. 1260-1266, Nov 2017, doi: 10.1177/1071100717723129.
[77] J. A. Cross, B. D. McHenry, R. Molthen, E. Exten, T. G. Schmidt, and G. F. Harris, "Biplane fluoroscopy for hindfoot motion analysis during gait: A model-based evaluation," *Med Eng Phys,* Mar 01 2017, doi: 10.1016/j.medengphy.2017.02.009.
[78] B. D. McHenry, K. M. Kruger, E. L. Exten, S. Tarima, and G. F. Harris, "Sagittal subtalar and talocrural joint assessment between barefoot and shod walking: A fluoroscopic study," *Gait Posture,* vol. 72, pp. 57-61, Jul 2019, doi: 10.1016/j.gaitpost.2019.05.024.
[79] S. E. Hoffman, C. D. Peltz, J. A. Haladik, G. Divine, M. A. Nurse, and M. J. Bey, "Dynamic in-vivo assessment of navicular drop while running in barefoot, minimalist, and motion control footwear conditions," (in eng), *Gait Posture,* vol. 41, no. 3, pp. 825-9, Mar 2015, doi: 10.1016/j.gaitpost.2015.02.017.
[80] J. A. Nichols, K. E. Roach, N. M. Fiorentino, and A. E. Anderson, "Predicting tibiotalar and subtalar joint angles from skin-marker data with dual-fluoroscopy as a reference standard," *Gait Posture,* vol. 49, pp. 136-143, Sep 2016, doi: 10.1016/j.gaitpost.2016.06.031.
[81] K. E. Roach *et al.*, "In Vivo Kinematics of the Tibiotalar and Subtalar Joints in Asymptomatic Subjects: A High-Speed Dual Fluoroscopy Study," *J Biomech Eng,* vol. 138, no. 9, Sep 1 2016, doi: 10.1115/1.4034263.
[82] K. E. Roach, K. B. Foreman, A. Barg, C. L. Saltzman, and A. E. Anderson, "Application of High-Speed Dual Fluoroscopy to Study In Vivo Tibiotalar and Subtalar Kinematics in Patients With Chronic Ankle Instability and Asymptomatic Control Subjects During Dynamic Activities," *Foot Ankle Int,* vol. 38, no. 11, pp. 1236-1248, Nov 2017, doi: 10.1177/1071100717723128.

[83] D. J. Blair, A. Barg, K. B. Foreman, A. E. Anderson, and A. L. Lenz, "Methodology for Measurement of in vivo Tibiotalar Kinematics After Total Ankle Replacement Using Dual Fluoroscopy," *Front Bioeng Biotechnol,* vol. 8, p. 375, 2020, doi: 10.3389/fbioe.2020.00375.

[84] A. L. Lenz *et al.*, "Compensatory Motion of the Subtalar Joint Following Tibiotalar Arthrodesis: An in Vivo Dual-Fluoroscopy Imaging Study," *J Bone Joint Surg Am,* vol. 102, no. 7, pp. 600-608, Apr 1 2020, doi: 10.2106/JBJS.19.01132.

[85] K. E. Roach, K. B. Foreman, B. A. MacWilliams, K. Karpos, J. Nichols, and A. E. Anderson, "The modified Shriners Hospitals for Children Greenville (mSHCG) multi-segment foot model provides clinically acceptable measurements of ankle and midfoot angles: A dual fluoroscopy study," *Gait Posture,* vol. 85, pp. 258-265, Mar 2021, doi: 10.1016/j.gaitpost.2021.02.004.

[86] C. B. Phan, D. P. Nguyen, K. M. Lee, and S. Koo, "Relative movement on the articular surfaces of the tibiotalar and subtalar joints during walking," *Bone Joint Res,* vol. 7, no. 8, pp. 501-507, Aug 2018, doi: 10.1302/2046-3758.78.BJR-2018-0014.R1.

[87] C. B. Phan, G. Shin, K. M. Lee, and S. Koo, "Skeletal kinematics of the midtarsal joint during walking: Midtarsal joint locking revisited," *J Biomech,* vol. 95, p. 109287, Oct 11 2019, doi: 10.1016/j.jbiomech.2019.07.031.

[88] C. B. Phan, K. M. Lee, S. S. Kwon, and S. Koo, "Kinematic instability in the joints of flatfoot subjects during walking: A biplanar fluoroscopic study," *J Biomech,* vol. 127, p. 110681, Oct 11 2021, doi: 10.1016/j.jbiomech.2021.110681.

[89] E. L. Brainerd *et al.*, "X-ray reconstruction of moving morphology (XROMM): precision, accuracy and applications in comparative biomechanics research," *J Exp Zool A Ecol Genet Physiol,* vol. 313, no. 5, pp. 262-79, Jun 1 2010, doi: 10.1002/jez.589.

[90] S. E. Kessler *et al.*, "A Direct Comparison of Biplanar Videoradiography and Optical Motion Capture for Foot and Ankle Kinematics," (in eng), *Front Bioeng Biotechnol,* vol. 7, p. 199, 2019, doi: 10.3389/fbioe.2019.00199.

[91] J. N. Maharaj *et al.*, "The Reliability of Foot and Ankle Bone and Joint Kinematics Measured With Biplanar Videoradiography and Manual Scientific Rotoscoping," (in eng), *Front Bioeng Biotechnol,* vol. 8, p. 106, 2020, doi: 10.3389/fbioe.2020.00106.

[92] J. N. Maharaj *et al.*, "Modelling the complexity of the foot and ankle during human locomotion: the development and validation of a multi-segment foot model using biplanar videoradiography," *Comput Methods Biomech Biomed Engin,* pp. 1-12, Oct 26 2021, doi: 10.1080/10255842.2021.1968844.

[93] S. Pitcairn, J. Kromka, M. Hogan, and W. Anderst, "Validation and application of dynamic biplane radiography to study in vivo ankle joint kinematics during high-demand activities," (in eng), *J Biomech,* vol. 103, p. 109696, Apr 16 2020, doi: 10.1016/j.jbiomech.2020.109696.

[94] J. A. Brown, T. Gale, and W. Anderst, "An automated method for defining anatomic coordinate systems in the hindfoot," (in eng), *J Biomech,* vol. 109, p. 109951, Aug 26 2020, doi: 10.1016/j.jbiomech.2020.109951.

[95] S. Yang, S. P. Canton, M. V. Hogan, and W. Anderst, "Healthy ankle and hindfoot kinematics during gait: Sex differences, asymmetry and coupled motion revealed through dynamic biplane radiography," *J Biomech,* vol. 116, p. 110220, Feb 12 2021, doi: 10.1016/j.jbiomech.2020.110220.

[96] K. Ito *et al.*, "Direct assessment of 3D foot bone kinematics using biplanar X-ray fluoroscopy and an automatic model registration method," *J Foot Ankle Res,* vol. 8, p. 21, 2015, doi: 10.1186/s13047-015-0079-4.
[97] K. Ito *et al.*, "Three-dimensional innate mobility of the human foot bones under axial loading using biplane X-ray fluoroscopy," (in eng), *R Soc Open Sci,* vol. 4, no. 10, p. 171086, Oct 2017, doi: 10.1098/rsos.171086.
[98] T. Negishi *et al.*, "Three-Dimensional Innate Mobility of the Human Foot on Coronally-Wedged Surfaces Using a Biplane X-Ray Fluoroscopy," (in eng), *Front Bioeng Biotechnol,* vol. 10, p. 800572, 2022, doi: 10.3389/fbioe.2022.800572.
[99] C. C. Lin, J. D. Li, T. W. Lu, M. Y. Kuo, C. C. Kuo, and H. C. Hsu, "A model-based tracking method for measuring 3D dynamic joint motion using an alternating biplane x-ray imaging system," *Med Phys,* Jun 11 2018, doi: 10.1002/mp.13042.
[100] Z. L. Teng *et al.*, "Effect of loading history on material properties of human heel pad: an in-vivo pilot investigation during gait," (in eng), *BMC Musculoskelet Disord,* vol. 23, no. 1, p. 254, Mar 15 2022, doi: 10.1186/s12891-022-05197-w.
[101] S. Canton, W. Anderst, and M. V. Hogan, "In Vivo Ankle Kinematics Revealed Through Biplane Radiography: Current Concepts, Recent Literature, and Future Directions," *Curr Rev Musculoskelet Med,* vol. 13, no. 1, pp. 77-85, Feb 2020, doi: 10.1007/s12178-020-09601-7.
[102] N. Kroupa, B. Pierrat, W. S. Han, S. Grange, F. Bergandi, and J. Molimard, "Bone Position and Ligament Deformations of the Foot From CT Images to Quantify the Influence of Footwear in ex vivo Feet," (in eng), *Front Bioeng Biotechnol,* vol. 8, p. 560, 2020, doi: 10.3389/fbioe.2020.00560.
[103] J. A. Cross, B. D. McHenry, R. Molthen, E. Exten, T. G. Schmidt, and G. F. Harris, "Biplane fluoroscopy for hindfoot motion analysis during gait: A model-based evaluation," *Med Eng Phys,* vol. 43, pp. 118-123, May 2017, doi: 10.1016/j.medengphy.2017.02.009.
[104] T. Miyamoto *et al.*, "4D-foot analysis on effect of arch support on ankle, subtalar, and talonavicular joint kinematics," (in eng), *J Orthop Sci,* Jan 27 2023, doi: 10.1016/j.jos.2022.10.009.
[105] T. Ahl, N. Dalen, A. Lundberg, and G. Selvik, "Mobility of the ankle mortise. A roentgen stereophotogrammetric analysis," *Acta Orthop Scand,* vol. 58, no. 4, pp. 401-2, Aug 1987. [Online]. Available: https://www.ncbi.nlm.nih.gov/pubmed/3673536.
[106] A. Lundberg, "Kinematics of the ankle and foot. In vivo roentgen stereophotogrammetry," *Acta Orthop Scand Suppl,* vol. 233, pp. 1-24, 1989. [Online]. Available: https://www.ncbi.nlm.nih.gov/pubmed/2686345.
[107] J. W. Arner *et al.*, "The Effects of Anterior Cruciate Ligament Deficiency on the Meniscus and Articular Cartilage: A Novel Dynamic In Vitro Pilot Study," *Orthop J Sports Med,* vol. 4, no. 4, p. 2325967116639895, Apr 2016, doi: 10.1177/2325967116639895.
[108] J. N. Irvine *et al.*, "Is There a Difference in Graft Motion for Bone-Tendon-Bone and Hamstring Autograft ACL Reconstruction at 6 Weeks and 1 Year?," *Am J Sports Med,* vol. 44, no. 10, pp. 2599-2607, Oct 2016, doi: 10.1177/0363546516651436.
[109] M. J. Bey, S. K. Kline, S. Tashman, and R. Zauel, "Accuracy of biplane x-ray imaging combined with model-based tracking for measuring in-vivo patellofemoral joint motion,"

Journal of orthopaedic surgery and research, vol. 3, p. 38, Sep 4 2008, doi: 10.1186/1749-799X-3-38.
[110] *OpenCV: Open Source Computer Vision Library*. (2022). [Online]. Available: https://opencv.org/
[111] *Eigen*. (2021). [Online]. Available: https://eigen.tuxfamily.org/
[112] R. a. Z. Hartley, Andrew, *Multiple View Geometry in Computer Vision*, Second ed. Cambridge University Press, 2003, p. 652.
[113] R. R. Liu, S. Rudin, and D. R. Bednarek, "Super-global distortion correction for a rotational C-arm x-ray image intensifier," *Med Phys,* vol. 26, no. 9, pp. 1802-10, Sep 1999, doi: 10.1118/1.598684.
[114] N. M. Alem, J. W. Melvin, and G. L. Holstein, "Biomechanics applications of direct linear transformation in close-range photogrammetry," in *Proceedings of the Sixth New England Bioengineering Conference*, D. Jaron Ed.: Pergamon, 1978, pp. 202-206.
[115] Y. Furukawa and J. Ponce, "Accurate camera calibration from multi-view stereo and bundle adjustment," *International Journal of Computer Vision,* vol. 84, pp. 257-268, 2009, doi: 10.1007/s11263-009-0232-2.
[116] A. Rougee, C. Picard, C. Ponchut, and Y. Trousset, "Geometrical calibration of X-ray imaging chains for three-dimensional reconstruction," *Comput Med Imaging Graph,* vol. 17, no. 4-5, pp. 295-300, Jul-Oct 1993. [Online]. Available: https://www.ncbi.nlm.nih.gov/pubmed/8306301.
[117] N. Borlin, T. Thien, and J. Karrholm, "The precision of radiostereometric measurements. Manual vs. digital measurements," *J Biomech,* vol. 35, no. 1, pp. 69-79, Jan 2002. [Online]. Available: https://www.ncbi.nlm.nih.gov/pubmed/11747885.
[118] *PMCMRplus: Calculate Pairwise Multiple Comparisons of Mean Rank Sums Extended*. (2023). [Online]. Available: http://CRAN.R-project.org/package=PMCMRplus
[119] K. L. Gwet, "Handbook of Inter-Rater Reliability," in *The Definitive Guide to Measuring the Extent of Agreement Among Raters - Volume 2: Analysis of Quantitative Ratings*, 5th ed. United States of America: AgreeStat Analytics, 2021, sec. Chapter 9: Intraclass Correlation and Multivariate Analysis.
[120] D. Mery, "Explicit geometric model of a radioscopic imaging system," *NDT & E International,* vol. 36, no. 8, pp. 587-599, 2003/12/01/ 2003, doi: https://doi.org/10.1016/S0963-8695(03)00084-7.
[121] I. Söderkvist and P. A. Wedin, "Determining the movements of the skeleton using well-configured markers," (in eng), *J Biomech,* vol. 26, no. 12, pp. 1473-7, Dec 1993, doi: 10.1016/0021-9290(93)90098-y.
[122] E. Thorhauer, M. French, T. Kimura, and W. R. Ledoux, "A Cadaveric Comparison of the Kinematic and Anatomical Axes and Arthrokinematics of the Metatarsosesamoidal and First Metatarsophalangeal Joints," (in eng), *J Biomech Eng,* vol. 145, no. 4, Apr 1 2023, doi: 10.1115/1.4056060.
[123] J. J. Crisco, E. Halilaj, D. C. Moore, T. Patel, A.-P. C. Weiss, and A. L. Ladd, "In Vivo kinematics of the trapeziometacarpal joint during thumb extension-flexion and abduction-adduction," (in eng), *The Journal of hand surgery,* vol. 40, no. 2, pp. 289-296, 2015, doi: 10.1016/j.jhsa.2014.10.062.
[124] W. Schallig *et al.*, "Precision of determining bone pose and marker position in the foot and lower leg from computed tomography scans: How low can we go in radiation dose?,"

(in eng), *Med Eng Phys,* vol. 69, pp. 147-152, Jul 2019, doi: 10.1016/j.medengphy.2019.05.004.
[125] S. Telfer, M. W. Kindig, B. J. Sangeorzan, and W. R. Ledoux, "Metatarsal shape and foot type: A geometric morphometric analysis," *Journal of Biomechanical Engineering,* vol. 139, no. 3, 2017, doi: 10.1115/1.4035077.
[126] M. R. Requist, T. Rolvien, A. Barg, and A. L. Lenz, "Morphologic analysis of the 1st and 2nd tarsometatarsal joint articular surfaces," (in eng), *Scientific reports,* vol. 13, no. 1, p. 6473, Apr 20 2023, doi: 10.1038/s41598-023-32500-z.
[127] T. M. Grant *et al.*, "Development and validation of statistical shape models of the primary functional bone segments of the foot," *PeerJ,* vol. 2020, no. 2, pp. 1-19, 2020, doi: 10.7717/peerj.8397.
[128] L. Zheng, R. Carey, E. Thorhauer, S. Tashman, C. Harner, and X. Zhang, "In vivo tibiofemoral skeletal kinematics and cartilage contact arthrokinematics during decline walking after isolated meniscectomy," *Med Eng Phys,* vol. 51, pp. 41-48, Jan 2018, doi: 10.1016/j.medengphy.2017.10.014.
[129] M. French, E. D. Thorhauer, T. Kimura, B. J. Sangeorzan, and W. R. Ledoux, "Displacement of the Metatarsal Sesamoids in Relation to First Metatarsophalangeal Joint Extension," (in eng), *Foot Ankle Orthop,* vol. 7, no. 3, p. 24730114221126457, Jul 2022, doi: 10.1177/24730114221126457.
[130] F. Lintz, P. Beaudet, G. Richardi, and J. Brilhault, "Weight-bearing CT in foot and ankle pathology," (in eng), *Orthop Traumatol Surg Res,* vol. 107, no. 1s, p. 102772, Feb 2021, doi: 10.1016/j.otsr.2020.102772.
[131] Y. Hu, W. R. Ledoux, M. Fassbind, E. S. Rohr, B. J. Sangeorzan, and D. Haynor, "Multi-rigid image segmentation and registration for the analysis of joint motion from three-dimensional magnetic resonance imaging," *J Biomech Eng,* vol. 133, no. 10, p. 101005, Oct 2011, doi: 10.1115/1.4005175.
[132] C. Li, C. Xu, C. Gui, and M. D. Fox, "Distance regularized level set evolution and its application to image segmentation," *IEEE Trans Image Process,* vol. 19, pp. 3243-3254, 2010, doi: 10.1109/TIP.2010.2069690.
[133] A. Pietrobelli *et al.*, "Comparability of skeletal fibulae surfaces generated by different source scanning (dual-energy CT scan vs. high resolution laser scanning) and 3D geometric morphometric validation," (in eng), *J Anat,* vol. 241, no. 3, pp. 667-682, Sep 2022, doi: 10.1111/joa.13714.
[134] J. M. Stephen, J. D. Calder, A. Williams, and H. El Daou, "Comparative accuracy of lower limb bone geometry determined using MRI, CT, and direct bone 3D models," *Journal of Orthopaedic Research,* vol. 39, no. 9, pp. 1870-1876, 2021, doi: https://doi.org/10.1002/jor.24923.
[135] N. A. DeVries, E. E. Gassman, N. A. Kallemeyn, K. H. Shivanna, V. A. Magnotta, and N. M. Grosland, "Validation of phalanx bone three-dimensional surface segmentation from computed tomography images using laser scanning," (in eng), *Skeletal Radiol,* vol. 37, no. 1, pp. 35-42, Jan 2008, doi: 10.1007/s00256-007-0386-3.
[136] A. A. Taha and A. Hanbury, "Metrics for evaluating 3D medical image segmentation: analysis, selection, and tool," (in eng), *BMC Med Imaging,* vol. 15, p. 29, Aug 12 2015, doi: 10.1186/s12880-015-0068-x.

[137] K. H. Zou *et al.*, "Statistical validation of image segmentation quality based on a spatial overlap index," (in eng), *Acad Radiol,* vol. 11, no. 2, pp. 178-89, Feb 2004, doi: 10.1016/s1076-6332(03)00671-8.
[138] *R: A language and environment for statistical computing.* (2023). R Foundation for Statistical Computing, Vienna, Austria.
[139] *Welcome to the tidyverse.* (2019).
[140] D. Bates, Maechler, M., Bolker, B., Walker, S., "Fitting Linear Mixed-Effects Models Using lme4," *Journal of Statistical Software* vol. 67 no. 1, pp. 1-48, 2015.
[141] A. Kuznetsova, Brockhoff, P., Christensen R., "lmerTest Package: Tests in Linear Mixed Effects Models," *Journal of Statistical Software,* vol. 82, no. 13, pp. 1-26, 2017, doi: 10.18637/jss.v082.i13.
[142] *Estimated Marginal Means, aka Least-Squares Means*. (2022). [Online]. Available: https://CRAN.R-project.org/package=emmeans
[143] M. Kitashiro, N. Ogihara, T. Kokubo, M. Matsumoto, M. Nakamura, and T. Nagura, "Age- and sex-associated morphological variations of metatarsal torsional patterns in humans," *Clinical Anatomy,* vol. 30, no. 8, pp. 1058-1063, 2017, doi: 10.1002/ca.22944.
[144] J. Cates, S. Elhabian, and R. Whitaker, "Chapter 10 - ShapeWorks: Particle-Based Shape Correspondence and Visualization Software," in *Statistical Shape and Deformation Analysis*, G. Zheng, S. Li, and G. Székely Eds.: Academic Press, 2017, pp. 257-298.
[145] S. Elhabian, P. Agrawal, J. Cates, M. Datar, and R. Whitaker, "ShapeWorksStudio v2.2 Particle-based Shape Correspondence and Visualization Software," 2012. [Online]. Available: https://github.com/SCIInstitute/ShapeworksStudio/releases
[146] R. Anwar, S. N. Anjum, and J. E. Nicholl, "Sesamoids of the foot," *Current Orthopaedics,* vol. 19, no. 1, pp. 40-48, 2005, doi: 10.1016/j.cuor.2005.01.001.
[147] E. G. Richardson, "Hallucal sesamoid pain: causes and surgical treatment," (in eng), *The Journal of the American Academy of Orthopaedic Surgeons,* vol. 7, no. 4, pp. 270-8, Jul-Aug 1999, doi: 10.5435/00124635-199907000-00007.
[148] A. Boike, M. Schnirring-Judge, and S. McMillin, "Sesamoid disorders of the first metatarsophalangeal joint," *Clinics in Podiatric Medicine and Surgery,* vol. 28, no. 2, pp. 269-285, 2011, doi: 10.1016/j.cpm.2011.03.006.
[149] E. O. Leventen, "Sesamoid disorders and treatment: An update," *Clinical Orthopaedics and Related Research,* no. 269, pp. 236-240, 1991, doi: 10.1097/00003086-199108000-00033.
[150] I. Goldberg and H. Nathan, "Anatomy and pathology of the sesamoid bones - The hand compared to the foot," *International Orthopaedics,* vol. 11, no. 2, pp. 141-147, 1987, doi: 10.1007/BF00266700.
[151] R. Derner, K. Goss, H. N. Postowski, and N. Parsley, "A plantarflexory-shortening osteotomy for hallux rigidus: A retrospective analysis," *Journal of Foot and Ankle Surgery,* vol. 44, no. 5, pp. 377-389, 2005, doi: 10.1053/j.jfas.2005.07.010.
[152] R. W. Smith, J. C. Reynolds, and M. J. Stewart, "Hallux valgus assessment: report of research committee of American Orthopaedic Foot and Ankle Society," (in eng), *Foot & ankle,* vol. 5, no. 2, pp. 92-103, Sep-Oct 1984, doi: 10.1177/107110078400500208.
[153] M. J. Shereff, F. J. Bejjani, and F. J. Kummer, "Kinematics of the first metatarsophalangeal joint," *Journal of Bone and Joint Surgery - Series A,* vol. 68, no. 3, pp. 392-398, 1986, doi: 10.2106/00004623-198668030-00012.

[154] B. Jamal, A. Pillai, Q. Fogg, and S. Kumar, "The metatarsosesamoid joint: An in vitro 3D quantitative assessment," *Foot and Ankle Surgery,* vol. 21, no. 1, pp. 22-25, 2015, doi: 10.1016/j.fas.2014.08.010.
[155] T. K. Ahn, H. B. Kitaoka, Z. P. Luo, and K. N. An, "Kinematics and contact characteristics of the first metatarsophalangeal joint," *Foot and Ankle International,* vol. 18, no. 3, pp. 170-174, 1997, doi: 10.1177/107110079701800310.
[156] D. Karasick and M. E. Schweitzer, "Disorders of the hallux sesamoid complex: MR features," (in eng), *Skeletal Radiol,* vol. 27, no. 8, pp. 411-8, Aug 1998, doi: 10.1007/s002560050410.
[157] C. Nery, D. Baumfeld, H. Umans, and A. F. Yamada, "MR Imaging of the Plantar Plate: Normal Anatomy, Turf Toe, and Other Injuries," (in eng), *Magnetic resonance imaging clinics of North America,* vol. 25, no. 1, pp. 127-144, Feb 2017, doi: 10.1016/j.mric.2016.08.007.
[158] X. Duan *et al.*, "Role of magnetic resonance imaging versus ultrasound for detection of plantar plate tear," (in eng), *Journal of orthopaedic surgery and research,* vol. 12, no. 1, p. 14, Jan 21 2017, doi: 10.1186/s13018-016-0507-6.
[159] K. Deschamps *et al.*, "Repeatability in the assessment of multi-segment foot kinematics," (in eng), *Gait Posture,* vol. 35, no. 2, pp. 255-60, Feb 2012, doi: 10.1016/j.gaitpost.2011.09.016.
[160] A. Leardini, M. G. Benedetti, L. Berti, D. Bettinelli, R. Nativo, and S. Giannini, "Rear-foot, mid-foot and fore-foot motion during the stance phase of gait," (in eng), *Gait Posture,* vol. 25, no. 3, pp. 453-62, Mar 2007, doi: 10.1016/j.gaitpost.2006.05.017.
[161] N. Okita, S. A. Meyers, J. H. Challis, and N. A. Sharkey, "Segmental motion of forefoot and hindfoot as a diagnostic tool," (in eng), *J Biomech,* vol. 46, no. 15, pp. 2578-85, Oct 18 2013, doi: 10.1016/j.jbiomech.2013.08.014.
[162] C. de Cesar Netto *et al.*, "Consensus for the Use of Weightbearing CT in the Assessment of Progressive Collapsing Foot Deformity," (in eng), *Foot & ankle international,* vol. 41, no. 10, pp. 1277-1282, Oct 2020, doi: 10.1177/1071100720950734.
[163] B. A. MacWilliams and R. B. Davis, "Addressing some misperceptions of the joint coordinate system," *Journal of Biomechanical Engineering,* vol. 135, no. 5, pp. 9-11, 2013, doi: 10.1115/1.4024142.
[164] D. Dabirrahmani and M. Hogg, "Modification of the Grood and Suntay Joint Coordinate System equations for knee joint flexion," (in eng), *Med Eng Phys,* vol. 39, pp. 113-116, Jan 2017, doi: 10.1016/j.medengphy.2016.10.006.
[165] E. S. Grood and W. J. Suntay, "A joint coordinate system for the clinical description of three-dimensional motions: application to the knee," (in eng), *J Biomech Eng,* vol. 105, no. 2, pp. 136-44, May 1983, doi: 10.1115/1.3138397.
[166] J. A. Brown, T. Gale, and W. Anderst, "An automated method for defining anatomic coordinate systems in the hindfoot," *Journal of Biomechanics,* vol. 109, pp. 109951-109951, 2020, doi: 10.1016/j.jbiomech.2020.109951.
[167] Y. Matsuura and N. Ogihara, "A Method for Quantifying Articular Surface Morphology of Metacarpals Using Quadric Surface Approximation," *International Journal of Primatology,* no. 31, pp. 263-274, 2010, doi: 10.1007/s10764-010-9397-3.
[168] E. Halilaj, M. J. Rainbow, C. J. Got, D. C. Moore, and J. J. Crisco, "A thumb carpometacarpal joint coordinate system based on articular surface geometry," *Journal of biomechanics,* vol. 46, no. 5, pp. 1031-1034, 2013, doi: 10.1016/j.jbiomech.2012.12.002.

[169] J.-B. Renault, G. Aüllo-Rasser, M. Donnez, S. Parratte, and P. Chabrand, "Articular-surface-based automatic anatomical coordinate systems for the knee bones," *Journal of Biomechanics,* vol. 80, pp. 171-178, 2018/10/26/ 2018, doi: https://doi.org/10.1016/j.jbiomech.2018.08.028.
[170] D. L. Miranda, M. J. Rainbow, E. L. Leventhal, J. J. Crisco, and B. C. Fleming, "Automatic determination of anatomical coordinate systems for three-dimensional bone models of the isolated human knee," *Journal of Biomechanics,* vol. 43, no. 8, pp. 1623-1626, 2010/05/28/ 2010, doi: https://doi.org/10.1016/j.jbiomech.2010.01.036.
[171] W. C. Parr, H. J. Chatterjee, and C. Soligo, "Calculating the axes of rotation for the subtalar and talocrural joints using 3D bone reconstructions," *J Biomech,* vol. 45, no. 6, pp. 1103-7, Apr 5 2012, doi: 10.1016/j.jbiomech.2012.01.011.
[172] L. Yin, K. Chen, L. Guo, L. Cheng, F. Wang, and L. Yang, "Identifying the Functional Flexion-extension Axis of the Knee: An In-Vivo Kinematics Study," (in eng), *PloS one,* vol. 10, no. 6, p. e0128877, 2015, doi: 10.1371/journal.pone.0128877.
[173] G. M. Best, Z. E. Mack, D. R. Pichora, J. J. Crisco, R. N. Kamal, and M. J. Rainbow, "Differences in the Rotation Axes of the Scapholunate Joint During Flexion-Extension and Radial-Ulnar Deviation Motions," (in eng), *The Journal of hand surgery,* vol. 44, no. 9, pp. 772-778, Sep 2019, doi: 10.1016/j.jhsa.2019.05.001.
[174] M. L. Hull, "Coordinate system requirements to determine motions of the tibiofemoral joint free from kinematic crosstalk errors," *Journal of biomechanics,* vol. 109, pp. 109928-109928, 2020, doi: 10.1016/j.jbiomech.2020.109928.
[175] T. F. Nagle, A. Erdemir, and R. W. Colbrunn, "A generalized framework for determination of functional musculoskeletal joint coordinate systems," *Journal of Biomechanics,* vol. 127, p. 110664, 2021/10/11/ 2021, doi: https://doi.org/10.1016/j.jbiomech.2021.110664.
[176] E. Most, J. Axe, H. Rubash, and G. Li, "Sensitivity of the knee joint kinematics calculation to selection of flexion axes," *J Biomech,* vol. 37, no. 11, pp. 1743-8, Nov 2004, doi: 10.1016/j.jbiomech.2004.01.025.
[177] E. Brenner, "The intersesamoidal ridge of the first metatarsal bone: anatomical basics and clinical considerations," (in eng), *Surgical and radiologic anatomy : SRA,* vol. 25, no. 2, pp. 127-31, May 2003, doi: 10.1007/s00276-003-0107-0.
[178] M. S. Drapeau and E. H. Harmon, "Metatarsal torsion in monkeys, apes, humans and australopiths," (in eng), *Journal of human evolution,* vol. 64, no. 1, pp. 93-108, Jan 2013, doi: 10.1016/j.jhevol.2012.10.008.
[179] J. P. Mortier, J. L. Bernard, and M. Maestro, "Axial rotation of the first metatarsal head in a normal population and hallux valgus patients," (in eng), *Orthop Traumatol Surg Res,* vol. 98, no. 6, pp. 677-83, Oct 2012, doi: 10.1016/j.otsr.2012.05.005.
[180] B. Hintermann, B. M. Nigg, and C. Sommer, "Foot Movement and Tendon Excursion: An In Vitro Study," *Foot & Ankle International,* vol. 15, no. 7, pp. 386-395, 1994, doi: 10.1177/107110079401500708.
[181] P. M. Aubin, "The Robotic Gait Simulator: A Dynamic Cadaveric Foot and Ankle Model for Biomechanics Research," PhD, Department of Mechanical Engineering, University of Washington, 2010.
[182] L. T. Jackson, P. M. Aubin, M. S. Cowley, B. J. Sangeorzan, and W. R. Ledoux, "A robotic cadaveric flatfoot analysis of stance phase," *Journal of Biomechanical Engineering,* vol. 133, no. 5, pp. 1-6, 2011, doi: 10.1115/1.4003869.

[183] Y. Hu, W. R. Ledoux, M. Fassbind, E. S. Rohr, B. J. Sangeorzan, and D. Haynor, "Multi-rigid image segmentation and registration for the analysis of joint motion from three-dimensional magnetic resonance imaging," *Journal of Biomechanical Engineering,* vol. 133, no. 10, pp. 1-8, 2011, doi: 10.1115/1.4005175.
[184] D. Mattes, D. R. Haynor, H. Vesselle, T. K. Lewellyn, and W. Eubank, "Nonrigid multimodality image registration," 2001, vol. 4322: SPIE, 1 ed., pp. 1609-1620, doi: 10.1117/12.431046.
[185] J. E. Beveridge, N. G. Shrive, and C. B. Frank, "Repeatability and precision of a weighted centroid method for estimating dynamic in vivo tibiofemoral surface interactions in sheep," *Computer Methods in Biomechanics and Biomedical Engineering,* vol. 17, no. 16, pp. 1853-1863, 2014, doi: 10.1080/10255842.2013.772592.
[186] C. W. Spoor and F. E. Veldpaus, "Rigid body motion calculated from spatial co-ordinates of markers," (in eng), *J Biomech,* vol. 13, no. 4, pp. 391-3, 1980, doi: 10.1016/0021-9290(80)90020-2.
[187] H. J. Woltring, R. Huiskes, A. de Lange, and F. E. Veldpaus, "Finite centroid and helical axis estimation from noisy landmark measurements in the study of human joint kinematics," (in eng), *J Biomech,* vol. 18, no. 5, pp. 379-89, 1985, doi: 10.1016/0021-9290(85)90293-3.
[188] R. M. Ehrig and M. O. Heller, "On intrinsic equivalences of the finite helical axis, the instantaneous helical axis, and the SARA approach. A mathematical perspective," *Journal of Biomechanics,* vol. 84, pp. 4-10, 2019, doi: 10.1016/j.jbiomech.2018.12.034.
[189] R. M. Ehrig, W. R. Taylor, G. N. Duda, and M. O. Heller, "A survey of formal methods for determining functional joint axes," *Journal of Biomechanics,* vol. 40, no. 10, pp. 2150-2157, 2007, doi: 10.1016/j.jbiomech.2006.10.026.
[190] *Gmedian: Geometric Median, k-Medians Clustering and Robust Median PCA.* (2020). [Online]. Available: https://CRAN.R-project.org/package=Gmedian
[191] H. J. Woltring, "Estimation of the trajectory of the instantaneous centre of rotation in planar biokinematics," *Journal of Biomechanics,* vol. 23, no. 12, pp. 1273-1274, 1990, doi: 10.1016/0021-9290(90)90385-G.
[192] H. J. Woltring, A. de Lange, J. M. G. Kauer, and R. Huiskes, "Instantaneous Helical Axis Estimation Via Natural, Cross-Validated Splines," in *Biomechanics: Basic and Applied Research.*, G. Bergmann, R. Kolbel, and A. Rolhmann Eds., no. 3). Dordrecht: Springer, 1987, ch. Developments in Biomechanics.
[193] K. V. Mardia and P. E. Jupp, *Directional Statistics*. J Wiley, 2000.
[194] *R: A language and environment for statistical computing.* (2019). R Foundation for Statistical Computing, Vienna, Austria.
[195] *Directional: A Collection of R Functions for Directional Data Analysis*. (2021). [Online]. Available: https://CRAN.R-project.org/package=Directional
[196] M. Peña Fernández *et al.*, "Centre of Rotation of the Human Subtalar Joint Using Weight-Bearing Clinical Computed Tomography," (in eng), *Scientific reports,* vol. 10, no. 1, p. 1035, Jan 23 2020, doi: 10.1038/s41598-020-57912-z.
[197] M. Durrant, L. Durrant, and T. McElroy, "Establishing a common instantaneous center of rotation for the metatarso-phalangeal and metatarso-sesamoid joints: A theoretical geometric model based on specific morphometrics," *Journal of Orthopaedic Surgery and Research,* vol. 14, no. 1, pp. 1-10, 2019, doi: 10.1186/s13018-019-1110-4.

[198] P. R. Cavanagh, "Plantar soft tissue thickness during ground contact in walking," (in eng), *J Biomech,* vol. 32, no. 6, pp. 623-8, Jun 1999, doi: 10.1016/s0021-9290(99)00028-7.
[199] E. D. Williams *et al.*, "The design and validation of a magnetic resonance imaging-compatible device for obtaining mechanical properties of plantar soft tissue via gated acquisition," (in eng), *Proc Inst Mech Eng H,* vol. 229, no. 10, pp. 732-42, Oct 2015, doi: 10.1177/0954411915606150.
[200] E. D. Williams *et al.*, "A preliminary study of patient-specific mechanical properties of diabetic and healthy plantar soft tissue from gated magnetic resonance imaging," (in eng), *Proc Inst Mech Eng H,* vol. 231, no. 7, pp. 625-633, Jul 2017, doi: 10.1177/0954411917695849.
[201] H. Kinoshita, T. Ogawa, K. Kuzuhara, and K. Ikuta, "In vivo examination of the dynamic properties of the human heel pad," (in eng), *Int J Sports Med,* vol. 14, no. 6, pp. 312-9, Aug 1993, doi: 10.1055/s-2007-1021184.
[202] A. Gefen, M. Megido-Ravid, and Y. Itzchak, "In vivo biomechanical behavior of the human heel pad during the stance phase of gait," (in eng), *J Biomech,* vol. 34, no. 12, pp. 1661-5, Dec 2001, doi: 10.1016/s0021-9290(01)00143-9.
[203] D. De Clercq, P. Aerts, and M. Kunnen, "The mechanical characteristics of the human heel pad during foot strike in running: an in vivo cineradiographic study," (in eng), *J Biomech,* vol. 27, no. 10, pp. 1213-22, Oct 1994, doi: 10.1016/0021-9290(94)90275-5.
[204] X. G. Yang *et al.*, "Comparison of material properties of heel pad between adults with and without type 2 diabetes history: An in-vivo investigation during gait," (in eng), *Front Endocrinol (Lausanne),* vol. 13, p. 894383, 2022, doi: 10.3389/fendo.2022.894383.
[205] B. K. P. Horn, H. M. Hilden, and S. Negahdaripour, "Closed-form solution of absolute orientation using orthonormal matrices," *J. Opt. Soc. Am. A,* vol. 5, no. 7, pp. 1127-1135, 1988/07/01 1988, doi: 10.1364/JOSAA.5.001127.
[206] S. Prichasuk, P. Mulpruek, and P. Siriwongpairat, "The heel-pad compressibility," (in eng), *Clin Orthop Relat Res,* no. 300, pp. 197-200, Mar 1994.
[207] N. Ahanchian, C. J. Nester, D. Howard, L. Ren, and D. Parker, "Estimating the material properties of heel pad sub-layers using inverse Finite Element Analysis," (in eng), *Med Eng Phys,* vol. 40, pp. 11-19, Feb 2017, doi: 10.1016/j.medengphy.2016.11.003.
[208] Y. Wang, D. W.-C. Wong, and M. Zhang, "Computational Models of the Foot and Ankle for Pathomechanics and Clinical Applications: A Review," *Annals of Biomedical Engineering,* vol. 44, pp. 213-221, 2016, doi: 10.1007/s10439-015-1359-7.